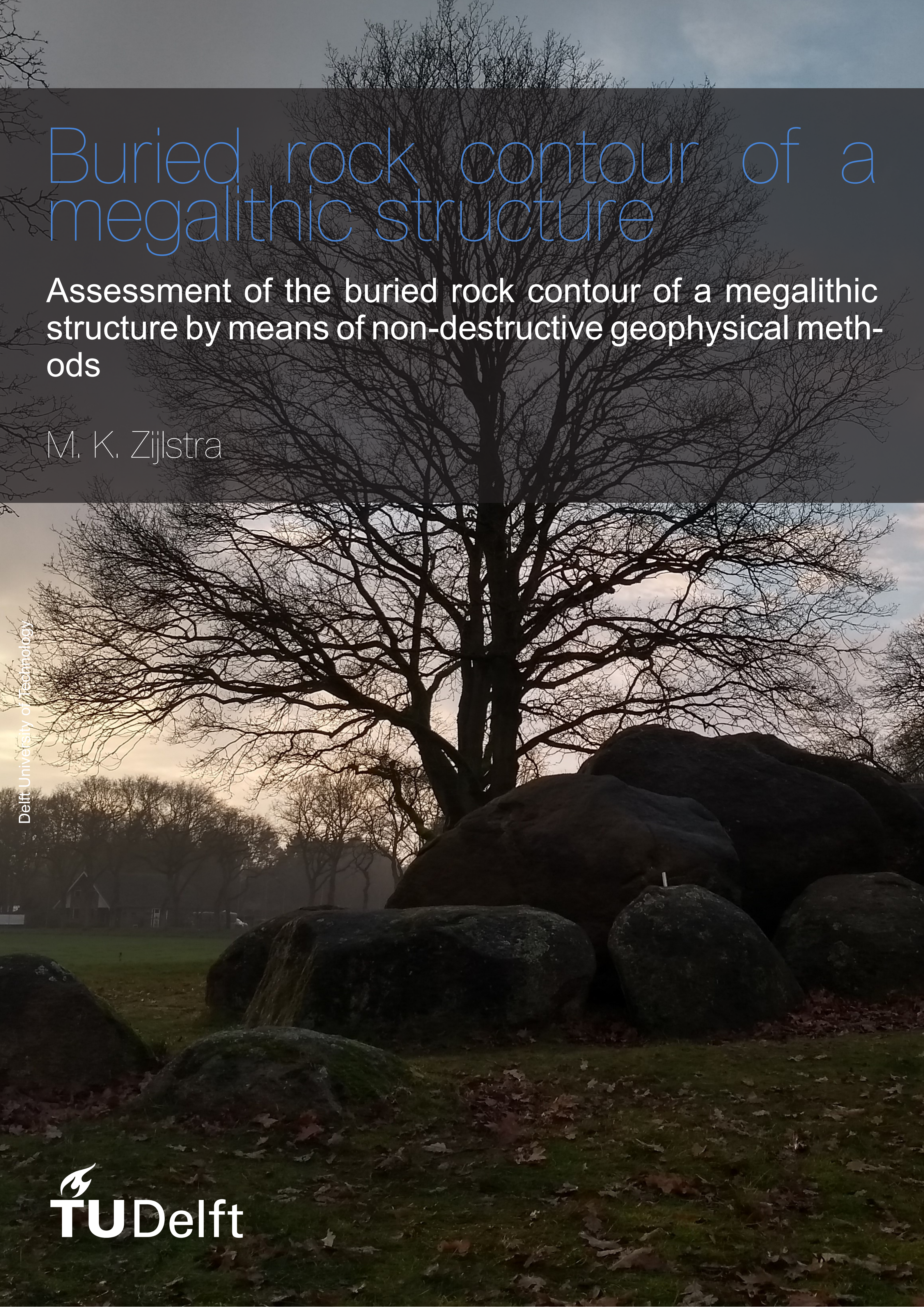

Buried rock contour of a megalithic structure

Assessment of the buried rock contour of a megalithic structure by means of non-destructive geophysical methods

M. K. Zijlstra

Delft University of Technology

Buried rock contour of a megalithic structure

Assessment of the buried rock contour of a megalithic structure by means of non-destructive geophysical methods

by

M. K. Zijlstra

Student Name	Student Number
Maarten Zijlstra	4591348

Institution: Delft University of Technology
Place: Faculty of Civil Engineering and Geosciences
Project Duration: February, 2021 - February, 2022

Thesis committee

Chair of Committee:	Dr. Ir. D.S. (Deyan) Draganov	TU Delft, Applied Geophysics and Petrophysics
University Supervisor:	Dr. Ir. D.J.M. (Dominique) Ngan-Tillard	TU Delft, Geo-Engineering
University Supervisor:	Dr. Ir. Y. (Yuguang) Yang	TU Delft, Concrete Structures

Cover Image: Hunebed D14 near Eexterhalte, Drenthe, The Netherlands, from North-East including the damaged capstone D9

Preface

This thesis forms the final product of my 2.5 years of studying Geo-Engineering, which I enjoyed very much. Even though Covid-19 was a bit of a displeasure throughout these years, to put it mildly, I consider my master's one of the best parts of my study experience and I am glad I was able to do that in Delft at the TU. The thesis took me almost exactly a year to write, which might have been a bit longer than originally anticipated by me, my committee and others involved, but I think it was a good experience from which I've learned a lot. I am nevertheless glad and proud to present this thesis to you.

The path I followed throughout my master thesis started a bit unusual. Geo-Engineering prepared me for evaluating rock types, designing foundations and understanding soil behaviour. However, when I encountered the opportunity of investigating the burial depths of rocks from a 'Hunebed', I felt like I had to switch to this more Geophysical topic. The experience of using the Ground Penetrating Radar and obtaining information on the buried rock contour was exciting and during the thesis, I became more comfortable with using the GPR as well as interpreting the results. Although the seismic measurements weren't that successful originally (and have not been applied in the field), I think I have learnt even more from the struggles and setbacks concerning doing research.

First of all, I want to thank the Rijksdienst voor het Cultureel Erfgoed and the Stichting Het Drentse Landschap for giving the opportunity to work on a 'Hunebed' for my master thesis and allowing me to perform surveys on it. As I'm originally from the province of Drenthe, I already had an affinity with said megalithic structures. I could therefore not pass the once-in-a-lifetime opportunity of researching the burial depth of the bearing stones of D14.

Furthermore, this project would not have been possible without my committee members. First, I would like to thank my chair supervisor, Deyan Draganov, for his knowledge regarding seismic measurements and his practical view which kept me on track and simplified problems. Then, I'd like to thank my university supervisor, Dominique Ngan-Tillard, for her support regarding the field works and GPR throughout my thesis as well as for checking in with me to make sure I kept making progress. Finally, I would like to thank my second university supervisor, Yuguang Yang, for helping me find transducers for the seismic measurements and making time to discuss possible research topics, even though those didn't happen in the end. A special thanks also to Karel Heller. While not part of my committee, he helped me by preparing and performing many seismic measurements. Although these weren't always promising, they did in the end contribute to my thesis.

Then, I would like to thank the Groningen Institute of Archaeology and especially Theo ten Anscher for sending me crystal clear historic photos of 'Hunebed' D14. Also big thanks to all the people who helped with the fieldworks (Emy, Lisa, Linh), which were essential for my thesis. Finally, thanks to my fellow students and friends to get me through the hardest parts.

Maarten Zijlstra
Delft, February 2022

Summary

The dolmens erected in the province of Drenthe between 3350-2700 BC are the most ancient monuments of the Netherlands. They consist of a long assemblage of rocks capped with boulders which served as burial chambers for the Funnel Beaker population. Despite their robust look, dolmens are vulnerable. For example, one of the caprocks of dolmen D14 fell off in 2019, once again. The method currently used to repair megaliths is not optimal: a crane is mobilized and the rocks are repositioned using a trial and error strategy. The reconstruction scenario should be selected and fine-tuned digitally beforehand. Moreover, the structural stability of the new assemblage of rocks should also be checked numerically. This necessitates a digital model of all the rocks that have to be rearranged. Not only the visible part of these rocks has to be digitized. The buried parts of the support rocks have to be modelled too as these rocks might have to be displaced and tilted to obtain a more compact and interlocked structure. Since dolmens occupy a prominent position in the Dutch heritage, only non-destructive see-through techniques have to be used for imaging the hidden contours of the bearing rocks. In addition, the bearing stones have complex geometries and are not isolated, which increases the complexity of the problem.

Two suitable geophysical methods are the Ground Penetrating Radar (GPR) and seismic techniques with a focus on reflection measurements. For the GPR specifically, we choose a Common Offset Survey, which can map reflections from the subsurface. For the seismic techniques, we choose a line array measurement, among others. We use the GPR to estimate the buried rock contour of the keystone Sl2 of megalith D14, which is a bearing stone formerly supporting capstone D9. We perform several reflection tests on various rocks unrelated to D14 using different seismic sources and receivers to estimate the reflection depths. We follow a proposed approach for both methods.

To evaluate the GPR data from the field, we assume a simplified GPR with zero-dimensional antennas (GPR point model). Subsequently, we develop two mathematical models (GPR point-to-GEO and GEO-to-GPR point model), based on this conceptual model in order to I) calculate the (buried) rock surfaces from field data and II) model field data from estimated buried rock contours.

We first perform the Common Offset Survey on a non-buried boulder on the campus of the TU Delft to evaluate the accuracy of the developed GPR point-to-GEO model and to optimise the second survey on keystone Sl2. We first perform the seismic reflection measurements on several rock samples to determine the best seismic source. Finally, we perform a line array measurement on a cylindrical basalt column using 300 kHz transducers.

We calculate rock contour coordinates from the GPR data and these show a reasonable fit with the contour of the TU Delft boulder, with an accuracy of 5-10 cm. For the keystone Sl2, the maximum burial depth is determined to be 80 cm at the southern side. The bottom of the keystone is sloping downward starting from ground level at the northern side. The southern, eastern and western rock faces are steep, almost vertical, which is confirmed by historic photographs. However, the calculated (buried) rock surface coordinates consist of an incoherent set of coordinates with locally a lack of data or blind-spots. Estimating a coherent buried rock contour, therefore, requires shortcuts and a decrease of accuracy is to be expected especially for rock surfaces near blind-spots in the GPR data. Furthermore, the identification of relevant reflection surfaces is rather subjective and combined with blind spots in the acquired GPR data, this can lead to wrongful interpretations of the buried rock contour.

The seismic reflection measurements we perform give clear reflections for the 300 kHz transducers on rocks of limited size with simple geometries. However, the transducers should first be applied on rocks with increasingly more complex geometries before being applied in the field. The accuracy in the order of 1 cm can be considered promising, but its applicability for complex geometries and reflection depths larger than 0.5 m remains unknown.

Contents

Nomenclature

Abbreviations

Abbreviation	Definition
AV	Average velocity
COS	Common Offset Survey
CMP	Common Midpoint Survey
DC	Direct current
D8	Capstone **8** ('**D**eksteen' in Dutch) of dolmen D14
D9	Capstone **9** ('**D**eksteen' in Dutch) of dolmen D14
D14	Dolmen **14** ('Hunebed' in Dutch) located in the Province of **D**renthe
(I)GEO-to-GPR point	Developed mathematical model to construct GPR data recorded during a Common Offset Survey on a rock surface for an estimated buried rock contour
GIA	Groningen Institute of Archaeology
GPR	Ground Penetrating Radar
(II)GPR point-to-GEO	Developed mathematical model to convert acquired GPR data during a Common Offset Survey on a rock surface to a buried rock contour
LiDAR	Light Detection and Ranging or Laser Imaging Detection and Ranging
NDT	Non-destructive testing
P-wave	Compressional (longitudinal) wave
Sl2	Keystone **2** ('**Sl**uitsteen' in Dutch) of dolmen D14
S-wave	Shear (transverse) wave
UPV	Ultrasonic Pulse Velocity
WARR	Wide Angle Reflection and Refraction

(I)/(II) *label to link parameters to either of the two mathematical models*

Symbols

Symbol	Definition	Unit
A	Amplitude	[V]
a	Non-linear parameter of empirical attenuation model	[1/s]
C	(I)Slopes, 2D coordinates and lengths of rock surfaces	[°, m]
C	(II)Slopes and 2D coordinates of rock surfaces	[°,m]
C^{GPR}	(II)Slopes and 2D coordinates of rock surfaces in GPR survey path	[°, m]
C_p	(I)Python dictionary of GPR survey path coordinates	[-]
C_r	(I)Python dictionary of rock surface coordinates	[-]

Symbol	Definition	Unit
c	Linear parameter of empirical attenuation model	[V]
c_b	(II)Buried rock surface contour coordinates	[m]
c_s	(II)Trace origin coordinates along exposed rock surface contour	[m]
crd_{GPR}	(I)Coordinates of GPR traces	[m]
crd_{prp}	(I)Coordinates of perpendicular traces	[m]
crd_{srf}	(I)Coordinates of surface traces	[m]
crd_{tr}	(I)Coordinates of reflection surfaces	[m]
crd_{vrt}	(I)Coordinates of vertical traces	[m]
crd_0	(I)(II)Start coordinate of the GPR survey	[-]
crd_1	(I)(II)End coordinate of the GPR survey	[-]
D	Depth of reflection surface w.r.t. center of GPR	[m]
D_{graph}	(I)(II)Graph size	[-]
div	(II)Index number of rock surface corresponding to trace	[-]
E	Young's or Elastic modulus	[Pa]
f	Frequency	[Hz]
f_c	Center frequency	[Hz]
G	Shear modulus	[Pa]
g	Gain function of Inverse Amplitude Model	[V]
H_r	Horizontal resolution	[m]
h	Vertical distance	[m]
I	(I)(II)Showing of GPR diagram	[-]
iD_{GPR}	(I)Index number of rock surface corresponding to GPR trace	[-]
iD_{tr}	(I)Index number of rock surface corresponding to reflection surface	[-]
iD_{vrt}	(I)Index number of rock surface corresponding to vertical trace	[-]
L	Distance to reflection surface	[m]
L_{GPR}	(I)Lengths of GPR traces	[m]
L_{appr}	Approximated travel path of reflection	[m]
L_{tr}	(II)One-way travel distances of traces	[m]
L_{tr}	(I)Origins of traces along rock surface	[m]
L_{tr}^{max}	(I)Maximum length of traces	[m]
L_{true}	True travel path of reflection	[m]
L_{1w}	One-way travel path of reflection	[m]
L_{2w}	Two-way travel path of reflection	[m]
l_{tr}	(II)One-way travel distance corresponding to trace	[m]
M	Constrained modulus	[Pa]
M_s	(II)Spatial steps of vertical traces with maximum time duration	[m]
M_s^{new}	(II)Spatial steps of vertical traces to reflection surfaces	[m]
M_t	(II)Time steps of vertical traces with maximum time duration	[s]
M_t^{new}	(II)Time steps of vertical traces to reflection surfaces	[s]
N_{dtr}	(I)(II)Number of steps within trace	[-]
N_{tr}	(I)(II)Number of traces	[-]
n_{cl}	(I)(II)Colour scheme indicator for graphs	[-]
P	(I)Slopes, 2D coordinates and lengths of rock surfaces in GPR survey path	[°, m]
R	Reflection coefficient	[-]
S	Length GPR survey path	[m]

Symbol	Definition	Unit
S	(II)Slopes and 2D coordinates of reflection surfaces	[°, m]
S_p	(I)GPR survey path slope coordinates	[m]
S_r	(I)Rock surface slope coordinates	[m]
S_{tr}	(I)(II)Trace origins along GPR survey path or horizontal axis of GPR diagram	[m]
S_0	(II)Spatial starting coordinates of reflection surfaces	[m]
S_1	(II)Spatial ending coordinates of reflection surfaces	[m]
s_{step}	(I)(II)Spacing between consecutive traces	[m]
s_0	(II)Spatial starting coordinate of reflection surface in GPR diagram	[m]
s_1	(II)Spatial ending coordinate of reflection surface in GPR diagram	[m]
T	Wave period	[s]
T_{GPR}	(I)Two-way travel times of GPR traces	[s]
T_{tr}	(I)Two-way travel times of traces in GPR diagram	[s]
T_{tr}^{max}	(II)Time steps along vertical axis GPR diagram	[s]
T_0	(II)Temporal starting coordinates of reflection surfaces	[s]
T_1	(II)Temporal ending coordinates of reflection surfaces	[s]
t_{tr}^{max}	(I)(II)Maximum time duration of trace	[s]
t_0	Time of signal emission	[s]
t_0	(II)Temporal starting coordinate of reflection surface in GPR diagram	[m]
t_1	(II)Temporal ending coordinate of reflection surface in GPR diagram	[m]
t_{1w}	One-way travel time	[s]
t_{2w}	Two-way travel time	[s]
V_r	Vertical resolution	[m]
v	Average velocity	[m/s]
v_{GPR}	(I)(II)Propagation velocity of radio waves through a medium	[m/s]
v_p	Propagation velocity of compressional waves through a medium	[m/s]
v_s	Propagation velocity of shear waves through a medium	[m/s]
v_{seis}	Propagation velocity of seismic waves through a medium	[m/s]
X_{GPR}	(I)Horizontal coordinates of GPR traces	[m]
X_{lim}	(I)Horizontal boundary coordinates of traces	[m]
X_{prp}	(I)Horizontal coordinates of perpendicular traces	[m]
X_{srf}	(I)Horizontal coordinates of surface traces	[m]
X_{vrt}	(I)Horizontal coordinates of vertical traces	[m]
X_0	(I)(II)Horizontal starting coordinates of rock surface	[m]
X_0^{GPR}	(II)Horizontal starting coordinates of rock surfaces in GPR survey path	[m]
X_1	(I)(II)Horizontal ending coordinates of rock surface	[m]
X_1^{GPR}	(II)Horizontal ending coordinates of rock surfaces in GPR survey path	[m]
x	Distance between antenna and GPR center	[m]
x_b	(II)Horizontal buried rock surface coordinate	[m]
x_s	(II)Horizontal trace origin coordinate	[m]
x_{tr}	(I)Horizontal trace origin coordinate	[m]

Symbol	Definition	Unit
x_0	(I)(II)Horizontal starting coordinate of rock surface	[m]
x_1	(I)(II)Horizontal ending coordinate of rock surface	[m]
Z_{GPR}	(I)Vertical coordinates of GPR traces	[m]
Z_{lim}	(I)Vertical boundary coordinates of traces	[m]
Z_{prp}	(I)Vertical coordinates of perpendicular traces	[m]
Z_{srf}	(I)Vertical coordinates of surface traces	[m]
Z_{vrt}	(I)Vertical coordinates of vertical traces	[m]
Z_0	(I)(II)Vertical starting coordinates of rock surface	[m]
Z_0^{GPR}	(II)Vertical starting coordinates of rock surfaces in GPR survey path	[m]
Z_1	(I)(II)Vertical ending coordinates of rock surface	[m]
Z_1^{GPR}	(II)Vertical ending coordinates of rock surfaces in GPR survey path	[m]
z_b	(II)Vertical buried rock surface coordinate	[m]
z_s	(II)Vertical trace origin coordinate	[m]
z_{tr}	(I)Vertical trace origin coordinate	[m]
z_0	(I)(II)Vertical starting coordinate of rock surface	[m]
z_1	(I)(II)Vertical ending coordinate of rock surface	[m]
A_s	(I)(II)Rock surface slopes	[°]
A_s^{GPR}	(II)Rock surface slopes in GPR survey path	[°]
α	Attenuation	[dB/m]
α_s	(I)(II)Slope of rock surface	[°]
α_{tr}	(II)Angle of reflection w.r.t slope of rock surface	[°]
B	(II)Reflection surface slopes	[°]
β	(II)Slope of reflection surface in GPR diagram	[°]
γ	(II)Angle of reflection w.r.t vertical	[°]
Δl	(I)(II)Length of rock surface slope	[m]
ΔL	(II)Rock surface lengths	[m]
ΔL	(I)Cumulative rock surface lengths	[m]
ΔL_{tr}	(I)Spatial step within traces	[m]
ΔL^{GPR}	(II)Cumulative rock surface lengths in GPR survey path	[m]
Δt_{tr}	(I)(II)Time step within trace	[s]
Δt_{2w}	(II)Two-way travel time corresponding to trace	[s]
Δx_a	Separation receivers in line array measurement	[m]
Δx_0	Separation source and receiver	[m]
ϵ	Relative Permittivity or dielectric constant	[-]
θ_i	Angle of incident wave	[°]
θ_r	Angle of reflected wave	[°]
λ	Wave length	[m]
ν	Poisson's ratio	[-]
ρ	Mass density	[kg/m^3]
σ	Electrical conductivity	[mS/m]

List of Figures

List of Tables

1

Introduction

This chapter contains the introduction to the MSc Thesis including the project context, the proposed techniques, the problem refinement and definition and finally, the research questions.

1.1. Pilot project

Megalithic structures in the Netherlands date back to about 3350-2700 BC according to Bakker (2010), and are locally known as ”Hunebedden” or ”Giant’s beds”. These dolmens were constructed by the Funnel Beaker Culture and functioned, among others, as burial chambers and were originally (partially) covered by sand or loam. The structures consist of erratic boulders transported to the Netherlands by the Saalian glaciers. The boulders are originally from Fenno-Scandia and the eastern Baltic.

The boulders are predominantly granitic, and a research into the stones performed by Bekkema et al. (2014) at three megalithic structures in the province of Drenthe, the Netherlands, identified mostly (south Scandinavian) Småland granites, Finnish microcline granites and Rapakivi granites. From Theuws (2021), it was concluded that D14 specifically consisted of at least five different granites, all originating roughly from southern Sweden. These are Småland, biotite, Växjö, microcline and Kinda granites.

In 2019, the ’Hunebed’ D14 near Eexterhalte, Drenthe, The Netherlands (Figure 1.1), was damaged and capstone D9, which was previously repaired after earlier damage, fell off (Timmer, 2019).

Figure 1.1: Hunebed D14 from south-east in 2021, with capstone D9 and keystone Sl2.

In order to safely restore D14 and to serve as a pilot project for possible future restorations, a multidisciplinary approach was proposed to make a digital 3D reconstruction of the megalithic structure. The digital reconstruction will be used to assess the stability of the hunebed and possibly to find the optimal placement for capstone D9 and perhaps other stones (Theuws, 2021). At the moment, no intention of altering the current state of D14 exists, and the reconstruction remains purely digital.

Besides the structural analysis, an investigation into the buried rock contour of the bearing stones is carried out, which leads to the aim of this research. The 3D reconstruction used in the structural analysis can be improved by determining the buried contour of the bearing stones. With these buried rock contours, the structural behaviour of the bearing stones can be included in the stability analysis (e.g. effect of horizontal earth pressure). Furthermore, it is beneficial that the shape of the bearing stones is known if it is concluded that specific bearing stones need to be rearranged to stabilise the megalithic structure.

As the megalithic structures in the Netherlands are cultural heritage, 'Hunebed' D14 is protected and any damage to the site is not allowed (Rijksdienst voor Cultureel Erfgoed, 2020). Therefore, non-invasive geophysical methods are considered, which do not require harming the site or the stones.

First, a brief history regarding Hunebed D14 is given, after which a short literature study into the applicability of the proposed non-invasive geophysical methods is given. Then, the research problem in this thesis is refined and defined. Finally, the research questions are stated.

1.2. Hunebed D14

Based on a technical report by Ten Anscher (2019) into the history of Hunebed D14 with special regard to the fallen capstone D9, a brief timeline of the megalithic structure since the start of the nineteenth century is given.

pre ± 1850 - D14 excavated through the ages, boulders removed and split, to be used in foundations of dykes and buildings, such as churches.
1871 - D14 becomes property of the Province of Drenthe and the hill still partially covering the dolmen is leveled.
1873 - Oldest known photograph of D14 by Julius von Kolkow.
1919 - D14 visited by Albert Egges van Giffen who studied the state of all dolmen in the Netherlands, commissioned by the Dutch government.
1925 - D14 featured, among others, in the publication of 'De Hunebedden van Nederland' ('The dolmen of the Netherlands') by van Giffen.
1927 - D14 excavated followed by a restoration attempt led by Van Giffen.
1957 - Statement indicating that capstone D9 has fallen into the basement of D14 and has broken in half in previous years. Furthermore, capstone D8 and keystone Sl2 were fractured.
1959 - Cracks in D8 and Sl2 presumably repaired with mortar.
1963 - Capstone D9 removed and possibly repaired. Pedestal of small boulder created to support D9.
1965 - Restoration attempt of D14. Repaired capstone D9 finally replaced, but the former north-facing side is now facing south. Furthermore, keystone Sl2 tilted to support D9.
1996 - Restoration attempt of D14. Pedestal supporting D9 removed, the capstone is now supported by a metal pin at the north side and cement like material at the south side. Moreover, the mortar used in previous repairs is replaced by epoxy.
2000 - Superficial damage to D14. Flakes were knocked off several stones.
2019 - Capstone D9 again fallen into the basement, presumably due to vandalism.

During the excavation in 1927 several photos were taken. A small selection is displayed in section 8.6. Figure 1.2 shows D14 from the south-east before the excavation of 1927. It can clearly be seen that capstone D9 has been dislocated and that keystone Sl2 has been rotated. Furthermore, the capstones in the current state are clearly positioned differently than in 1925-1927.

Figure 1.2: Hunebed D14 from south-east between 1925-1927 from GIA (Groningen Institute of Archaeology) (Ten Anscher, 2019), with capstone D9 and keystone Sl2.

1.3. Non-destructive geophysical methods

A small literature research was carried out into promising non-destructive geophysical methods.

Martinho and Dionísio (2014) performed a review study into non-destructive evaluations in cultural built heritage. They looked into the main geophysical techniques that are applied to investigate monuments and cultural artifacts. It was shown that, among others, seismic methods and the Ground Penetrating Radar (GPR) were successfully used into obtaining information on the internal integrity of rock masses. From Martinho and Dionísio (2014), it was determined that the GPR is a widely used technique in many fields and different researchers applied the GPR to study the geological contact between different superficial materials and bedrock (Dallimore & Davis, 1987), detection of voids, fractures, seepage and soil and groundwater contamination (Benson, 1995, Stevens et al., 1995, Longoni et al., 2012), non-destructive testing of stone quality in quarries (Lualdi & Zanzi, 2004) and pre-excavation for archaeological investigations (Conyers & Leckebusch, 2010).

Martinho and Dionísio (2014) also concluded that seismic methods (both sonic and ultrasonic techniques) are often applied to detect the thickness and position of weathering layers, physical properties of different materials (incl. mechanical characteristics), the state of cracking, fractures and other discontinuous elements (Cosentino et al., 2009, Capizzi et al., 2013).

Masini et al. (2010) monitored a wall, a masonry pillar and a marble column with GPR in order to detect cracks, characterize the masonry and use imaging techniques to identify metallic reinforcement bars. The monitoring of several columns showed that an investigated calcarenite column of up to 2.5 m thickness showed no internal anomalies, whereas the reinforcement bars in a 60 cm thick marble column were clearly identifiable as well as a restored fracture.

(Ultra-)sonic techniques have often been used in the analysis of the internal integrity, both in-situ and in laboratory, of various building materials according to Martinho and Dionísio (2014). Cardarelli and Nardis (2001) successfully identified internal damages by applying seismic refraction and seismic transmission tomography on three marble columns in Rome, Italy. They could distinguish fractures, small cracks and determine the depth of weathering and anisotropy. Fort et al. (2013) performed a study in which they assessed granitic rocks from two architectural heritage monuments in Madrid, Spain, using indirect ultrasound velocity measurements and the Schmidt Hammer. A similar assessment was conducted on the rock from which the granite was originally quarried for comparison. They concluded that non-destructive geophysical methods are reliable indicators (estimated ultrasound velocity and surface strength measured by the Schmidt Hammer) of the degree of decay in stone materials.

Martinho and Dionísio (2014) compared the applicability of the GPR and (Ultra-)sonic techniques to the analysis of the preservation state of ancient monuments, masonry and stone columns. They concluded that GPR is adequate for determining the:

1. Thickness of walls,
2. Location of detachments, voids or cracks,
3. Location and size of reinforcement bars,
4. Moisture content,
5. Evaluation of repair interventions,

while (ultra-)sonic techniques are appropiate to establish the:

1. Location of detachments, voids or cracks,
2. Decay of building material,
3. Evaluation of repair interventions.

It can be concluded that both the GPR and the seismic (ultra-)sonic techniques are already widely applied in preserving monuments, masonry and stone columns. The applicability of these methods to estimate the buried rock contour of the bearing stones is discussed in the next section.

1.4. Problem refinement and definition

The main areas of interest for this research are the fallen capstone D9 and the partially buried eastern keystone Sl2. Capstone D9 has fallen into the basement (Figure 1.3a and 1.3b) and therefore the bearing stones formerly supporting D9 are easily accessible of which keystone Sl2 is the most interesting. The keystone is supposed to lock the assemblage of rocks forming the megalith structure and may work as a buttress. Sl2 has not fulfilled this function since the restoration attempt in 1965. Since then, the top of Sl2 lies flat and has not been in contact with D9, even before the fall of D9 in 2019. It is therefore logical to consider a reconstruction scenario in which Sl2 is titled to its position from before 1965 to fulfill the function of keystone again. Hence, the topography of the hidden faces of Sl2 has to be revealed. This buried rock contour can be partially obtained with help from historic and modern photographs. However, to fully capture the buried rock contour of the keystone, more advanced methods are required.


(a) (b) (c)

Figure 1.3: Capstone D9 and keystone Sl2 from north-east (a), south-east (b) and east (c). The metal pin in the northern bearing stone in (a) was used to fixate capstone D9 during the restoration attempt in 1996. A repaired crack in (b) can be seen, presumably from the restoration attempt in 1965 and 1996. Another repaired fracture indicated in red, can be seen in (c), presumably from the restoration attempts in 1959 and 1996.

As stated in section 1.1, non-invasive or non-destructive geophysical methods are considered to estimate the buried rock contour in order to not disturb the site of D14. Non-destructive geophysical methods are already widely applied in the preservation of (ancient) monuments (see section 1.3). The Ground Penetrating Radar and seismic (ultra-)sonic techniques can be used to determine the location of cracks and thicknesses of walls and therefore appear to be suitable for estimating the distance to buried rock faces. However, the applicability of the GPR and seismic methods on megalithic structures to determine the buried rock contours of the bearing stones is not yet proven.

First of all, the bearing stones are partially buried, which reduces the available surface that can be surveyed drastically. Furthermore, this means that reflection or indirect measurements are required to estimate the buried rock contour.

Secondly, the geometries of the bearing stones of D14 differ from the often smooth cylindrical or rectangular columns/stones and planar masonry walls mentioned in section 1.3. The exposed surfaces of the bearing stones are irregular and rough, which increases the difficulty in obtaining accurate measurements (contact).

Thirdly, interference of other, buried, rocks or bearing stones located close-by can cause difficulties in interpreting the origin of the reflections due to the 3-dimensional nature of the reflections. Similar interpretation difficulties can occur due to interference of reflections from (repaired) cracks in the keystone, see Figure 1.3c. On the other hand, it was established in section 1.3 that the geophysical methods are able to detect detachments, voids and cracks. This means that the integrity of the rocks could possibly be assessed if the reflections from these discontinuities are distinguishable from reflections from the buried rock faces.

Consequently, (accurately) estimating the buried rock contour of the keystone might be difficult and this problem therefore displays the importance of this research.

1.5. Research questions

From the previous section, it becomes clear that some uncertainties exist with respect to the applicability of non-destructive geophysical methods to estimate the contour of a buried rock. Combined with the partially buried keystone Sl2 of megalith D14, this leads to the main research question, which reads as follows,

- What is the buried rock contour of the bearing stones of megalith D14 estimated using non-destructive geophysical methods?

Four more subquestions are created, which assist in answering the main research question,

- Which geophysical methods are suitable for finding the buried rock contour of the bearing stones?
- How can geophysical methods be applied in order to find the buried rock contour of rocks with complex topography?
- How can historic photographs assist in proving the buried rock contour derived from geophysical data?
- What is the accuracy of the found buried rock contour?

Non-destructive geophysical methods are already applied on (ancient) monuments to locate detachments, voids or cracks. As keystone Sl2 of megalith D14 might be repositioned during reconstruction (section 1.4, the stone should be able to undergo such a movement. Therefore, a stand-alone research (sub-)question is created to possibly evaluate the integrity of the bearing stones (and Sl2 specifically),

- What is the integrity of the bearing stones?

This thesis aims to answer the research questions by first discussing suitable geophysical methods for finding the buried rock contour in Chapter 2. Furthermore, a stepwise approach is proposed to I) estimate the buried rock contour of the keystone Sl2 using the GPR and to II) estimate the reflection depths of various rocks unrelated to D14 using seismic sources and receivers.

Chapter 3 contains the description of a conceptual model (*GPR point model*), which assumes zero-dimensional antennas for the GPR for the sake of simplification. Two mathematical models are developed based on this conceptual model in Chapter 4 and 5 to I) calculate the (buried) rock surfaces of rocks from field data (*GPR point-to-GEO*) and to II) model field data for estimated (buried) rock contours (*GEO-to-GPR point*). Then, a detailed methodology for the Ground Penetrating Radar is given in Chapter 6 for the stepwise approach proposed in Chapter 2.

First, a field survey is performed on a non-buried boulder to evaluate the accuracy of the calculated buried rock surfaces using the *GPR point-to-GEO* model and to serve as a guide to optimise future surveys for megalith D14. Then, a field survey is performed on the keystone Sl2 of megalith D14 to estimate its buried rock contour using both mathematical models. The results from these two field surveys are given in Chapter 7 and 8. Chapter 9 then contains the discussion regarding these results.

Chapter 10 gives the methodology used for the seismic methods following from the stepwise approach proposed in Chapter 2. Then, seismic tests are performed on various rocks unrelated to D14 to determine the best seismic source and receivers as well as calculating the reflection depths. The results are given in Chapter 11. Chapter 12 then contains the discussion regarding these results.

Finally, the conclusion can be found in Chapter 13, which contains the answers to the research questions and recommendations regarding future research.

2

Geophysical testing methods

The research question is stated in Chapter 1 and is answered with help of geophysical testing methods. The proposed methods are the Ground Penetrating Radar (GPR) and (Ultra-)sonic seismic techniques. First, the GPR and the seismic methods are briefly explained including the possible types of data acquisition for each. Furthermore, the resolution and limitations/requirements are given for both geophysical methods. This is then followed by the determination of the most suitable types of data acquisition and their application to either keystone SI2 or other rocks. It also contains the proposed approach to I) estimate the buried rock contour of the keystone SI2 using the GPR and to II) estimate reflection depths of rocks unrelated to the dolmen D14 using seismic sources and receivers.

2.1. GPR

Ground Penetrating Radar or GPR is a high-resolution technique using electromagnetic waves with a center frequency in the range of 10-2600 MHz to image the subsurface. The GPR signals can penetrate a medium and detect anomalies due to differences in dielectric properties within that medium (Martinho & Dionísio, 2014).

Several survey methods can be distinguished for the GPR. These are:

1. Reflection Profiling / Common Offset Survey
2. Common Midpoint Survey (CMP) or Wide Angle Reflection and Refraction (WARR)
3. Transillumination Survey / Radar Tomography

2.1.1. Common Offset Survey

The Common Offset Survey is the most used GPR survey mode (in reflection), see Figure 2.1a. The distance between the transmitter and (single) receiver is fixed. The transmitter and receiver are moved along a path, and data is collected at every new position. It is useful for the estimation of the buried rock contour of the stones as the signal reflects off from changes in the subsurface, such as rock-soil interfaces. From the resulting (2D) radargrams these changes and objects can be located (Oldenburg et al., 2017b), see Figure 3.1b in section 3.1 for an example of such a radargram.

2.1.2. Common Midpoint Survey

Contrary to the Common Offset Survey, the distance between the transmitter and receiver is not fixed in the Common Midpoint Survey, see Figure 2.1b. The halfway point between them, however, is fixed while the distance increases. This is very useful to determine the thickness of and velocity through a layer, but also offers a good approach to determine the buried rock contour of the stones (Oldenburg et al., 2017b). An alternative is the WARR in which the transmitter is fixed, but the receiver is moved away from the transmitter at increasing offsets (Martinho & Dionísio, 2014).

2.1.3. Transillumination Survey

In Transillumination Surveys, multiple transmitters and receivers can be used to, for example, asses a mineshaft, the area between boreholes or pillars, see Figure 2.1c (Oldenburg et al., 2017b). This way, an adequate cross-sectional velocity distribution can be made. The biggest difference with respect to the previous surveys is that instead of measuring reflection rays, transmission rays are measured. This technique offers high resolutions (from cm's to dm's) at high frequencies (900 MHz) and is therefore common in NDT of (man-made) structures (Martinho & Dionísio, 2014). It can be used to determine the propagation velocity through a rock by doing multiple measurements.

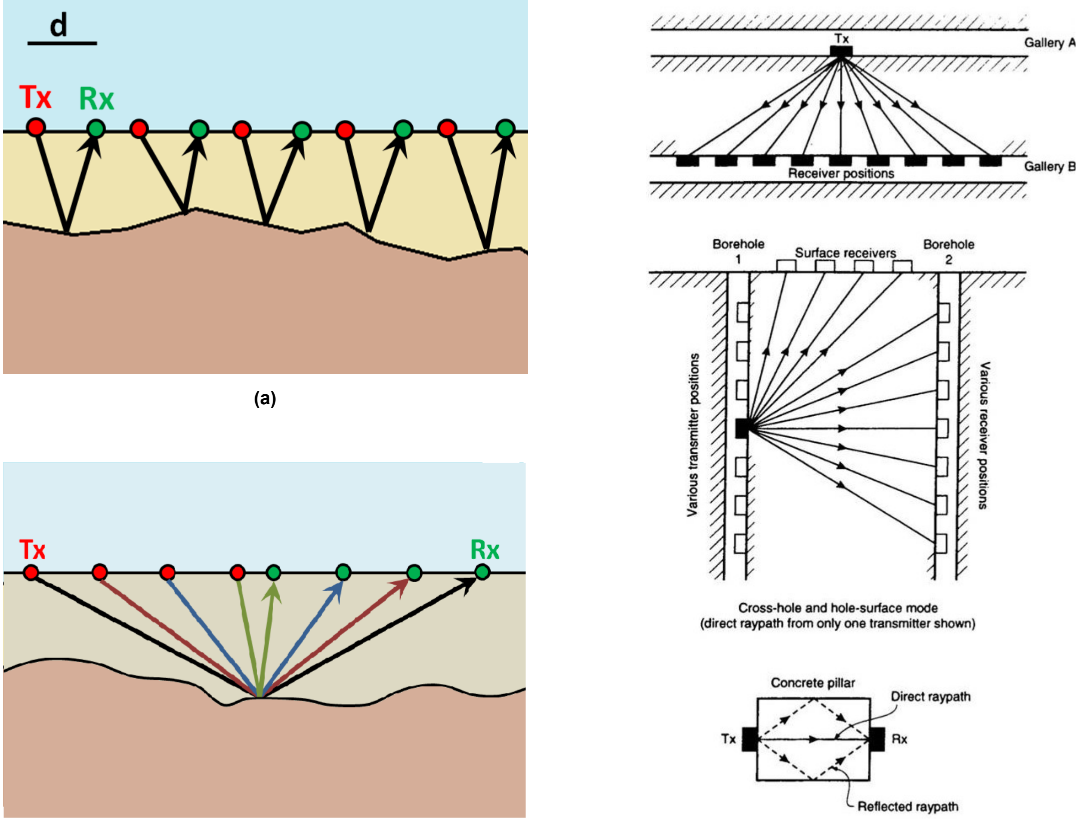

(a)

(b)

(c)

Figure 2.1: GPR survey geometries from Oldenburg et al. (2017b), with (a) the Common Offset Survey, (b) the Common Midpoint Survey and (c) several forms of a Transillumination Surveys

2.1.4. Resolution

The vertical or radial resolution of the GPR is theoretically a quarter wave length of the center frequency and independent on the depth. The actual vertical resolution is often in the order of half a wavelength, due to the bandwidth of the operating frequency (up to twice as high) and the attenuation of the higher frequencies. The used definition of the vertical resolution V_r of the GPR is then given by

$$V_r = \frac{\lambda}{4} = \frac{v_{GPR}}{4 \cdot f_c}, \tag{2.1}$$

where λ is the wavelength, f_c is the center frequency and v_{GPR} is the propagation velocity through the medium (Oldenburg et al., 2017b, Rial et al., 2009).

The horizontal resolution for a Common Offset Survey, the minimum distinguishable horizontal distance between two objects, depends on depth and has several definitions. The radius of the first Fresnel zone is often used to define the horizontal, or lateral, resolution, see Figure 2.2. The radius is given by

$$H_r = R_{f1} = \sqrt{\frac{h_1 h_2 \lambda}{h_1 + h_2}} = \sqrt{\frac{h\lambda}{2}} = \sqrt{\frac{v_{GPR} \cdot h}{2 \cdot f_c}}, \tag{2.2}$$

in which h_1 and h_2 represent the vertical distance from, respectively, the transmitter and receiver to a reflector at depth h. The fraction $\frac{h_1 h_2}{h_1+h_2}$ is then equal to $h/2$ (Perez-Gracia et al., 2008).

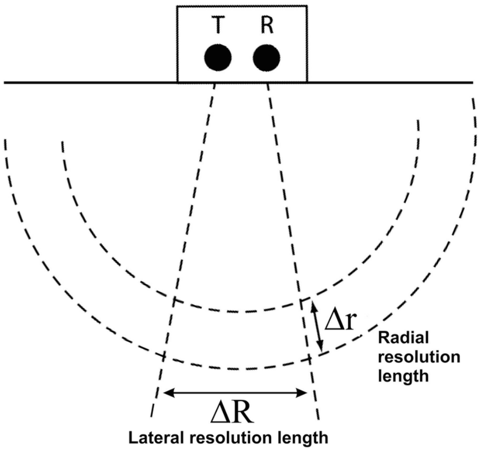

Figure 2.2: Fresnal zone for lateral resolution GPR from Nobes and Deng (2019).

It should be noted that the used definition of the center frequency f_c in Eq. 2.2 varies in the literature, as the nominal center frequency of the antenna, the dominant center frequency, and the center frequency based on the instrument bandwidth are all used according to Perez-Gracia et al. (2008). For now, the center frequency emitted by the transmitter of the GPR is used, keeping in mind that the actual measured center frequency during surveys deviates due to, among others, attenuation of higher frequencies.

2.1.5. Limitations and requirements

The GPR technique has a high potential in surveys of structures, but is also highly dependent on the circumstances in which the GPR is applied. The radio waves propagate with different speeds in different materials (natural or man-made), which has to be accounted for in depth or thickness estimations. An example of these circumstances include air in between the GPR and the surface, due to for example rough terrain. Also, the more heterogeneous the object is (e.g. many voids, reinforcement, etc.), the poorer the results become. Futhermore, water (in the form of rain, moist or pore water) severely affects the performance of the GPR (Topczewski et al., 2007).

Furthermore, radio waves from other sources or returning signals from above-ground objects (e.g. trees) can distort the results. Moreover, echoing of radio waves give unclear results, known as ringing (Oldenburg et al., 2017b). The technique itself is also inherently flawed due to noise in the data from scattering of waves due to localized non-uniformities in the material (material heterogeneity).

Finally, with decreasing GPR antenna frequencies, the penetration depth generally increases, but the resolution decreases. This means a compromise must be made between the penetration depth and the resolution (Martinho & Dionísio, 2014).

2.2. Seismic methods

Ultrasonic and sonic techniques are based on the propagation velocity differences of elastic waves in different rocks and can be applied on both in-situ rocks as well as laboratory samples. A velocity distribution within an object can be determined by using sonic or ultrasonic transducers that emit and detect signals that propagate through a medium. Based on the travel path and travel time between the source and receiver, the velocity of the wave can be estimated. It depends on the polarization of the transducers if the velocity of the shear (S) waves or compressional (P) waves is measured (Martinho & Dionísio, 2014), see Figure 2.3a. When measuring reflections, the measured wave reflections depend on the reflection surfaces, see Figure 2.3b. Shear waves cannot propagate through fluids as fluids cannot sustain shear stresses, see Figure 2.3b. However, an interface between two solids can cause reflections in the form of both P- and S-waves (Ma et al., 2021).

The Ultrasonic Pulse Velocity (UPV) is explained in the next section.

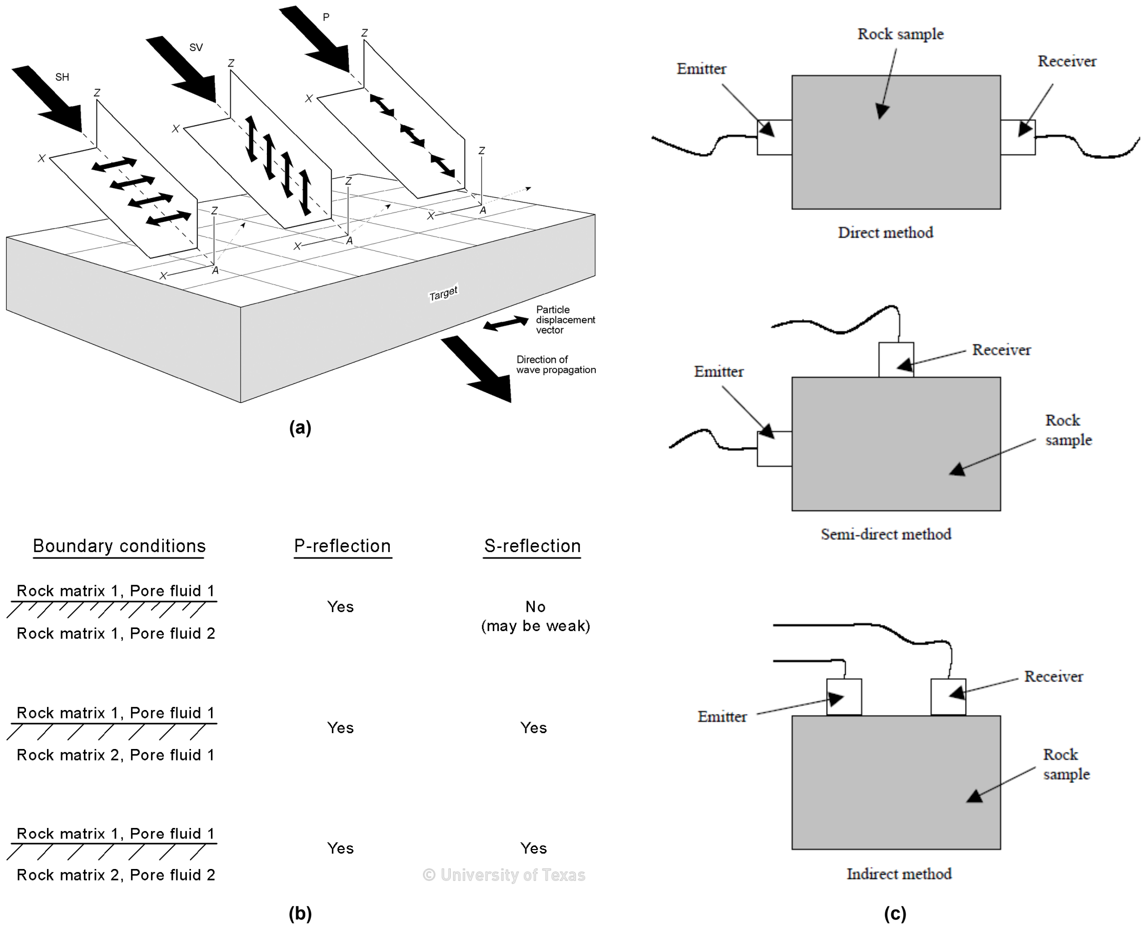

Boundary conditions	P-reflection	S-reflection
Rock matrix 1, Pore fluid 1 Rock matrix 1, Pore fluid 2	Yes	No (may be weak)
Rock matrix 1, Pore fluid 1 Rock matrix 2, Pore fluid 1	Yes	Yes
Rock matrix 1, Pore fluid 1 Rock matrix 2, Pore fluid 2	Yes	Yes

Figure 2.3: Definitions of P- and S-waves from Petrowiki (2015) (a), conditions for P- and S-reflections from Hardage (1996) (b) and three different measurement methods using transducers from Kahraman (2002) (c).

2.2.1. Ultrasonic Pulse Velocity

The ultrasonic pulse velocity (UPV) is a convenient method to asses an object, such as a column or statue, as a 2D or even 3D velocity distributions can be made by taking measurements at different locations (see also the Transillumination Survey for the GPR). The so-called ultrasonic tomography is often used in the analysis of concrete structures or ancient artefacts and monuments and even offers insight into the properties of rocks (Martinho and Dionísio, 2014, Wanniarachchi et al., 2017, Vasconcelos et al., 2008).

As can be seen in Figure 2.3c, depending on the positioning of the transducer and receiver, reflection or transmission/attenuation measurements are taken. The direct method in Figure 2.3c measures the transmission of a signal through a medium, which can therefore also be used to measure the attenuation of a signal. For the indirect method, the emitter/transmitter and receiver are placed at the same surface of a sample, which means the receiver measures the arrival of a reflection. The reflection measurements in this indirect method are useful in obtaining the buried rock surfaces. The semi-direct method can measure both direct and reflected waves. Depending on the transducer type, these can both be P- and S-waves.

2.2.2. Resolution

The vertical or radial resolution of the seismic measurements is theoretically a quarter wave length of the center frequency and independent on the depth, but this may be lower if the data experiences a lot of noise. The vertical resolution V_r can then also be given by Eq. 2.1.

2.2.3. Limitations and requirements

Several limitations can be mentioned for UPV testing, but they are largely the same as for the GPR. Mohamed Sutan and Meganathan (2003) made a comparison between direct and indirect methods and specified that the use op UPV is very helpful for assessing (concrete) structures, but that absolute measurements should be treated with caution. This is confirmed by Wendrich et al. (2006) as they specify that first results can be regarded as qualitative instead of quantitative values while evaluating a masonry wall and column with direct and semi-direct measurements, respectively.

Also, the performance of UPV testing is poor if water is present in cracks and it is also lacking for very rough surfaces as good contact is required between the transducer and the structure. This is in agreement with the findings of Martinho and Dionísio (2014) where the main factors influencing the pulse velocity are the degree of saturation, the density and the state of preservation (fractures etc.). Fort et al. (2013) found from literature that the main petrological factors affecting the pulse velocity are compactness, porosity, moisture content and micro-cracks as well as the degree of decay.

2.3. Proposed approach

This section contains an explanation of the approach used to estimate the buried rock contour using the GPR and to estimate the reflection depths using seismic sources and receivers.

GPR

The keystone SI2 of dolmen D14 is selected to assess the potential of GPR at imaging the hidden surfaces of partially buried rocks and at detecting weaknesses within the rocks. It is proposed to perform a Common Offset Survey on the keystone using the GPR (reflection profiling). The GPR should be able to indicate the change in dielectric properties between the granite of SI2 and its foundation layer, which is assumed to consist of sand and small boulders based on photos of Van Giffen's 1927 excavation (Theuws, 2021). A Transillumination Survey is also required to obtain the propagation velocity through the keystone. Using the travel times of the measured reflections and the obtained velocity, 2D depth sections can then be derived. By considering profiles in two or more directions, a pseudo-3D reconstruction can be made.

However, the process of estimating the buried rock contour is not as straight-forward as listed above due to several factors, such as the variable topography of the rock surface on which the Common Offset Survey is conducted, the limited surface area available for the survey, and the 3-dimensional nature of the reflections. Therefore, a conceptual GPR point model is assumed for the GPR during a Common Offset Survey. A zero-dimensional GPR is assumed for the sake of simplification, which is further explained in Chapter 3 along with a detailed working of the GPR during a Common Offset Survey.

Based on the conceptual GPR point model, two mathematical models are developed to assist in obtaining the buried rock contour of the keystone. The so-called GPR point-to-GEO model determines (buried) rock surfaces from reflection surfaces identified in the GPR radargrams obtained during a Common Offset Survey. The model is extensively described in Chapter 4.

The second mathematical (GEO-to-GPR point) models GPR data based on an assumed buried rock contour. It serves as a check for the obtained buried rock surface coordinates by plotting reflection surfaces in the actual GPR data and is based on the same principles as the GPR point-to-GEO model. It is mainly used in an iterative process to update the buried rock contour based on the found buried rock surfaces from the GPR point-to-GEO model. The model is extensively described in Chapter 5.

The two models are thus used in obtaining the buried rock contour. However, a more detailed approach is required to estimate the buried rock contour. Seven steps can be distinguished in the proposed approach, which are fully described in the methodology for the GPR in Chapter 6 and are listed below:

1. Acquisition of GPR data
2. Processing of GPR data
3. Identification of reflection surfaces
4. Acquisition of exposed rock contour
5. Calculation of rock surfaces
6. Estimation of buried rock contour
7. Modelling of GPR data

Important to remark is that the last two steps of this list are part of an iterative process of updating the estimated buried rock contour until a satisfactory result has been accomplished. The details regarding this process are explained in Chapter 6.

Seismics

The use of seismic reflection method (indirect method) is proposed to evaluate the potential of seismic sources and receivers at measuring dimensions of rocks. Ideally, a seismic reflection survey is performed on the keystone SI2, but that requires seismic sources and receivers that can successfully measure reflections. Therefore, this thesis focuses on capturing reflections and not on estimating the buried rock contour of keystone SI2. The seismic tests are thus not performed on the keystone SI2 or other boulders of dolmen D14, but are performed on various rocks unrelated to D14 that differ in size, contour and type.

Transducers of varying center frequency and hammers are used as seismic source to produce seismic waves, while only transducers of varying center frequency are used as receivers to detect reflections. The propagation velocity through the rock is determined using the direct method (similar to the transillumination survey for the GPR) and the reflections are captured using the indirect method. The reflection depth can then be calculated with the found velocity and travel times of the reflections. It is also proposed to perform a reflection measurement for an array of receivers. The velocity and travel times of the reflection can then be calculated directly. The aim is to detect (reflected) P-waves and therefore, P-wave sources and receiver transducers are used in this research.

The proposed approach consists of the following steps, which are fully described in the methodology for the seismic measurements in Chapter 10:

1. Acquisition of seismic data
2. Calculation of seismic wave velocity
3. Calculation of reflection depth

3

GPR point model

This chapter contains the explanation of the conceptual GPR point model, which is a simplification of the behaviour of a Ground Penetrating Radar during a Common Offset Survey. First, the general theory and working of the GPR and the Common Offset Survey is explained. Secondly, the basic principle behind the conceptual GPR point model is described. Then, the applied assumptions are mentioned the limitations of the model are indicated.

3.1. Theory

The basic principle behind the GPR or Ground Penetrating Radar is that reflected radio waves are used to gain insight into the subsurface. The reflections occur due to differences in the dielectric properties of geological media. These not only differ between soils, but also for changes in saturation. Among others, the dielectric properties of the soil influence the propagation velocity of the radio waves through the media. Table 3.1 contains the electrical properties for several geological media as well as the average velocities.

Table 3.1: Electrical Properties of several geological media from Davis and Annan, 1989

	Electrical Properties			
Material	Relative Permittivity ϵ_r (-)	Electrical Conductivity σ (mS/m)	Average Velocity v (m/ns)	Attenuation α (dB/m)
Air	1	0	0.3	0
Distilled water	0.01	0	0.0333	0.002
Fresh water	80	0.5	0.033	0.1
Sea water	80	30000	0.01	1000
Dry sand	3-5	0.01	0.15	0.01
Saturated sand	20-30	0.1-1	0.06	0.03-0.3
Limestone	4-8	0.5-2	0.12	0.4-1
Shale	5-15	1-100	0.09	1-100
Silt	5-30	1-100	0.07	1-100
Clay	4-40	2-1000	0.06	1-300
Granite	4-6	0.01-1	0.13	0.01-1
Salt (dry)	5-6	0.01-1	0.13	0.01-1
Ice	3-4	0.01	0.16	0.01

The velocity through a, non-magnetic, geological medium is given by

$$v = \frac{c}{\sqrt{\epsilon_r}}, \tag{3.1}$$

with the relative permittivity ϵ_r and the speed of light c=2.998· 10^8 m/s (Oldenburg et al., 2017a). The relative permittivity is the ratio of the permittivity of a medium, the electric polarizability of a material, to that of a free space (vacuum). The relative permittivity of a granite is 4-6 (Table 3.1), which corresponds to a velocity of 0.12-0.15 m/ns.

The polarity of a reflection can also be used to obtain information on the geological media in the subsurface. The so-called reflection coefficient is given by

$$R = \frac{\sqrt{\epsilon_{r,1}} - \sqrt{\epsilon_{r,2}}}{\sqrt{\epsilon_{r,1}} + \sqrt{\epsilon_{r,2}}}, \tag{3.2}$$

in which ϵ_r is the relative permittivity (Oldenburg et al., 2017a). The index number 1 denotes the medium through which the incident and reflected wave travel and the index number 2 denotes the medium at the other side of the reflection boundary. The reflection coefficient ranges between $-1 < R < 1$, in which $R < 0$ indicates a reverse in polarity and $R > 0$ does not. The polarity of the reflected radiowaves can be used to determine if $\epsilon_{r,1}$ is greater than $\epsilon_{r,2}$, which can be used to determine the material below medium 1, i.e. medium 2. Expected R values for granite-air, granite-dry sand and granite-saturated sand are, respectively, +0.38, +0.06 and -0.38. When a reverse in polarity can be observed in acquired data, this most likely indicates saturated conditions beneath the stone in the field. For dry sandy soils, the expected reflection is only minimal due to the reflection coefficient close to zero, which would make it hard to distinguish a granite-dry sand boundary in acquired data. If an air pocket exists, this would give remarkable reflections similar to that of saturated sand, but it wouldn't show signs of reversed polarity.

In short: the greater the difference in the relative permittivity (or dielectric constant), the greater the reflection coefficient and therefore the stronger the reflection.

A common type of GPR data acquisition is the Common Offset Survey as mentioned previously in Chapter 6. The transmitter and receiver antennas are mounted behind each other and travel over an area of interest for a certain distance, which is measured by the attached odometer. From Billings and Kingdon (2021), the beam of energy emitted by the GPR transmitter can be described as a conical. The resulting footprint is then elliptical which increases in size with depth, see Figure 3.1. The energy in the form of radio waves is thus 1) emitted, 2) reflected at a reflection surface and 3) received during the survey. The angle of the incident or emitted wave with the normal θ_i is equal to the angle of the reflected wave with the normal θ_r, see Figure 3.1a. The depth d, or distance to the reflection surface, can then be determined if the velocity of the radio waves through the medium is known.

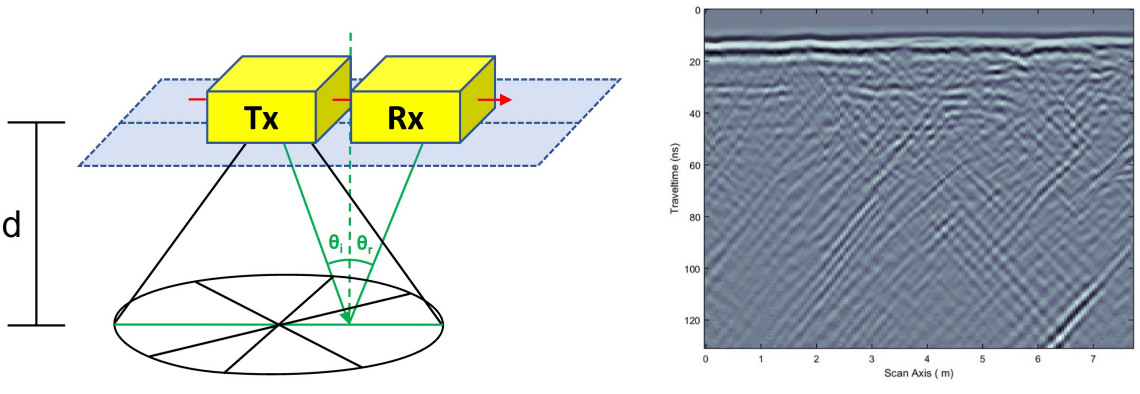

(a) **(b)**

Figure 3.1: Emitted signal from the GPR transmitter Tx presented as a cone and a reflected radio wave in green received at the receiver Rx for a depth d (a). (b) shows an example of a GPR radargram resulting from a Common Offset Survey, in which the amplitude of the received signal is plotted as function of the travelled distance of the GPR vs. the two way travel time of the reflected radio waves.

Usually, the GPR is applied in, at most, slightly undulating or sloping ground surfaces, see Figure 3.2a. It can among others identify man-made structures and utilities as well as geological layers (Semik Group P.C., 2021), which show up in the resulting GPR radargram, see Figure 3.2b. This 2D radargram plots the amplitude of the reflected radio waves as a function of the surveyed path and the two way travel time. The surveyed path is measured by the odometer and the two-way travel time is the time between emitting and receiving of the reflected radio wave.

The amplitude of the wave decreases on its propagation path due to geometrical spreading and material-attenuation losses. The total energy loss from material losses is the results of surface scattering at interfaces, volume scattering from inhomogeneous materials, and exponential thermal-conversion losses (Slob et al., 2010).

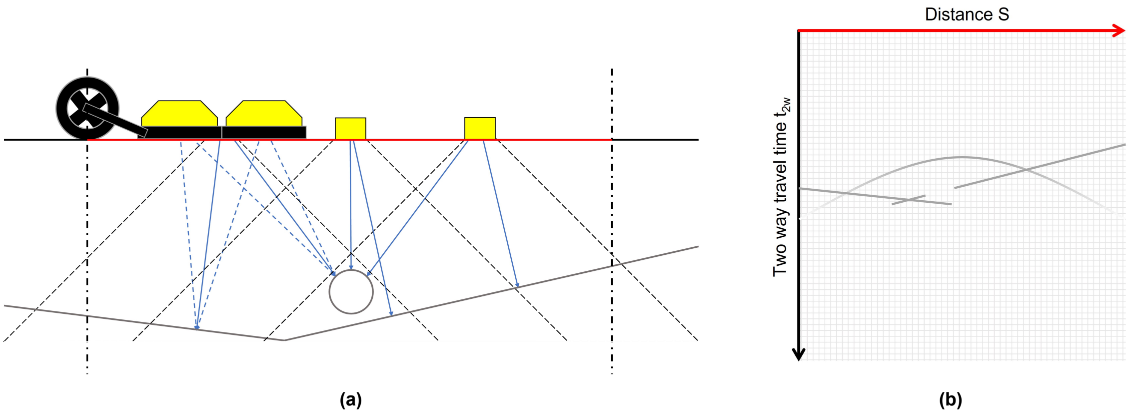

(a) (b)

Figure 3.2: GPR during a Common Offset Survey on horizontal ground surface with sloping soil horizons and a buried pipeline, in which the yellow blocks represent the moving GPR (a) and a simplified GPR radargram in which the amplitudes of the reflected radio waves are plotted as a function of the the travel path and the two way travel time (b). The parabola indicates the pipeline and the sloping reflections indicate the soil horizons. The dotted reflections shown in blue in (a) are approximated by the plain blue reflections.

3.2. GPR point model

The GPR point model is a conceptual model based on the 2D geometry of a cross-section of a rock surveyed in a Common Offset Survey. It is developed to determine the buried rock contour of a half-buried rock. Figure 3.3a gives the idea behind the Common Offset Survey on a half-buried rock. The resulting GPR radargram with reflection surfaces can be seen in Figure 3.3b in a simplified radargram.

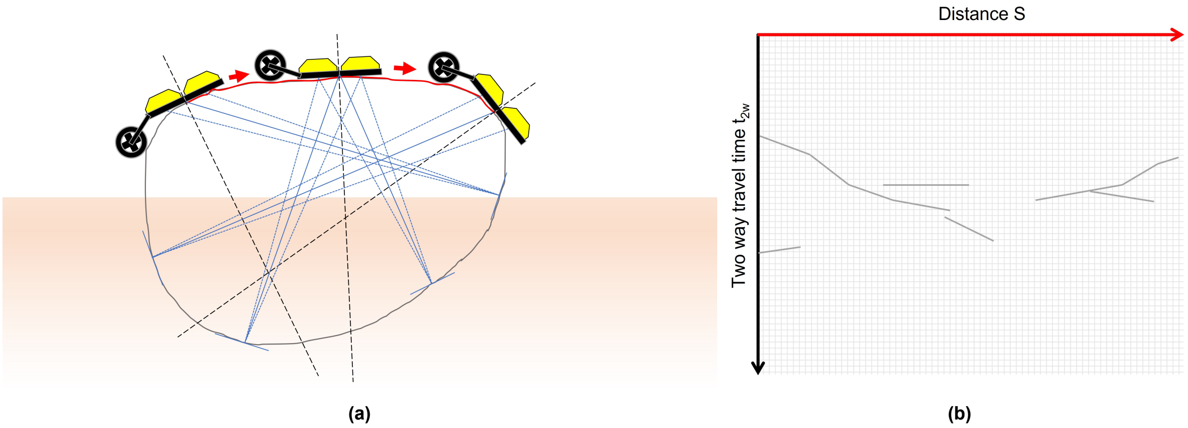

(a) (b)

Figure 3.3: GPR during a Common Offset Survey on a buried rock (a) and the (simplified) GPR radargram from the survey, indicating the reflection surfaces (b). The dotted black and blue lines in (a) represent the angle of the GPR with respect to the vertical and the reflected radio waves, respectively.

The reflection surfaces from this GPR radargram can be used to determine the buried rock contour. However, this is difficult to determine in a 3D reality for a GPR with dimensions. This means the reflection surface can lie outside the cross-section and that the exact arrival position at the receiving antenna is unknown. Yet, in order to retrieve those coordinates, the GPR point model is created, see Figure 3.4.

However, this has important consequences. Whereas the GPR antennas have certain dimensions in practice, these will be assumed very small in order to assume a GPR point model, see Figure 3.4a. While this is a large simplification, the GPR radargram inherently also assumes a unique location along its horizontal axis for a signal that can be emitted/received over the entire antenna. Of course, this means a deviation in the origin of the reflection can be expected. However, with the to be mentioned uncertainties in data acquisition (e.g. reflection measurements, survey paths, 3D effects) and the rock surface coordinates, this is deemed accurate enough for a first approach.

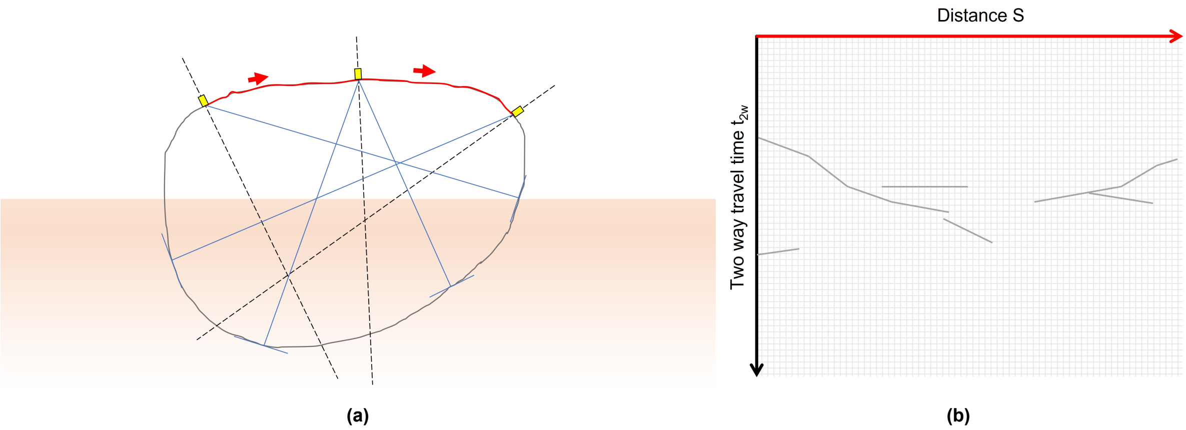

(a) **(b)**

Figure 3.4: GPR during a Common Offset Survey on a buried rock as assumed in the GPR point model (a) and the (simplified) GPR radargram from the survey, indicating the reflection surfaces (b). The dotted and blue lines in (a) represent the angle of the GPR with respect to the vertical and the reflected radio waves, respectively.

To demonstrate that the deviation is not significant, the reflection in the conceptual model and true conditions is shown in Figure 3.5. It is assumed that **on average**, the reflection in true conditions is emitted and received from the center of the transmitting and receiving antennas. Whereas in the conceptual model, the reflection is emitted and received at the center of the GPR (at the interface of both antennas).

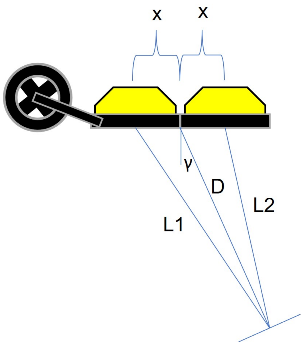

Figure 3.5: GPR, reflections and variable clarification

Then, the ratio between the approximated travel path of the reflection L_{appr} and the true travel path L_{true} is given by

$$\frac{L_{appr}}{L_{true}} = \frac{2 \cdot D}{L_1 + L_2} = \frac{2 \cdot D}{\sqrt{D^2 + 2 \cdot x \cdot D \cdot \sin(\gamma) + x^2} + \sqrt{D^2 - 2 \cdot x \cdot D \cdot \sin(\gamma) + x^2}} \tag{3.3}$$

with in this Equation:

x = Distance between the centers of the separate antennas and the center of the GPR (m)
D = Depth of reflection surface with respect to the center of the GPR (m)
L_1 = Distance between reflection surface and center of antenna 1 (m)
L_2 = Distance between reflection surface and center of antenna 2 (m)
γ = Angle of the reflection in point model with respect to the vertical (°)

The ratio between the travel paths is calculated for a range of angles and depths and can be seen in Table 3.2. Important to note: due to symmetry, no negative angles are required. Furthermore, the evaluated depth range is limited as it can be seen that no sudden increase in ratio are to be expected below 0.9 meters in Table 3.2. For the dimensions of the GPR, $x = 7.5$ cm is chosen as it represents the dimensions of the 1000 MHz GPR used in the field. The distance x would increase for lower frequency antennas, but as the model was not developed with another GPR in mind, this is not considered.

It is shown that at most a 3% under estimation can be expected for depths greater than or equal to 0.3 meter. Only for very shallow depths, larger ratios can be expected. As these shallow depths are not expected in the field, this is deemed sufficient. Furthermore, a direct reflection at such a limited depth would most likely not arrive at the center of the antenna, but rather at the edge.

Table 3.2: Ratio between travel paths in point model and true conditions with $x = 0.075$ m.

	Ratio (%)						
$D(m)$	$\gamma = 0°$	$\gamma = 15°$	$\gamma = 30°$	$\gamma = 45°$	$\gamma = 60°$	$\gamma = 75°$	$\gamma = 90°$
0.1	80.0	80.6	82.6	85.9	90.7	96.5	100.0
0.3	97.0	97.2	97.7	98.4	99.2	99.8	100.0
0.5	98.9	99.0	99.2	99.4	99.7	99.9	100.0
0.7	99.4	99.5	99.6	99.7	99.9	100.0	100.0
0.9	99.7	99.7	99.7	99.8	99.9	100.0	100.0

To give an idea of the deviations, Table 3.3 contains the deviations in centimeters with respect to the GPR point model. It can be concluded that for depths $>$ 0.3 meter, a small underestimation (less than a centimeter) of the true depths can be expected. Even for shallow depths, the deviations are in the order of centimeters.

Table 3.3: Deviation of depth in true conditions with respect to the point model, with $x = 0.075$ m.

	Deviation (cm)						
$D(m)$	$\gamma = 0°$	$\gamma = 15°$	$\gamma = 30°$	$\gamma = 45°$	$\gamma = 60°$	$\gamma = 75°$	$\gamma = 90°$
0.1	+2.50	+2.40	+2.11	+1.64	+1.02	+0.36	+0.00
0.3	+0.92	+0.87	+0.71	+0.48	+0.24	+0.07	+0.00
0.5	+0.56	+0.52	+0.42	+0.28	+0.14	+0.04	+0.00
0.7	+0.40	+0.37	+0.30	+0.20	+0.10	+0.03	+0.00
0.9	+0.31	+0.29	+0.23	+0.16	+0.08	+0.02	+0.00

3.3. Assumptions

The GPR point model is a simplification of the true GPR. Therefore, the assumptions that are made in this conceptual model are given. These are listed below and include unwanted effects that may occur. The assumptions are then discussed.

1. The GPR (incl. antennas) is assumed to be zero-dimensional
    - Underestimation of reflection depth (1-3% for depths > 0.3 m)
2. All reflections are assumed to originate from within the vertical cross-section following from the GPR survey path
    - Over- or underestimation of reflection depth
3. All reflections are assumed to be direct
    - Overestimation of reflection depth
4. The GPR survey path is assumed to be equal to the (scanned) surface of the rock
    - Translation or shift of reflection surface
    - Rotation of reflection surface
5. The GPR survey path, incl. start and end, is assumed to be accurately determined based on pictures taken during data acquisition
    - Translation or shift of reflection surface
    - Rotation of reflection surface

As mentioned in the previous section, assuming a zero dimensional GPR gives a small underestimation (less than a centimeter for depths larger than 0.3 m) of the reflection depth (distance to the reflection surface), which was deemed not significant.

Secondly, any reflections outside of the vertical cross-section of the GPR point survey, see Figure 3.6a, are assumed to be non-existing. This means that any reflection outside of the vertical cross-section is projected onto the vertical cross-section, see the marine blue direct reflection in Figure 3.6b. Consequently, an over- or underestimation of the reflection depth can occur, depending on the difference between the distances to the true reflection surface and the assumed reflection surface.

Thirdly, only direct reflections are considered. This means that indirect reflections (reflected more than once) are assumed to be direct (reflected only once). The consequence is that all indirect reflections are assumed to be direct reflections from a deeper reflection surface, see the grey blue indirect reflection in Figure 3.6b, which leads to an overestimation of the reflection depth.

It is expected that the most clear and strong reflections will by approximation come from within the vertical cross-section following from the GPR survey path. If true, this would mean that only small overestimations of the reflection depth would occur. Also, by only considering the ”shallowest reflection surfaces” or reflection surfaces with relative short two way travel times in the GPR radargram, the assumption that only direct reflections would occur is not that far fetched. Indirect reflections would naturally end up ”deeper” in the GPR radargram with relative long two way travel times. Moreover, the indirect reflections are most likely weaker than the direct reflections, so they would be less clear in the GPR radargram.

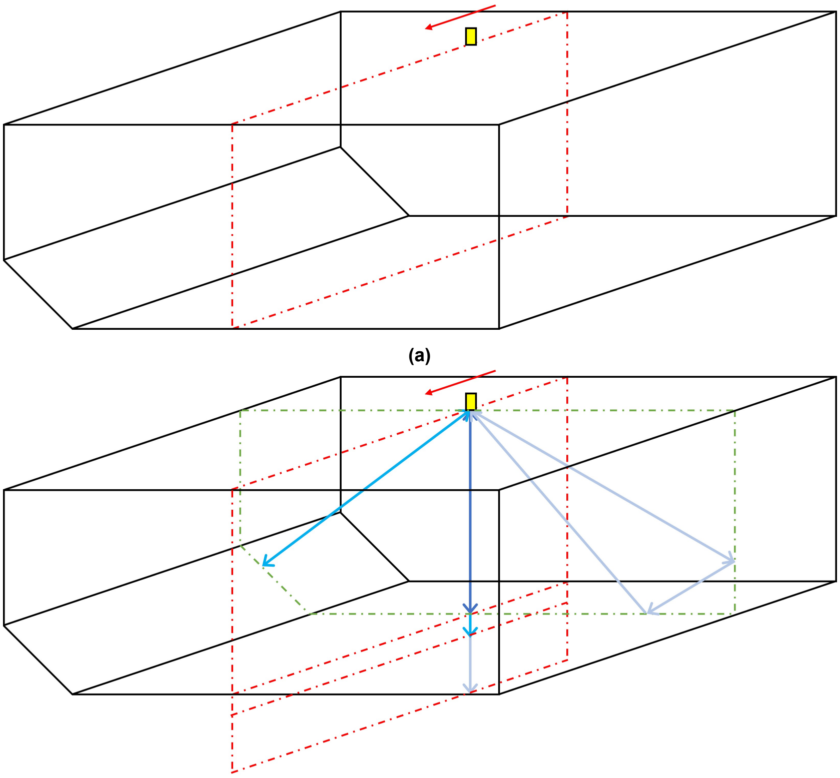
(a)

(b)

Figure 3.6: GPR survey on a simplified rock with corresponding vertical cross-section in red (a) and perpendicular cross-section in green in which the radio waves reflect (b). The reflections all originate within the green cross-section due to the parallel surfaces of the survey and the boundaries. The GPR point model, however, assumes the reflections to originate from the vertical cross-section in red, which results in overestimation of reflection depth. The shown reflections can be classified as: 1) direct reflection inside vertical cross-section (dark blue), 2) direct reflection outside vertical cross-section (marine blue) and 3) indirect reflection outside vertical cross-section (grey blue).

The fourth important assumption is that the survey path of the GPR on the surface of the rock is equal to the actual rock contour. This is definitely true in a GPR point model (Figure 3.4a), but is an important approximation in case of a GPR with dimensions (Figure 3.3a). The rock is scanned with LiDAR, with an accuracy of 2 mm. The rock surfaces following from the LiDAR point cloud can then experience small translations and rotations with respect to the true rock contour surfaces. However, more important is that the GPR will never follow the exposed rock contour exactly as its stiff and large and won't bend around the rock contour. This then leads to a shift or rotation of the reflection surface. Especially for rough rock contours, this can lead to noticeable deviations. Therefore, it is very important to guide the GPR over smooth contours in the field and limit the amount of rough transitions. It is a crucial assumption in the GPR point model that unfortunately cannot be avoided. However, a smoothed' 3D model taking into account a more realistic survey path of the GPR could offer more realistic results, but it lies outside of the scope of this research and would also not prevent shifts and rotations that happen during data acquisition.

The final important assumption for the GPR point model is that the survey paths, including the start and end position, can be reasonably estimated from the pictures during the fieldwork. However, deviations are likely and therefore also translations and rotations of the rock surface with respect to the true rock contour surfaces. Translations and rotations of the reflection surfaces are thus likely to occur. As the step from 3D model (LiDAR) to 2D cross-section has to be performed manually, it is thus important to pay close attention to the start and end of the GPR survey path as well as the travel path itself. The survey path start and end in the GPR point model are equal to the start and end position of the center of the GPR (Figure 3.3a and 3.4a). Moreover, the survey path itself in the GPR point model is the path followed by the center of the antennas for a GPR with dimensions.

4

GPR point to GEO model

This chapter contains the basic principle behind the GPR point-to-GEO model and the input that is required. The output from this mathematical model is also discussed. Finally, the inner workings of the model are explained.

4.1. Basic Principle

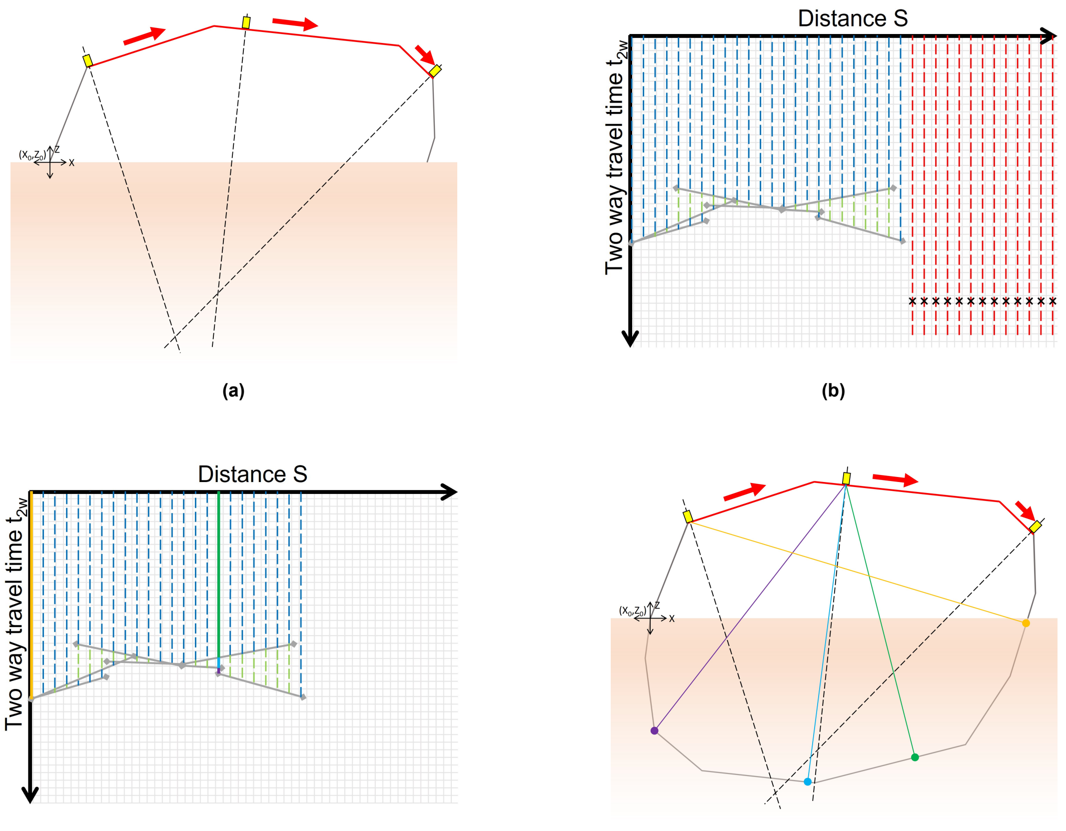

(a)

(b)

(c)

(d)

Figure 4.1: Summary of the GPR point-to-GEO model. A Common Offset Survey, as defined by the GPR point model, is performed on a buried rock (a) and results in a GPR radargram in which reflection surfaces can be identified (b). The GPR point-to-GEO model then creates model traces, which either end (blue/green) at an identified reflection surface or are removed (red) as no reflection surface exists (b). Finally, the model traces are then converted from the coordinate system in the GPR radargram (c) to the 2D spatial coordinate system of the rock cross-section (d). The colored lines in (d) show the converted model traces corresponding to the coloured model traces in (c), with the dots indicating the buried rock surface coordinates. The dotted lines in (a) and (d) represent the angle of the GPR with respect to the normal to the rock surface.

The GPR point-to-GEO model is a mathematical model developed in Python based on the conceptual GPR point model described in Chapter 3. It is used to convert the results from the Common Offset Survey of a Ground Penetrating Radar (GPR) into a known buried rock geometry (GEO), see Figure 4.1. A summarised overview of the model is shown, which is discussed in more detail in section 5.4 with an extensive explanation of each calculation step.

4.2. Input

The input of the model consists of a) the identified reflection surfaces from the GPR radargram, b) the exposed rock surface contour and c) several input parameters. Each of them is shortly described in the following subsections, including the appropriate manner to process the input.

4.2.1. Identified reflection surfaces

The reflection surfaces are required to be given as a python dictionary containing the start and end coordinates of each reflection surface as in the following equation:

$$S_r = \left\{ \begin{matrix} 's1' : S_{r,0} \\ ... \\ 'sX' : S_{r,N} \end{matrix} \right\}^{python\ dictionary} , \tag{4.1}$$

with each reflection given as

$$S_{r,i} = [[s_{0,i}, s_{1,i}], [t_{0,i}, t_{1,i}]] \tag{4.2}$$

and X being equal to $N + 1$. The start coordinates s_0 and t_0 of each reflection are defined as the left hand side coordinates of the linear fit, which means that the end coordinates s_1 and t_1 are defined as the right hand side coordinates of the linear fit.

4.2.2. Exposed rock surface contour

The exposed rock surface contour needs to be given as a python dictionary containing the coordinates of the rock surface as in the following equation:

$$C_r = \left\{ \begin{matrix} 'c1' : C_{r,0} \\ ... \\ 'cX' : C_{r,N} \end{matrix} \right\}^{python\ dictionary} , \tag{4.3}$$

with each coordinate given as

$$C_{r,i} = [x_i, z_i] \tag{4.4}$$

and X being equal to $N + 1$. These coordinates will need to be imported in python and arranged in such a way, that consecutive coordinates can form (linear) rock surfaces. The coordinates should start from $(x, z) = (0, 0)$ to end at $(x, z) = (x_{max}, 0)$, so clockwise from left to right, in order for the model to work properly.

4.2.3. Parameters

The input parameters are listed below, including two optional parameters. Each parameter will be shortly explained.

- Start and end coordinate of the GPR survey (from rock surface coordinates) crd_0 and crd_1 (-)
- Velocity through medium v_{GPR} (m/ns)
- Spacing between consecutive traces s_{step} (m)
- Time step within trace Δt_{tr} (ns)
- Maximum time duration of trace t_{tr}^{max} (ns)
- Colour scheme indicator for graphs n_{cl} (-)
- Optional parameters
    - Showing of GPR radargram I (-))
    - Graph size D_{graph} (-))

Start and end coordinates GPR survey
The start and end coordinates are required in order to retrieve the correct GPR survey path coordinates from the rock surface contour. They are defined as the number i+1 of coordinate i, starting from number 1 for coordinate 0.

Velocity through medium
The velocity through the medium is the velocity that was determined during the Transillumination survey.

Spacing between consecutive traces
The spacing between consecutive traces is an optimization parameter for accurate results. However, a balance between accuracy and running time of the model needs to be considered. The smaller the spacing, the more accurate the buried rock contour can be determined from the GPR radargram. However, the smaller this value, the longer the running time. The same spacing used during the data acquisition is logical. It has to be mentioned that using smaller values would give a false sense of reliability. On the other hand, as the reflection surfaces are determined for the spacing used in the field, it would not change the outcome. Therefore, smaller values can enhance the visibility of buried rock contour without changing the actual buried rock contour.

Time step within trace
The time step within each trace is also an optimization parameter for accurate results. As explained for the spacing parameter, a balance has to be found between accuracy and running time of the model. The same conclusion as for the spacing parameter can be drawn, a smaller time step than used during data acquisition can enhance the visibility of buried rock contour without changing the actual buried rock contour.

Maximum time duration
The maximum time duration of the traces simply describes the final length of each trace, which can be kept the same as the time window in the GPR radargram.

Colour scheme indicator for graphs
Finally, the colour scheme indicator is a number representing a colour distribution. It does not influence the buried rock contour and is only used for graphs.

Optional parameters
The two optional parameters are used for visual purposes only. The showing of the GPR radargram is pre-defined as 'off', but can be achieved by inputting the image and its extent as ['GPR_radargram.jpg', $[x_0^{ext}, x_1^{ext}, y_0^{ext}, y_1^{ext}]$]. The optional graph size is pre-defined (20, 5), but can be changed if required.

4.3. Output

The output of the model is a list of all (buried) rock surface coordinates, as can be seen in

$$C_b = [X_b, Z_b], \tag{4.5}$$

with X_b and Z_b given for N number of coordinates as.

$$X_b = [X_{b,0}, ..., X_{b,N}] \tag{4.6}$$

and

$$Z_b = [Z_{b,0}, ..., Z_{b,N}]. \tag{4.7}$$

Furthermore, a graph consisting of a) the rock contour, including the (buried) rock surfaces and GPR survey path, in the 2D spatial coordinate system (left) and b) the GPR radargram including the identified reflection surfaces is plotted (right), see Figure 4.2.

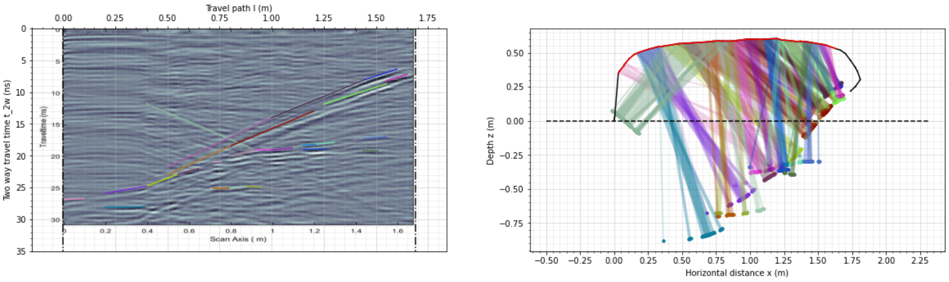

Figure 4.2: Example output GPR point-to-GEO model with the identified reflections in the GPR radargram at the left and the (buried) rock surfaces and the exposed rock contour at the right.

4.4. Model calculations

If the input of the GPR-to-GEO model is correctly processed and every parameter is defined, the model can be run to retrieve the buried rock coordinates. A concise overview of the model and its calculation steps can be seen in subsection 4.4.1. A more comprehensive explanation of each calculation step can be found in subsections 4.4.2 to 4.4.8.

4.4.1. Model steps

The model can be divided in 7 steps, which are numbered in the flowchart given in Figure 4.3. An overview and clarification of the parameters in the flowchart is given above the flowchart.

crd_0 = Start coordinate of the GPR survey (from rock surface coordinates) (-)
crd_1 = End coordinate of the GPR survey (from rock surface coordinates) (-)
v_{GPR} = Velocity through medium (m/ns)
s_{step} = Spacing between consecutive traces (m)
Δt_{tr} = Time step within trace (ns)
t_{tr}^{max} = Maximum time duration of trace (ns)
n_{cl} = Colour scheme indicator for graphs (-)
I = Showing of GPR radargram (-)
D_{graph} = Graph size (-)
S_r = Python dictionary of reflection surface coordinates
C_r = Python dictionary of exposed rock surface coordinates
S = List of slopes and 2D coordinates of the reflection surfaces
C = List of slopes and 2D coordinates of the rock surfaces
C^{GPR} = List of slopes and 2D coordinates of the rock surfaces in the GPR survey
ΔL^{GPR} = List of distances between end of rock surface and starting point of GPR survey (m)
M_s = Matrix containing the spatial steps of vertical traces with maximum time duration (m)
M_t = Matrix containing the time steps of the vertical traces with maximum time duration (s)
M_s^{new} = Matrix containing the spatial steps of vertical traces to reflection surfaces (m)
M_t^{new} = Matrix containing the time steps of vertical traces to reflection surfaces (s)
div = Index numbers of reflection surfaces corresponding to each trace (-)
S_{tr} = List of origins of vertical traces along horizontal axis of GPR radargram (m)
L_{tr} = List of length of vertical traces (m)
c_b = Buried rock surface contour coordinates (m)
c_s = Exposed rock surface contour coordinates (m)

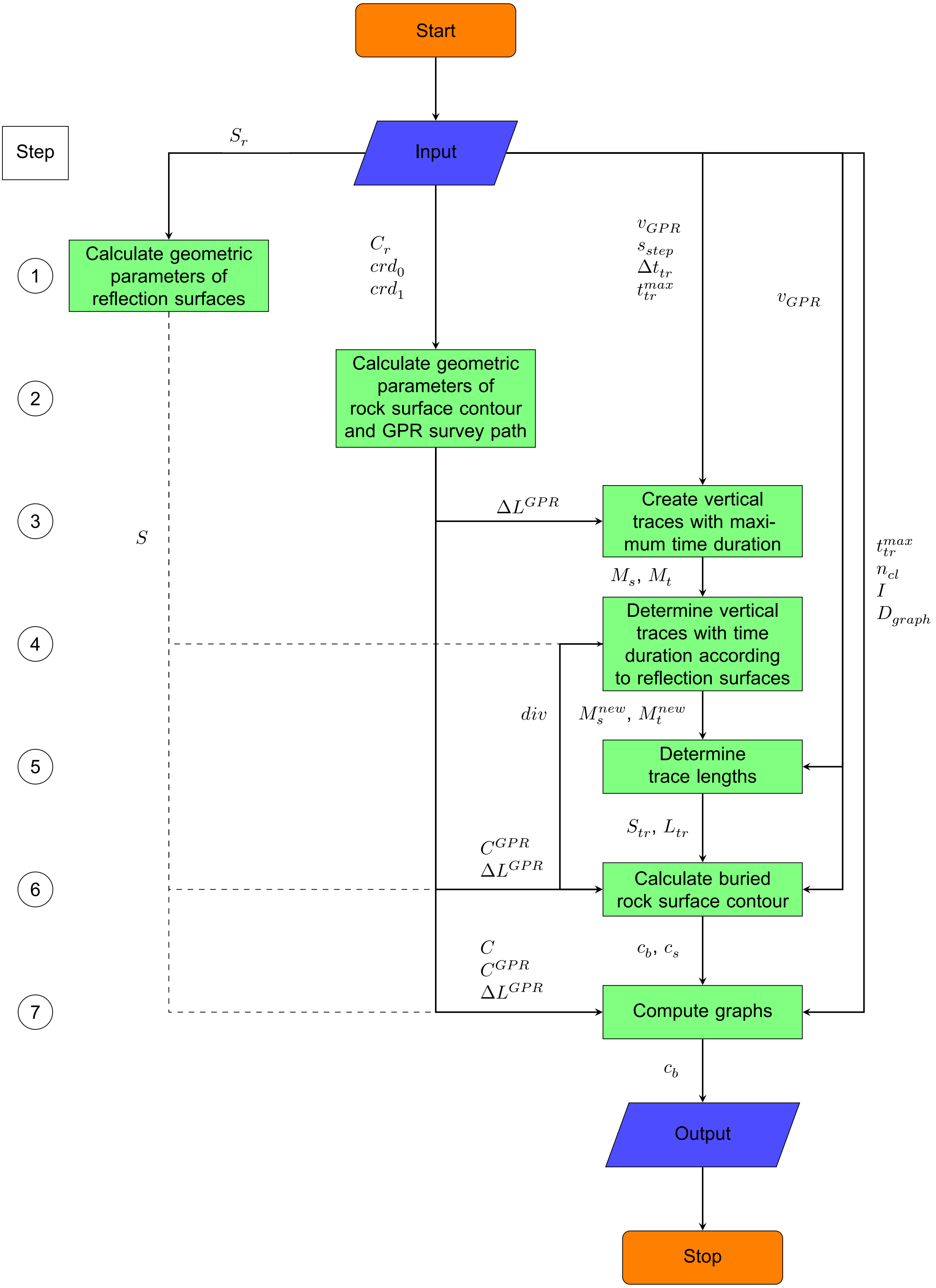

Figure 4.3: Flowchart of GPR point-to-GEO model including the 7 calculations steps further explained in the subsequent subsections. The input parameters are shown as input for every step as well as the parameters between each calculation step.

4.4.2. Step 1

A schematic drawing of a GPR radargram with identified reflection surfaces can be seen in Figure 4.4. It shows the five geometric parameters that are required for further calculations.

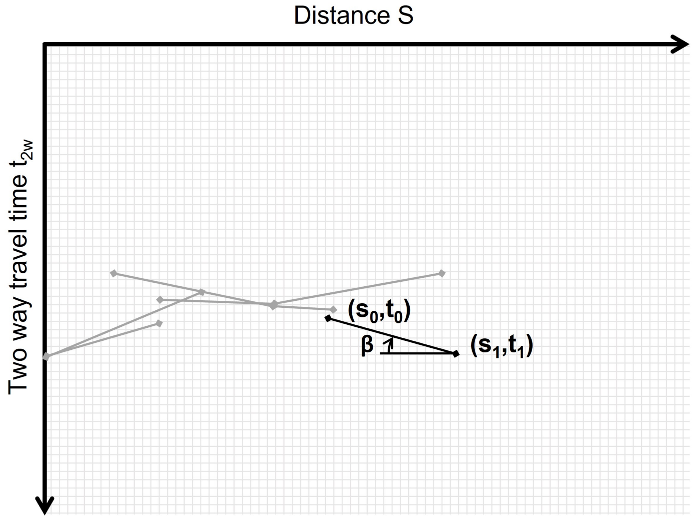

Figure 4.4: Reflections in GPR radargram with reflection surfaces (grey) and its coordinates s and t and slope β.

The reflection surfaces in the GPR radargram are given as a Python dictionary as can be seen in Eq. 4.1 in section 4.2. The reflection surface $S_{r,i}$ was given in Eq. 4.2, with $s_{0,i}$, $s_{1,i}$ and $t_{0,i}$, $t_{1,i}$ as horizontal and vertical coordinates in the GPR radargram, respectively.

The slope of the reflection surface β_i is given as

$$\beta_i = \text{arctan}\left(\frac{s_{1,i} - s_{0,i}}{t_{1,i} - t_{0,i}}\right), \tag{4.8}$$

with:

$s_{0,i}$ = Starting horizontal coordinate (distance) of reflection i in GPR radargram (m)
$s_{1,i}$ = Ending horizontal coordinate (distance) of reflection i in GPR radargram (m)
$t_{0,i}$ = Starting vertical coordinate (time) of reflection i in GPR radargram (ns)
$t_{1,i}$ = Ending vertical coordinate (time) of reflection i in GPR radargram (ns)

Now the five geometric parameters of the reflection surfaces (s_0, s_1, t_0, t_1 and β) are stored in a list

$$S = [S_0, S_1, T_0, T_1, \mathrm{B}], \tag{4.9}$$

in which S_0, S_1, T_0, T_1 and B are given as

$$S_0 = [s_{0,0}, ..., s_{0,N}], \tag{4.10}$$

$$S_1 = [s_{1,0}, ..., s_{1,N}], \tag{4.11}$$

$$T_0 = [t_{0,0}, ..., t_{0,N}], \tag{4.12}$$

$$T_1 = [t_{1,0}, ..., t_{1,N}], \tag{4.13}$$

$$\mathrm{B} = [\beta_0, ..., \beta_N]. \tag{4.14}$$

4.4.3. Step 2

A drawing of the rock surface cross-section including an GPR survey path can be seen in Figure 4.5. It shows the 2D coordinate system in which the rock surface coordinates, slopes and lengths will be given.

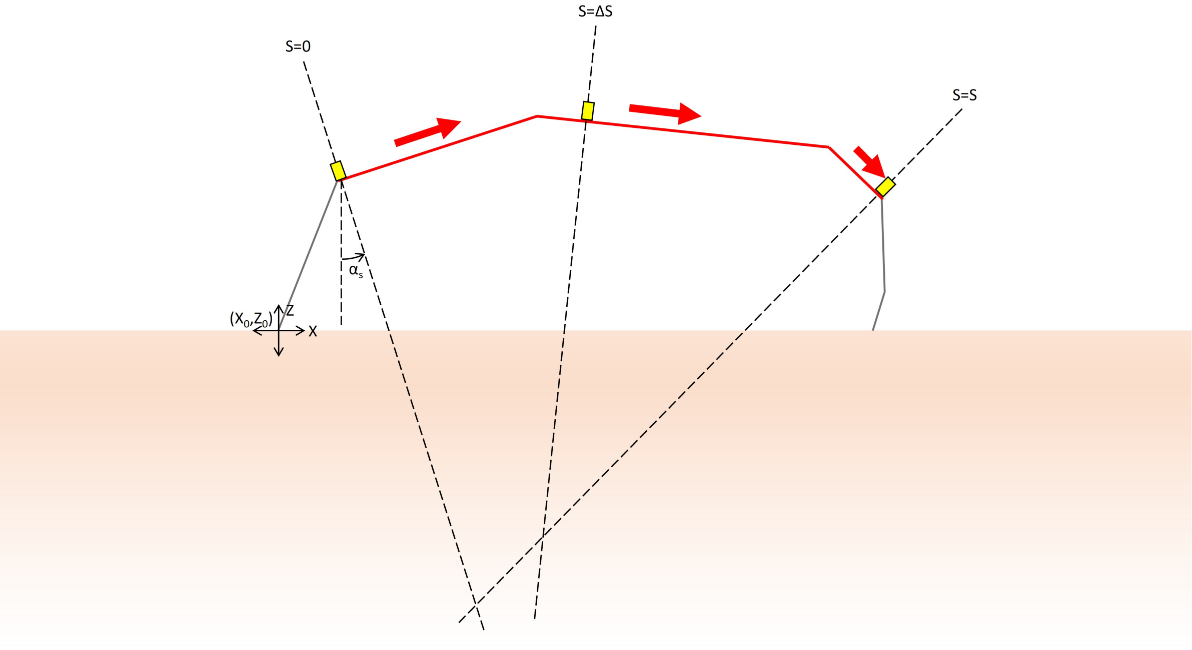

Figure 4.5: Rock surface C (grey) and GPR survey path (red) in $x-z$ coordinate system.

The rock surface coordinates are given as a Python dictionary as can be seen in Equation 4.3 in section 4.2. The rock surface coordinate $C_{r,i}$ was given as in Equation 4.4, with x_i and z_i as horizontal and vertical coordinate respectively.

The slope α_s and length Δl of each rock surface is given by

$$\alpha_{s,i} = \text{arctan}\left(\frac{z_{i+1}-z_i}{x_{i+1}-x_i}\right) \tag{4.15}$$

and

$$\Delta l_i = \sqrt{(x_{i+1}-x_i)^2+(z_{i+1}-z_i)^2}, \tag{4.16}$$

with:

x_i = Horizontal coordinate of rock surface coordinate i (m)
x_{i+1} = Horizontal coordinate of rock surface coordinate $i+1$ (m)
z_i = Vertical coordinate of rock surface coordinate i (m)
z_{i+1} = Vertical coordinate of rock surface coordinate $i+1$ (m)

Rock surfaces

Now the five geometric parameters of the rock surfaces (x_i, x_{i+1}, z_i, z_{i+1} and $\alpha_{s,i}$) are stored in a list

$$C = [X_0, X_1, Z_0, Z_1, \mathrm{A}_s], \tag{4.17}$$

in which X_0, X_1, Z_0, Z_1 and A_s are given as

$$X_0 = [x_0, ..., x_{N-1}], \tag{4.18}$$

$$X_1 = [x_1, ..., x_N], \tag{4.19}$$

$$Z_0 = [z_0, ..., z_{N-1}], \tag{4.20}$$

$$Z_1 = [z_1, ..., z_N], \tag{4.21}$$

$$\mathrm{A}_s = [\alpha_{s,0}, ..., \alpha_{s,N-1}]. \tag{4.22}$$

The length Δl is stored separately and is given as

$$\Delta L = [\Delta l_0, ..., \Delta l_{N-1}]. \tag{4.23}$$

Path GPR survey

To obtain only the rock surfaces on which the GPR survey is performed, the geometric parameters of the rock surfaces C that are not part of the GPR survey are removed. This is done with help of the starting and ending coordinates crd_0 and crd_1 of the GPR survey given as input.

Now the five geometric parameters of the GPR survey path (X_0^{GPR}, X_1^{GPR}, Z_0^{GPR}, Z_1^{GPR} and A_s^{GPR}) are stored in a list

$$C^{GPR} = [X_0^{GPR}, X_1^{GPR}, Z_0^{GPR}, Z_1^{GPR}, \mathrm{A}_s^{GPR}] = \begin{cases} X_0^{GPR} = X_0 & (x_{0,crd_0} \leq x_{0,i} \leq x_{0,crd_1}) \\ X_1^{GPR} = X_1 & (x_{1,crd_0} \leq x_{1,i} \leq x_{1,crd_1}) \\ Z_0^{GPR} = Z_0 & (z_{0,crd_0} \leq z_{0,i} \leq z_{0,crd_1}) \\ Z_1^{GPR} = Z_1 & (z_{1,crd_0} \leq z_{1,i} \leq z_{1,crd_1}) \\ A_s^{GPR} = A_s & (a_{s,crd_0} \leq a_{s,i} \leq a_{s,crd_1}) \end{cases} . \tag{4.24}$$

The rock surface length ΔL is now stored as the distance of the rock surface to the starting point of the GPR survey

$$\Delta L^{GPR} = [\Delta l_{crd_0}, (\Delta l_{crd_0} + \Delta l_{crd_0+1}), ..., (\Delta l_{crd_0} + \Delta l_{crd_0+1} + ... + \Delta l_{crd_1})]. \tag{4.25}$$

4.4.4. Step 3

In this step the vertical traces are created in the GPR radargram which will eventually be converted to the (buried) rock surfaces. This can be seen in Figure 4.6

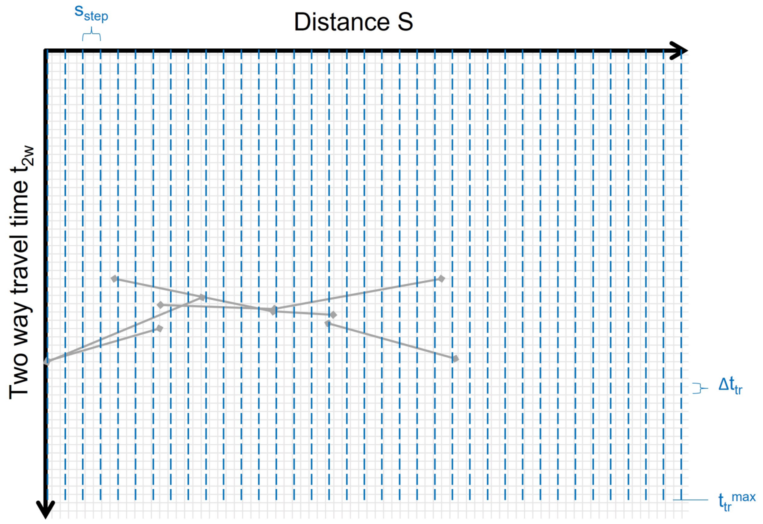

Figure 4.6: GPR radargram including reflection surfaces (grey) with vertical traces (blue) and the input parameters: spacing between consecutive traces s_{step}, time step within each trace Δt_{tr} and the maximum duration of the traces t_{tr}^{max}.

First, the number of traces is determined based on the total length of the GPR survey path (from the last value of ΔL^{GPR}, see Eq. 4.25 in section 4.4.3) and the spacing between consecutive traces s_{step}. The number of traces N_{tr} (rounded down to the nearest integer) is then given as

$$N_{tr} = \lfloor \frac{\Delta L_N^{GPR}}{s_{step}} \rfloor \tag{4.26}$$

and the origins for the vertical traces i along the horizontal axis of the GPR radargram is given as

$$S_{tr}^{GPR} = [0, s_{step}, ..., i * s_{step}, ..., N_{tr} * s_{step}]. \tag{4.27}$$

The time duration of the traces is given by t_{tr}^{max} and the corresponding time step is given by Δt_{tr}. Then, the rounded down number of time steps within each trace N_{dtr} is given as

$$N_{dtr} = \lfloor \frac{t_{tr}^{max}}{\Delta t_{tr}} \rfloor \tag{4.28}$$

and the time steps j along the time axis of the GPR radargram is given as

$$T_{tr}^{GPR} = [0, \Delta t_{tr}, ..., j * \Delta t_{tr}, ..., N_{dtr} * \Delta t_{tr}]. \tag{4.29}$$

In order to get the coordinates of each point along each vertical trace, two matrices are created for the trace origin M_s and trace duration M_t as can be seen in

$$M_s = \left.\overbrace{\begin{bmatrix} \begin{bmatrix} 0 * s_{step} \\ ... \\ 0 * s_{step} \end{bmatrix}, ..., \begin{bmatrix} i * s_{step} \\ ... \\ i * s_{step} \end{bmatrix}, ..., \begin{bmatrix} N_{tr} * s_{step} \\ ... \\ N_{tr} * s_{step} \end{bmatrix} \end{bmatrix}}^{N_{tr}} \right\} N_{dtr} \tag{4.30}$$

and

$$M_t = \left.\overbrace{\begin{bmatrix} \begin{bmatrix} 0 * \Delta t_{tr} \\ ... \\ j * \Delta t_{tr} \\ ... \\ N_{dtr} * \Delta t_{tr} \end{bmatrix}, ..., \begin{bmatrix} 0 * \Delta t_{tr} \\ ... \\ j * \Delta t_{tr} \\ ... \\ N_{dtr} * \Delta t_{tr} \end{bmatrix}, ..., \begin{bmatrix} 0 * \Delta t_{tr} \\ ... \\ j * \Delta t_{tr} \\ ... \\ N_{dtr} * \Delta t_{tr} \end{bmatrix} \end{bmatrix}}^{N_{tr}} \right\} N_{dtr} \ , \tag{4.31}$$

with in these Equations:

N_{tr} = Total number of traces
N_{dtr} = Total number of (time) steps within trace
i = Trace number, $0 \leq i \leq N_{tr}$
j = (Time) step number within trace, $0 \leq j \leq N_{dtr}$

4.4.5. Step 4

The vertical traces all have the maximum time duration according to the input t_{tr}^{max}, but the traces need to take the reflection surfaces into account. Therefore, each trace either has to be cutoff at a certain time t_j when it has reached a reflection surface, see blue traces in Figure 4.7, or the trace has to be removed as no reflection surface exists at S_i, see red traces in Figure 4.7. This means that the number of traces may decrease and that the length of each trace varies. However, depending on the number of stacked reflections in the GPR radargram, multiple traces at the same origin S_i may exist and therefore the number of traces could also increase, see green traces in Figure 4.7.

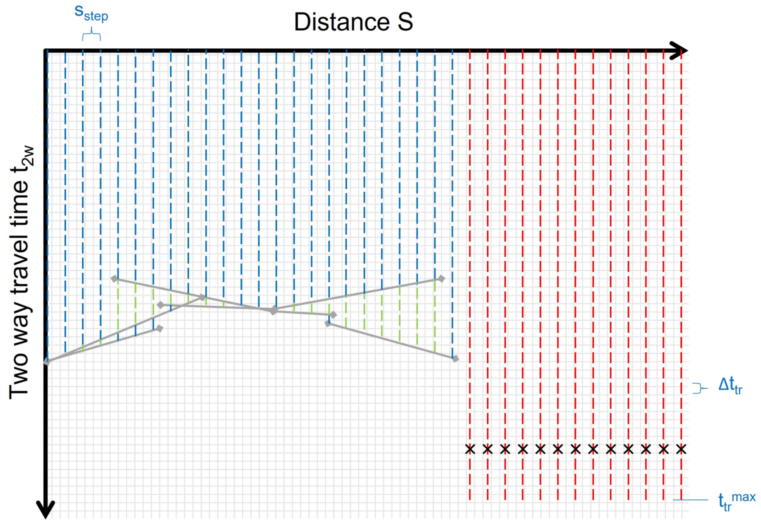

Figure 4.7: GPR radargram including reflection surfaces (grey), traces up until reflection surfaces (blue/green) and removed traces (red).

The newly constructed matrices M_s^{new} and M_t^{new} will therefore both consist of m vectors, with new trace number k, of varying lengths n_k, with new time step number j_k. The matrices M_s^{new} and M_t^{new} contain the new coordinates of each trace k as can be seen in

$$M_s^{new} = \left[\overbrace{\begin{bmatrix} k^{(0)} * s_{step} \\ \ldots \\ k^{(0)} * s_{step} \end{bmatrix}, \ldots, \begin{bmatrix} k * s_{step} \\ \ldots \\ k * s_{step} \end{bmatrix}, \ldots, \begin{bmatrix} k^{(m)} * s_{step} \\ \ldots \\ k^{(m)} * s_{step} \end{bmatrix}}^{m} \right] \tag{4.32}$$

and

$$M_t^{new} = \left[\overbrace{\begin{bmatrix} 0 * \Delta t_{tr} \\ \ldots \\ j_0 * \Delta t_{tr} \\ \ldots \\ n_0 * \Delta t_{tr} \end{bmatrix}, \ldots, \begin{bmatrix} 0 * \Delta t_{tr} \\ \ldots \\ j_k * \Delta t_{tr} \\ \ldots \\ n_k * \Delta t_{tr} \end{bmatrix}, \ldots, \begin{bmatrix} 0 * \Delta t_{tr} \\ \ldots \\ j_m * \Delta t_{tr} \\ \ldots \\ n_m * \Delta t_{tr} \end{bmatrix}}^{m} \right], \tag{4.33}$$

with in these Equations:

m = Total number of traces, $m \geq 0$
k = Trace number, $0 \leq k \leq N_{tr}$
n_k = Total number of (time) steps within trace k, $0 \leq n_k \leq N_{dtr}$
j_k = (Time) step number for trace number k, $0 \leq j_k \leq n_k$

Finally, the reflection surface number s corresponding to trace i is stored in a list as can be seen in

$$div_i = s \tag{4.34}$$

and

$$div = [div_0, ..., div_m]. \tag{4.35}$$

4.4.6. Step 5

The trace duration matrix M_t^{new} from the vertical traces now contains the time difference between emitting and receiving of the signal (Δt_{2w}), but this needs to be converted to the distance between the rock surface and the (buried) rock surface with help from the velocity through the medium. Furthermore, the origin of each trace with respect to the start of the GPR survey (ΔS) is required from the trace origin matrix M_s^{new}.

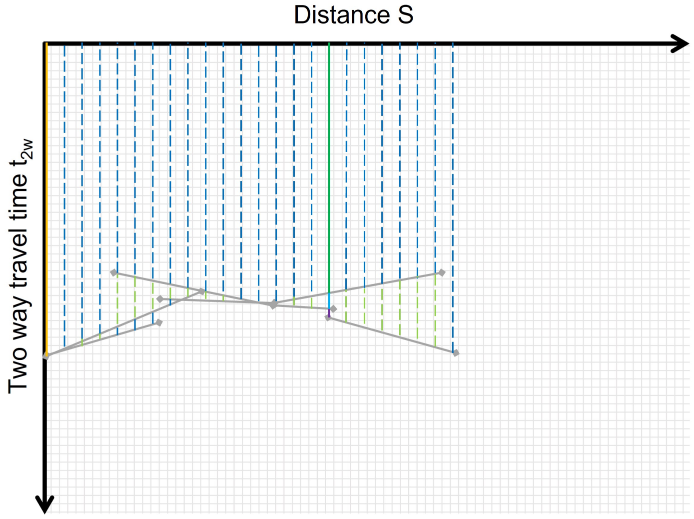

Figure 4.8: GPR radargram including reflection surfaces (grey), traces up until reflection surfaces (blue/green) and highlighted traces (various colors) with two way travel time duration Δt_{2w} and origin of the trace with respect to the start of the GPR survey ΔS.

The time difference or two way travel time Δt_{2w} of each trace is given as

$$\Delta t_{2w}^{(k)} = M_{t,k,n_k}^{new} - M_{t,k,0}^{new} = n_k * \Delta t_{tr} - 0. \tag{4.36}$$

The relation between the one way travel distance l_{tr}, the two way travel time Δt_{2w} and velocity v_{GPR} of each trace is then given as

$$l_{tr}^{(k)} = \Delta t_{2w}^{(k)} * \frac{v_{GPR}}{2}. \tag{4.37}$$

The corresponding origin of each trace s_{tr}, or ΔS, can be determined by retrieving the first value of $M_{s,k}^{new}$

$$s_{tr}^{(k)} = M_{s,k,0}^{new} = k * s_{step}. \tag{4.38}$$

The two parameters are then stored in lists S_{tr} and L_{tr} as can be seen in

$$S_{tr} = [s_{tr}^{(0)}, ..., s_{tr}^{(k)}, ..., s_{tr}^{(m)}] \tag{4.39}$$

and

$$L_{tr} = [l_{tr}^{(0)}, ..., l_{tr}^{(k)}, ..., l_{tr}^{(m)}]. \tag{4.40}$$

4.4.7. Step 6

In order to find the (buried) rock surfaces from the trace, the angles of the traces need to be determined. As the trace length L_{tr} and the trace origin along the GPR survey path S_{tr} are known, only the angle γ (with respect to the vertical) is required for the (buried) rock surfaces, see Figure 4.9.

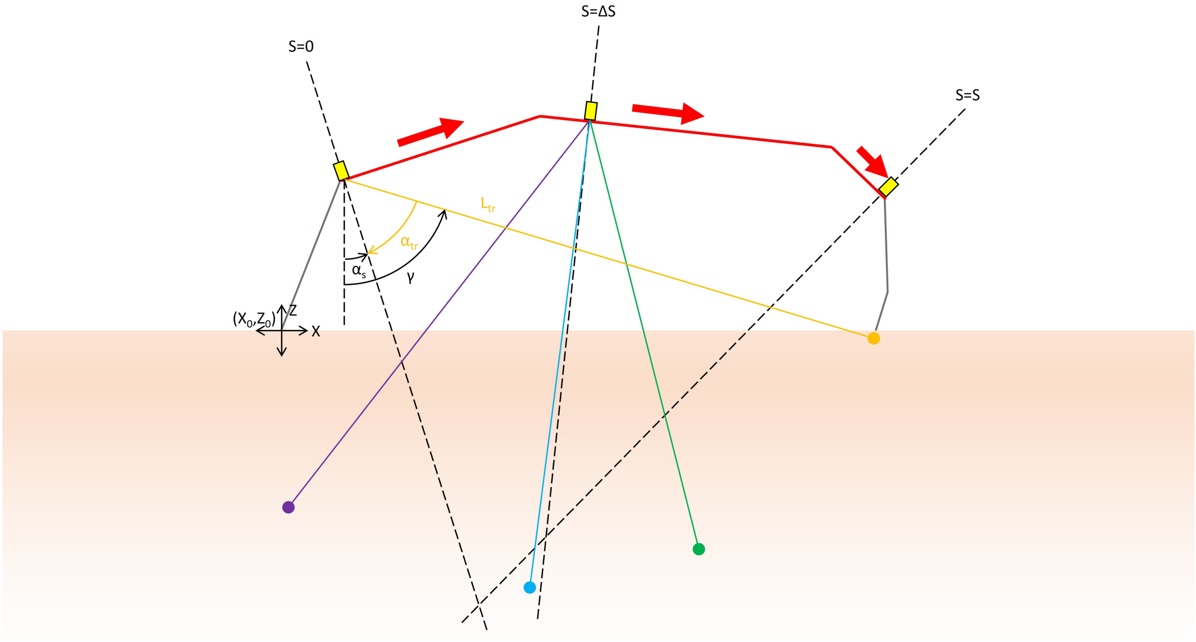

Figure 4.9: Converted traces (various colors) indicating the buried rock surface (dots) with the rock surface C (grey) and the GPR survey path (red) in $x-z$ coordinates. The trace angle γ is shown consisting of the rock surface slope α_s and the reflection surface slope $\alpha_{tr}(\beta)$.

From the reflection surfaces in the GPR radargram, the slope of the reflection surface β was determined in step 4.4.2. This angle indicates the slope of the (buried) rock surface, but it first needs to be converted to the spatial 2D coordinate system (x and z) from the GPR coordinate system (s and t) as can be seen in

$$\alpha_{tr} = \text{arcsin}\,(\text{tan}\,(\beta) * \frac{v_{GPR}}{2}). \tag{4.41}$$

Secondly, the angle of the rock surface determined in step 4.4.3 needs to be accounted for in order to get the angle γ with respect to the vertical. The relation between α_s^{GPR}, α_{tr} and γ is then given in

$$\gamma = \alpha_s^{GPR} - \alpha_{tr}. \tag{4.42}$$

As the trace lengths L_{tr}, the trace origins along the GPR survey path S_{tr} and the trace angles γ with respect to the vertical are known, the (buried) rock surface coordinates (x_b and z_b) can be determined. However, first the trace origins S_{tr} needs to be converted to the 2D spatial coordinate system with help from the rock surface parameters determined in step 4.4.3 (X_0^{GPR}, Z_0^{GPR}, A_s^{GPR}).

The angle a_s^{GPR} of rock surface i corresponding with the trace origin s_{tr} or trace k is required to retrieve the correct rock surface coordinates. Therefore, the distance along the horizontal axis of the GPR radargram for each rock surface i of the GPR survey (ΔL_i^{GPR}) is used. When the bounds in which s_{tr} is located are identified, the correct rock surface i is found. Therefore the trace origin coordinates for trace k ($x_s^{(k)}$ and $z_s^{(k)}$) can be calculated as can be seen in

$$x_s^{(k)} = \text{cos}\,(\mathrm{A}_{s,i}^{GPR}) * (S_{tr,k} - \Delta L_i^{GPR}) + X_{0,i}^{GPR} \tag{4.43}$$

and

$$z_s^{(k)} = \text{sin}\,(\mathrm{A}_{s,i}^{GPR}) * (S_{tr,k} - \Delta L_i^{GPR}) + Z_{0,i}^{GPR}. \tag{4.44}$$

Now that the trace origin coordinates are known, the (buried) rock surface coordinates for trace k can be calculated by multiplying the trace lengths L_{tr} with the trace angles γ and adding/subtracting these to the trace origin coordinates $x_s^{(k)}$ and $z_s^{(k)}$ as can be seen in

$$x_b^{(k)} = x_s^{(k)} + \sin(\gamma_k) * L_{tr,k} \tag{4.45}$$

and

$$z_b^{(k)} = z_s^{(k)} - \cos(\gamma_k) * L_{tr,k}. \tag{4.46}$$

The (buried) rock surface coordinates for each trace are then stored in c_b and c_s

$$c_b = [[x_b^{(0)}, ..., x_b^{(k)}, ...x_b^{(m)}], [z_b^{(0)}, ..., z_b^{(k)}, ..., z_b^{(m)}]], \tag{4.47}$$

$$c_s = [[x_s^{(0)}, ..., x_s^{(k)}, ...x_s^{(m)}], [z_s^{(0)}, ..., z_s^{(k)}, ..., z_s^{(m)}]]. \tag{4.48}$$

4.4.8. Step 7

In this final step, the rock surface, GPR survey path and the (buried) rock surfaces are plotted in the 2D spatial coordinate system, which should theoretically coincide with the true (buried) rock surfaces, see Figure 4.10. This graph also includes the GPR radargram including the identified reflection surfaces.

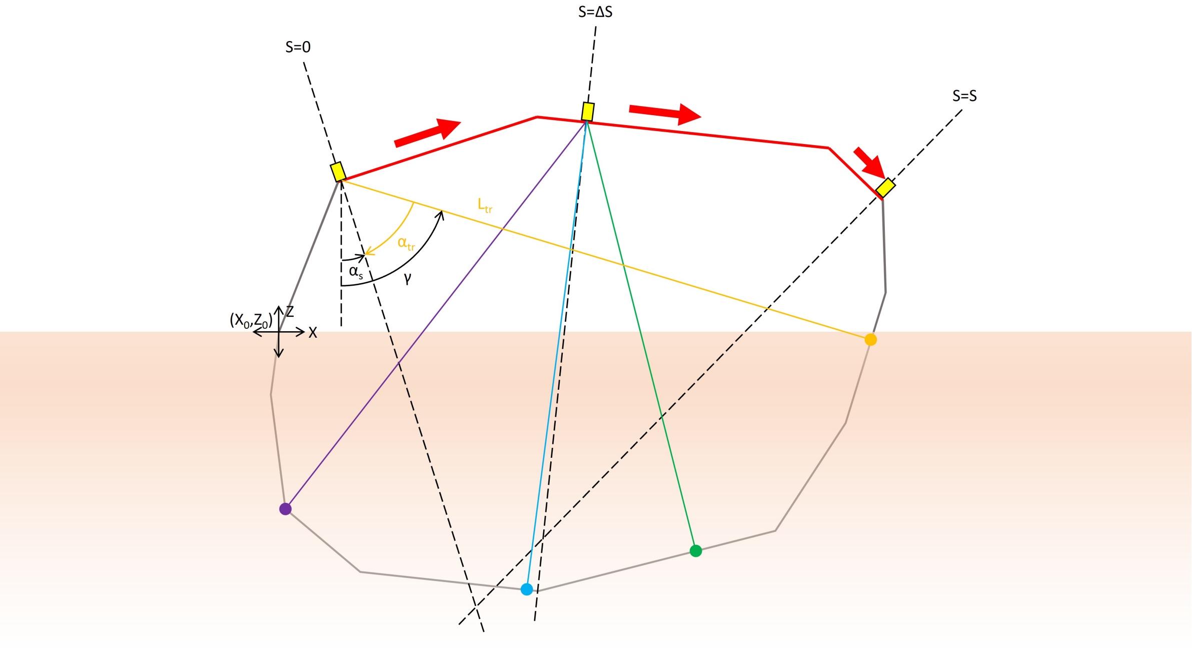

Figure 4.10: Converted traces (various colors) indicating the buried rock surface (dots) on top of the true (exposed + buried) rock surface C (grey), with the GPR survey path (red) in $x - z$ coordinates.

5

GEO to GPR point model

This chapter contains the basic principle behind the GEO-to-GPR point model and the input that is required. The output from this mathematical model is also discussed. Finally, the inner workings of the model are explained.

5.1. Basic principle

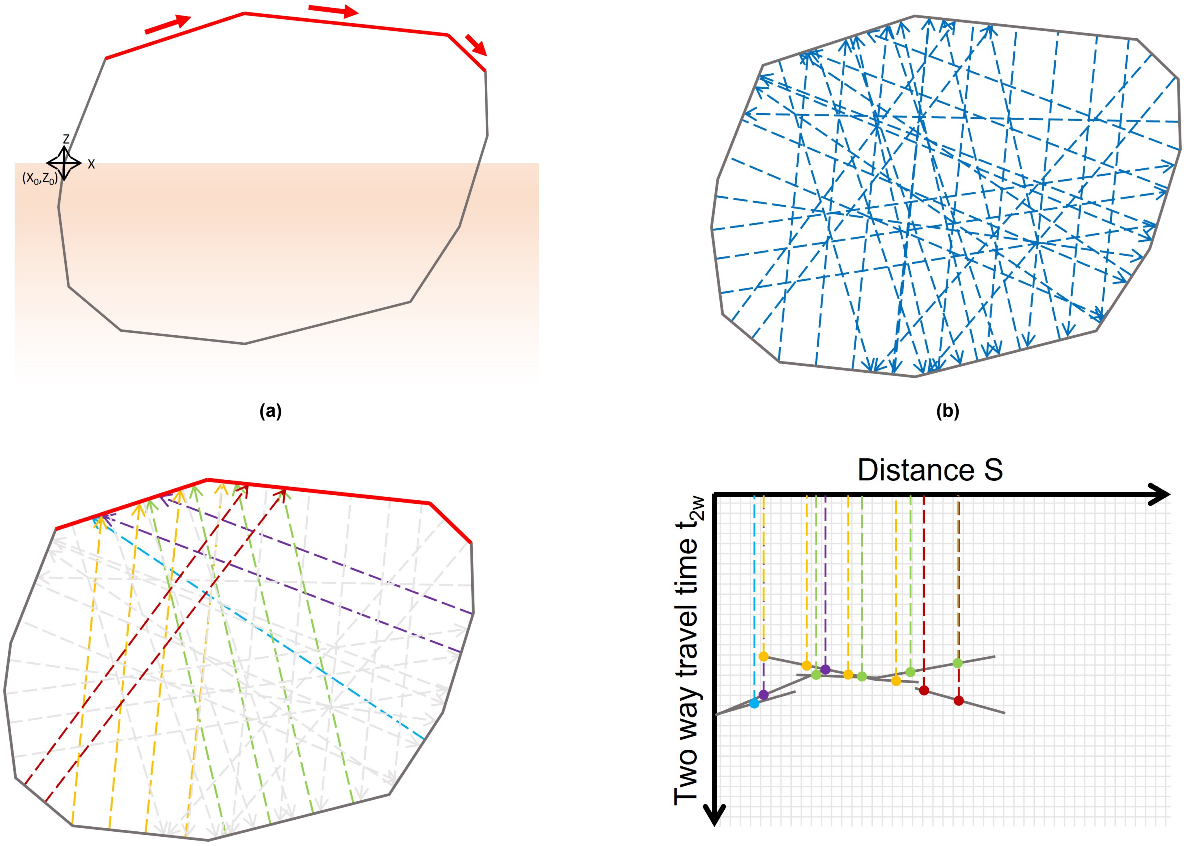

(a) (b) (c) (d)

Figure 5.1: Summary of the GEO-to-GPR point model. A Common Offset Survey, as defined by the GPR point model, is performed on a buried rock for an assumed buried rock contour (a). The GEO-to-GPR point model creates traces perpendicular to all rock surfaces, which represent reflections (b). The traces, or model reflections, ending at rock surfaces part of the GPR survey (c) are then converted into traces in a GPR radargram (d). The dots at the end of these traces indicate reflection surface coordinates.

The GEO-to-GPR point model is a mathematical model developed in Python based on the conceptual GPR point model described in Chapter 3. It is used to simulate a GPR radargram from a Common Offset Survey of a Ground Penetrating Radar (GPR) from an assumed rock surface, exposed and buried, contour (GEO), see Figure 5.1. A summarised overview of the model is shown, which is discussed in more detail in section 5.4 with an extensive explanation of each calculation step.

5.2. Input

The input of the model consists of a) the (exposed and buried) rock surface contour and b) several input parameters. Each of them is shortly described in the following subsections, including the appropriate manner to process the input.

5.2.1. Rock surface contour

The rock surface contour needs to be given as a python dictionary containing the exposed and buried coordinates of the rock surface in the following equation:

$$C_r = \left\{ \begin{matrix} 'c1' : C_{r,0} \\ ... \\ 'cX' : C_{r,N} \end{matrix} \right\}^{python\,dictionary}, \tag{5.1}$$

with each coordinate given as

$$C_{r,i} = [x_i, z_i] \tag{5.2}$$

and X being equal to $N+1$. These coordinates will need to be imported in python and arranged in such a way, that consecutive coordinates can form (linear) rock surfaces. The coordinates should start and end at $(x,z) = (0,0)$, going counter clockwise, in order for the model to work properly, which means that the buried rock surface coordinates are added in front of the exposed rock surface coordinates. The start and end coordinate $(x,z) = (0,0)$ is automatically added. The counter clockwise order of all coordinates is different from the GPR point-to-GEO model, which can be confusing and also means that the GPR survey path start and end coordinates are different.

5.2.2. Parameters

The input parameters are listed below, including three optional parameters.

- Start and end coordinate of the GPR survey (from rock surface coordinates) crd_0 and crd_1 (-)
- Velocity through medium v_{GPR} (m/ns)
- Spacing between consecutive traces s_{step} (m)
- Time step within trace Δt_{tr} (ns)
- Maximum time duration of trace t_{tr}^{max} (ns)
- Colour scheme indicator for graphs n_{cl} (-)
- Optional parameters
  - Showing of GPR radargram I (-))
  - Showing of traces at surface including trace lines $line$, default 'off'
  - Graph size D_{graph} (-))

Except for the $line$ parameter, all parameters were already defined for the GPR point-to-GEO model in section 4.2.3 in Chapter 4. However, the spacing parameter s_{step} now represents the spacing between the traces along the rock contour. In practice, this gives very similar results, but the parameter has a different physical meaning. The $line$ parameter is an extra optional parameter for visual purposes as it indicates if the traces within the rock contour in the output graphs are shown.

5.3. Output

The output of the GEO-to-GPR point model is a plot consisting of a) a GPR radargram containing the reflection coordinates and actual reflection surfaces from the GPR survey (left) and b) a schematic of the rock contour (exposed and buried) in the 2D spatial coordinate system including the reflection traces and their origin (righ), see Figure 5.2.

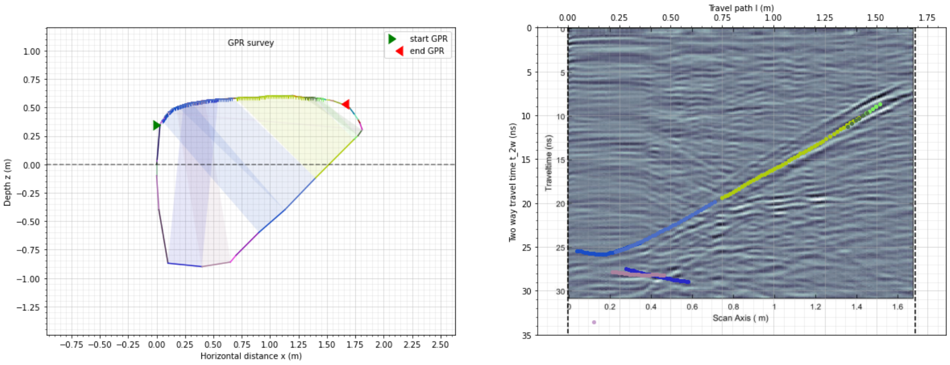

Figure 5.2: Example output GEO-to-GPR point model with the schematic of the rock contour at the left and the GPR radargram including modelled reflections at the right.

5.4. Model calculations

If the input of the GEO-to-GPR model is correctly processed and every parameter is defined, the model can be run to simulate the GPR radargram. A concise overview of the model and its calculation steps can be seen in subsection 5.4.1. A more comprehensive explanation of each calculation step can be found in subsections 5.4.2 to 5.4.12.

5.4.1. Model steps

The model can be divided in 11 steps, which are numbered in the flowchart given in Figure 5.3. An overview and clarification of the parameters in the flowchart is given above the flowchart.

crd_0 = Start coordinate of the GPR survey (from rock surface coordinates) (-)
crd_1 = End coordinate of the GPR survey (from rock surface coordinates) (-)
v_{GPR} = Velocity through medium (m/ns)
s_{step} = Spacing between consecutive traces (m)
Δt_{tr} = Time step within trace (ns)
t_{tr}^{max} = Maximum time duration of trace (ns)
n_{cl} = Colour scheme indicator for graphs (-)
I = Showing of GPR radargram (-)
$line$ = Showing of traces at surface including trace lines, default ’off’
D_{graph} = Graph size (-)
C_r = Python dictionary of rock surface coordinates
C_r^p = Python dictionary of GPR survey path coordinates
S_r = Rock surface slope coordinates
S_p = GPR survey path slope coordinates
C = Slopes, 2D coordinates and lengths of rock surface slopes
P = Slopes, 2D coordinates and lengths of GPR survey path slopes
crd_{vrt} = Coordinates of vertical traces of maximum time duration [(m), (m)]
L_{tr} = Origins of vertical traces along GPR survey with respect to start coordinate (m)
ΔL_{tr} = Spatial step within trace [(m), (m)]
iD_{vrt} = Index numbers of rock surface slope corresponding to each trace (-)
crd_{prp} = Coordinates of vertical traces perpendicular to rock surface slopes [(m), (m)]
crd_{srf} = Coordinates of perpendicular traces to opposing rock surface [(m), (m)]
crd_{GPR} = Coordinates of surface traces in GPR survey path [(m), (m)]
iD_{GPR} = Index numbers of GPR survey path slopes corresponding to each trace (-)
crd_{tr} = Coordinates of reflections in GPR radargram from GPR traces [(m), (ns)]
iD_{tr} = Index numbers of GPR survey path slopes corresponding to reflection coordinates (-)

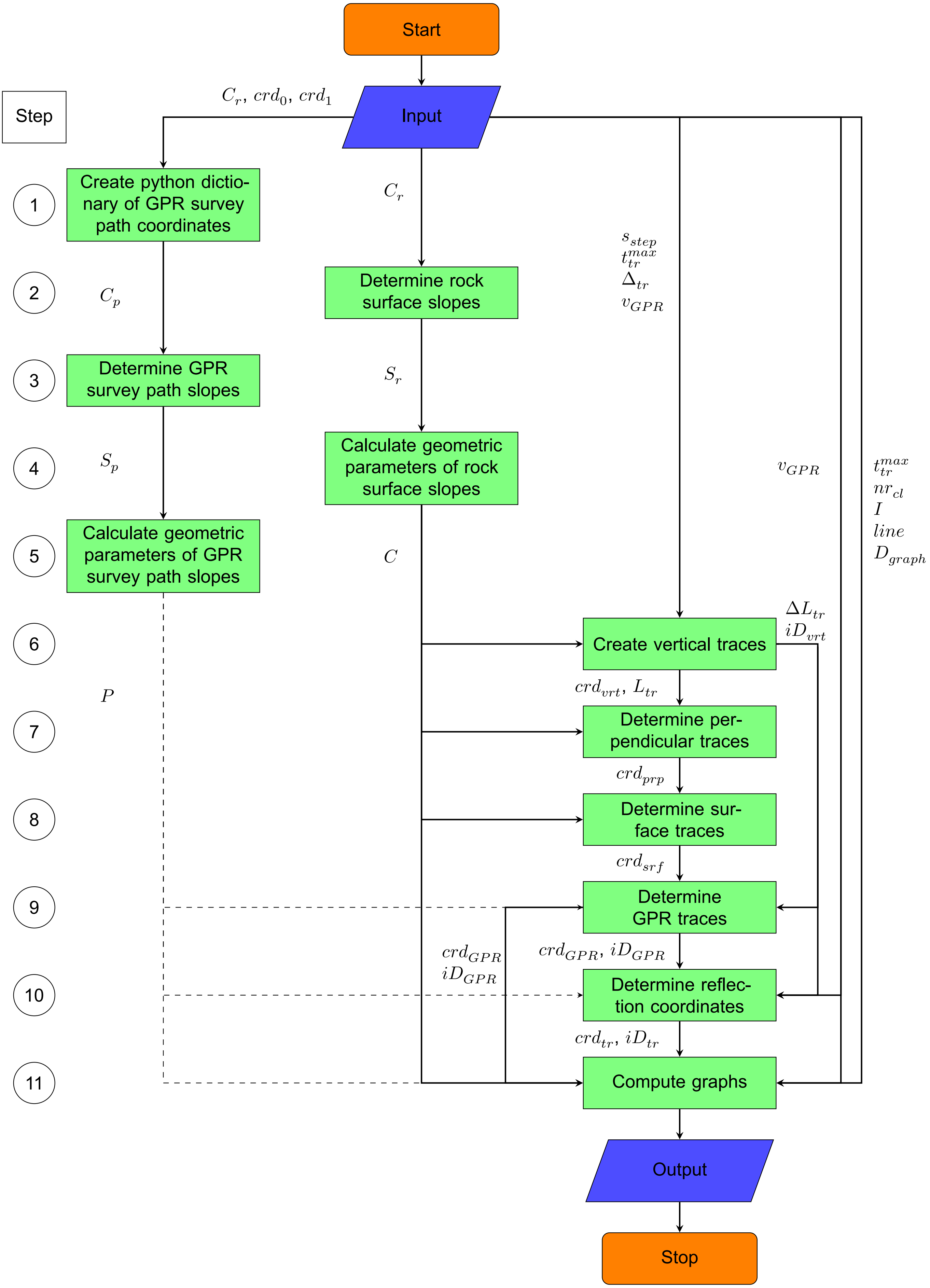

Figure 5.3: Flowchart of GEO-to-GPR point model including the 11 calculations steps further explained in the subsequent subsections. The input parameters are shown as input for every step as well as the parameters between each calculation step.

5.4.2. Step 1

A drawing of the rock surface cross-section including a GPR survey path can be seen in Figure 5.4. It shows the 2D coordinate system in which the rock surface coordinates are given.

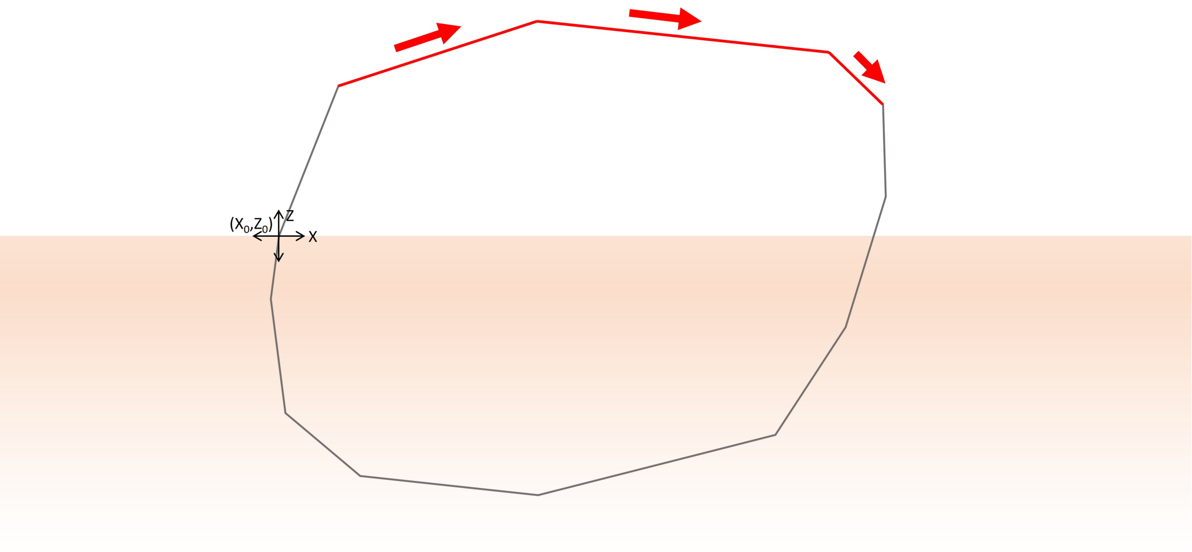

Figure 5.4: Rock surface C (grey) and GPR survey path (red) in $x - z$ coordinate system

The rock surface coordinates are given as a Python dictionary as can be seen in Eq. 5.1 in section 5.2. The rock surface coordinate $C_{r,i}$ was given as in Eq. 5.2, with x_i and z_i as horizontal and vertical coordinate respectively.

To determine the GPR survey path coordinates, the input parameters crd_0 and crd_1 are used. A new Python dictionary is created containing only the rock surface coordinates which are part of the GPR survey path. The newly created dictionary with X number of coordinates can be seen in

$$C_p = \left\{ \begin{matrix} 'c1' : C_{r,crd_0} \\ ... \\ 'cX' : C_{r,crd_1} \end{matrix} \right\}^{python\ dictionary} . \tag{5.3}$$

5.4.3. Step 2

The rock surface coordinates are given as a Python dictionary as can be seen in Eq. 5.1 in section 5.2. The coordinates are used to determine the rock surface slopes. This means that out of a number of coordinates N from C_r, a list of N-1 slopes can be formed. The rock surface slopes are the given as in

$$S_r = [S_{r,0}, ..., S_{r,i}, ..., S_{r,N-1}], \tag{5.4}$$

with the coordinates of rock surface slope $S_{r,i}$ given as

$$S_{r,i} = [x_i, z_i, x_{i+1}, z_{i+1}]. \tag{5.5}$$

5.4.4. Step 3

The GPR survey path coordinates are given as a Python dictionary as can be seen in Eq. 5.3 in section 5.4.2. The coordinates are used to determine the GPR survey path slopes. This means that out of a number of coordinates N from C_p, a list of N-1 slopes can be formed. The GPR survey path slopes are given in

$$S_p = [S_{p,0}, ..., S_{p,i}, ..., S_{p,N-1}], \tag{5.6}$$

with the coordinates of rock surface slope $S_{p,i}$ given as

$$S_{p,i} = [x_i, z_i, x_{i+1}, z_{i+1}]. \tag{5.7}$$

5.4.5. Step 4

In this step, the geometric parameters of the rock surface slopes S_r from section 5.4.3 are determined. The coordinates system in which the slope coordinates, slope angle and slope length are calculated can be seen in Figure 5.4 in section 5.4.2.

The slope angle α_s and length Δl of each rock surface are given by

$$\alpha_s = \text{arctan}\left(\frac{z_1 - z_0}{x_1 - x_0}\right) \tag{5.8}$$

and

$$\Delta l = \sqrt{(x_1 - x_0)^2 + (z_1 - z_0)^2}, \tag{5.9}$$

with:

x_0 = Horizontal start coordinate of rock surface slope S_r (m)
x_1 = Horizontal end coordinate of rock surface slope S_r (m)
z_0 = Vertical start coordinate of rock surface slope S_r (m)
z_1 = Vertical end coordinate of rock surface slope S_r (m)

The six geometric parameters of the rock surface slopes (x_0, x_1, z_0, z_1, α_s and Δl) are then stored in a list

$$C = [X_0, X_1, Z_0, Z_1, \mathrm{A}_s, \Delta L], \tag{5.10}$$

in which X_0, X_1, Z_0, Z_1, A and ΔL are given for a number of N slopes as

$$X_0 = [x_{0,0}, ..., x_{0,N}], \tag{5.11}$$

$$X_1 = [x_{1,0}, ..., x_{1,N}], \tag{5.12}$$

$$Z_0 = [z_{0,0}, ..., z_{0,N}], \tag{5.13}$$

$$Z_1 = [z_{1,0}, ..., z_{1,N}], \tag{5.14}$$

$$\mathrm{A}_s = [\alpha_{s,0}, ..., \alpha_{s,N}], \tag{5.15}$$

$$\Delta L = [\Delta l_0, (\Delta l_0 + \Delta l_1), ..., (\Delta l_0 + \Delta l_1 + ... + \Delta l_N)]. \tag{5.16}$$

Important to note is that the cumulative length of each slope is stored, not the actual length of each slope.

5.4.6. Step 5

In this step, the geometric parameters of the GPR survey path slopes S_p from section 5.4.4 are determined. The coordinates system in which the slope coordinates, slope angle and slope length are calculated can be seen in Figure 5.4 in section 5.4.2.

The slope angle α_s and length Δl of slope are calculated according to Equation 5.8 and 5.9 in section 5.4.5. In these Equations:

x_0 = Horizontal start coordinate of GPR survey path slope S_p (m)
x_1 = Horizontal end coordinate of GPR survey path slope S_p (m)
z_0 = Vertical start coordinate of GPR survey path slope S_p (m)
z_1 = Vertical end coordinate of GPR survey path slope S_p (m)

The six geometric parameters of the GPR survey path slopes (x_0, x_1, z_0, z_1, α_s and Δl) are then stored in a list

$$P = [X_0, X_1, Z_0, Z_1, \mathrm{A}_s, \Delta L], \tag{5.17}$$

in which X_0, X_1, Z_0, Z_1, A_s and ΔL are given for a number of N slopes as

$$X_0 = [x_{0,0}, ..., x_{0,N}], \tag{5.18}$$

$$X_1 = [x_{1,0}, ..., x_{1,N}], \tag{5.19}$$

$$Z_0 = [z_{0,0}, ..., z_{0,N}], \tag{5.20}$$

$$Z_1 = [z_{1,0}, ..., z_{1,N}], \tag{5.21}$$

$$\mathrm{A}_s = [\alpha_{s,0}, ..., \alpha_{s,N}], \tag{5.22}$$

$$\Delta L = [\Delta l_0, (\Delta l_0 + \Delta l_1), ..., (\Delta l_0 + \Delta l_1 + ... + \Delta l_N)]. \tag{5.23}$$

Important to note is that the cumulative length of each slope is stored, not the actual length of each slope.

5.4.7. Step 6

In this step, the vertical traces at the rock surfaces are created which will eventually be converted into traces in the GPR radargram. The vertical traces in the rock contour can be seen in Figure 5.5.

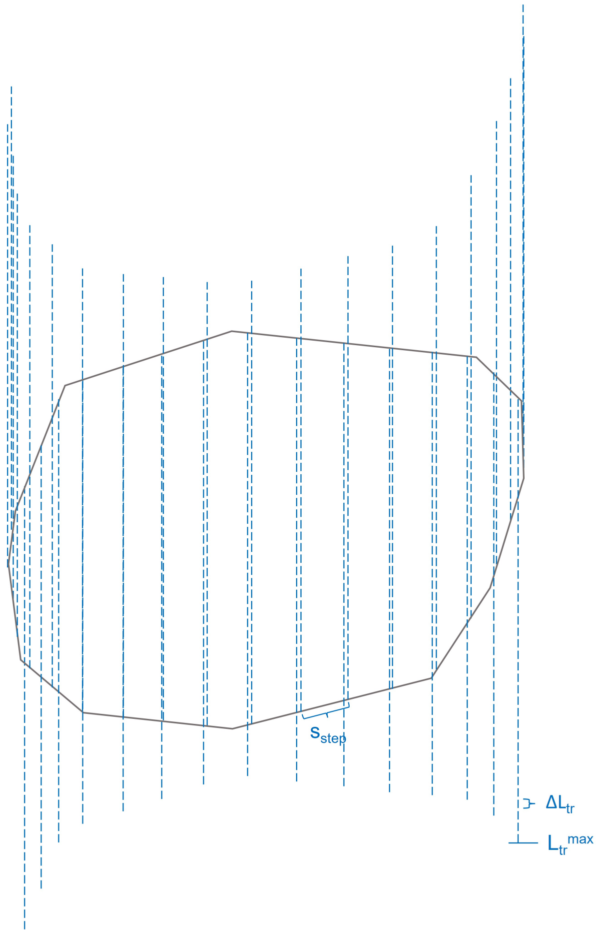

Figure 5.5: Vertical traces at the rock surfaces of the rock contour, with the step size between consecutive traces along the rock contour s_{step}, the spatial step within the trace ΔL_{tr} and the maximum trace length L_{tr}^{max}

First, the number of traces is determined based on the circumference of the rock and the spacing between consecutive traces s_{step}. The circumference is equal to the last value of ΔL from C in Eq. 5.10 in section 5.4.5. The, rounded down, number of traces N_{tr} can then be determined using

$$N_{tr} = \lfloor \frac{\Delta L_N}{s_{step}} \rfloor. \tag{5.24}$$

The origins for the vertical traces along the rock surface, but not yet in 2D coordinates, are then given as

$$L_{tr} = [0, s_{step}, ..., i * s_{step}, ..., N_{tr} * s_{step}]. \tag{5.25}$$

The length of the vertical traces L_{tr}^{max} is based on the maximum time duration t_{tr}^{max} in a GPR radargram, given as input, and can be determined with

$$L_{tr}^{max} = t_{tr}^{max} * \frac{v_{GPR}}{2}. \tag{5.26}$$

The corresponding spatial step ΔL_{tr} is based on the input time step Δt_{tr} in the GPR radargram, which can be seen in

$$\Delta L_{tr} = \Delta t_{tr} * \frac{v_{GPR}}{2}. \tag{5.27}$$

The number of spatial steps, rounded down, along the vertical trace for a maximum time duration can then be determined using

$$N_{dtr} = \lfloor \frac{L_{tr}^{max}}{\Delta L_{tr}} \rfloor. \tag{5.28}$$

However, the vertical trace origins need to be converted to the 2D spatial coordinate system mentioned before. Therefore, the trace origin coordinates are required to be given in horizontal and vertical coordinates. In order to calculate the origin in 2D, the cumulative slope lengths ΔL from C are required. If a trace i lies on a rock surface slope j, the horizontal and vertical origin coordinates can be determined using

$$x_{tr,i} = \cos(\alpha_{s,j}) * (L_{tr,i} - \Delta L_{j-1}) + X_{0,j} \tag{5.29}$$

and

$$z_{tr,i} = \sin(\alpha_{s,j}) * (L_{tr,i} - \Delta L_{j-1}) + Z_{0,j}. \tag{5.30}$$

For the slope with index $j = 0$, the corresponding cumulative slope length $\Delta L = 0$. The horizontal and vertical coordinates of the vertical traces with maximum time duration or maximum length can then be given respectively as

$$X_{vrt,i} = [x_{tr,i}^{(0)}, ..., x_{tr,i}^{(N_{dtr})}] \tag{5.31}$$

and

$$Z_{vrt,i} = [z_{tr,i}, ..., z_{tr,i} + \frac{j}{N_{dtr}} * L_{tr}^{max}, ..., z_{tr,i} + L_{tr}^{max}], \tag{5.32}$$

in which i is the trace number for $0 \leq i \leq N_{tr}$ and j is the spatial step for $0 \leq j \leq N_{dtr}$. In Eq. 5.32, the vertical trace is defined as being in upward direction, but depending on the orientation of the slope, the vertical traces can also be in downward direction. The vertical trace coordinates are given as

$$crd_{vrt} = [X_{vrt}, Z_{vrt}], \tag{5.33}$$

with X_{vrt} and Z_{vrt} defined as

$$X_{vrt} = [X_{vrt,0}, ..., X_{vrt,N_{tr}}] \tag{5.34}$$

and

$$Z_{vrt} = [Z_{vrt,0}, ..., Z_{vrt,N_{tr}}]. \tag{5.35}$$

Finally, the index number of the slope corresponding to a vertical trace is given as

$$iD_{vrt,i} = j, \tag{5.36}$$

with the trace number i and slope number j. The list of index numbers for each trace is then given by

$$iD_{vrt} = [iD_{vrt,0}, ..., iD_{vrt,N_{tr}}]. \tag{5.37}$$

5.4.8. Step 7

In this step the perpendicular traces at the rock surfaces are determined which will eventually be converted into traces in the GPR radargram. The perpendicular traces in the rock contour can be seen in Figure 5.6. Figure 5.6.

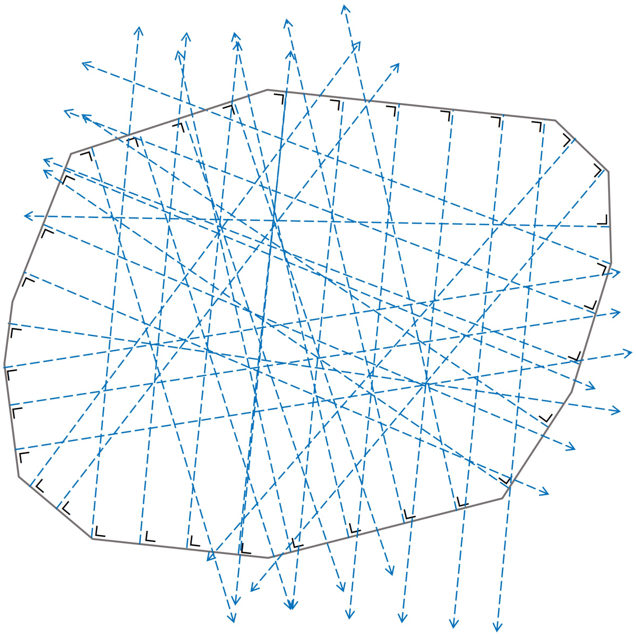

Figure 5.6: Perpendicular traces with maximum length

The coordinates of the vertical traces are given as in Eq. 5.31 and 5.32 in section 5.4.7. Perpendicular traces are required for further calculations, so the following calculations are performed. For a vertical trace i originating on a rock surface slope j, the coordinates of the trace perpendicular to that slope j are given by

$$X_{prp,i} = X_{vrt,i} - (Z_{vrt,i} - Z^{(0)}_{vrt,i}) * \sin(\alpha_{s,j}) \tag{5.38}$$

and

$$Z_{prp,i} = Z_{vrt,i} - (Z_{vrt,i} - Z^{(0)}_{vrt,i}) * (1 - \cos(\alpha_{s,j})). \tag{5.39}$$

The perpendicular trace coordinates are then given as

$$crd_{prp} = [X_{prp}, Z_{prp}], \tag{5.40}$$

with X_{prp} and Z_{prp} defined as

$$X_{prp} = [X_{prp,0}, ..., X_{prp,N_{tr}}] \tag{5.41}$$

and

$$Z_{prp} = [Z_{prp,0}, ..., Z_{prp,N_{tr}}]. \tag{5.42}$$

5.4.9. Step 8

In this step the surface traces, perpendicular traces which end at opposing rock surface, are determined which will eventually be converted into traces in the GPR radargram. The surface traces in the rock contour can be seen in Figure 5.7.

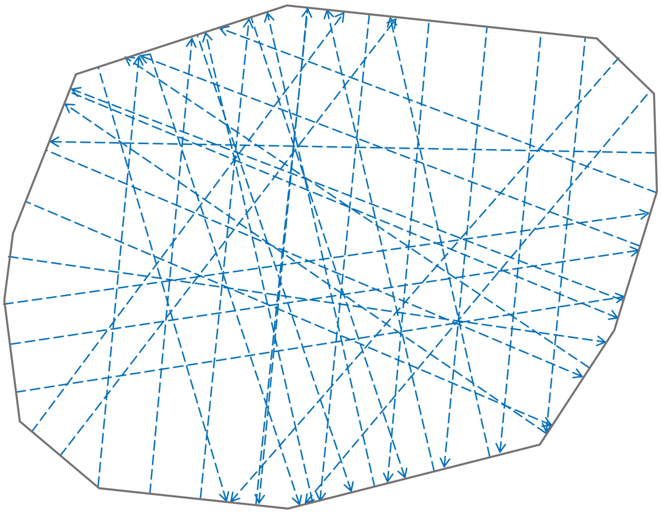

Figure 5.7: Surface traces limited by the rock contour

The perpendicular traces are cutoff after the last coordinate set which is still located inside the rock contour. In order to determine this cutoff point, each coordinate set is evaluated for its boundaries. The boundaries are defined as the slopes of surrounding rock surface. These are the slopes j for which the k^{th} set of coordinates of trace i ($X^{(k)}_{prp,i}$ and $Z^{(k)}_{prp,i}$) are located within the ranges of these slopes. Four different slope orientations with respect to its coordinates can be distinguished, which give different physical meanings of the boundaries. Depending on the exact orientation, the vertical boundary can either be a upper or lower limit. For the horizontal boundary, this means either a limit at the left hand side or right hand side. For each orientation, the boundaries are given by

$$Z_{lim} = \tan(\alpha_{s,j}) \cdot (X^{(k)}_{prp,i} - X0,j) + Z_{0,j} \tag{5.43}$$

and

$$X_{lim} = \frac{Z^{(k)}_{prp,i} - Z0,j}{\tan(\alpha_{s,j})} + X_{0,j}. \tag{5.44}$$

If the four boundary conditions are met ($X^{(k)}_{prp,i} \leq X_{lim,right}$, $X^{(k)}_{prp,i} \geq X_{lim,left}$, $Z^{(k)}_{prp,i} \leq Z_{lim,up}$ and $Z^{(k)}_{prp,i} \geq Z_{lim,down}$), the trace coordinate is assumed to be within the rock contour. When these conditions are not met, the trace coordinates are excluded. The horizontal and vertical coordinates of the surface traces can then be given by

$$X_{srf,i} = [X^{(0)}_{prp,i}, ..., X^{(K_i)}_{prp,i}] \tag{5.45}$$

and

$$Z_{srf,i} = [Z^{(0)}_{prp,i}, ..., Z^{(K_i)}_{prp,i}], \tag{5.46}$$

with variable length $K_i \leq N_{dtr}$. The surface trace coordinates are then given by

$$crd_{srf} = [X_{srf}, Z_{srf}], \tag{5.47}$$

with X_{srf} and Z_{srf} defined as

$$X_{srf} = [X_{srf,0}, ..., X_{srf,N_{tr}}] \tag{5.48}$$

and

$$Z_{srf} = [Z_{srf,0}, ..., Z_{srf,N_{tr}}]. \tag{5.49}$$

5.4.10. Step 9

In this step the GPR traces, surface traces ending in GPR survey path, are determined which will eventually be converted into traces in the GPR radargram. The GPR traces in the rock contour can be seen in Figure 5.8.

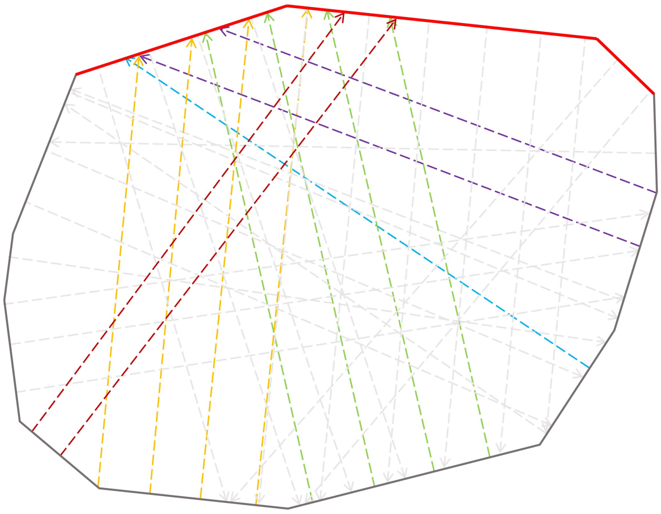

Figure 5.8: GPR traces (various colors) in GPR survey (red) and the excluded surface traces (grey)

In section 5.4.6, the slope parameters P were determined. To exclude the surface traces that do not appear in the GPR survey path, the final trace coordinate K_i of trace i should be located very close ($\Delta x \leq \Delta L_{tr}$ and $\Delta z \leq \Delta L_{tr}$) to a GPR survey path slope. If this condition is met for both the horizontal and vertical direction, the surface trace i can be assumed to be GPR survey path trace m as can be seen in

$$X_{GPR,m} = X_{srf,i} \tag{5.50}$$

and

$$Z_{GPR,m} = Z_{srf,i}, \tag{5.51}$$

with $i \leq N_{tr}$ and $m \leq N_{tr}^{new} \leq N_{tr}$. This means a reduction of trace numbers, which means that the list of index numbers iD_{vrt} of slope j for each trace i also changes as can be seen in

$$iD_{GPR,m} = iD_{vrt,i} = j \tag{5.52}$$

and

$$iD_{GPR} = [iD_{GPR,0}, ..., iD_{GPR,N_{tr}^{new}}]. \tag{5.53}$$

The GPR trace coordinates are then given by

$$crd_{GPR} = [X_{GPR}, Z_{GPR}], \tag{5.54}$$

with X_{GPR} and Z_{GPR} defined as

$$X_{GPR} = [X_{GPR,0}, ..., X_{GPR,N_{tr}^{new}}] \tag{5.55}$$

and

$$Z_{GPR} = [Z_{GPR,0}, ..., Z_{GPR,N_{tr}^{new}}]. \tag{5.56}$$

5.4.11. Step 10

In this step the GPR traces are converted into reflection coordinates. The reflection coordinates in the GPR radargram can be seen in Figure 5.9.

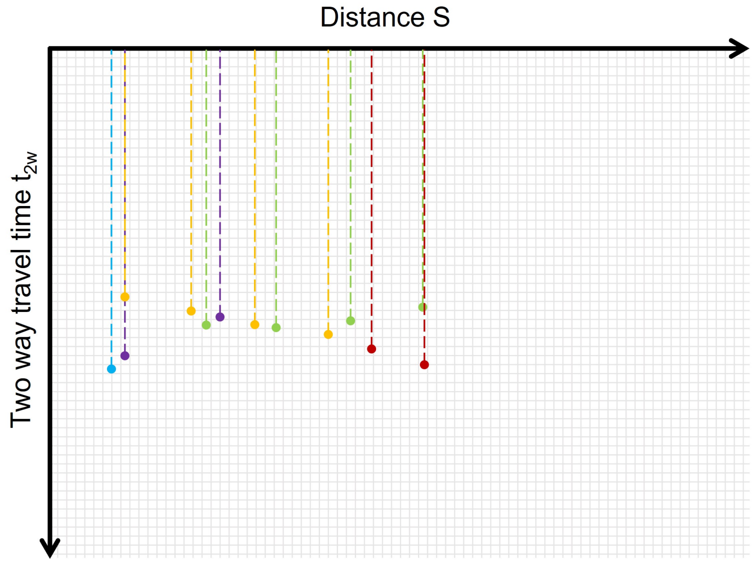

Figure 5.9: GPR radargram with reflection coordinates in various colors corresponding to certain rock surface slopes

The length of each GPR trace L_{GPR} needs to be converted into a time duration T_{GPR}. The length of each GPR trace m is defined as the difference between the first (0) and last (K_m^{th}) coordinate

$$L_{GPR,m} = \sqrt{(X_{GPR,m}^{(K_m)} - X_{GPR,m}^{(0)})^2 + (Z_{GPR,m}^{(K_m)} - Z_{GPR,m}^{(0)})^2}, \tag{5.57}$$

while the conversion of the one way travel length of each trace $L_{GPR,m}$ into a two way travel time $T_{GPR,m}$ is defined as

$$T_{GPR,m} = 2 \cdot \frac{L_{GPR,m}}{v_{GPR}}. \tag{5.58}$$

The time coordinates of the reflection surfaces are now known as well as the origin of the reflection at the GPR survey path. However, the origin coordinates of the reflections ($X_{GPR,m}^{(K_m)}$ and $Z_{GPR,m}^{(K_m)}$) first need to be ordered along the GPR survey path. The origin along the horizontal axis of the GPR radargram S_{GPR,m^*} of each trace m on a GPR survey path slope j is given as

$$S_{tr,m^*} = \sqrt{(X_{GPR,m}^{(K_m)} - X_{0,j})^2 + (Z_{GPR,m}^{(K_m)} - Z_{0,j})^2} + \Delta L_{j-1}. \tag{5.59}$$

For slope $j = 0$, the distance to the start coordinate of the GPR survey $\Delta L = 0$. The corresponding time duration T_{tr,m^*} is given by

$$T_{tr,m^*} = T_{GPR,m}. \tag{5.60}$$

As the index numbers are also re-arranged, the new list of index numbers of slope j for GPR survey path trace m is shown in

$$iD_{tr} = [iD_{tr,0}, ..., iD_{tr,N_{tr}^{new}}], \tag{5.61}$$

with

$$iD_{tr,m^*} = iD_{GPR,m}. \tag{5.62}$$

The reflection surface coordinates are then given as

$$crd_{tr} = [S_{tr}, T_{tr}], \tag{5.63}$$

with S_{tr} and T_{tr} defined as

$$S_{tr} = [S_{tr,0}, ..., S_{tr,N_{tr}^{new}}] \tag{5.64}$$

and

$$T_{tr} = [T_{tr,0}, ..., T_{tr,N_{tr}^{new}}]. \tag{5.65}$$

5.4.12. Step 11

In this final step, the reflection are plotted in a GPR radargram on top of the actual reflection surfaces from the GPR survey, see Figure 5.10. The graph also includes a schematic of the rock contour (exposed and buried) and the GPR survey path in the 2D spatial coordinate system.

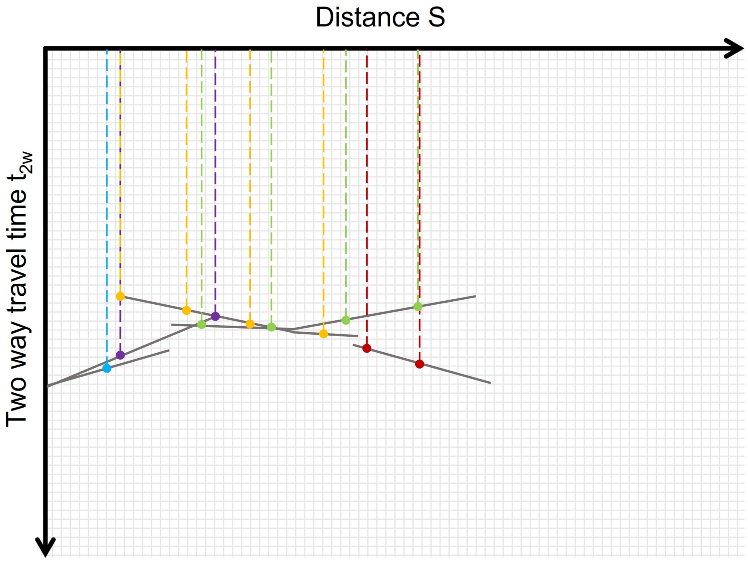

Figure 5.10: GPR radargram with reflection coordinates on top of the reflection surfaces from the GPR survey

6

Methodology GPR

This chapter contains the method used in obtaining the buried rock surface using the Ground Penetrating Radar. It is an extensive approach and contains several crucial steps that need to be taken in order to determine the buried rock surfaces. A concise overview of the most important steps is given below:

1. Acquisition of GPR data
2. Processing of GPR data
3. Identification of reflection surfaces
4. Acquisition of exposed rock contour
5. Calculation of rock surfaces
6. Estimation of buried rock contour
7. Modelling of GPR data

Acquisition of GPR data will be done in the field by performing a Common Offset Survey with a high-frequency Ground Penetrating Radar, preferably in a grid in order to obtain information in all directions. Also, a transillumination survey will be performed in order to determine the cross-sectional propagation velocity through the rock. The data is processed in MatGPR in order to identify the reflective surfaces in the next step (Tzanis, 2010), which is performed manually. The rock is scanned with LiDAR, which results in a 3D model containing a mesh from which the exposed rock surface can be retrieved.

The most important step, the calculation of the (buried) rock surface coordinates, is done with help from a self-developed Python model. The so-called GPR point-to-GEO model is based on the two-dimensional geometry of a cross-section of a rock surveyed in a Common Offset Survey, assuming that the Ground Penetrating Radar has no dimensions and can therefore be considered a point during its survey.

After the determination of the (buried) rock surfaces, an approximation of the buried rock contour can be made. The assumed buried rock surfaces can then be analysed with another self-developed Python model based on the same principles as the GPR point-to-GEO model. The GEO-to-GPR point can model reflections from the assumed buried geometry. It is an iterative process in which the buried rock contour is continuously updated based on the fit of the modelled reflections with the acquired GPR data from the field until a satisfactory fit has been achieved.

Each step is discussed in more detail in the upcoming sections.

6.1. GPR Data acquisition

Two types of data acquisition will need to be performed in the field: a) a Common Offset Survey and b) a Transillumination Survey

6.1.1. Common Offset Survey

To gain insight into the buried rock contour, the use of a Common Offset Survey is proposed in the field despite the relatively small scale of the area of interest. The GPR was not developed to identify the dimensions of small-scale areas with buried planes significantly non-parallel to the survey path. This means that the survey over a rock inherently encounters blind spots. For the survey, several straight lines over the rock should be made, avoiding rough transition zones. Each line should be surveyed in both directions in order to check the reproducibility of the measurements and to collect as much information on the subsurface as possible.

The obtained data requires processing to be able to see clear reflection surfaces. This is explained in section 6.2.

6.1.2. Transillumination Survey

A transillumination survey is required to determine the propagation velocity of the signal through the rock. By placing the receiving and transmitting antennas at different sides of the rock, a travel time can be measured by calculating the difference between the arrival times. Important is that at least two measurements at different distances have to be performed in order to calculate two arrival times and thereby removing the time delay between the antennas. Alternatively, placing the antennas directly against each other will result directly in the time delay, which means only one measurement has to be performed. The distance between transmitter and receiver can be retrieved from the 3D model from the LiDAR scan, which combined with the travel time will then result in a propagation velocity.

The Transillumination Survey data does not require processing as the arrival times can be easily retrieved from the data. By repeating the measurements many times with the antennas at the same position and then stacking the resulting signals, an arrival time can be determined. The used definition of the arrival time, or time zero, is given in section 6.2.

From Table 3.1, expected velocities for rocks range between 0.12-0.13 m/ns, with 0.13 m/ns for granites and 0.12 m/ns for limestones.

6.2. GPR Data processing

Once the GPR data is acquired, the Common Offset Survey data needs to be processed in order to analyse the reflective surfaces in the GPR radargram. This can be done in any GPR processing program, but is performed in MatGPR. The processing steps that are taken are listed below.

- Adjust time zero
- Remove (global) background
- Remove DC
- Dewow
- Inverse Amplitude Decay

6.2.1. Adjust time zero

As mentioned for the Transillumination survey, a time delay exists for the antennas as the signal originates from within the antenna, not on the interface of antenna-air. In order to remove this time delay from the measurements, a shift has to be performed. Different time zero definitions exist, see Figure 6.1, and option A is chosen as it represents the time zero that is often used in seismic measurements. As these measurements are also considered in this thesis, this time zero is chosen for continuity purposes. (Yelf, 2004)

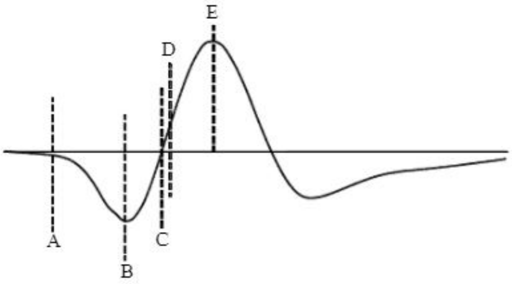

Figure 6.1: Examples of time zero used for the GPR from Yelf (2004)

6.2.2. Remove (global) background

Removing the global background means that the background trace is removed. The background trace is the average trace determined by adding all existing traces and dividing it over the number of traces. This is also called stacking. It reduces the randomly varying signal or noise and enhances the coherent signal, which is the horizontal banding often seen in GPR data. By removing it, the appearance of the data is improved.

6.2.3. Remove DC

DC or Direct Current is the arithmetic mean of a trace. This is the mean offset of the signal with respect to its expected neutral position at an amplitude of zero. By removing the DC for each trace, a more uniform GPR radargram can be expected.

6.2.4. Dewow

This step is taken to remove the very low-frequency component from the GPR data. It basically removes the slowly undulating GPR trace baseline, which enhances the appearance of the data.

6.2.5. Inverse Amplitude Decay

An unprocessed GPR radargram has very limited readability for the lower parts of the radargram, especially for a high-frequency GPR. In order to see these parts, a gain function has to be applied. An example of a gain function is the Inverse Amplitude Decay, which increases the amplitude of the lower parts of the GPR radargram (reflections far from the surface) and decreases the amplitude of the shallow parts of the GPR (reflections close to the surface).

First, the analytic signal is computed for all traces. Then, a median and mean amplitude attenuation function is computed based on the analytic signals. Furthermore, an empirical best fitting attenuation model is computed with the function that can be seen in Equation 6.1 with N linear parameters and N non-linear parameters.

$$A(t) = c_1 e^{-a_1 t} + c_2 e^{-a_2 t} + ... + c_N e^{-a_N t} \tag{6.1}$$

Depending on the best fit (mean or median attenuation), the gain function can be determined. The gain function is the normalized inverse of the amplitude decay model, see Equation 6.2.

$$g(t) = \left(\frac{A(t)}{\max A(t)} \right)^{-1} \tag{6.2}$$

Other gain functions exists, but this model was chosen as it gave the clearest results.

6.3. Reflection surface identification

When the GPR data is processed, the reflection surfaces in the GPR radargrams can be identified. The coordinates of each reflection need to be determined by manually analysing the GPR radargrams. A reflection surface is defined as a linear fit of a strong reflection. If the reflection appears to be curved in the GPR radargram, it is assumed to consist of multiple, smaller, linear reflection surfaces. The reflection is defined as the first indication of a strong reflection which is consistent with the determination of time zero, so not at the point of maximum amplitude. Every reflection surface is then given as a set of coordinates in a python dictionary, as explained in Chapter 4 in section 4.2.1

6.4. Exposed rock surface acquisition

The rock surface contour is needed to identify the GPR survey path. The exposed rock surface can be acquired from the 3D model of the rock. The 3D model is a mesh that is calculated from a point cloud model made by the LiDAR (accuracy of 2 mm). The rock mesh is described by vertices. To extract relevant two-dimensional cross-sections, a plane with limited thickness can be extracted from the mesh. This plane with a certain thickness contains vertices that are assumed to be approximately on a 2D plane (zero thickness), which can be extracted as a text file.

The cross-section will then consist of a number of coordinates, depending on the resolution of the mesh. The coordinates in the text file are required to be re-arranged in clockwise order. Every rock surface coordinate must then be given in a python dictionary, as explained in section 4.2.2.

6.5. Rock surfaces calculation

The most important step is the calculation of the (buried) rock surfaces. This is done with the help of the already mentioned GPR point-to-GEO model, which was explained in Chapter 4. Besides the exposed rock surface contour C_r and the reflection surfaces S_r, some other input parameters are required. The input parameters are listed below, including two optional parameters. Each parameter is explained in Chapter 4 in section 4.2.

- Start and end coordinate of the GPR survey (from rock surface coordinates) crd_0 and crd_1 (-)
- Velocity through medium v_{GPR} (m/ns)
- Spacing between consecutive traces s_{step} (m)
- Time step within trace Δt_{tr} (ns)
- Maximum time duration of trace t_{tr}^{max} (ns)
- Colour scheme indicator for graphs n_{cl} (-)
- Optional parameters
  - Showing of GPR radargram I (-))
  - Graph size D_{graph} (-))

When the required input is given, the GPR point-to-GEO model can be run. As output, the (buried) rock surface coordinates are given as well as an explanatory graph consisting of the (buried) rock surfaces with respect to the exposed rock surfaces and the input GPR radargram with the identified reflection surfaces.

6.6. Buried rock contour estimation

From the rock surface coordinates, an educated guess with respect to the buried rock contour can be made. It is important to note that this is based on the **indirect** results from the GPR survey and not the **direct** results, which means that deviations from the true buried rock contour can already exist before starting this analysis step. It is thus crucial that the results from this step are not considered to reflect the true conditions. However, as a first approach, it offers insight into a possible buried rock surface.

Then, the result is a series of buried rock surface coordinates that can be added to the existing set of exposed rock surface coordinates to create an assumed rock surface contour. The details regarding the final input for the GEO-to-GPR point model are described in Chapter 5 and mentioned in the next and final step.

6.7. GPR data modelling

In this step, a GPR radargram is simulated based on an estimated rock contour. This is done with the help of the already mentioned GEO-to-GPR point model, which was explained in Chapter 5. Besides the estimated rock surface contour C_r (exposed and buried), some other input parameters are required. The input parameters are listed below, including three optional parameters. Each parameter is explained in section 5.2.

- Start and end coordinate of the GPR survey (from rock surface coordinates) crd_0 and crd_1 (-)
- Velocity through medium v_{GPR} (m/ns)
- Spacing between consecutive traces s_{step} (m)
- Time step within trace Δt_{tr} (ns)
- Maximum time duration of trace t_{tr}^{max} (ns)
- Colour scheme indicator for graphs n_{cl} (-)
- Optional parameters
  - Showing of GPR radargram I (-))
  - Showing of traces at surface including trace lines $line$, default 'off'
  - Graph size D_{graph} (-))

When the required input is given, the GEO-to-GPR point model can be run. As output, the reflection coordinates are given as well as an explanatory graph consisting of the (buried) rock surfaces with respect to the exposed rock surface and the input GPR radargram with the identified reflection surfaces. This indicates the 'fit' of the estimated rock contour with the GPR survey results. It is, however, important to not conclude that the estimated rock contour can be considered true based only on an excellent fit due to the many simplifications and assumptions explained in Chapter 3. The simulation only offers insight into an interpretation of the buried rock contour, which is already an indirect result of the GPR survey.

7

GPR results TU Delft boulder

This chapter contains the results from the GPR survey done at a non-buried boulder on the campus of the TU Delft. The survey is used to evaluate the accuracy of the calculated hidden rock surfaces and also serves as a guide to optimise future surveys for Hunebed D14. The steps discussed in Chapter 6 are followed sequentially which is reflected in the structure of this Chapter. The last two steps are not performed as the entire rock contour is already known. First, the survey is described after which the processed GPR data is given. Then, the reflection surfaces are identified which is followed by the acquisition of the exposed rock contour. The GPR point-to-GEO model is then used to determine the hidden rock surfaces. Finally, the resolution of the GPR results is determined.

7.1. GPR survey

The survey was performed on a granitic rock of dimensions approximately similar to the keystone at Hunebed D14, see Figure 7.1. It was chosen not to perform a grid of survey lines. A set of survey lines which intersected at a central point was chosen as it was more adequate considering the dimensions and contour of the boulder, see Figure 7.2. These lines were surveyed in both directions. Furthermore, as the purpose of the survey was to evaluate the accuracy of the GPR point to GEO procedure, it was not deemed necessary to do a lot of measurements.

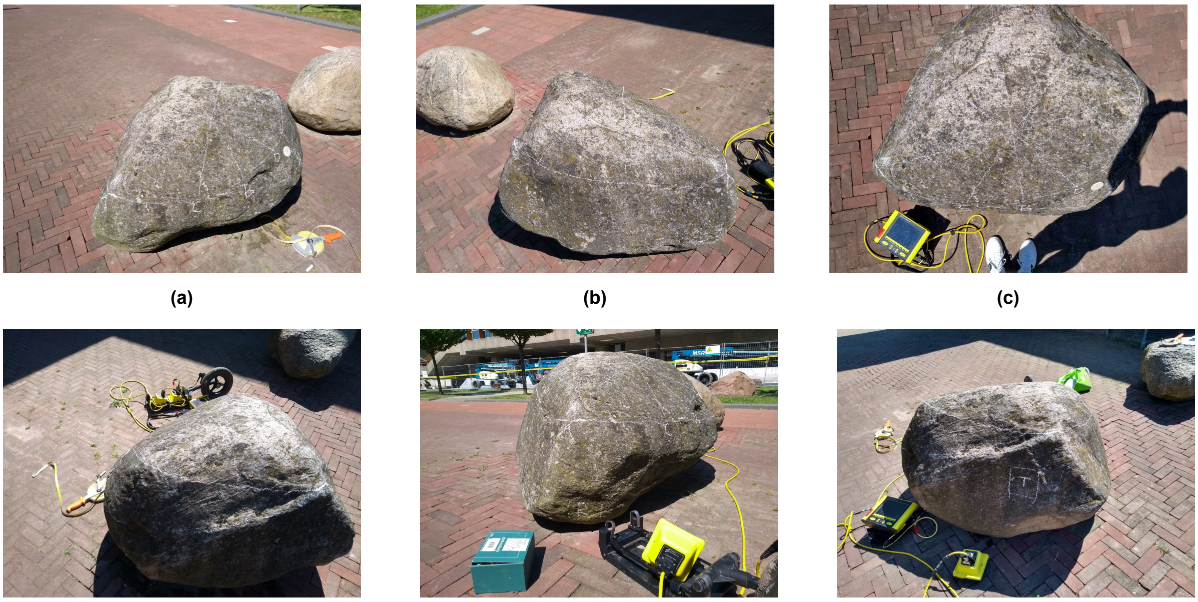

(a) **(b)** **(c)**

(d) **(e)** **(f)**

Figure 7.1: Boulder near the Aula at the TU Delft Campus from east (a), south-west (b), top (c), north-west (d), south-east (e) and west (f).

(a) (b) (c)

Figure 7.2: GPR survey at rock near the Aula at the TU Delft Campus. (a) shows the surveyed lines for the Common Offset Survey, with A=1.15m, B=0.95m, C=0.95m and D=0.95m. (b) and (c) show the positions of the receiver and transmitter for the Transillumination Survey, respectively.

The frequency of the GPR used in this survey was chosen to be 1000 MHz. From previous experiences during surveying at the Hunebed D14, the 500 MHz and 250 MHz frequencies didn't offer additional benefits (clearer results) and would result in a loss of resolution. Furthermore, the larger dimensions of these GPR antennas caused issues for the relative small scale transitions with respect to the survey path. The used GPR is the pulseEKKO® GPR 1000 MHz Transducers.

7.2. Data processing

The processing steps and the resulting processed GPR radargrams from the Common Offset Survey are given in section 7.2.1. The calculation of the propagation velocity v_{GPR} from the Transillumination Survey is given in section 7.2.2

7.2.1. Common Offset Survey

Table 7.1 contains the processing steps that were performed on the GPR data from the survey. It shows a description of each processing step as explained in section 6.2.

Background removal was not performed on the data to prevent interfering with sloped reflections. However, it became clear that no significant distortion effect could be found, so the removal of the background is done in future processing.

Table 7.1: Parameters for processing of GPR radargrams from survey. n/a: not applicable.

Data processing steps					
Step	Description	Performed	Time zero (ns)	Att. func.	Order
1	Adjust time zero	yes	4.0	n/a	n/a
2	Remove background	no	n/a	n/a	n/a
3	Remove DC	yes	n/a	n/a	n/a
4	Dewow	yes	n/a	n/a	n/a
5	Inverse Amplitude Decay	yes	n/a	Median	5

The processed GPR diagrams for the 8 surveyed lines can be found in Appendix A.

7.2.2. Transillumination Survey

The survey was performed for two distances ΔL, namely for 1.24 m and 0.00 m and was repeated 20 times for both. The distance $\Delta L = 1.24$ m between transmitter and receiver was retrieved from the point cloud, see Figure 7.3.

Figure 7.3: $\Delta L = 1.24$ m from point cloud.

As explained in Section 6.1.2, the traces are stacked, which results in an average trace. From the stacked trace, the arrival times for both distances ΔL can be determined. Figure 7.4 shows these stacked traces including first arrival times.

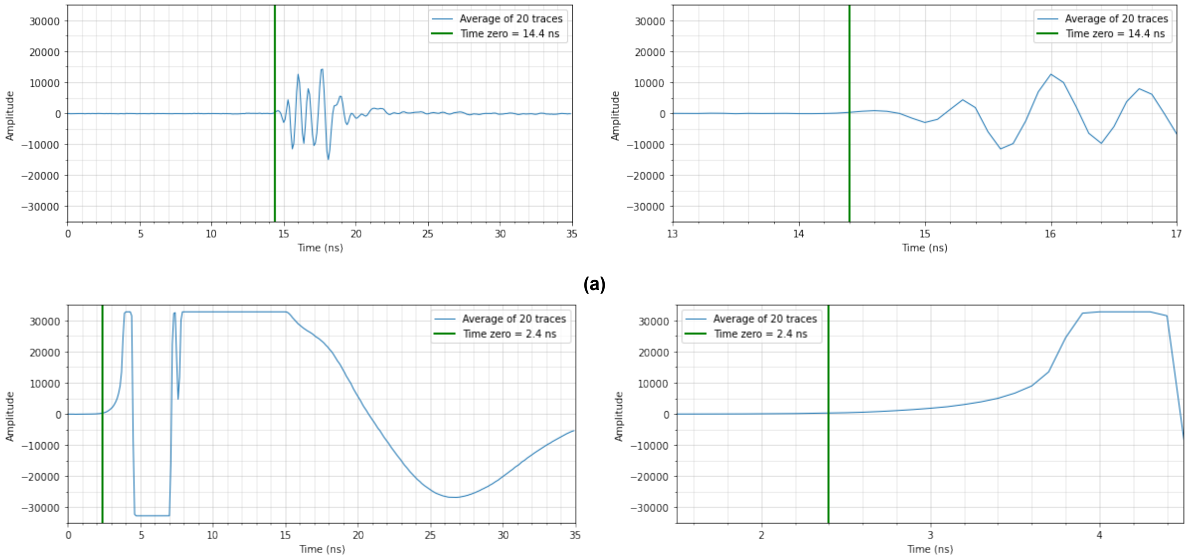

(a)

(b)

Figure 7.4: Stacked traces for $\Delta L = 1.24$ m (a) and $\Delta L = 0.00$ m (b) with the whole trace (left) and the zoom on the first arrivals (right). The respective first arrival times are 14.4 ns and 2.4 ns. The left

The propagation velocity through the rock v_{GPR} is then calculated to be 0.103 m/ns. This appears to be low with respect to the lower bound of the velocity range of 0.12 m/ns determined in section 3.1 for granites. This could be attributed to the low confining pressure, but the rock may also have been weathered.

7.3. Reflection surfaces

From the processed GPR radargrams in section 7.2, the reflection surfaces were identified, see Figure 7.5 for line A. Appendix B contains 8 tables with the coordinates of the 8 survey lines. Note that some surfaces will be filtered out after the calculation of the hidden rock surfaces, as they do not make sense/show illogical buried surfaces.

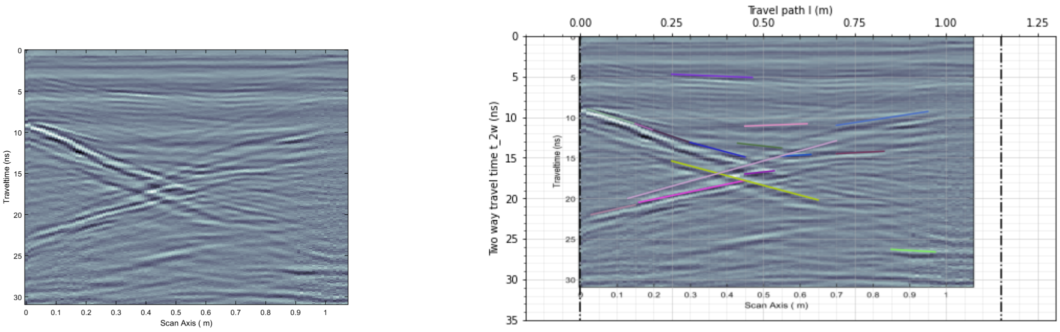

(a)

(b)

Figure 7.5: Processed GPR radargram for line A (a) and the corresponding reflection surfaces (b).

7.4. Exposed rock contour

The point cloud model from which the exposed rock contours were directly retrieved can be seen in Figure 7.6. Important to note is that for this survey, the rock contours were directly extracted from the point cloud model, see Figure 7.6c and 7.6d, and not from a mesh created from the point cloud model. This could be done, because the point clouds acquired to record the entire boulder were merged very well. Also, the extracted contours were cut in order to have only the contour of the rock and not parts of the floor, see Figure 7.6a and 7.6b.

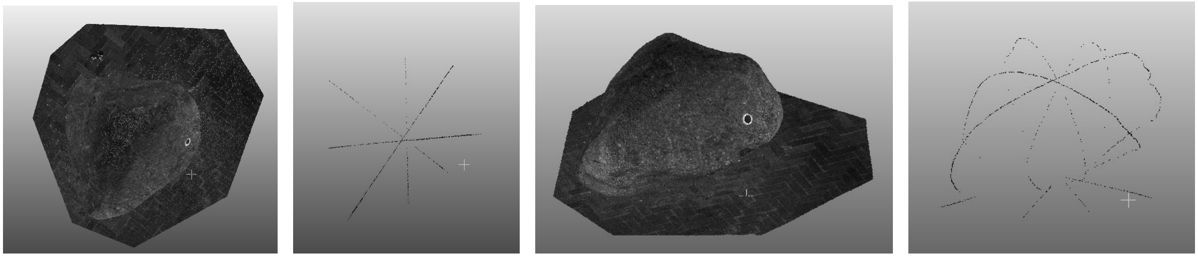

(a) (b) (c) (d)

Figure 7.6: Point cloud model and extracted rock contours from top (a and b) and from an angle (c and d).

Then, the rock contours were extracted as text files and subsequently cut and re-arranged correctly in Python. The resulting rock contour lines, including the GPR survey paths, are shown in Figure 7.7.

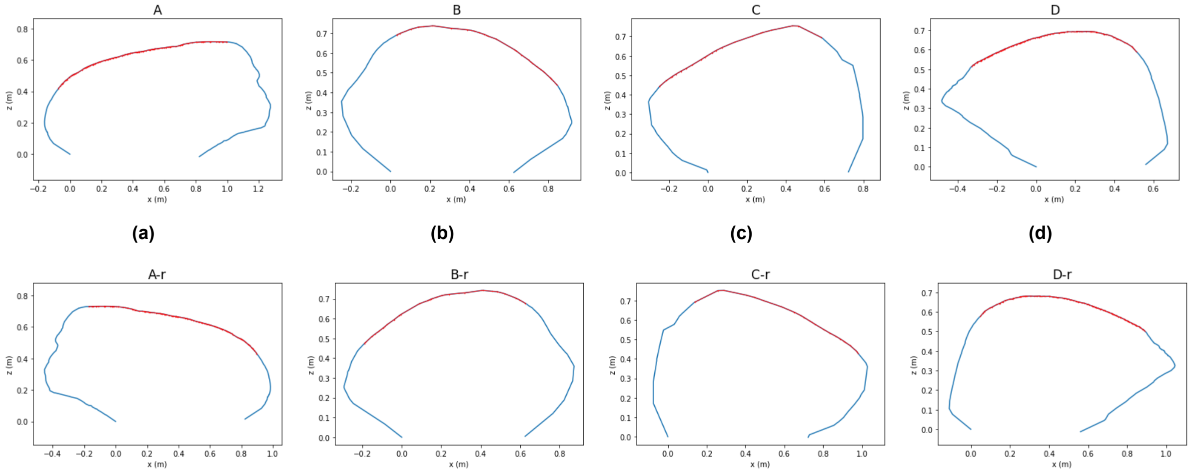

(a) (b) (c) (d)

(e) (f) (g) (h)

Figure 7.7: Rock contours including GPR survey paths in red for each surveyed line.

7.5. Rock surfaces

The hidden rock surfaces can be calculated with the reflection surfaces identified in section 7.3 and the exposed rock contour from section 7.4. The required input parameters for the GPR point-to-GEO model are listed in Table 7.2.

Table 7.2: Input parameters for GPR point-to-GEO model for the 8 surveyed lines.

		Input GPR-to-GEO							
Parameter	unit	A	B	C	D	$A-rev$	$B-rev$	$C-rev$	$D-rev$
crd_0	-	65	20	18	85	104	16	15	43
crd_1	-	200	48	39	218	239	44	37	176
v_{GPR}	m/ns	0.103	0.103	0.103	0.103	0.103	0.103	0.103	0.103
s_{step}	m	0.002	0.002	0.002	0.002	0.002	0.002	0.002	0.002
Δt_{tr}	ns	0.02	0.02	0.02	0.02	0.02	0.02	0.02	0.02
t_{tr}^{max}	ns	35	35	35	35	35	35	35	35
n_{cl}	-	30	30	30	30	30	30	30	30

The (hidden) rock surface coordinates including the corresponding reflection surfaces can be found in Appendix C. The (hidden) rock surface coordinates itself are shown in Figure 7.8. The entire rock including the (hidden) rock surface coordinates is shown in 3D in 7.9.

Some remarks can be made with respect to the (hidden) rock surface contours, including the graphs in Appendix C. The hidden rock contour is, by approximation, known and equal to a horizontal plane connecting to the rock contours at their ends. From Figure 7.8, Figure 7.9 and Appendix C, it can be seen that multiple hidden rock surfaces appear several dm's into the subsurface, but that overall an accurate fit of the rock surface coordinates to the known rock contour is achieved. However, deviations of up to 10 cm are common (both over- and underestimation) and some unexplained reflection surfaces remain.

Also, the rock surfaces in normal and reverse direction appear at similar positions and depths, which indicates reproducibility of the measurements in both directions. Furthermore, shallow reflections at roughly the same location in the upper part of the rock are visible for multiple lines. It is suspected that a internal fracture or discontinuity might be present, but this can neither be confirmed nor denied.

These remarks are further discussed and interpreted in Chapter 9.

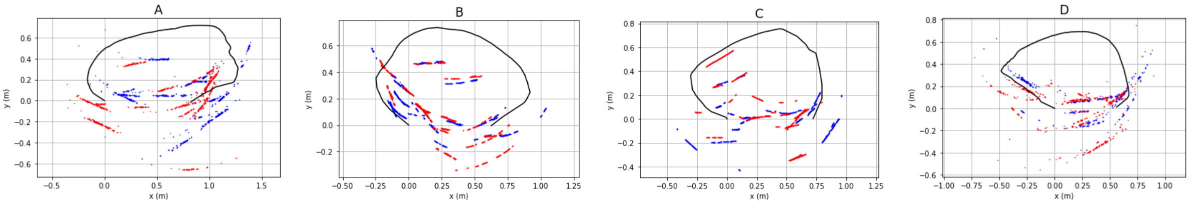

(a) (b) (c) (d)

Figure 7.8: Rock surface coordinates from GPR point-to-GEO model for the 4 surveyed line of the Aula rock. The red coordinates represent the coordinates of the lines A to D and the blue coordinates represent the coordinates of the lines A reverse to D reverse. The figures are all shown in normal direction.

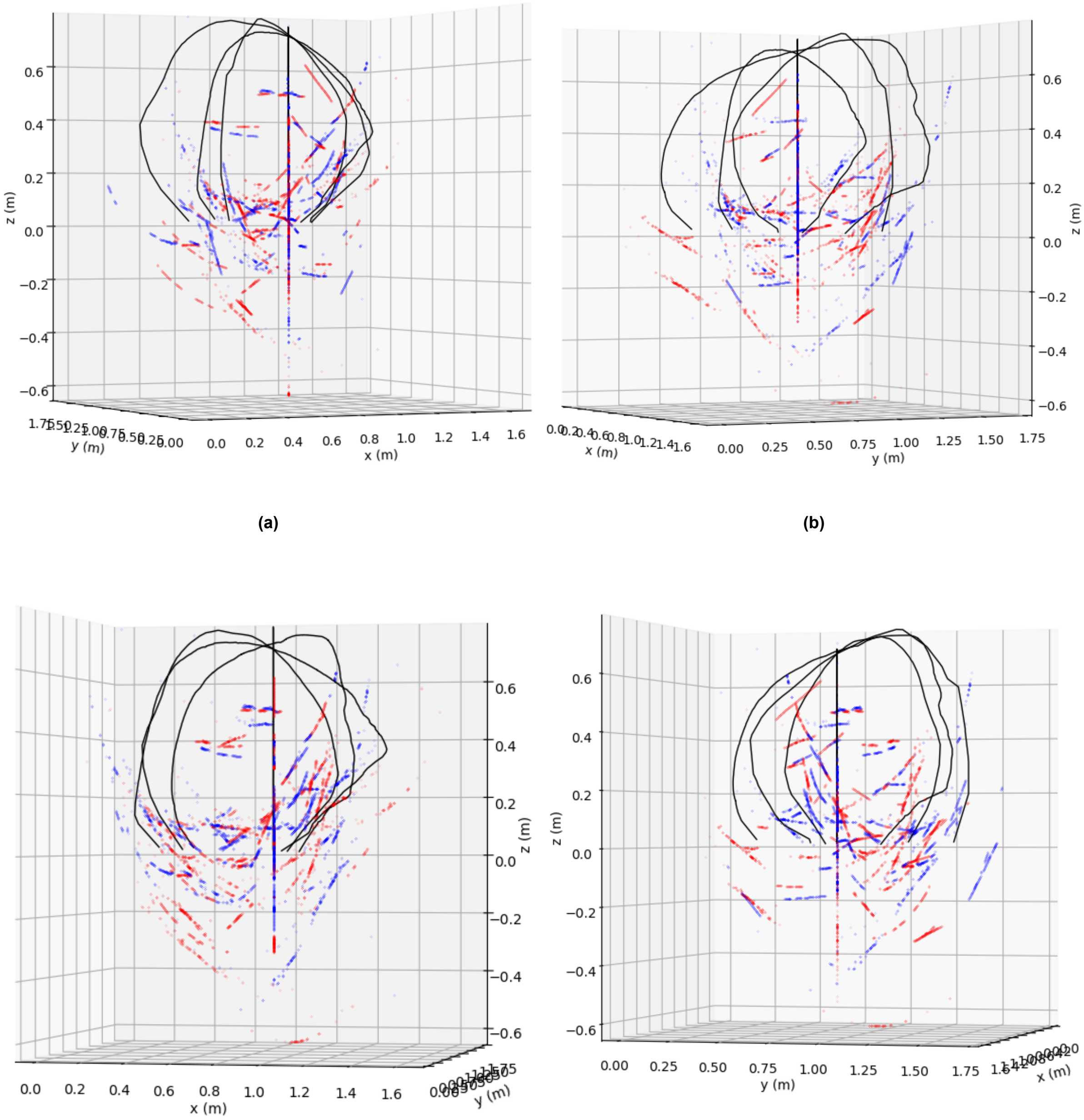

(a)

(b)

(c)

(d)

Figure 7.9: Rock surface coordinates from GPR point-to-GEO model for Aula rock. The red coordinates represent the coordinates of the lines A to D and the blue coordinates represent the coordinates of the lines A reverse to D reverse. The figures show the view in the normal direction of line A (a), line B (b), line C (c) and line D (d).

7.6. Resolution

The resolution of the GPR can be given by Eq. 2.2 and 2.1 in section 2.1.4. The assigned center frequency to the GPR is used for the resolutions, which is 1000 MHz. The velocity of the radio waves through the rock was estimated to be 0.103 m/ns (section 7.2.2). The vertical or radial resolution is then 2.6 cm.

The horizontal or lateral resolution depends on the depth or distance from the rock surface to the reflective surfaces. This distance ranges between 0.2-1.0 m in the results, which gives a horizontal resolution of 10.3-22.7 cm.

8

GPR results keystone SI2

This chapter contains the results from the GPR survey done at the keystone of Hunebed D14. The survey is used to gain insight into the buried rock contour of the keystone to complete the 3D model of the keystone using LiDAR by Theuws (2021). The steps discussed in Chapter 6 are followed sequentially which is reflected in the structure of this Chapter.

First, the survey is described after which the processed GPR data is given. Then, the reflection surfaces are identified which is followed by the acquisition of the exposed rock contour. The GPR point-to-GEO model is then used to determine the (buried) rock surfaces. Furthermore, an estimation of the buried rock contour is made, which is then modelled with the GEO-to-GPR point model to evaluate the fit with the GPR survey results. Finally, the resolution of the GPR results is determined.

8.1. GPR survey

The survey was performed on the keystone at Hunebed D14, see Figure 8.1. The survey consisted of a grid of survey lines, measured in a Common Offset Survey (Figure 8.2a) and a Transillumination Survey between two faces of the keystone (Figure 8.2c and 8.2b).

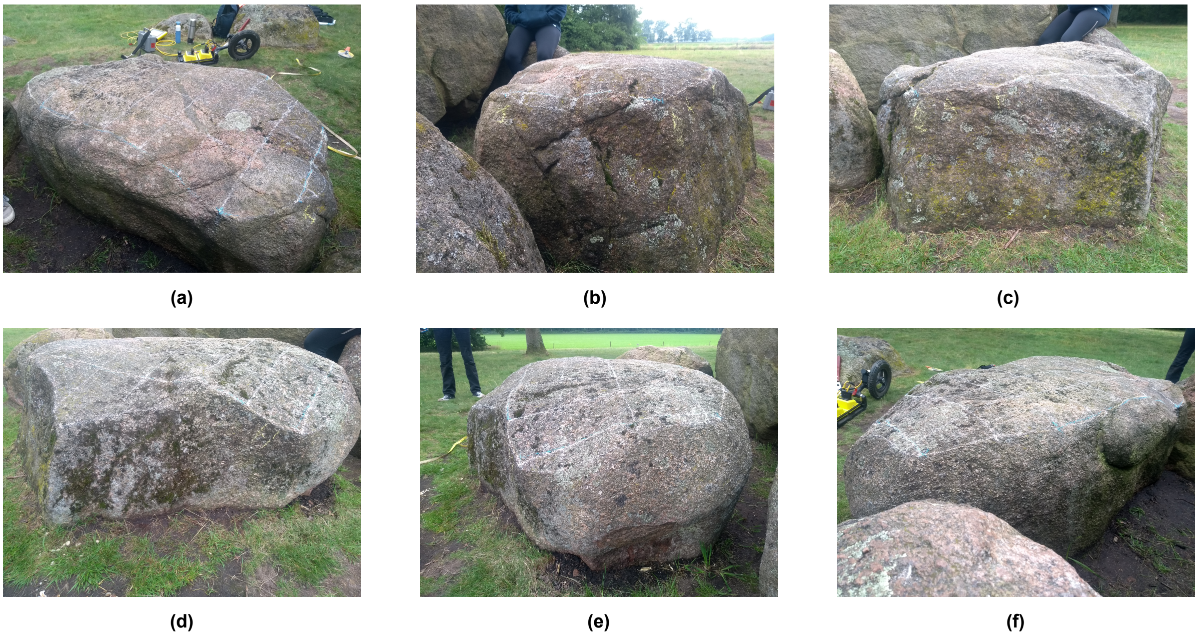
(a) (b) (c)

(d) (e) (f)

Figure 8.1: Keystone of Hunebed D14 from south-west (a), south (b), south-east (c), north-east (d), north (e) and north-west (f).

(a) (b) (c)

Figure 8.2: GPR survey at keystone Hunebed D14. (a) shows the gridlines for the Common Offset Survey. (b) and (c) show the positions of the receiver and transmitter for the Transillumination Survey, respectively.

Initially, a test survey was performed over the rock during dry and wet conditions of the soil in order to improve the reflections (dry soil-rock vs. wet soil-rock interface), but it didn't appear to yield significant improvements. However, from the almost identical GPR radargrams in the test survey, it can be concluded that surveying the keystone during wet/dry conditions and along the same line indicate reproducibility. Appendix D contains the (un)processed GPR radargrams from this test survey. The processing steps taken, are the same as explained in section 8.2. Then, a grid of survey lines was chosen to obtain information in two dimensions. Also, a grid was suitable as the dimensions and contour of the keystone (i.e. flat top) were favourable. The grid lines in Figure 8.3a and 8.3b were not surveyed over, but in between. The spacing between each line is equal to the width of the GPR antenna (15 cm). The lines were surveyed in both directions. The length of each surveyed line is given in Table 8.1.

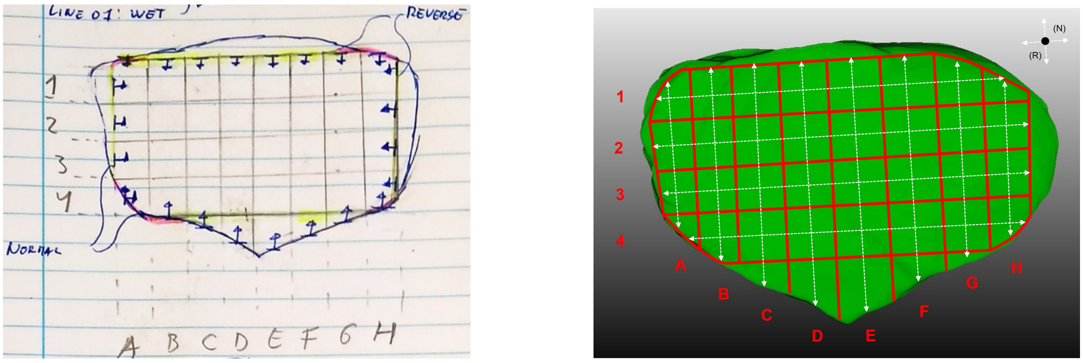

(a) (b)

Figure 8.3: Grid of 2x12 survey lines (Normal and Reverse direction) for Common Offset Survey at keystone Hunebed D14. (a) shows a sketch and (b) shows the grid projected on the mesh.

Table 8.1: Lengths of surveyed lines

Lengths (m)											
1	2	3	4	A	B	C	D	E	F	G	H
1.50	1.53	1.50	1.35	0.68	0.80	0.90	0.95	1.10	0.98	0.80	0.70

The frequency of the GPR in this survey was chosen to be 1000 MHz. From previous experiences during surveying at the Hunebed D14 and the rock near the Aula of the TU Delft, the 1000 MHz was found to be the most suitable. The pulseEKKO® GPR with 1000 MHz Transducers is used.

8.2. Data processing

The processing steps and the resulting processed GPR radargrams from the Common Offset Survey are given in section 8.2.1. The calculation of the propagation velocity v_{GPR} from the Transillumination Survey is given in section 8.2.2.

8.2.1. Common Offset Survey

Table 8.2 contains the processing steps that were performed on the GPR data from the survey. It shows a description of each processing step as explained in section 6.2.

Table 8.2: Parameters for processing of GPR radargrams from survey. n/a: not applicable.

Data processing steps					
Step	Description	Performed	Time zero (ns)	Att. func.	Order
1	Adjust time zero	yes	4.1	n/a	n/a
2	Remove background	yes	n/a	n/a	n/a
3	Remove DC	yes	n/a	n/a	n/a
4	Dewow	yes	n/a	n/a	n/a
5	Inverse Amplitude Decay	yes	n/a	Median	5

The processed GPR radargrams for the 24 surveyed lines can be found in Appendix E.

8.2.2. Transillumination Survey

The survey was performed for two distances ΔL, namely for 1.05 m and 0.00 m and was repeated 100 times for both. The distance $\Delta L = 1.05$ m between transmitter and receiver was retrieved from the point cloud, see Figure 8.4a and 8.4b.

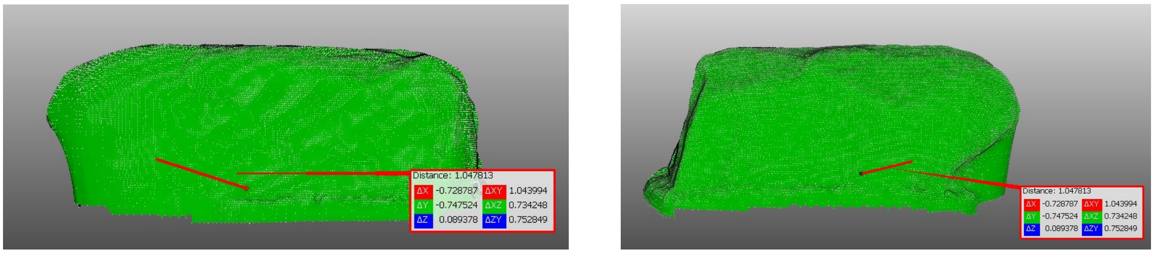

(a) (b)

Figure 8.4: $\Delta L = 1.05$ m from point cloud from transmitter (a) and receiver (b).

As explained in Section 6.1.2, the traces are stacked, which results in an average trace. From the stacked trace, the arrival times for both distances ΔL can be determined. Figure 8.5 shows these stacked traces including first arrival times.

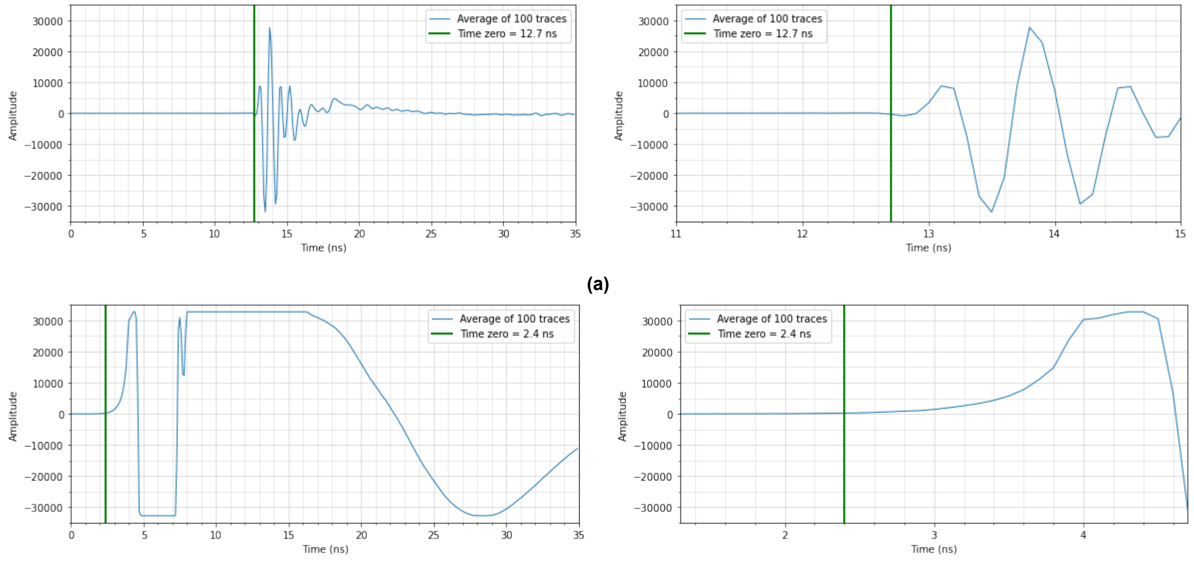

(a)

(b)

Figure 8.5: Stacked traces for $\Delta L = 1.05$ m (a) and $\Delta L = 0.00$ m (b). The respective first arrival times are 12.7 ns and 2.4 ns.

The propagation velocity through the rock v_{GPR} is then calculated to be 0.102 m/ns. This appears to be low with respect to the lower bound of the velocity range of 0.12 m/ns determined in section 3.1 for granites.

8.3. Reflection surfaces

From the processed GPR radargrams in section 8.2, the reflection surfaces were identified, see Figure 8.6 for line 1(N). Appendix F contains 24 tables with the coordinates of the 24 survey lines.

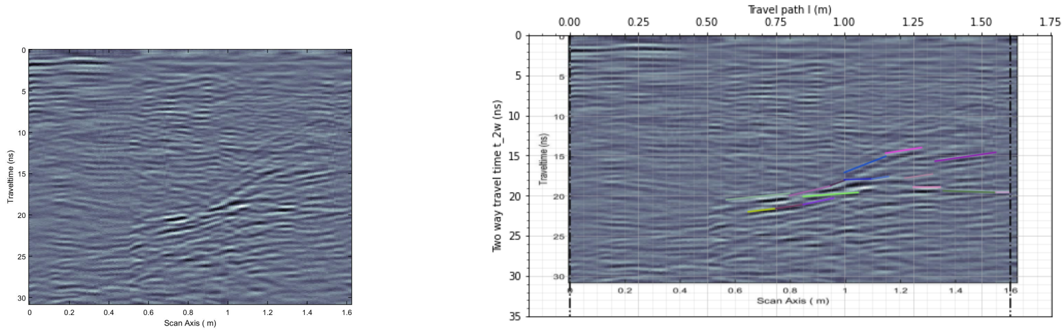

(a)

(b)

Figure 8.6: Processed GPR radargram for line 1(N) (a) and the corresponding reflection surfaces (b).

8.4. Exposed rock contour

The mesh from which the exposed rock contours of keystone Sl2 were retrieved was obtained by Theuws (2021) and can be seen in Figure 8.7. The rock contours are shown in Figure 8.7b and 8.7d. Note that the contours do not correspond with the lines shown in Figure 8.2a in section 8.1 as these show the width of the GPR path. The lines correspond to the center of these paths. Also, the extracted contours were cut in order to have only the contour of the rock and not parts of the soil surface, see Figure 8.7a and 8.7c.

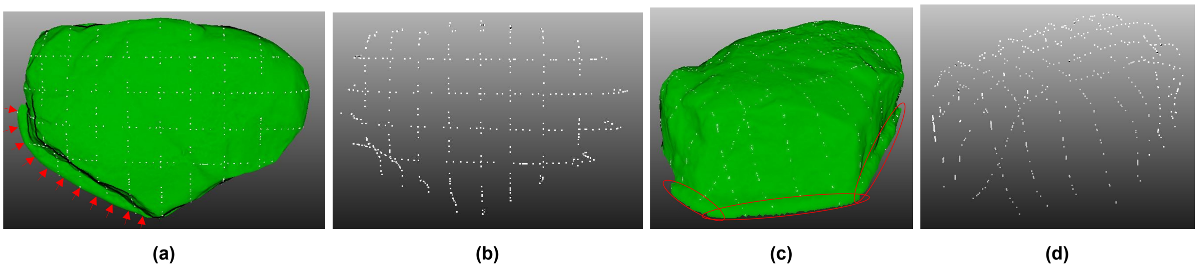

Figure 8.7: 3D mesh and extracted rock contours from top (a and b) and from an angle (c and d). The red arrows and ovals indicate parts of the soil surface.

Then, the rock contours were extracted as text files and subsequently cut and re-arranged correctly in Python. The resulting rock contour lines, including the GPR survey paths, are shown in Figure 8.8. The grid consists of two perpendicular sets of surveyed lines of which the first set of contours (1-4 in Figure 8.8a-8.8h) is longer than the second set (A-H in Figure 8.8i-8.8x).

As can be seen for rock contour lines E and H (Figure 8.8b, 8.8f and 8.8t, 8.8x), the contour lines show not the entire exposed rock surface. This is due to the point model on which the mesh was based. The point model experienced some blind or empty zones, which resulted in locally undefined meshes with little vertices. Therefore, the corresponding extracted rock contours lack coordinates in these zones. This also explains the sharp corners in rock contours A and H (Figure 8.8i, 8.8m and 8.8t, 8.8x).

Furthermore, the GPR survey paths should be at the exact same positions for both the normal and reverse directions. However, in the GPR radargram this doesn't appear to be correct as the lengths of the measured paths do not always match the horizontal axes of the GPR radargrams. Therefore, the paths do change within one rock contour, which was done manually. This is expected to cause deviations of the origins for the reflections and thus the (buried) rock surface coordinates.

Also, rock contours 4, A and B contain rough transitions (Figure 8.8d,8.8h and 8.8i, 8.8m and 8.8j, 8.8n). These seem to be a little exaggerated in this smale scale, but do cause deviations as the GPR obviously cannot follow this exact path due to its size and stiffness.

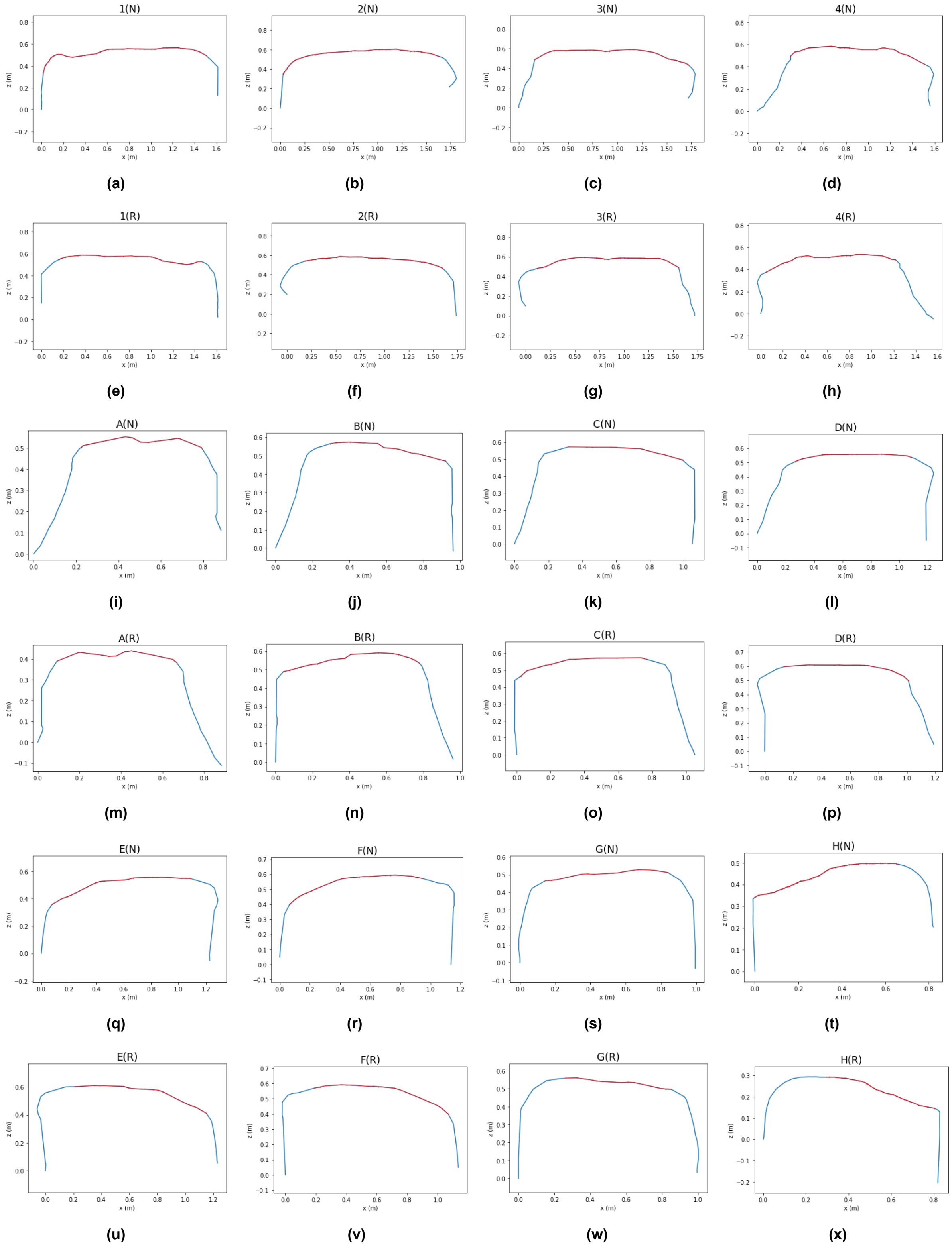

(a) (b) (c) (d)

(e) (f) (g) (h)

(i) (j) (k) (l)

(m) (n) (o) (p)

(q) (r) (s) (t)

(u) (v) (w) (x)

Figure 8.8: Rock contours including GPR survey paths for each of the 24 surveyed lines

8.5. Rock surfaces

The (buried) rock surfaces can be calculated with the reflection surfaces identified in section 8.3 and the exposed rock contour from section 8.4. The required input parameters for the GPR point-to-GEO model are listed in Table 8.3.

Table 8.3: Input parameters for GPR point-to-GEO model for the 24 surveyed lines.

Input GPR-to-GEO									
Parameter	unit	1(N)	2(N)	3(N)	4(N)	1(R)	2(R)	3(R)	4(R)
crd_0	-	27	6	17	21	10	16	13	14
crd_1	-	66	43	49	52	41	46	40	44
v_{GPR}	m/ns	0.102	0.102	0.102	0.102	0.102	0.102	0.102	0.102
s_{step}	m	0.002	0.002	0.002	0.002	0.002	0.002	0.002	0.002
Δt_{tr}	ns	0.02	0.02	0.02	0.02	0.02	0.02	0.02	0.02
t_{tr}^{max}	ns	35	35	35	35	35	35	35	35
n_{cl}	-	30	30	30	30	30	30	30	30
Parameter	unit	A(N)	B(N)	C(N)	D(N)	A(R)	B(R)	C(R)	D(R)
crd_0	-	23	24	20	18	12	12	7	14
crd_1	-	34	39	30	33	23	32	20	31
v_{GPR}	m/ns	0.102	0.102	0.102	0.102	0.102	0.102	0.102	0.102
s_{step}	m	0.002	0.002	0.002	0.002	0.002	0.002	0.002	0.002
Δt_{tr}	ns	0.02	0.02	0.02	0.02	0.02	0.02	0.02	0.02
t_{tr}^{max}	ns	35	35	35	35	35	35	35	35
n_{cl}	-	30	30	30	30	30	30	30	30
Parameter	unit	E(N)	F(N)	G(N)	H(N)	E(R)	F(R)	G(R)	H(R)
crd_0	-	14	6	15	10	17	10	13	33
crd_1	-	32	25	29	77	33	29	24	88
v_{GPR}	m/ns	0.102	0.102	0.102	0.102	0.102	0.102	0.102	0.102
s_{step}	m	0.002	0.002	0.002	0.002	0.002	0.002	0.002	0.002
Δt_{tr}	ns	0.02	0.02	0.02	0.02	0.02	0.02	0.02	0.02
t_{tr}^{max}	ns	35	35	35	35	35	35	35	35
n_{cl}	-	30	30	30	30	30	30	30	30

The (buried) rock surface coordinates including the corresponding reflection surfaces are given in Appendix G, but the (buried) rock surface coordinates for each line separately can be seen in Figure 8.9. To show the burial depth and rock contour without interference of nearby rock faces, the (buried) rock coordinates for lines 2, 3, D and E are given in 3D in Figure 8.10.

Some remarks can be made with respect to the (buried) rock surface contours, including the graphs in Appendix G. A feature can be seen near the top surface of the keystone at lines 4 and C in both directions in Figure 8.9d and 8.9g. This coincides with the location of the repaired crack. Furthermore, a downward sloping trend to the south is visible in the coordinates of the buried surfaces in Figure 8.10. At the south and east facing side (left in Figure 8.10a and 8.10b, respectively), a lack of rock surface coordinates can be concluded. This indicates steep angles (vertical) of the buried rock surfaces at the south and east face. Deviations of 5-10 cm can be seen for the fit of the rock surface coordinates with the exposed rock surface, but sometimes larger deviations occur. Finally, rock surface coordinates within the rock at soil surface level can be distinguished. The reason for this is unknown.

These remarks are further discussed and interpreted in Chapter 9.

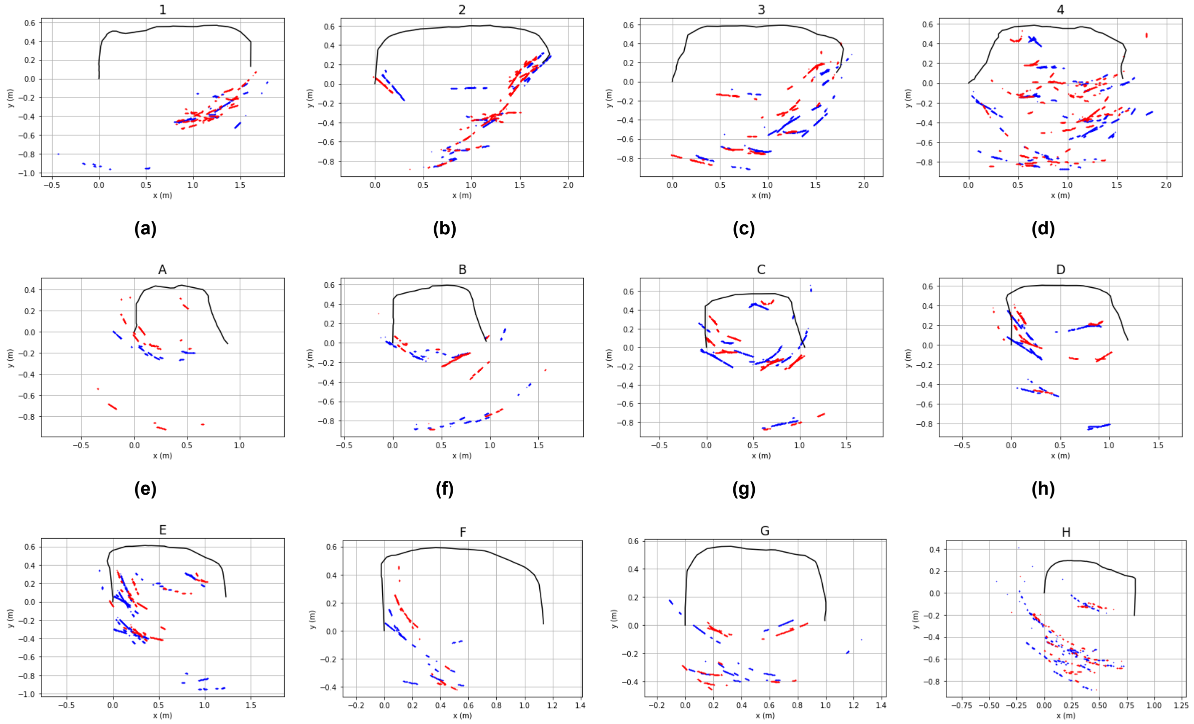

(a) (b) (c) (d)

(e) (f) (g) (h)

(i) (j) (k) (l)

Figure 8.9: (Buried) rock surface coordinates for each of the 12 grid lines. Grid lines 1 to and including 4 are shown in the normal direction (S-N), whereas grid lines A to and including H are shown in reverse direction (W-E). The (buried) rock surface coordinates are shown in red and blue for the Normal and Reverse direction, respectively.

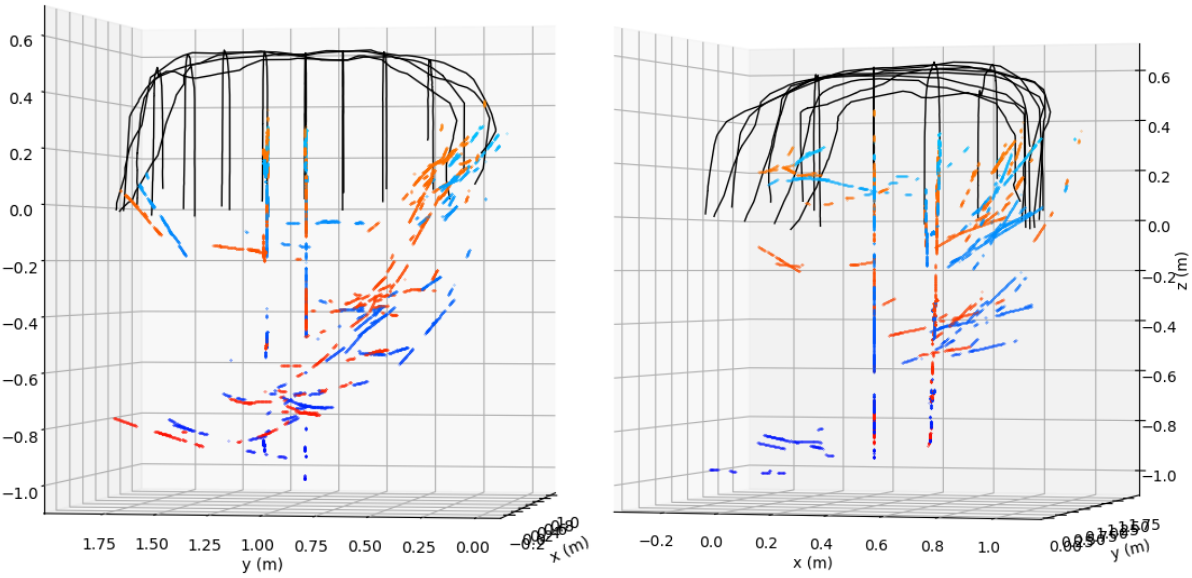

(a) (b)

Figure 8.10: (Buried) rock surface coordinates from GPR point-to-GEO model for keystone Hunebed D14 for grid lines 2, 3, D and E. The cyan-blue and orange-red color gradient visualises the depth of the coordinates, with the darker the color, the deeper the coordinate. The orange-red coordinates represent the calculated surface coordinates of the lines in N(ormal) direction and the cyan-blue coordinates represent the calculated surface coordinates of the lines in R(everse) direction. (a) shows the view from the east (S-N) and (b) from the north (E-W).

8.6. Buried rock contour estimation

To estimate the buried rock contour, first the orientation of the keystone in 1927 is compared to the present with help from pictures taking during excavation and before the restoration attempt in 1927. Then, with help from the (buried) rock surface coordinates from the GPR point-to-GEO model, the buried rock contour can be estimated for each of the 12 survey lines.

8.6.1. Historic and present orientation

Figure 8.11 shown below, contains a comparison of several rock faces. It can be seen that the rock has been in roughly the same orientation except that it has been tilted. This can clearly be seen as a rotation to the south around the east-west axis and a slight tilt to the east around the north-south axis. With respect to the buried rock contour, it can be concluded that the **currently** buried rock surface at the south facing side (red in Figure 8.11) extends almost vertically downwards for several decimeters.

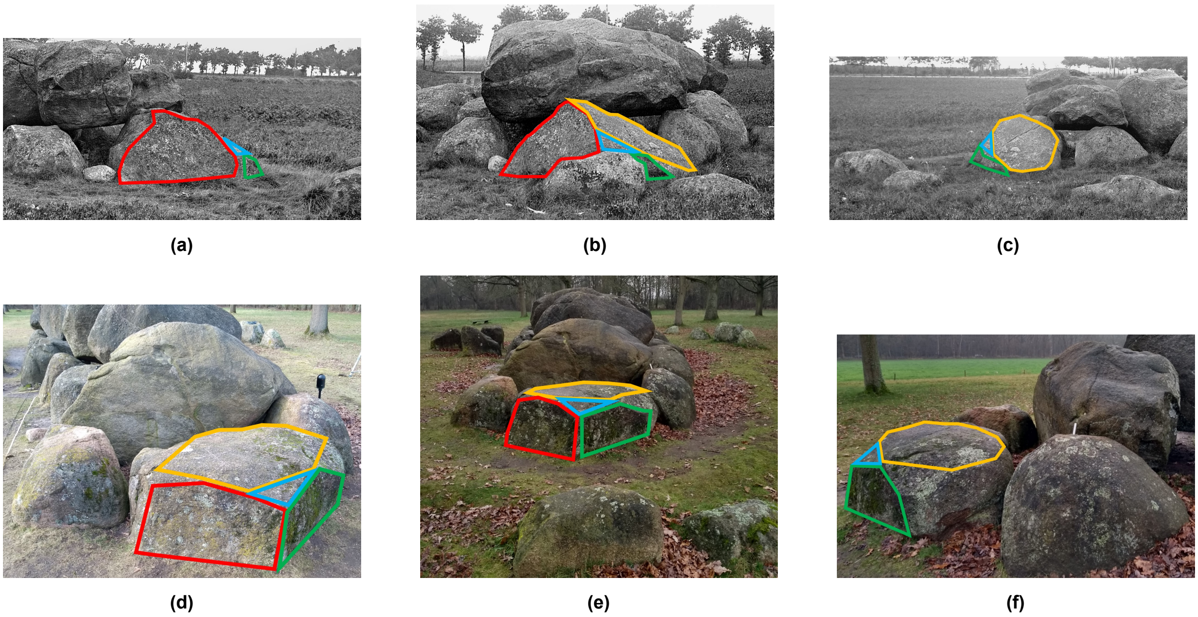
(a) (b) (c)
(d) (e) (f)

Figure 8.11: Keystone of Hunebed D14 in 1925-1927 from GIA (Ten Anscher, 2019) and 2021, including rock faces highlighted in various colors. The top row consists of photos from 1925-1927 before the restoration attempt, showing the former southern rock face in red (a), the former eastern rock face in green (b) and the former northern rock face in yellow (c). The bottom row consists of photos from 2021 after several restoration attempts, showing the red rock face (d), the yellow rock face (e) and the green rock face (f). The current top of SI2 in yellow (f) was already entirely visible in 1927 (c).

Then, Figure 8.12 shows the west facing side of the keystone during excavation (before restoration) in 1927 and the same western rock face in 2021. The tilt to the south can clearly be seen when looking at the red and orange highlighted rock features. The green and blue lines represent the historic and present ground level, respectively, keeping in mind that the picture was taken during excavation. The tilt angle is then approximately 15°. It can be concluded that also the west facing side extends at least several decimeters downwards at the center of the keystone. Unfortunately, it cannot be clearly seen if the deepest part of the buried rock that is visible in Figure 8.12a and 8.12b is a) the bottom of the rock and b) more or less parallel to the historic ground level. It appears to be the case, but the shadows might be misleading. This would mean that the current bottom of the rock would be slightly sloping downward in the southern direction. This is in agreement with what can be seen at the currently exposed north facing side of the keystone, which shows an inclination with such a slope.

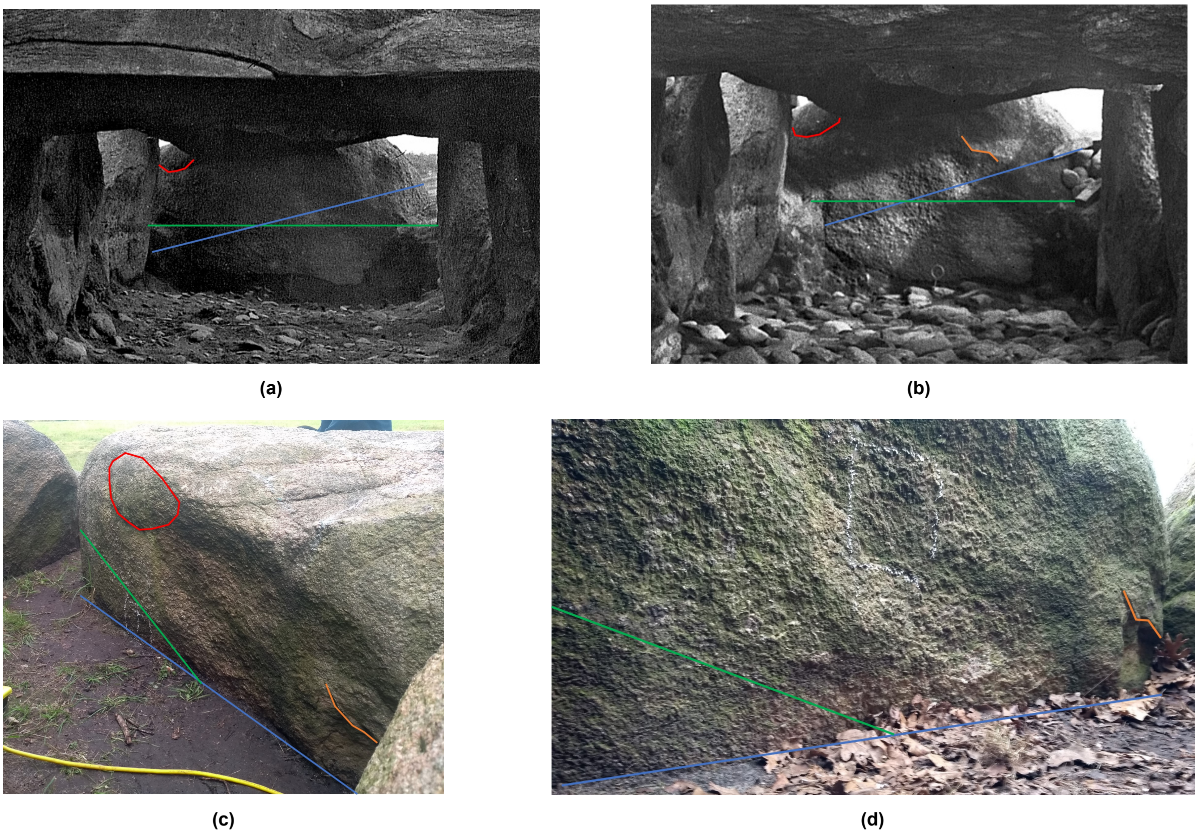

Figure 8.12: Keystone of Hunebed D14 in 1927 from GIA (Ten Anscher, 2019) and 2021, including rock features highlighted in various colors. The top row (a, b) consists of photos from 1927 during the initial excavation before the restoration attempt, showing the red and orange rock features and the historic (green) and present (blue) ground level. The bottom row (c, d) consists of photos from 2021 after several restoration attempts, showing the same rock features and the historic and present ground level.

The vertically extending rock face at the southern 'red' rock face and the downward sloping bottom in the direction of the southern 'red' rock face (from historic photos in Figure 8.12a and 8.12b) are in agreement with the found results in the previous section in Figure 8.10a. The lack of buried rock surface coordinates at the south side (left in Figure 8.10a) can be explained due to the steep angle of the rock face, which causes signals to reflect away from the receiver. The western rock face does appear to be at least slightly angled as this can be seen in the found buried rock surfaces (right in Figure 8.10b). Unfortunately, only historic photos from one angle exist, so the assumed vertical direction of the buried western rock face might be wrong. The eastern 'green' rock face does appear to be extending vertically downward from the found buried rock surface coordinates (lack of coordinates at the left in Figure 8.10b), which could not be determined from historic photos. However, this is to be expected from present pictures, which show a flat, almost vertically downward, rock face (green in Figure 8.11).

8.6.2. Buried rock contours

The exposed rock contours, which were determined by LIDAR, are extended with manually inputted coordinates (black dots in Figure 8.13) based on the calculated (buried) rock surface coordinates. This means that very accurate rock contours cannot be expected. A certain uncertainty and deviation of the true buried rock contour can already be expected after the calculation in the GPR-to-GEO model. Therefore, the extra uncertainty that comes from estimating a **coherent rock contour** from **incoherent buried rock surface coordinates**, gives rise too larger deviations from the true buried rock contour. However, to present the data more clearly and to check the resulting theoretical GPR radargram of the GPR point model in the next section, an estimation is still made.

The estimated rock contours were based on the calculated (buried) rock surface coordinates (red and blue dots in Figure 8.13. However, the rock contour was continuously updated based on the GPR data modelled with the GEO-to-GPR point model. This iteration process was repeated until a sufficiently 'accurate' rock contour was estimated. This means that either the differences in time between the modelled and field reflections were in the order of 1-2 ms or the modelled reflections consistently captured the field reflections even though no 'accurate' fit could be determined.

The estimated rock contours for the 12 lines are shown in Figure 8.13. Important to note is that several blind spots were present in the calculated (buried) rock surfaces. These are defined as areas in the 2D cross-section with no information with respect to the buried contour. Consequently, a local slope has to be assumed to complete the contour. As the contour is determined manually, most often a direct connection between two known coordinates was assumed to prevent a false sense of reliability. This means that sometimes rough transitions (sharp corners) can be seen in the rock contours, see especially Figure 8.13e to 8.13h.

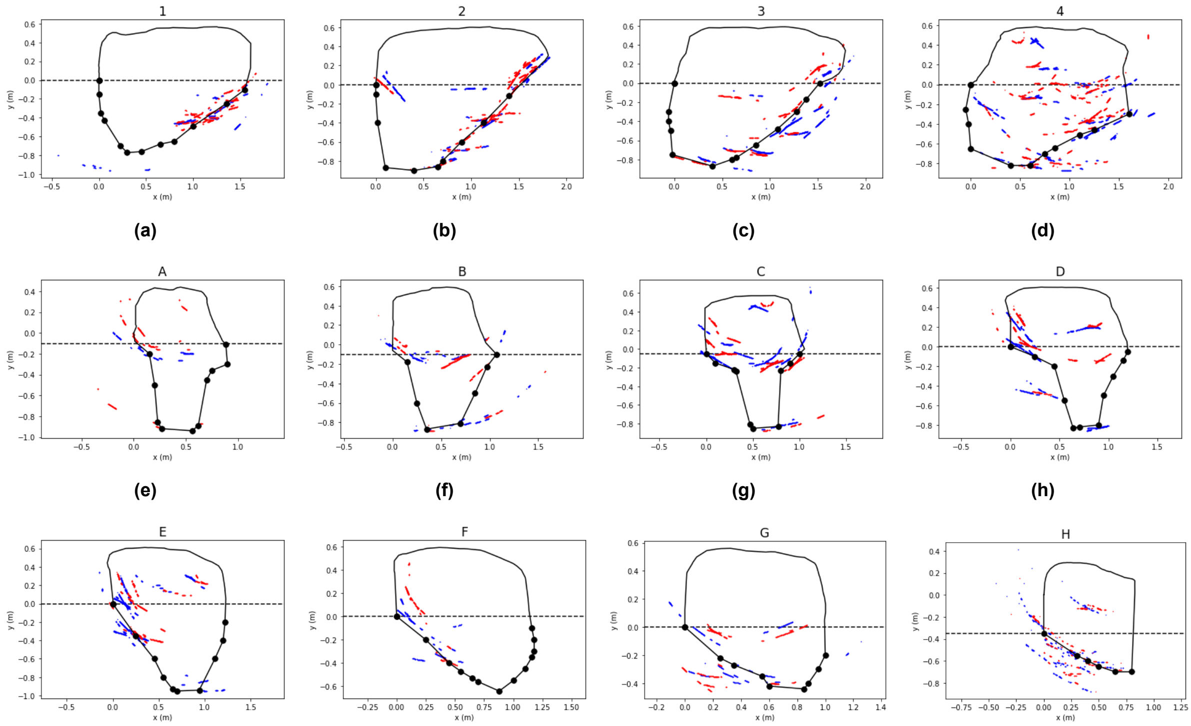

(a) (b) (c) (d)

(e) (f) (g) (h)

(i) (j) (k) (l)

Figure 8.13: Estimated (buried) rock contours for each of the 12 grid lines. Contours 1 to and including 4 are shown in the normal direction (S-N), whereas contours A to and including H are shown in reverse direction (W-E). The buried contour is based on the interpolation between the input coordinates (black dots). The (buried) rock surface coordinates on which the contours are based are also shown for the Normal (red) and Reverse (blue) direction.

An important remark has to be made. The historic photos showing the partially excavated keystone and presently buried rock faces do not always agree with the assumed rock contour. Especially the (buried) west facing side of the rock, which appeared to be vertical by approximation, differentiates from the estimated rock contour. The author is aware of the contradiction, but concluded that the GPR data should be the starting point in this process to be able to evaluate the usefulness of the GPR in obtaining the buried rock contour and answering the research question.

8.7. GPR data modelling

The GPR radargram can be modelled with the estimated rock contour from section 8.6. The required input parameters for the GEO-to-GPR point model are listed in Table 8.4.

Table 8.4: Input parameters for GEO-to-GPR point model for the 24 surveyed lines.

Input GEO-to-GPR									
Parameter	unit	1(N)	2(N)	3(N)	4(N)	1(R)	2(R)	3(R)	4(R)
crd_0	-	60	62	54	56	22	26	27	25
crd_1	-	21	25	22	25	53	56	54	55
v_{GPR}	m/ns	0.102	0.102	0.102	0.102	0.102	0.102	0.102	0.102
s_{step}	m	0.01	0.01	0.01	0.01	0.01	0.01	0.01	0.01
Δt_{tr}	ns	0.02	0.02	0.02	0.02	0.02	0.02	0.02	0.02
t_{tr}^{max}	ns	35	35	35	35	35	35	35	35
n_{cl}	-	30	30	30	30	30	30	30	30
Parameter	unit	A(N)	B(N)	C(N)	D(N)	A(R)	B(R)	C(R)	D(R)
crd_0	-	34	33	31	29	44	48	43	42
crd_1	-	45	48	41	44	33	28	30	25
v_{GPR}	m/ns	0.102	0.102	0.102	0.102	0.102	0.102	0.102	0.102
s_{step}	m	0.01	0.01	0.01	0.01	0.01	0.01	0.01	0.01
Δt_{tr}	ns	0.02	0.02	0.02	0.02	0.02	0.02	0.02	0.02
t_{tr}^{max}	ns	35	35	35	35	35	35	35	35
n_{cl}	-	30	30	30	30	30	30	30	30
Parameter	unit	E(N)	F(N)	G(N)	H(N)	E(R)	F(R)	G(R)	H(R)
crd_0	-	24	19	24	18	40	38	35	74
crd_1	-	42	38	38	85	24	19	24	19
v_{GPR}	m/ns	0.102	0.102	0.102	0.102	0.102	0.102	0.102	0.102
s_{step}	m	0.01	0.01	0.01	0.01	0.01	0.01	0.01	0.01
Δt_{tr}	ns	0.02	0.02	0.02	0.02	0.02	0.02	0.02	0.02
t_{tr}^{max}	ns	35	35	35	35	35	35	35	35
n_{cl}	-	30	30	30	30	30	30	30	30

The modelled radargrams for each rock contour are given in Appendix H, The rock contours and modelled radargrams for rock contours 2, 3, D and E (surveyed in their respective normal direction) are shown in Figure 8.14 to highlight the rock contours with minimal interference of nearby rock faces. Figure 8.15 visualises the entire rock in 3D, with the rock contours 2 and 3 highlighted in blue and rock contours D and E highlighted in red.

From the results it can be seen that the modelled reflections from the GEO-to-GPR model do not coincide with the field reflections perfectly. However, they do generally appear to be reasonable based on the small deviations in time (±1-2 ns). This is further confirmed by the modelled reflections from the scanned exposed rock contour that often 'fits' the reflections from the field reasonably well (for exampled the modelled bright green reflection in the top left of the radargram in Figure 8.14a or the modelled dark pink reflection in the bottom left of the radargram in Figure 8.14b). Sometimes the modelled reflections are shifted with respect to the reflections in the radargrams (for example the modelled reflections in the top right of the radargram in Figure 8.14b), indicating deviating GPR paths for the GEO-to-GPR model and in practice. Also, the GPR data from the normal and reverse direction wasn't always in agreement for a surveyed line, which means that the estimated rock contour not always coincides with the modelled reflections of either the normal or reverse direction. This can be seen in Figure 8.14d for the strong 'white' reflection that doesn't fully show up as a modelled reflection. Deep reflections (< 0.7 m) are often unclear as they resulted in very deep burial surfaces, which are difficult to connect to other reflection surfaces.

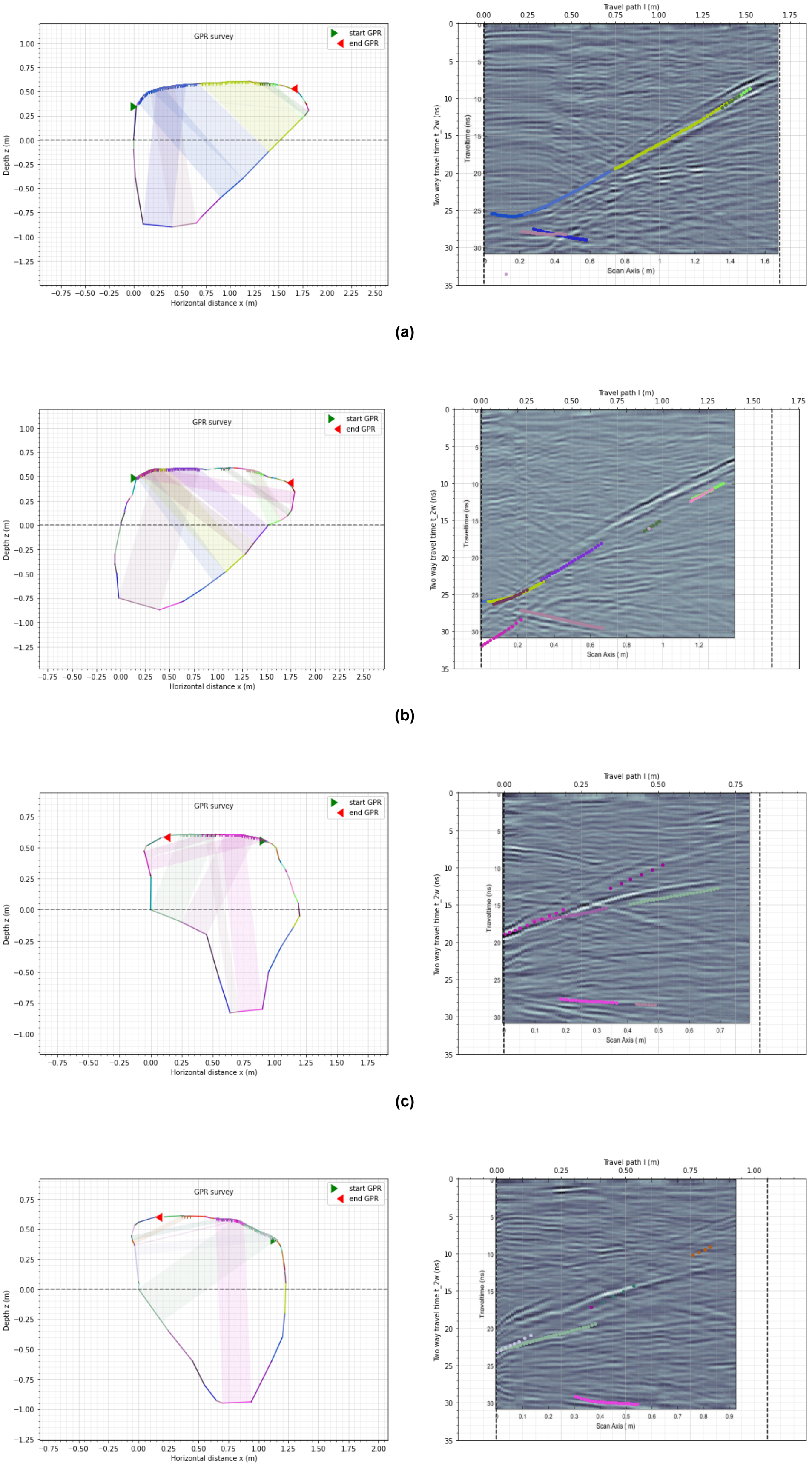

(a)

(b)

(c)

(d) Modelled GPR data of estimated rock contour from GEOtoGPR point model. The rock contours (left) and modelled GPR data (right) for lines 2 (a), 3 (b), D (c) and E (d) are given, all for their respective normal direction. Rock contours 2 and 3 are shown south-north, while the rock contours D and E are shown west-east. The reflections and rock contour surfaces are colored and correspond to the reflection surfaces in the GPR radargrams of equal color.

Figure 8.14

The buried rock contour from the modelled GPR reflections in the north-south direction is generally slightly deeper than in east-west direction, see Figure 8.15b and 8.15a. This can especially be seen at the shallower North-Western part for the red rock contours compared to the blue rock contours in Figure 8.15b. The red rock contours show very rough transitions of shallow to deep buried rock surfaces. The blind spots that cause these rough transitions yield difficulties in obtaining a buried rock contour.

Finally, strong reflections in the acquired GPR data are not always explained by the modelled reflections based on the estimated rock contour. Also, important is to again highlight the mismatch between the data from historic photos and GPR data as the west facing side of the keystone is different in both.

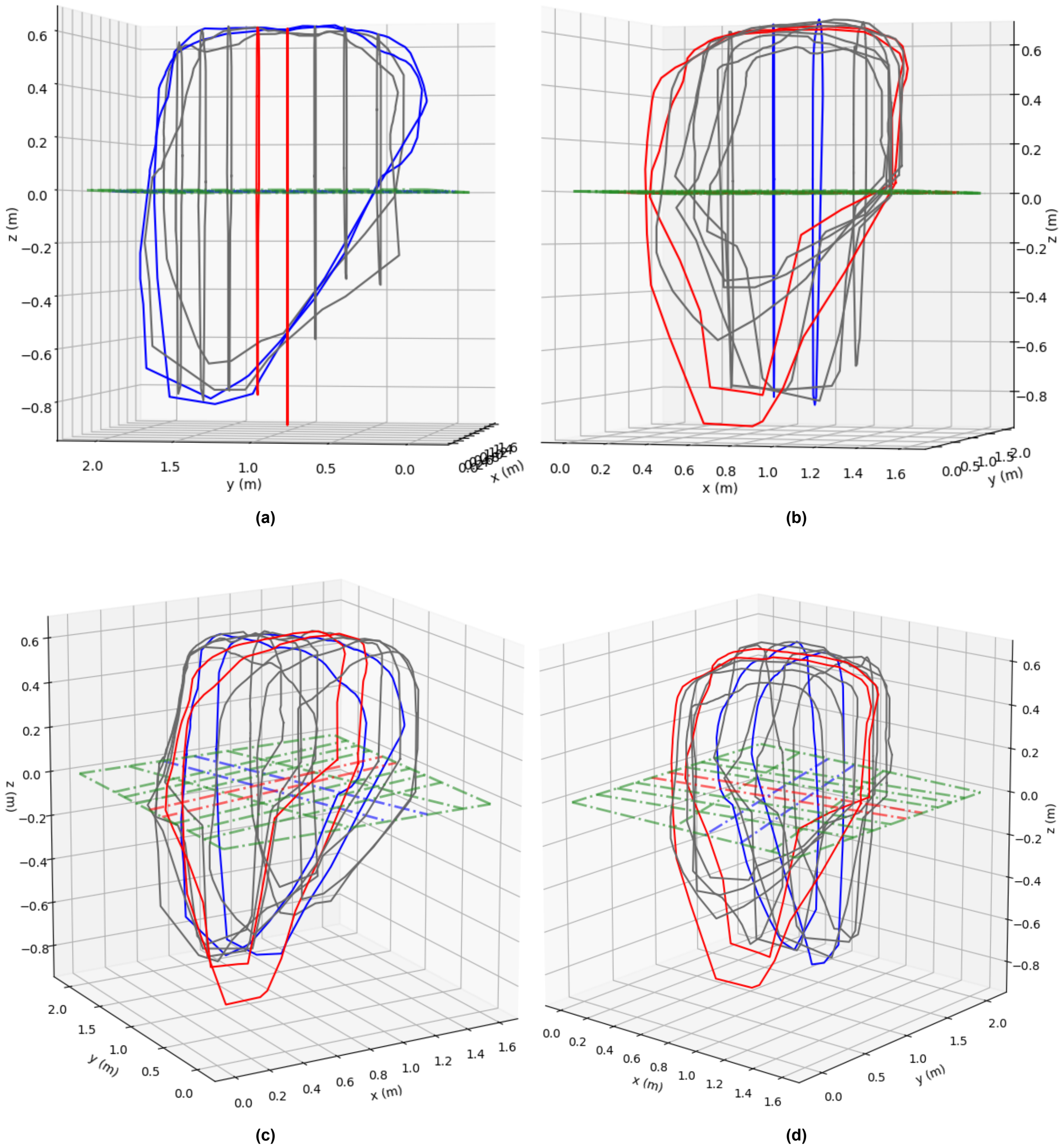

(a) (b)

(c) (d)

Figure 8.15: Rock contour according to modelled GPR data from GEO-to-GPR point model for keystone Hunebed D14. The contour lines for line 2 and 3 (blue) and D and E (red) are highlighted to show the burial depth for the rock with minimum interference of other rock faces. (a) shows the view from the east (S-N), (b) from the north (E-W), (c) from the north-east and (d) from the north-west.

8.8. Resolution

The resolution of the GPR can be given by Eq. 2.2 and 2.1 in section 2.1.4. The assigned center frequency to the GPR is used for the resolutions, which is 1000 MHz. The velocity of the radio waves through the rock was estimated to be 0.102 m/ns (section 8.2.2). The vertical or radial resolution is then 2.6 cm.

The horizontal or lateral resolution depends on the depth or distance from the rock surface to the reflective surfaces. This distance ranges between 0.2-1.4 m in the results, which gives a horizontal resolution of 10.1-26.7 cm.

9

Discussion GPR

This chapter contains the discussion with regard to the GPR results of both the boulder at the TU Delft in Chapter 7 and the keystone SI2 of Hunebed D14 in Chapter 8. At the end, the applicability of the proposed approach and its models from Chapter 6 is discussed, including the accuracy.

9.1. TU Delft boulder

The rock on the campus at the TU Delft was analysed and its results were presented in Chapter 7. First, the direct results from the GPR survey are discussed, which comprises the (processed) GPR radargram and the estimated velocity through the rock. Secondly, the calculated rock surfaces from the GPR point-to-GEO model are discussed.

9.1.1. Survey results

The processed GPR radargram for line B-reverse and the resulting identified reflection surfaces and rock contour are shown in Figure 9.1 and 9.2 to assist in discussing the results. Figure 9.1 shows strong and clear reflections as expected for mostly granite-air boundaries with R=+0.38. Two reflection surfaces can be seen at roughly 16 ns and 20 ns between 0 and 0.1 meter in Figure 9.1. The purple reflection at 20 ns appears to have a different polarity ('black-white-black') than the green reflection at 16 ns ('white-black-white'). The rock surface coordinates corresponding to these reflection surfaces (green and purple coordinates in red oval in Figure 9.2) show that the green coordinates may indicate the boundary between granite and the pavement, whereas the purple coordinates most likely indicate the granite-air boundary. The green coordinates, however, show largely the same polarity as the other reflective surfaces, which are expected to mostly indicate the granite-air boundary ('white-black-white').

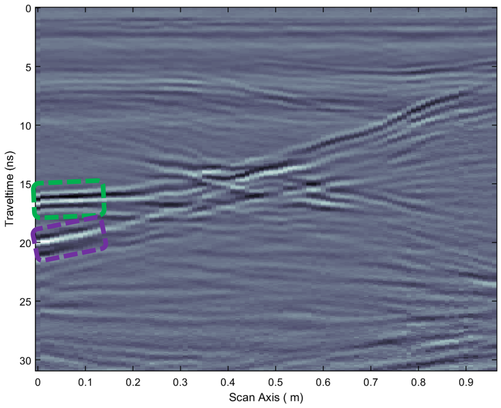

Figure 9.1: Processed GPR radargram for line B-reverse in (a), including two highlighted reflections in green and purple.

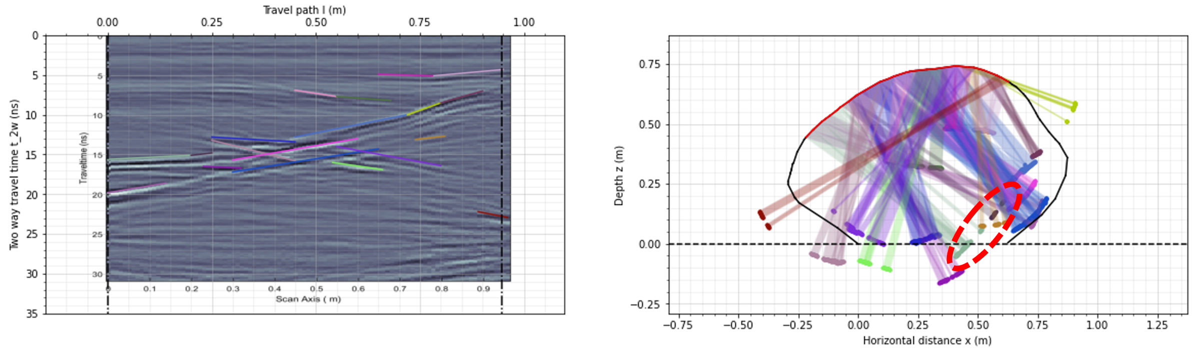

Figure 9.2: The identified reflection surfaces (left) and 'buried' rock contour coordinates for line B-reverse (right). The red oval indicates the calculated rock surface coordinates for the reflections in green and purple.

A reverse in polarity indicates, for example, a granite-saturated sand boundary (R=-0.38). The purple reflection surface in Figure 9.1 should therefore not indicate a granite-air boundary (no reverse in polarity), but rather a granite-saturated sand boundary. This is contrary to what can be seen for the corresponding purple rock coordinates in Figure 9.2 that do indicate a granite-air boundary. An explanation could be that the projection of the rock surface coordinates is not correct, but that is discussed in the next section. another possibility is that the reflection does not indicate a boundary involving the boulder, but a pavement-soil (saturated) boundary, see light blue reflection in Figure 9.3.

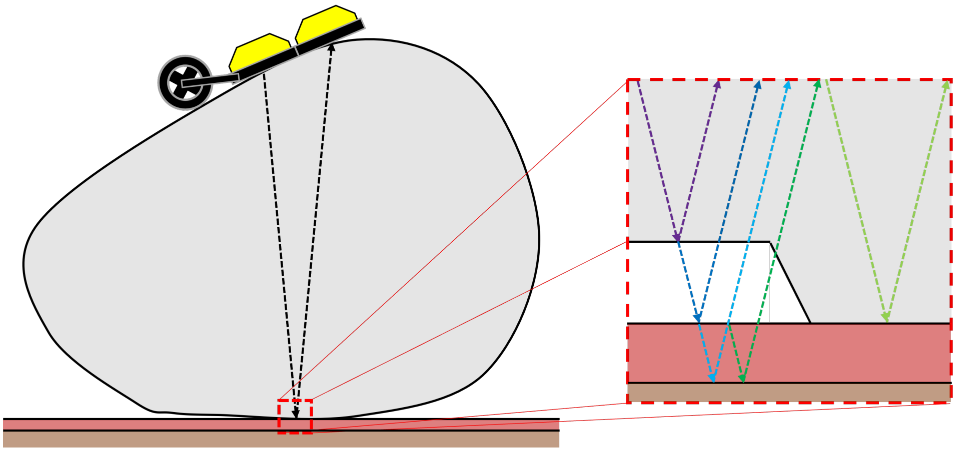

Figure 9.3: Reflection at several boundaries, with granite-air (purple), air-pavement (dark blue), pavement-soil (light blue) and granite-pavement (light green). The dark green line indicates a multiple reflected radio wave.

As can be seen in Figure 9.3, the radio waves can reflect at different boundaries with different reflection coefficients. The granite and pavement are most likely not in direct contact for all hidden rock surfaces, because the boulder is placed on the pavement and not buried in it. Therefore, granite-air, air-pavement and granite-pavement boundaries exist, see Figure 9.3. Furthermore, the pavement is placed on an unknown soil, so a pavement-soil boundary is also present.

For a direct granite-pavement boundary, the reflection won't be very strong due to the very similar dielectric constant of brick and granite (comparable to granite-dry sand boundary with R=+0.06). However, the pavement covers an unknown soil. A pavement-soil boundary does give strong reflections with a reverse in polarity if the soil is assumed saturated sand and the brick is assumed similar to dry sand/brick (R=-0.43), see also the light blue reflection in Figure 7.3. The purple rock surface coordinates in Figure 9.2 could therefore indicate the pavement-soil boundary, with the soil being saturated as the polarity is reversed ('black-white-black') . Unfortunately, these coordinates do seem to follow the contour of the rock above ground level and do not appear below the hidden faces, but this might have to do with the accuracy of the results and is not considered in this section.

Then, the estimated velocity is low (0.103 m/ns) compared to the lower-bound of the expected velocity for granite (0.12 m/ns) from section 3.1. An explanation could be weathering of the rock (although not clear from the exposed rock surface).

Finally, some remarks have to be made. Difficulties existed in obtaining the correct GPR survey path from rock contour, which may cause shifts of hidden rock surface coordinates with respect to their origin. The measured lengths of survey lines often deviated up to 10 cm from the horizontal axes of the resulting GPR radargrams, which means that the origin of the reflections in the GPR radargram does not always correspond to the actual origin. It is therefore important to carefully follow the survey lines.

9.1.2. Rock surfaces results

Identifying reflection surfaces was not difficult as the reflections were strong and clear to distinguish, but determining the exact coordinates for the linear reflection surfaces requires a prolonged amount of time. Also, due to the number of reflective surfaces and human interference, a consistent definition of a reflective surface may not have been applied. Preferably, the identification process would be automated in future analysis to increase the identification rate and consistency between survey lines. Automatically detecting reflection surfaces in a processed GPR diagram is, however, challenging, but a program that allows the user to draw the linear lines directly on top of the reflections would already be a major improvement.

Deep reflections ($t_{2w} > 25$ ns) were filtered out for most surveys. They would give reflection surfaces that did not indicate the bottom contour of the rock correctly as they were either suspected to be not direct reflections or reflections from boundaries not involving granite. Still, reflections from non-relevant rock contours remain to show how arbitrary the identifying of the reflection surfaces is and to not give a false sense of accuracy. An example can be seen in Figure 9.4, which shows multiples of reflections roughly following the same shape, but at different depths. Compared to Figure 9.2, the rock contour is turned 180 degrees and some deeper reflections are not filtered out.

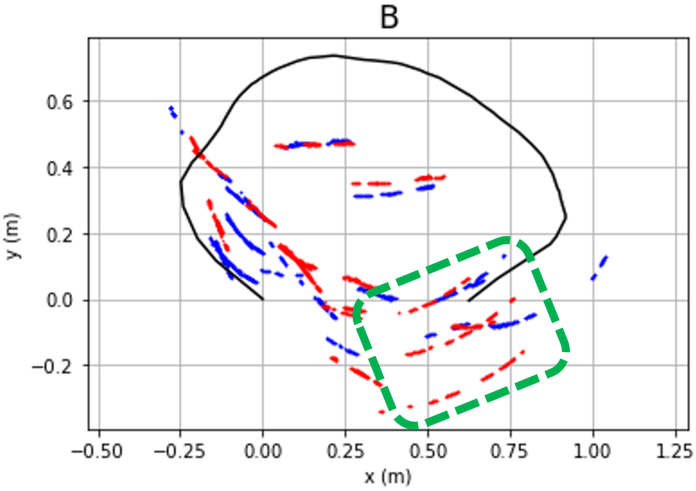

Figure 9.4: Rock surface coordinates for line B with the red coordinates showing the normal direction and the blue coordinates showing the reverse direction. The green area indicates multiples or "layering" of reflections.

In general, the rock contour was captured well by the results in Appendix C when compared to the known rock contour. Both the rock contour as well as the horizontal plane on which the rock rests can be seen. However, it is hard to distinguish the relevant reflections in the GPR radargram from the non-relevant reflections, which causes large deviations of the rock contour results compared to the actual rock contour.

For the individual reflections that indicate the rock contour fairly well, high precision and accuracy can be seen. The accuracy is then roughly 5-10 cm, but deviations of only a couple of cm's can be seen, see Figure 9.4. Still, large over- or underestimations are present in the figures in Appendix C and section 7.5.

Also, multiple reflections sometimes indicate the same contour, but for different distances. This 'layering' (green in Figure 9.4) of the contour is most likely attributed to reflections that reflect multiple times between surfaces (e.g. dark green reflection at soil-pavement-soil in Figure 9.3), but are still received. This gives similar rock contours, but in a layered manner. It can be prevented by only considering the first reflection in the GPR radargram.

It can also be concluded that the measurements in different directions along the same survey line could be obtained while still showing similar results (red and blue coordinates overlap in Figure 9.4), which means that the measurements are reproducible. Moreover, not only the rock contour could be captured. An interesting zone in the upper part of the rock (Figure 9.4) appears in the results for several surveyed lines. Clear reflections were visible close to the surface at the top. It may indicate an internal fracture and therefore gives information into the internal structure of the rock. However, this reflection should be treated with caution as it is already shown that identifying reflection surfaces is challenging.

9.2. Keystone Hunebed D14

The keystone of Hunebed D14 was analysed and its results were presented in Chapter 8. First, the direct results from the GPR survey are discussed, which comprises the (processed) GPR radargram and the estimated velocity through the rock. Secondly, the calculated rock surfaces from the GPR point-to-GEO model are discussed. Thirdly, the estimated buried rock contour and the modelled GPR data from the GEO-to-GPR point model are discussed.

9.2.1. Survey results

The processed GPR radargram for line 4N and the resulting identified reflection surfaces and rock contour are shown in Figure 9.5 and 9.6 to assist in discussing the results. The GPR radargram of the keystone shows a couple of strong reflections (Figure 9.5), but most reflections are much weaker compared to the TU Delft Boulder (Figure 9.1). The strongest reflections are expected for the granite-air boundary (R=+0.38), while the weaker reflections are most likely from the granite-dry sand boundary (R=+0.06) as the keystone is partially buried. Furthermore, possibly granite-saturated sand boundaries exist in the field (R=-0.38), depending on the local soil humidity conditions.

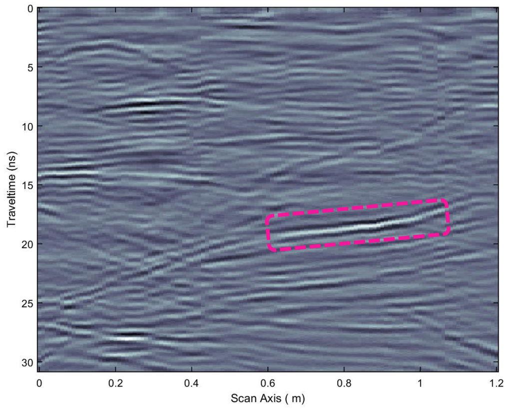

Figure 9.5: Processed GPR radargram for line 4N, including a highlighted reflection in pink.

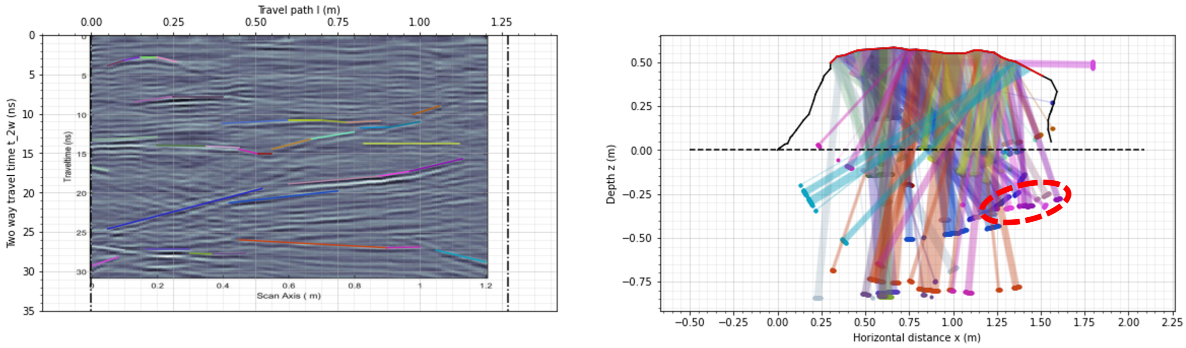

Figure 9.6: The identified reflection surfaces (left) and 'buried' rock contour coordinates for line 4N (right). The red oval indicates the calculated rock surface coordinates for the reflection in pink.

Most reflections are not strong and do not show signs of reverse polarity ('white-black-white'), which would be in agreement with granite-dry sand boundaries. However, one reflection surface in particular shows strong amplitudes with signs of reverse polarity ('black-white-black'). The reflection surface between 0.6 and 1 m at roughly 20 ns or pink in Figure 9.5 seems to indicate a granite-saturated sand boundary (R=-0.38), which is also visible for the reverse direction in Figure E.8 in Appendix E. Its corresponding buried rock surface coordinates do appear at -0.25 m (see red oval in Figure 9.6), so the local rock surface could be buried in (partially) saturated sand. A counterargument would be that most other reflection surfaces appear not to indicate the presence of water.

Another possibility is the air-dry sand boundary (R=-0.33), see dark green reflection in Figure 9.7, or air-granite boundary (R=-0.38), shown for a light blue reflection at a soil-granite instead of air-granite boundary in Figure 9.7. A radio wave could have reflected at the air-soil or air-granite interface. This would also explain the depth at which the reflection originates according to Figure 9.6 as the reflection does not indicate the rock surface, but the rock surface coordinates are discussed in the next section.

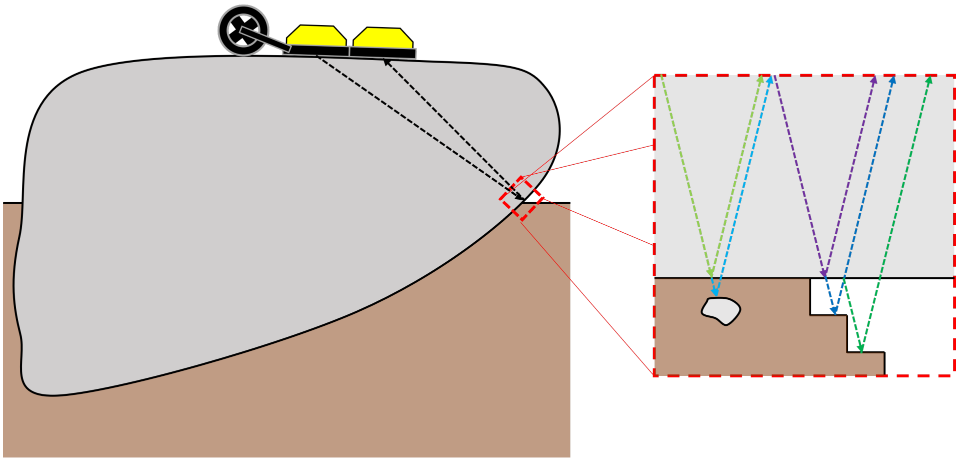

Figure 9.7: Reflection at several boundaries for the keystone, with granite-air (purple), air-soil (dark blue), granite-soil (light green), soil-gravel (light blue). The dark green line indicates a multiple reflected radio wave.

As mentioned in section 8.1, the soil surrounding the keystone has been irrigated with water to saturate the rock-soil interface (saturated sand-granite with R=-0.38 vs dry sand-granite with R=+0.38) and increase the visibility of the reflection surface. It is unlikely that the soil is fully saturated and more likely is that only a small portion of water infiltrated. Nevertheless, it is still worth considering to explain the ink reflection in Figure 9.5. Line 4 does coincide with the eastern side of the keystone, so the strong pink reflection could be caused by the irrigation. Especially at the north-eastern side of the keystone does line 4 (both in normal and reverse direction) closely passes the irrigated rock-soil interface, see Figure 9.8a. Moreover, the keystone is locally overhanging (Figure 9.8b, which could mean that the sand is saturated even though the water only infiltrated slightly.

(a) **(b)**

Figure 9.8: Test survey for which the soil surrounding the keystone was irrigated (a) and the north-eastern corner of the keystone.

Finally, the estimated velocity is low (0.102 m/ns) compared to the expected lower-bound velocity (0.12 m/ns) from section 3.1. The same can be said as for the rock at the TU Delft, which is that the lower velocity can be explained by weathering of the rock (crumbling areas at the exposed surface were visible).

It is important to remark that the measured lengths of the gridlines in the survey did significantly deviate from the horizontal axes lengths of the GPR radargram. Furthermore, shifts or sudden steeper slopes of reflections in the GPR radargram were visible, which indicates slip of the odometer (wheel attached to the GPR to measure survey path) during the survey. It also explains the differentiating lengths of the measured survey lines. Especially at the start of the survey lines, this slip occurs.

9.2.2. Rock surfaces results

Originally, deeper reflections were ignored as was advised after the survey for TU Delft rock. However, in a later stage, the deeper reflection surfaces were considered as several survey lines seemed to lack information into the buried rock contour.

In general, the rock contour shown by the (buried) rock surface coordinates in Figure 8.10 in section 8.5, seems to indicate a downward slope in the southern direction with steep faces at the south and east side. The west face is controversial as historical photos seem to indicate again a steep almost vertical face, but based on the (buried) rock surface coordinates a slight inward slope should be expected. The rock surface coordinates do sometimes coincide with the exposed rock surface, with similar deviations of 5-10 cm as concluded from the TU Delft rock, see Figure 9.9a.

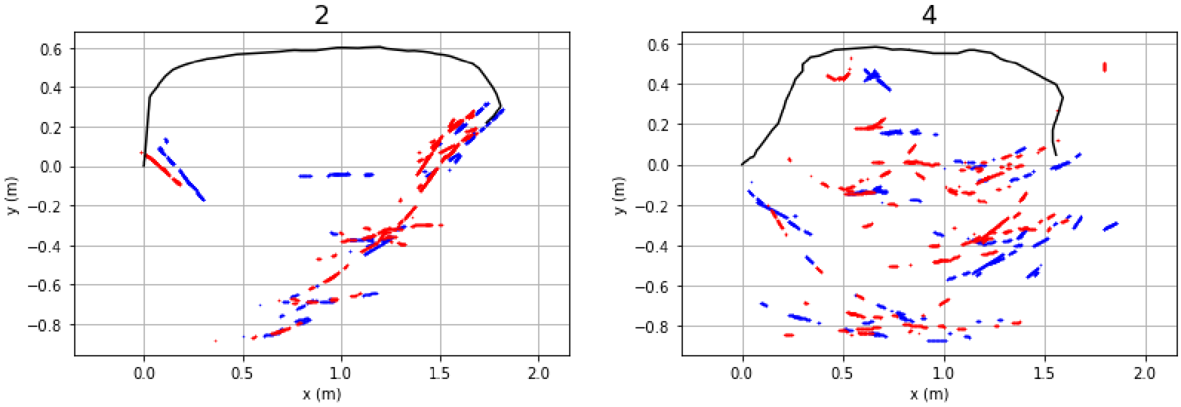

(a) **(b)**

Figure 9.9: Rock surface coordinates for line 2 (a) and 4 (b) with the red coordinates showing the normal direction and the blue coordinates showing the reverse direction.

The overall accuracy cannot be qualified as a large part of rock contour is not known. However, the coordinates for each line and both directions appear reproducible, which can be seen as an overlap between the rock surface coordinates for normal and reverse directions in Figure 9.9a and 9.9b. Furthermore, they do show a rough trend, especially the slope in Figure 9.9a. However, the resulting 'point cloud' of (buried) rock surface coordinates is still inconsistent and should be treated carefully. It was concluded from the TU Delft rock that identifying reflection surfaces is challenging, which is clearly shown by Figure 9.6. The layered contour is not visible now in the results in Appendix G as the advice based on the TU Delft rock was followed by only considering the first reflection of a set.

Figure 9.9b contains many rock surface coordinates as the GPR radargram contained a lot of reflections that could not be distinguished from each other. It can be seen that a lot of reflections originate from within the rock, even above ground level. The reflections near ground level are often seen in the results in section 8.5 and caused confusion at the western rock race which seems vertical according to historic photographs, but doesn't appear as such in the GPR data. A possible explanation is internal fractures, but it is unlikely that these somehow all occur near ground level.

The deeper reflections are also considered, but could originate from gravel or other boulders in the subsurface. During an excavation in 1927, the basement of D14 was dug out, which uncovered a floor of rocks stretching over the entire structure, see Figure 9.10. These rocks could contribute to reflections from different origins than the contour of the keystone. Another possibility is reflections from nearby bearing stones.

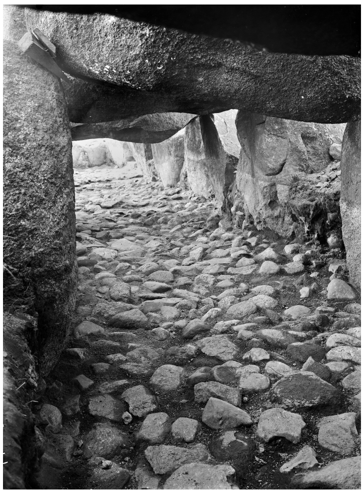

Figure 9.10: Basement of D14 during excavation led by Van giffen in 1927 from GIA (Groningen Institute of Archaeology) (Ten Anscher, 2019). The photograph is taken from the south-east and therefore does not show the keystone SI2.

An interesting feature is visible near the top of the keystone for lines B, D, 3 and 4 (Figure 9.9b) for both directions, which seems to indicate the fracture from 1957 and repaired in 1959 and 1996. As the fracture is reported and can be seen in recent photos, it is highly likely that the feature indeed indicates the fracture.

9.2.3. Buried rock contour

The estimated rock contours and the corresponding modelled GPR radargrams of lines 4N and 4R are shown in Figure and 9.11 to assist in discussing the results. First, it can be seen that obtaining a coherent rock contour from an incoherent set of (buried) rock surface coordinates is difficult and more importantly, subjective (Figure 9.11a). A useful manner of evaluating the GEO-to-GPR model is by looking at the modelled GPR data based on the exposed rock surface, which is known. The response of the GPR should theoretically coincide with a reflection in the GPR radargram, perfectly. Furthermore, as this reflection is a granite-air boundary, it should be strong and clearly visible.

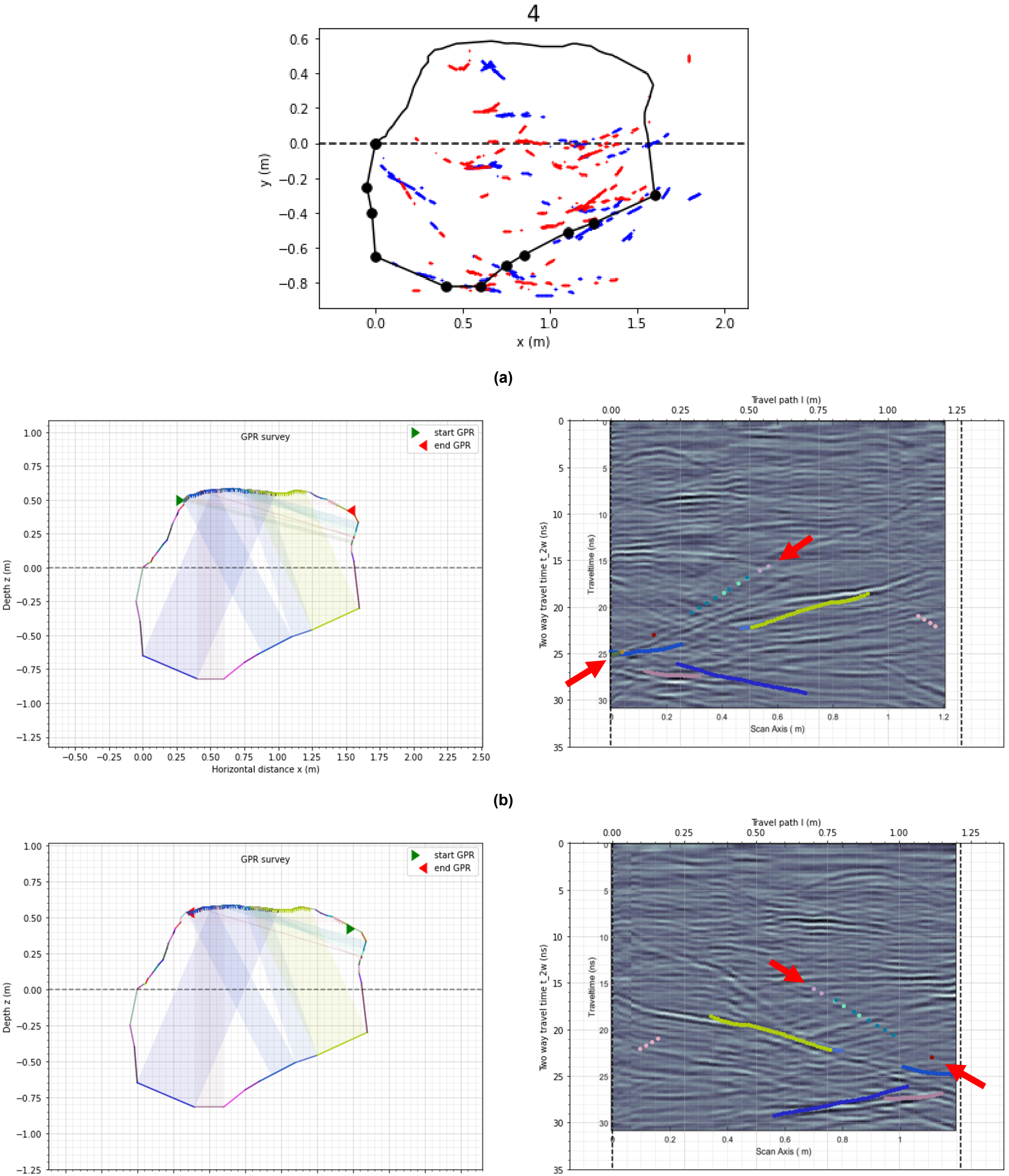

(a)

(b)

(c)

Figure 9.11: Estimated buried rock contour of line 4 (a) and the modelled GPR radargrams (right) from buried rock contour (left) of line 4N (b) and 4R (c). The red arrows indicate the modelled reflection from the exposed rock surface.

For both line 4N and 4R in Figure 9.11b and 9.11c, respectively, a reflection from the exposed rock surface exists. However, where the modelled GPR reflection is a good fit with an existing reflection in the GPR radargram for line 4N (red arrows in Figure 9.11b), this is not the case for line 4R (red arrows in Figure 9.11c. This is most likely attributed to slightly deviating GPR survey path starts in the model and during data acquisition. Furthermore, a balance has to be found between the buried rock surface coordinates for normal and reverse direction for the estimated rock contour as they do not coincide perfectly. This may cause differences between the modelled reflection and the found reflection.

The other modelled reflections do resemble the found reflections, but do not always appear at the right position. This can be attributed to the aforementioned deviating GPR survey paths in the model and in practice.

The buried rock contour was continuously updated after modelling the GPR response, but in the end, the buried rock contour in the north-south direction is generally slightly deeper than in the east-west direction (section 8.7). An explanation for this is likely the 3D effects. As the reflections may not always come from within the cross-section of the GPR survey path, slight deviations in north-south and east-west can be expected. As this appears to be consistent among the two perpendicular directions, it is likely that 3D effects play a role and not only the arbitrary identification of reflection surfaces for which random varying deviations would be expected.

Regarding the mismatch for the western facing side of the keystone between data from historic photos and the GPR, this problem probably coincides with the unforeseen reflection surfaces near soil surface level. Apparently, reflection surfaces exist around ground level, which are not considered for the buried rock contour if they appear at the center of the rock, but are considered to be part of the rock contour when they appear at the side. Again, this highlights the challenge that arises for identifying reflection surfaces, but also the importance of considering blind spots. A local lack of rock surface coordinates, indicating steep rock surfaces, should result in a steep western face of the keystone, which seems to be confirmed by historic photographs. However, as no clear reflections are visible, other slightly less clear reflections are considered for the rock contour, which results in a mismatch between historic photographs and GPR data. This phenomenon is visible near ground level at the left side of the keystone in Figure 9.11a. Here, a sharp corner near ground level could be assumed part of the buried rock contour, while it (likely) shouldn't be. It therefore also highlights the need to consult historic data, if existent, to determine a set of initial conditions from which a first estimate can be made for blind spots in the GPR data.

9.3. Applicability

First, the accuracy of the buried rock contour is determined based on the resolution and the obtained results. Then, the implications of the buried rock contour of the keystone for the 3D reconstruction and the broader project are given. Finally, a discussion regarding the applicability of the GPR and the proposed approach to estimate the buried rock contour is given.

9.3.1. Accuracy

The radial or vertical resolution of the 1000 MHz GPR was calculated to be 2.6 cm for both granitic rocks (boulder at the TU Delft and keystone of D14). The horizontal or lateral resolution ranges between 10 and 25 cm for an increasing depth.

The rock contour was estimated based on the distance between the rock surface coordinates and their point of detection along the GPR survey path. The radial resolution should then also be Vr = 2.6 cm, which means two rock surfaces can be distinguished for a minimum distance of 2.6 cm. However, the actual accuracy of the rock surface coordinates to the estimated rock contour appears to be around 5-10 cm in practice. However, identifying relevant reflections that indicate either a granite-soil or granite-air boundary is difficult. The strength and polarity of the reflections could help in interpreting the origin of the reflections, but this hypothesis could not be fully confirmed as doubts remain. However, the accuracy could possibly be increased if the reflection picking was done on individual traces instead of the radargrams. Furthermore, the polarity could be assessed better.

The horizontal resolution indicates the minimum distinguishable distance between two objects, using the GPR in a Common Offset Survey. This would mean that in the small scale at which the GPR is applied (rock diameters of 1-2 m), the distinguishable distance between two features could easily vary 10% of the dimension of the rock (Hr = 10-25 cm). However, in the context of the GPR point model in which the GPR is applied, this is not directly a cause of concern as the slopes of the reflections are considered which indicate the origin of the reflections. While the horizontal resolution means that features smaller than 10-25 cm (depending on depth) cannot be distinguished from other features, it is not that detrimental for a general rock contour. This is confirmed by the estimated rock contour for the TU Delft rock and the keystone, which show (supposedly) respectable fits with the actual rock contours although deviations occur.

The difference between the theoretical resolution (2.6 cm) and the actual accuracy of the GPR point model (5-10 cm) can be attributed to several events in the proposed approach. First, unwanted events during data acquisition in a Common Offset Survey influence the results, which are:

- Slip of the odometer wheel
- The start of the GPR survey deviating from the pre-defined start of the survey line

Secondly, the GPR point model inherently simplifies the GPR in practice by assuming the following:

- Radio waves reflect perpendicular to rock surface
- Reflections outside cross-section are projected into cross-section (3D effects ignored)
- Only direct reflections are considered
- GPR survey paths are equal to the rock contours extracted from the point cloud model from a LiDAR scan

Thirdly, estimating the buried rock contour from buried rock surface coordinates gives rise to inaccuracies due to:

- Challenging identification of reflection surfaces
- Manual extraction of rock contours
- Manual definition of GPR survey paths, including start and end
- Blind spots in GPR data hidden by irrelevant reflection surfaces
- Mismatch between buried rock surface coordinates for different directions due to 3D effects

9.3.2. Project

From the GPR survey results, it is estimated that the buried bottom of the keystone starts at ground level in the north and slopes downward to the south. The rock faces at the south, east and possibly west are steep, almost vertical. This means that before the alteration of the keystone in 1965, the bottom of the keystone was approximately parallel with the ground surface, while the current top of the keystone was sloping downward to the north.

In the current position, the keystone is buried at an estimated maximum depth of 80 cm at the southern side, which is likely deeper than it was before 1965. This means for the 3D reconstruction that the keystone is currently very stable due to its burial depth, but this might change due to a shallower burial depth if SI2 would be tilted to fulfill its role as keystone again. However, as the keystone has been positioned in such a way for thousands of years before, this is not concluded to be a problem. The true stability problem lies in the capstone D9, which is outside of the scope of this thesis.

It was also established that a fracture was most likely detected close to the current top of the keystone, which is confirmed by photographs. Besides the reflection from this fracture, some reflections at the center and sides of the keystone near ground level (in its current position) could be seen localised in a relatively small area. These reflections are not considered to indicate the buried rock contour, but it could also not be determined if these reflections indicate fractures. It would be surprising if they were as they are grouped together only at ground level. It is suspected that they may indicate reflections from other nearby rocks or bearing stones.

In short: the keystone is most likely not internally damaged and can therefore be tilted if necessary following from the stability analysis by Theuws (2021).

9.3.3. GPR application

The proposed approach in Chapter 6 and the conceptual and mathematical models from Chapter 3-5 yielded varying results. Although the rock contour was captured well with deviations of 5-10 cm for the TU Delft boulder, excluding wrongfully identified reflections and blind spots, the 1000 MHz GPR was difficult to deploy in the field for both the boulder and the keystone. Especially the complex geometries of the rocks and the relatively large size of the GPR compared to the rocks, made it difficult to gather reliable data.

A smaller GPR could therefore offer better results. Consequently, this would automatically lead to higher frequencies of up to 2.6 GHz, which means an increase in resolution. Important is that the penetration depth of the signals is greater than the buried rock contour of the surveyed rock. Otherwise, the complete buried rock contour can not be estimated.

Up until now, the GPR has been widely applied to detect fractures and voids and locate features (e.g. rebar) in columns, masonry walls, etc. However, these are isolated structures with simple geometries. The proposed approach could be better evaluated if similar surveys on rocks with simple geometries would be performed. The current results are promising, but a clear assessment of the approach is difficult due to the many uncertainties listed in the previous subsection.

10

Methodology Seismic

This chapter contains the method used in obtaining the distance to reflection surfaces using seismic (ultrasonic) methods. It is a simple and relatively concise approach and contains only several steps that are required. A concise overview of the most important steps is given below:

1. Acquisition of seismic data
2. Calculation of seismic wave velocity
3. Calculation of reflection depth

Acquisition of the seismic data is largely done on sample rocks, which vary between granites, sandstones and basaltic rock types. First, transmission tests on rock samples are performed to estimate the seismic velocities from P-wave arrivals. Then, reflection tests on the same rock samples can be carried out to investigate the accuracy of the possible reflection depths for known dimensions. Important in this step is the choice of source. Several sources are available: I) Transducers with varying center frequencies, II) Mechanical hammers, III) Standard hammers.

Then, the reflection depths can be calculated if the seismic velocity is estimated. Finally, the setup can be improved using an array of receivers. Each step is discussed in more detail in the upcoming sections.

10.1. Seismic data acquisition

Two different tests can be performed in order to estimate reflection measurements: a) Transmission Test and b) Reflection Test. Figure 10.1 shows the principle behind both tests. First, a signal is emitted (blue incident wave). Then, the direct arrival at the opposite end of the rock with respect to the origin of the signal (green transmitted wave) can be measured. The velocity can be estimated if the time difference and distance are known. Knowing the velocity, the reflected signal (partially reflected red wave) indicates the depth or distance to the reflection surface.

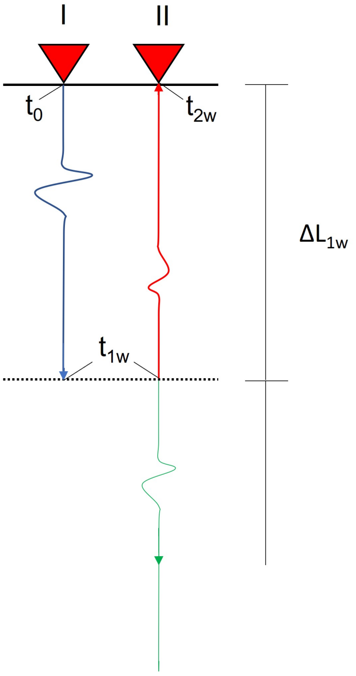

Figure 10.1: Schematic of a propagating wave (either P or S) through a medium of length Δx_{1w}.
I) Incident wave (blue) emitted at surface at $t = t_0$ reaching the boundary at $t = t_{1w}$.
II) Partially reflected (red) wave at boundary at $t = t_{1w}$ reaching the surface again at $t = t_{2w}$ and transmitted (green) wave.
The red triangles represent transmitters and/or receivers.

10.1.1. Transmission Test

In order to estimate the velocity through the rock, a transmission test has to be performed. First, the distance between the signal source/transmitter and receiver is measured. Then, the time difference can be obtained by measuring the time of the first arrival of the direct P-wave, after which the velocity can be calculated. This means a direct measurement has to be done.

10.1.2. Reflection Test

At a change in material properties such as the stone-soil boundary, an ultrasonic wave is partially reflected. Based on this principle, the two-way travel time of a P-wave can be measured and if the velocity is known, the travel distance can be estimated. Ideally, half of this two-way travel distance is equal to the burial depth of the bearing stones. It can occur that a shear wave (S-wave) is measured by the P-wave receiver transducers, but this is highly unlikely as long as the surfaces are approximately parallel (and the offset between the source and receiver is small.

The setup of the Reflection Test for one set of transducers is given in Figure 10.2. The source on top in Figure 10.2a is displayed separately of the top receiver, which gives a time delay t_0. The time delay is required as it gives the correct time $t = 0$ of the source at which the signal is emitted.

The top diagram at in Figure 10.2b shows an illustration of the received signal, with the first arrival at t_0 being the first direct arrival and the second arrival at t_{2w} being the reflection. In the case of a bottom receiver, the diagram at the bottom shows the direct arrival at t_{1w} being the transmitted wave with which the velocity can be determined if the distance L is known.

It is assumed that the distance between the source and the top receiver Δx_0 in Figure 10.2a is very small compared to the one-way travel path L. This is important as it then only gives a very small error in the two-way travel time $(t_{2w} - t_0)$, and can therefore be assumed negligible. If the distance Δx_0 becomes too big, the time delay t_0 becomes greater, which results in a smaller two-way travel time. Therefore the velocity may be significantly overestimated due to an underestimation in time. For transducers, no time delay exists generally as the time of emission is known. Therefore, the time $t_0 = 0.0$ can be used for transducers.

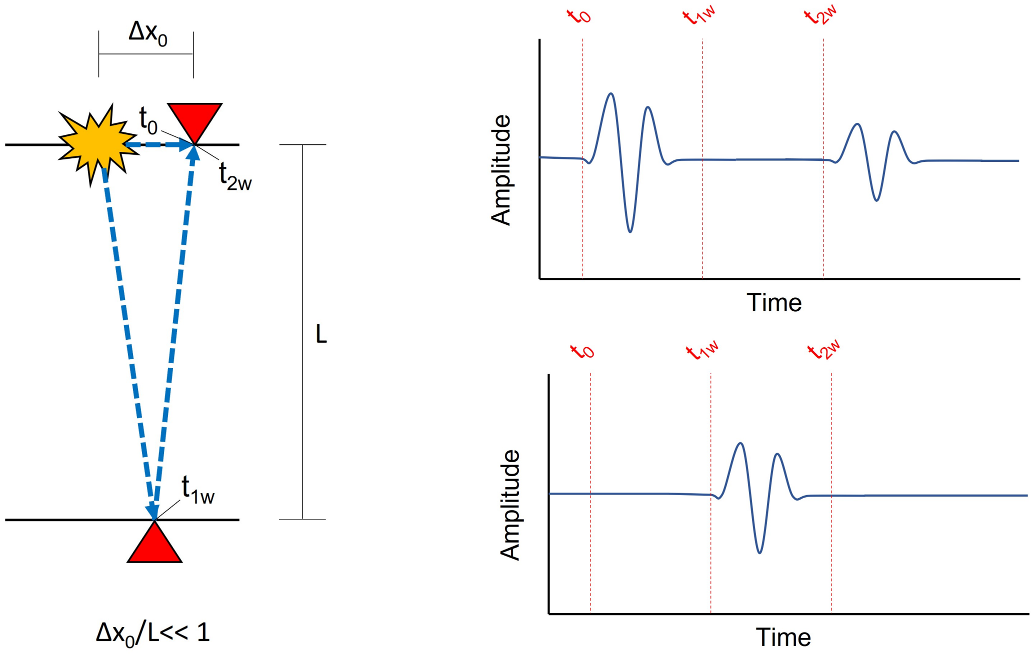

(a) Schematic drawing with receivers as red triangles **(b)** Expected results (idealised) from top receiver (top) and bottom receiver (bottom)

Figure 10.2: Idealised Reflection Test setup

In order to have sufficient separation between the two signals at t_0 and t_{2w}, the period T should be smaller than the time it takes the signal to reflect at the bottom and arrive at the receiver on top, which is the two way travel time t_{2w}. The respective definitions of the period T and the two way travel time t_{2w} are

$$T = \frac{1}{f} \tag{10.1}$$

and

$$t_{2w} = \frac{2 \cdot L}{v_{seis}}. \tag{10.2}$$

Then, the derivation of the minimum frequency required in order to get a sufficiently short period T is given by

$$T < t_{2w}, \tag{10.3a}$$

$$\frac{1}{f} < \frac{2 \cdot L}{v_{seis}}, \tag{10.3b}$$

$$f > \frac{v_{seis}}{2 \cdot L}, \tag{10.3c}$$

with v_{seis} as the seismic velocity and L as the one-way travel path.

It is important to note that the center frequency of the source may not be the frequency of either the first direct arrival or the reflected wave. However, as the separation depends on the first direct arrival arriving at t_0, this is the limiting factor. The minimum frequencies for several seismic wave velocities over a varying distance are shown in Table 10.1. It can be concluded that the frequency of the source should at a minimum be in the order of 10^1 kHz to ensure a separated arrival of the reflected wave at t_{2w} (for high P-wave velocities from Table 10.2 in section 10.2.1).

Table 10.1: Minimum frequencies for varying seismic wave velocities and distances L

Minimum frequency (kHz)					
v_{seis} (m/s)	L (m)				
-	0.30	0.60	0.90	1.20	1.50
2000	3.3	1.7	1.1	0.8	0.7
3000	5.0	2.5	1.7	1.3	1.0
4000	6.7	3.3	2.2	1.7	1.3
5000	8.3	4.2	2.8	2.1	1.7
6000	10	5.0	3.3	2.5	2.0

More advanced testing using a line array form is also possible. Then, multiple receivers are evenly placed along a line originating at the source, with a certain step Δx_a. This is done in order to estimate the P-wave velocity to the reflection surface and consequently the distance to the reflection surface. The exact location of the reflection is not traceable due to 3D ambiguity. An important condition for this measurement is that the reflecting surface should be more or less flat in order to correctly estimate the velocity and distance. The setup in Figure 10.3 illustrates the approach in which the reflection in green is used to determine t_0. However, this is not required if the time delay is known or if the time zero at which the signal is sent is known. It depends on the source, if this is necessary.

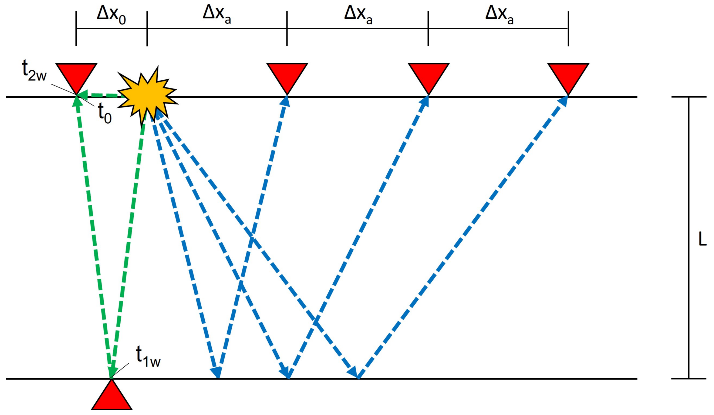

Figure 10.3: Schematic drawing with an array of receivers. The red triangles represent transmitters and/or receivers, while the blue arrows represent reflections from a reflection surface. The green reflection gives the time zero if required for the source.

10.2. Seismic wave velocity calculation

Once the Transmission Test is done, the seismic wave velocity can be estimated. This is if the array measurements are not performed. Otherwise, the velocity calculations can be done directly. First, the expected velocities are determined in section 10.2.1. The calculation of the velocity is then explained in section 10.2.2.

10.2.1. Theoretical seismic wave velocities

The wave propagation (longitudinal/compressional/pressure wave and transverse/shear wave) in a medium can be given as a function of the constrained modulus $M(Pa)$, shear modulus $G(Pa)$ and mass density $\rho(kg/m^3)$. The P-wave velocity v_p is given by

$$v_p = \sqrt{\frac{M}{\rho}} = \sqrt{\frac{E}{\rho} \cdot \frac{(1-\nu)}{(1+\nu)(1-2\nu)}}, \tag{10.4}$$

in which the constrained modulus M is expressed in the Young's or Elastic modulus $E(Pa)$ and the Poisson's ratio $\nu(-)$. The shear wave velocity v_s is given by

$$v_s = \sqrt{\frac{G}{\rho}} = \sqrt{\frac{E}{\rho} \cdot \frac{1}{2(1+\nu)}}, \tag{10.5}$$

in which the shear modulus G is also expressed in the Young's or Elastic modulus E and the Poisson's ratio ν (Sawangsuriya, 2012). The Young's modulus E is affected by the confining pressure of the medium. For higher confining pressures, the Young's modulus increases. This is important as it means that the wave velocities through a medium increase during compression as was shown by Stanchits et al. (2006). They measured P- and S-wave velocities approaching a maximum of 6 km/s and 3.7 km/s, respectively, in intact granites, but these were only 5.1 and 3.3 km/s for low confining pressures. Furthermore, a decrease in P-wave velocity is expected for an increase in temperature, porosity and pore pressure. v_p increases with, for example, increasing bulk density, cementation and saturation (Dondurur, 2018). Al-Harthi et al. (1999) found that P-wave velocities in basalt range from almost 7 km/s to 2 km/s for porosities ranging between 0% to 60%, determined by image analysis for vesicular basalt.

In general, a range of velocities can occur as the properties and quality of the rock vary. For granites, this range can be given as roughly 4.5-6.0 km/s for P-waves and 2.5-3.3 km/s for S-waves. Table 10.2 contains ranges of expected seismic velocities for several rock types (Oldenburg et al., 2017c).

Table 10.2: Typical ranges for seismic velocities for several rock types.(^{1}Oldenburg et al., 2017c,^{2}Dondurur, 2018)

	Seismic velocities	
Rock types	$^{1,2}v_p$ (m/s)	^1v_s (m/s)
Sandstone	1900-4900	800-1800
Limestone	2000-6200	2000-3300
Granite	4100-6000	2500-3300
Basalt	3500-6000	2400-2800
Gneiss	3500-6600	2700-3200

10.2.2. Seismic-wave velocity calculation

The theoretical velocity was determined in section 10.2.1. However, in order to estimate the propagation velocity through the rock, a Transmission Test as described in section 10.1.1 has to be performed. By doing a direct measurement, the apparent seismic velocity v_{seis} can then be calculated as in

$$v_{seis} = \frac{\Delta L_{1w}}{\Delta t} = \frac{\Delta L_{1w}}{t_{1w} - t_0}, \tag{10.6}$$

with the one-way travel path L_{1w}, the one-way travel time t_{1w} and the time delay t_0. It is important to perform several transmission measurements to estimate an average velocity, which can be assumed relevant for the entire rock (sample). Small-scale inhomogeneities and possibly anisotropy can influence the measured velocity as rocks are often not homogeneous and can have different properties in different directions. Furthermore, repeating the measurement and stacking them (e.g. summing and averaging), can reduce unwanted noise and enhances features such as reflections.

10.3. Reflection depth calculation

When the seismic velocity is known, the Reflection Test results as described in section 10.1.2 can be used to determine the depth of the reflection surface L. When a presumed reflected wave is measured, the depth to the reflection surface can be estimated by

$$L = \frac{1}{2} \cdot \sqrt{(\Delta L_{2w})^2 - (\Delta x_0)^2} = \frac{1}{2} \cdot \sqrt{(v_{seis} \cdot \Delta t)^2 - (\Delta x_0)^2} = \frac{1}{2} \cdot \sqrt{v_{seis}^2 \cdot (t_{2w} - t_0)^2 - (\Delta x_0)^2}, \quad (10.7)$$

in which t_{2w} is the two-way travel time, t_0 is the time delay, Δx_0 is the offset between source and receiver and v_{seis} is the seismic velocity obtained from the Transmission Test. The calculation of the reflection depth can of course only be done for measurements of which the velocity was not estimated from. Alternatively, if the reflection depth is known, the supposed two-way travel time is given by

$$t_{2w} = \sqrt{\frac{4 \cdot L^2 + (\Delta x_0)^2}{v_{seis}^2}} + t_0. \quad (10.8)$$

11

Results Seismic

This chapter contains the results from several seismic tests done at several rock samples varying in rock type and size for a number of sources. The aim is to find the best approach to perform a line array test. This approach could then be recommended for field surveys at, for example, megalithic structures. The steps discussed in Chapter 10 are followed and resemble the structure of this Chapter.

First, the rock samples are described. Then, the seismic velocities and reflection depths are estimated for two rock samples with help of several sources. Furthermore, a reflection test in line array form is performed and its results are discussed. The resolution of the results is given in the last section.

11.1. Rock samples

Several tests were performed in order to estimate propagation velocities and possibly detect reflections. As the aim of the thesis is to find the burial depth of the Hunebed bearing stones, the test are preferably performed on rocks resembling those. One such granitic rock has been stored indoors for years and is therefore not exposed to the elements, see Figure 11.1a. A disadvantage is that the boulder has an irregular shape, which makes finding reflections (and their origin) difficult. Therefore, also a rock with favourable dimensions and shape was tested on, see Figure 11.1b. As it is a bentheimer sandstone, it doesn't necessarily resemble the Hunebed stones. It is mainly used for testing with different sources in order to find the best signal. Finally, a cylindrical basalt rock is used for line array measurements due to its favourable shape and size, see Figure 11.1c. It can serve as an idealised first approach to testing in the field.

(a) Granitic rock **(b)** Bentheimer sandstone **(c)** Basalt

Figure 11.1: Rock (samples) used for seismic testing

11.2. Reflection depth estimation

Transmission tests on a granitic rock and a Bentheimer sandstone are performed to estimate the propagation velocity. Then reflections tests are done to check if reflections can be distinguished for different sources. The best source (type) is used in the next section to perform line array measurements.

11.2.1. Bentheimer sandstone

Using three different sources (300 kHz transducer, alternative transducer and a hammer), the reflection was measured on a bentheimer sandstone block of 20 cm thickness. The three different setups used are shown in Figure 11.2. A 300 kHz P-wave receiver was placed on top next to the source. Another receiver was placed at the bottom, which can be used to estimate the propagation velocity of the direct P-wave through the rock sample. The transducers were glued onto the surface to ensure good contact.

(a) (b) (c)

Figure 11.2: Setup of reflection test for 300 kHz transducers (a), alternative transducers (b) and hammer (c) on a Bentheimer sandstone.

The found propagation velocities for the three different sources can be seen in Table 11.1. The found velocities are in agreement with the velocities in the literature, see Table 10.2 in section 10.2.1. The offset between the source and receiver on top is approximately 2 cm for the transducers and 4 cm for the hammer, which gives a supposed two-way travel time as can be seen in Table 11.1. Important to note is the negative t_0 for the hammer as source in Table 11.1, which is theoretically impossible. The signal emission time consistently appears to be slightly negative using the aforementioned setup and is therefore also expected to be caused by the setup. Further analysis of the recorded arrivals is therefore limited for the hammer due to reliability issues during data acquisition.

Table 11.1: Transmission velocities for the direct P-wave and supposed arrival time of the reflection in Bentheimer sandstone

Bentheimer sandstone						
Source	t_0 (ms)	t_{1w} (ms)	L (m)	v_{seis} (m/s)	Δx_0 (m)	t_{2w} (ms)
300 kHz transducer	0.0000	0.0763	0.20	2620	0.02	0.1529
Alternative transducer	0.0000	0.0783	0.20	2553	0.02	0.1569
Hammer	-0.0080	0.0480	0.20	3571	0.04	0.1046

The received signals for the three setups is shown in Figure 11.3. The signal was first smoothed using double exponential smoothing to improve the estimation of the arrival times, and then the absolute wave envelope was plotted using the Hilbert transform function to possibly help with the visibility of the reflection.

It can be seen that a reflection is visible shortly after t_{2w} at roughly $t = 0.152$ ms in both Figure 11.3a and 11.3b, so both the velocity estimate and the expected arrival time of the reflection are properly estimated with time differences of 0.0009 and 0.0049 ms. Generally, the reflection for the 300 kHz transducer shows weaker signals compared to the alternative source, but the amplitude ratio between the direct arrival and the reflection is more favorable. However, this can not be concluded from the setup which uses the hammer as source. No reflection can be distinguished from the signal in Figure 11.3c as the wave period appears too long. Moreover, the expected arrival time may be compromised due to the aforementioned reliability issues. These remarks are further discussed in Chapter 12.

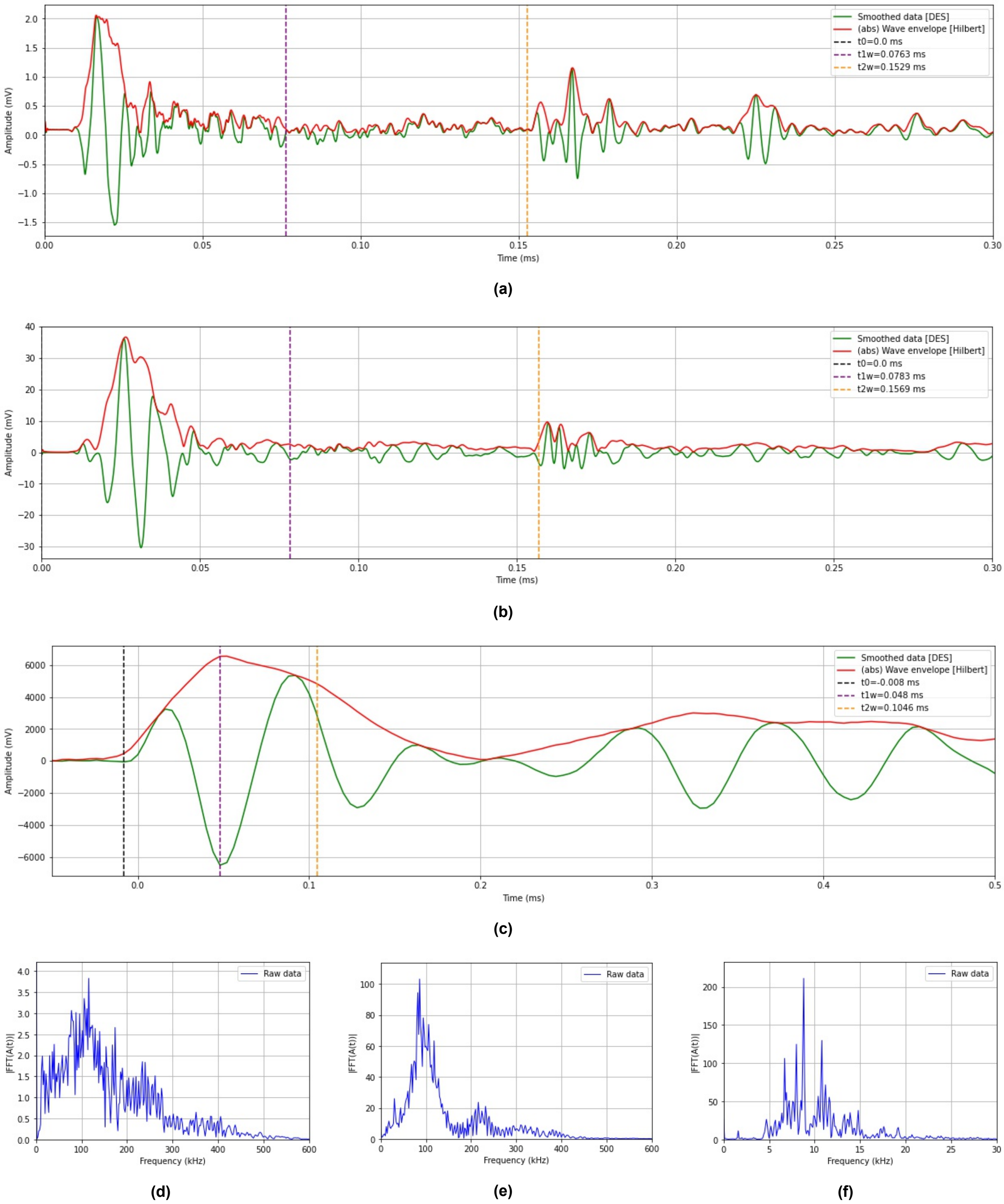

Figure 11.3: Recorded arrivals at top receiver for 300 kHz transducer (a), alternative transducers (b) and hammer (c) and frequency amplitude spectrum at bottom receiver for the same sources in (d,e,f). The expected reflection at time t_{2w} is shown as a vertical yellow line. The signal in green is smoothed using double exponential smoothing. The red signal is the absolute wave envelope, which was shown to possibly increase the visibility of the reflection. The blue signal is the raw data from the measurement.

11.2.2. Granitic rock

A similar reflection setup with the same hammer used in the previous section was done on a granitic rock, but for a larger distance of approximately 1.10 m, see Figure 11.4. This will ensure a sufficient separation of the direct arrival and the reflection. The hammer and a 100 kHz receiver transducer was placed at one side, and another 100 kHz receiver transducer at the other side. The sides were deemed roughly parallel, so a reflection arrival time can be estimated with the estimated propagation velocity. The receiver transducers were glued onto the surface to ensure good contact.


(a)

(b)

Figure 11.4: Setup of reflection test for hammer from top (a) and from 'bottom' receiver (b) on a granitic rock.

The found propagation velocity can be seen in Table 11.2. This velocity is in agreement with the velocities found in literature, see Table 10.2 in section 10.2.1. The offset between the source and receiver on top is approximately 4 cm, which gives a supposed two-way travel time as can be seen in Table 11.2. Again, a negative t_0 can be seen, which was mentioned in the previous subsection. Despite the limited reliability and therefore the uncertainty in the expected arrival time of the reflection, the recorded arrival is still analysed for possible reflections.

Table 11.2: Transmission velocities for the direct P-wave and supposed arrival time of the reflection in granitic rock

Granitic rock						
Source	t_0 (ms)	t_{1w} (ms)	L (m)	v_{seis} (m/s)	Δx_0 (m)	t_{2w} (ms)
Hammer	-0.0706	0.1320	1.10	5430	0.04	0.3346

The received signal is shown in Figure 11.5a. The signal was first smoothed using double exponential smoothing to improve the estimation of the arrival times, and then the absolute wave envelope was plotted using the Hilbert transform function to possibly help with the visibility of the reflection.

The separation between the direct wave arrival and the expected arrival time of the reflection is now sufficient, but no reflection can be seen in Figure 11.5a around the expected arrival time. The signal is surprisingly weak (very small amplitude) directly after the yellow line at $t = 0.36$ ms. The lack of reflection can therefore most likely be attributed to either the aforementioned reliability issues or to destructive interference. Around $t = 0.7$ ms, there appears to be a strong arrival, but it's origin is unknown.

Important is that a possible reflection might be visible around $t = 0.2$ ms, but it would have to be a reflection with another, unknown, origin. These remarks are further discussed in Chapter 12.

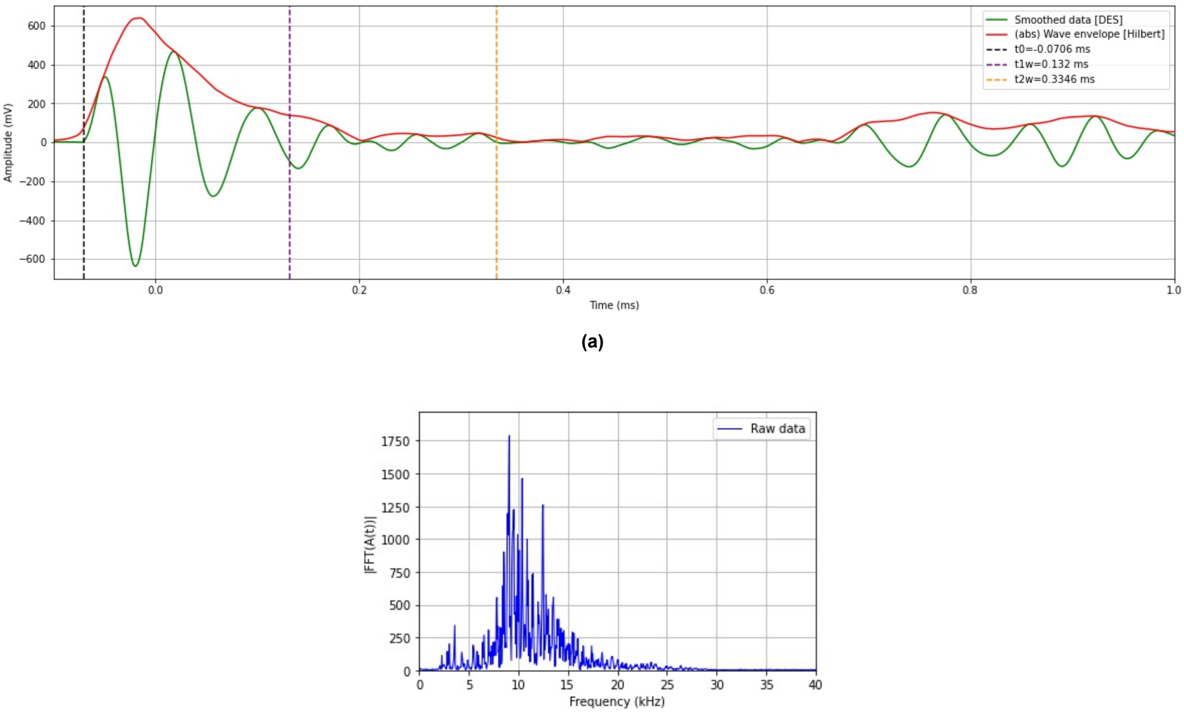

(a)

(b)

Figure 11.5: Recorded signal at 'top' receiver (a) and frequency amplitude spectrum at 'bottom' receiver (b) for hammer. The expected reflection at time t_{2w} is shown as a vertical yellow line. The signal in green is smoothed using double exponential smoothing. The red signal is the absolute wave envelope, which was shown to possibly increase the visibility of the reflection. The blue signal is the raw data from the measurement.

11.3. Line array measurements

The array measurement is performed on a basalt cylinder, see Figure 11.6, which appears very porous based on the surface. 100 kHz P-wave detecting transducers were used in combination with conductive gel in order to increase the coupling between transducer and rock.

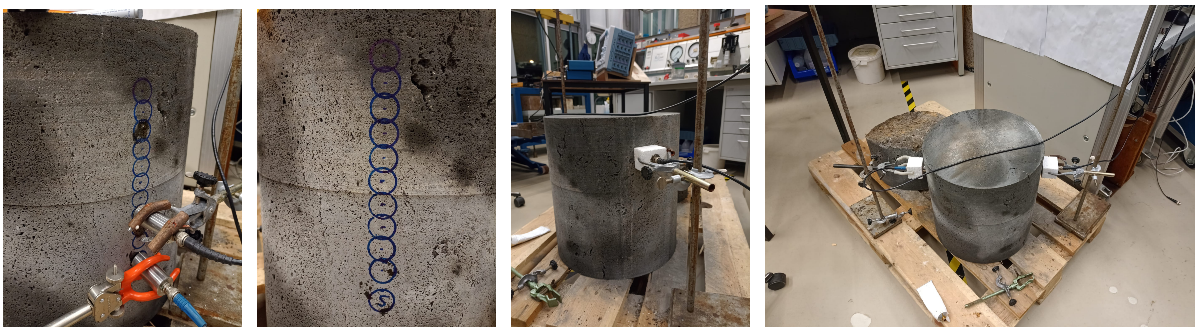

(a) (b) (c) (d)

Figure 11.6: Basalt cylinder used for array measurements, including array positions and measurement (a,b and c) and setup for transmission measurement (d). The cylinder top and bottom were cut some hours before and therefore some wet spots are still visible.

First, a transmission measurement was performed, see Figure 11.6d. The velocity that was estimated based on this measurement can be seen as measurement 3 in Table 11.3. The other two velocities were estimated a week before, which resulted in slightly lower velocities, but were determined with the same set of transducers. This may be attributed due to the wetting of the rock during sawing several hours before, which may have caused a slight, local, increase in saturation. An increase in saturation results in higher P-wave velocities, but the suspected infiltration is very low, so it likely doesn't explain the difference entirely. The deviations in velocity could also be attributed to locally varying porosity as could be seen at the surface of the rock with large deviations of visible porosity. The transmission test were not performed at the same locations, so it could explain the velocity differences. Furthermore, the measured velocities in basalt are lower than expected from literature, see Table 10.2 in section 10.2.1. As the basalt is very porous, velocities as small as 2000 m/s can be expected.

Table 11.3: Transmission velocities measured with 100 kHz transducers through a basalt cylinder with D=0.39 m.

P-wave velocities for D=0.39 m	
Measurement	v_p (m/s)
1	2588
2	2539
3	2843

Then, the array measurement was performed according to the setup in Figure 11.6a-11.6b and 11.7. The cylindrical shape is favorable as the emitted signal will reflect back to the source if the reflective surface is the exact opposite side. Reflections from other surfaces will not directly be received due to the circular cross-section. However, it is likely that the reflections from the side (rectangular cross-section) will be received first as the two-way travel distances are smaller than twice the diameter of the cylinder.

One receiver is moved along the array line with a spacing of 2 cm. Initially, ten receiver positions were used, but due to the dimensions of the source and receiver, the first position was not simultaneously possible for both source and receiver. The resulting array consists therefore of nine receiver positions, starting 5 cm from the source and ending 21 cm from the source. The interval step should be around a half wavelength using the centre frequency. An interval step of 2 cm was chosen for a frequency 100 kHz, which should be sufficient for a seismic velocity of $v_{seis} = 2 \cdot \frac{1}{2} \cdot \lambda \cdot f = 2 \cdot 0.02 \cdot 100 \cdot 10^3 = 4000 m/s$. This velocity is reasonable as can be seen in Table 10.2 in section 10.2.1.

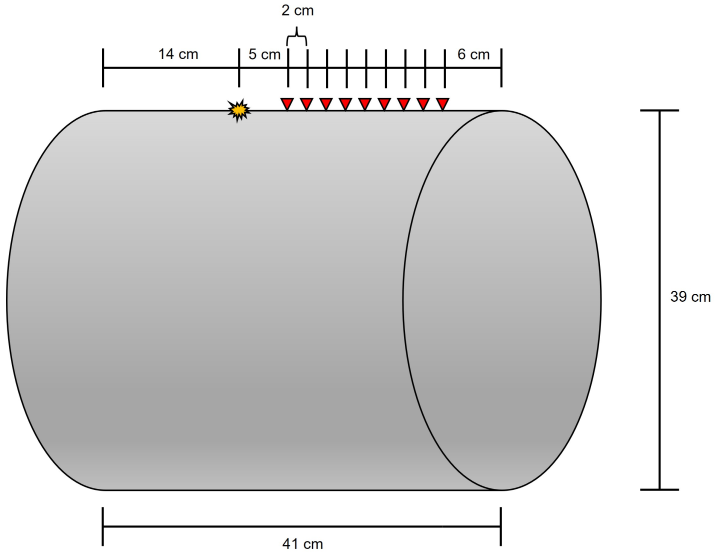

Figure 11.7: Schematic drawing of the basalt column and the set-up of the array of receivers.

The resulting nine traces are shown in Figure 11.8 as separate signals and as a contour plot. First, a squared time gain was applied, and secondly, a linear increasing factor along the array was applied. The former multiplies the amplitude of each signal with the squared time axis to enhance the signals for $t > t_0$, while the latter multiplies each signal with a linear increasing factor in order to enhance the signals for $x_{receiver} > x_{source}$.

The direct first arrival, shown in red in Figure 11.8a and 11.8b, is the emitted signal that travels directly to the receivers. It's direction is perpendicular to the direction of the receivers, so that would mean that a S-wave or converted P-wave is measured, which is supported by the rather low velocity. Assuming that this wave reflects from the side of the basalt rock, the red dotted line is expanded in Figure 11.8a and 11.8b in order to investigate if the line coincides with possible reflections.

The 95% confidence interval based on the six transmission velocities in Table 11.3 is also plotted in blue, which should confine the zone in which a reflection is expected. As the highest velocity was the only velocity estimated on the same day as the array measurement, the reflection would be expected at the top part of the confidence interval (green in Figure 11.8a and 11.8b).

Lastly, three interesting peaks are highlighted in purple, which may indicate the targeted reflection as they consistently appear for the receivers further away from the source. Other peaks are visible in Figure 11.8a and 11.8b, but are difficult to interpret. These remarks are further discussed in Chapter 12.

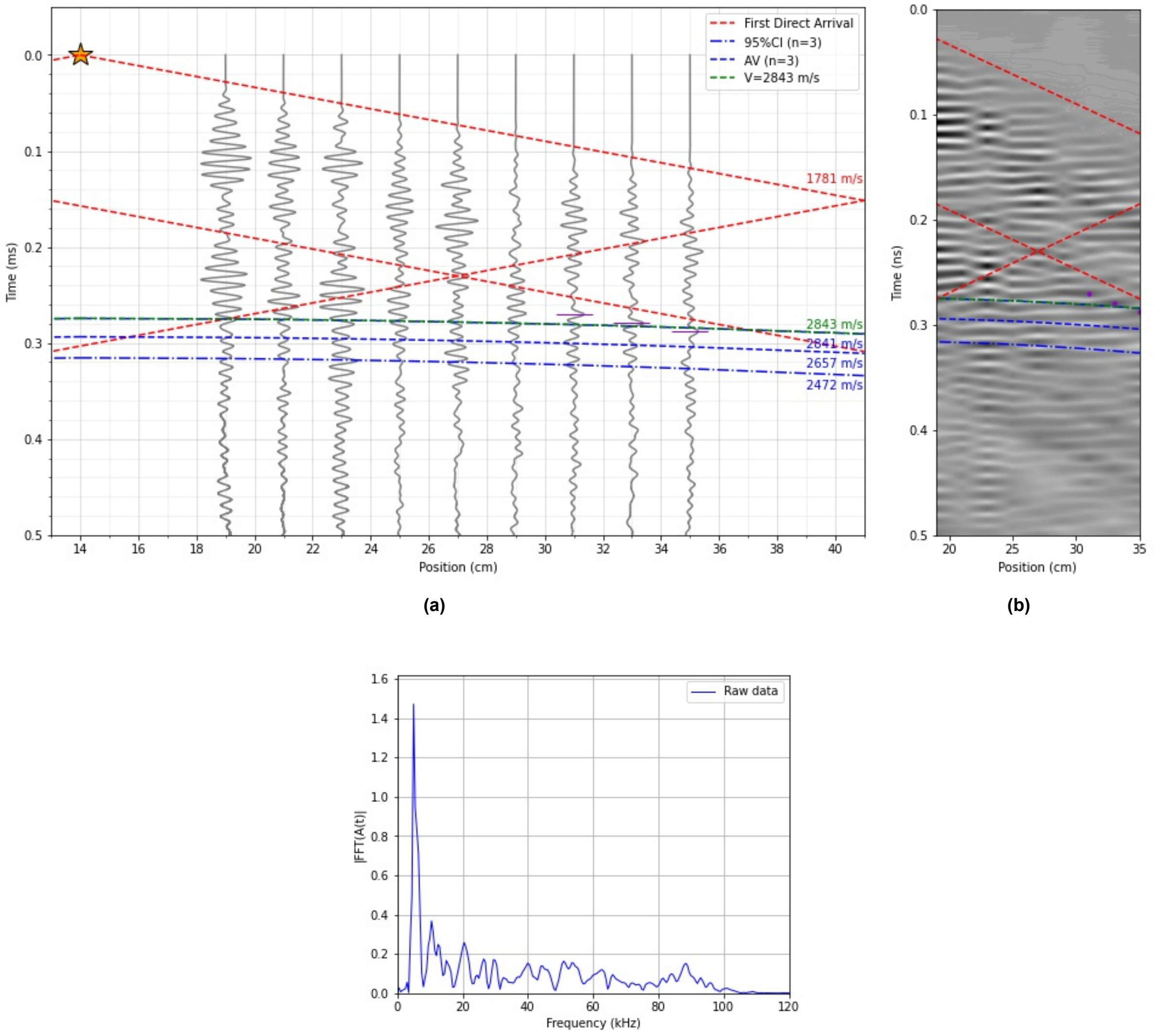

(a)

(b)

(c)

Figure 11.8: Results from array measurement shown in (a) as signals and in (b) as contour. The frequency amplitude spectrum for the transmission measurement is shown in (c). The red dotted line represents the linear fit through the first direct arrivals, reflected at the sides of the basalt column. The blue lines represent the expected reflections based on a set of transmission measurements with a 95% confidence interval. The green dotted line is the expected arrival reflection for the maximum estimated velocity from the transmission measurements. The orange star represents the source and the purple indicators represent interesting peaks.

11.4. Resolution

The radial or vertical resolution of the seismic measurements can be given by Eq. 2.1 in section 2.1.4. The frequency of the first arrival during the transmission test is used for the resolution as it most likely resembles the frequency of the reflected wave. The used propagation velocity is also the same as determined in the transmission test. The tests performed with the hammer as source are not considered due to reliability issues.

For the reflection tests on the sandstone and granite, the frequency ranges around 100 kHz for the transducer sources (Figure 11.3d and 11.3e). The propagation velocity through the sandstone was estimated to be 2620 and 2553 m/s for the 300kHz and alternative transducer, respectively (Table 11.1). For the line array measurement, a propagation velocity of roughly 2843 m/s was found (Table 11.3). While the peak frequency is around 5 kHz (Figure 11.8c), the suspected frequency of the recorded signal is expected to be around 20 kHz (local peak) if the signal length is considered in Figure 11.8a.

The vertical resolution of the seismic measurements in sandstone for the 300 kHz transducer and alternative transducer is then 0.66 and 0.64 cm, respectively. Finally, the resolution of the array measurement is 3.55 cm.

The resulting margin of errors for the reflection in the seismic measurements for the 300 kHz transducer and alternative transducer on sandstone is then $0.0066/2620 = 2.5 \cdot 10^{-6} = 0.0025$ ms and $0.0064/2553 = 2.5 \cdot 10^{-6} = 0.0025$ ms, respectively. For the array measurement, the margin of error for the reflection is then $0.0355/2843 = 1.2 \cdot 10^{-5} = 0.012$ ms.

12

Discussion Seismic

This chapter contains the discussion with regard to the seismic results from Chapter 11. First, the results from the reflection and transmission tests are discussed. Then, the results from the line array measurements are discussed. At the end, the applicability of the seismic reflection methods and the proposed approach in Chapter 10 is discussed, including the accuracy.

12.1. Reflection and transmission test results

The propagation velocities in sandstone is around 2600 m/s using transducers, which is in agreement with the literature (1900-4900 m/s in Table 10.2) although rather low. The velocities from the hammer are not discussed as the calculated velocity is compromised due to reliability issues.

It was determined that with the transducers, a clear reflection could be distinguished although the amplitude of the signal was rather small. Also, the difference between the expected arrival time and the actual arrival time for the 300 kHz and alternative transducer is roughly 0.0009 and 0.0049 ms, respectively. The theoretical margin of error to distinguish two reflection surfaces is approximately 0.0025 ms for both transducers, which means that the uncertainty for the transducers, at minimum, ranges between 0.5-2 times the theoretical margin of error.

For the hammer on sandstone, no reflection could be distinguished at the expected arrival time. However, the test is unreliable due to the slightly negative first arrival time (t_0=-0.0080 ms). The reason is not clear, but what can be concluded is that the wave period of the direct arrival at the top receiver was too large with respect to the reflection depth of 20 cm, which means that any reflections would be hidden within the direct arrival. In other words, the two-way travel path, and therefore two-way travel time, for the Bentheimer sandstone is too small compared to the wave period.

The best source seems to be either one of the transducers, but as the reflection depth has a limited length of 20 cm and the signals are already weak, doubts remain about the applicability of these sources. The hammer yielded very strong signals, but it is not applicable for these limited depths as the wave period of the direct arrival is too large. In other words: the frequency of the direct waves is too low, which means the reflection cannot be distinguished. It is shown with other sources that the reflection does appear at roughly 0.152 ms, so it should also exist with the hammer as source.

The test for the hammer on granite for a distance also didn't yield a reflection around the expected arrival time. It should again be noted that the test is unreliable due to the negative first arrival time (t_0=-0.0706 ms) for which the reason is not clear. It could be that the offset of 4 cm between hammer and receiver is too small, which causes interference from the hammer to the receiver. Consequently, the signal would be moved to the left (negative side of the graph). However, this wouldn't change the time of the expected arrival as it is based on $t_1 w - t_0$ and therefore would only move in an absolute manner, but not relative to t_0. Another explanation is destructive interference of the reflection with another signal, which might be indicated by locally surprisingly small amplitudes at $t = 0.36$ ms.

Also, possible wave arrivals are visible at 0.2 and 0.7 ms, for which the 0.2 ms arrival could indicate a reflection from a reflection surface that was not originally considered. Assuming a two-way travel path perfectly perpendicular to the reflective surface and the parameters in Table 11.2, a two-way travel time of 0.2706 ms gives a reflection depth of $\frac{1}{2} \cdot v_{seis} \cdot (t_{1w} - t_0) = \frac{1}{2} \cdot 5430 \cdot (0.2 - -0.0706) \cdot 10^{-3} = 0.73$ m. As the origin is unknown, there is no way of verifying the calculated reflection depth, so it remains purely theoretical.

The arrival at 0.7 ms is highly unlikely to represent a (direct) reflection as it has a high amplitude and arrived very late, which would mean a very low velocity. Furthermore, the propagation velocity should be twice as low as the two-way travel time is twice as high as for the expected reflection, but the distance of 1.10 m is the maximum direct distance within the granitic rock that could be measured.

It is shown that the hammer does not give the wanted reflection, but this is most likely caused by the time picking of the first arrival/direct wave. Also, the irregular shape of the granitic rock could explain the lack of a clear reflection as the origin of the reflection could be outside the considered area between transmitter and receiver. Consequently, no meaningful discussion about the applicability of the hammer can be given.

12.2. Line array measurement results

The propagating P-wave velocities that were measured through the basalt during the transmission test ranged between 2500-2900 m/s. According to the literature, the expected range should be 3500-6000 m/s, see Table 10.2. The S-wave or converted P-wave velocity was found to be 1781 m/s, which is again larger than the velocities from the literature. The most likely explanation for the low velocities is the porosity as explained in section 10.2.1. The basalt rock surface appeared very porous, which means that a lot of air is present in the rock. This can then give propagation velocities as low as 2000 m/s, which coincides more with the estimated velocities. Furthermore, the surface of the (cut) basalt was porous which made good contact between the transducers and the rock difficult.

Another possibility is that the wave with a velocity of 1781 m/s is a Lamb wave. Knowing the peak frequency in the frequency amplitude spectrum of 5 kHz (Figure 11.8c), the wavelength $\lambda = v/f = 1781/5000 = 0.36 = 36$ cm. The total height of the basalt cylinder is 41 cm, while its diameter is 39 cm. Lamb waves are similar to surface waves, but can only be generated in materials of only a few wavelengths thick, which causes not only oscillations of the surface, but of the entire material. As the diameter of the basalt cylinder is only slightly longer than the estimated wavelength, the direct wave could be a Lamb wave. The direct arrivals in the reflection tests on sandstone and granite could, for the same reason, also be a Lamb wave. This explains the large wave periods which hide the reflections for relatively small two-way travel paths. Therefore, a frequency spectrum analysis should be performed to filter out the lower frequencies (f < 5 kHz). A simple high-pass filter has been applied on the third receiver from the right (at 31 cm in Figure 11.8a) to possibly improve the visibility of the suspected reflection, see the peak indicated by the pink arrows in Figure 12.1. Unfortunately, no clear improvement can be seen for the unprocessed signal. This was also done for the other receivers and even after processing (squared time gain and linear increasing factor along with the array), no improvements were visible. More advanced filtering is recommended to decrease the interference of the direct (either surface of Lamb) wave.

The peaks indicated in purple in Figure 11.8a and 11.8b could be interpreted as the expected reflection as they approximately appear on the plotted green line for the maximum velocity of 2843 m/s. The calculated margin of error for the radial resolution of 3.55 cm is 0.012 ms and the peaks fall roughly within this margin. The largest time difference between the peak at third to last receiver and the expected reflection arrival is only 0.007 ms, which would give an accuracy of $0.007 * 10^{-3} * 2843 = 0.019 = 1.9$ cm (important to remark that the peak of a signal is not the used definition of arrival time, and the obtained 'accuracy' can not be compared to the resolution). However, the peaks appear to follow a steeper line, which would only be possible for a higher velocity, but the wave would then come from a different origin than the source.

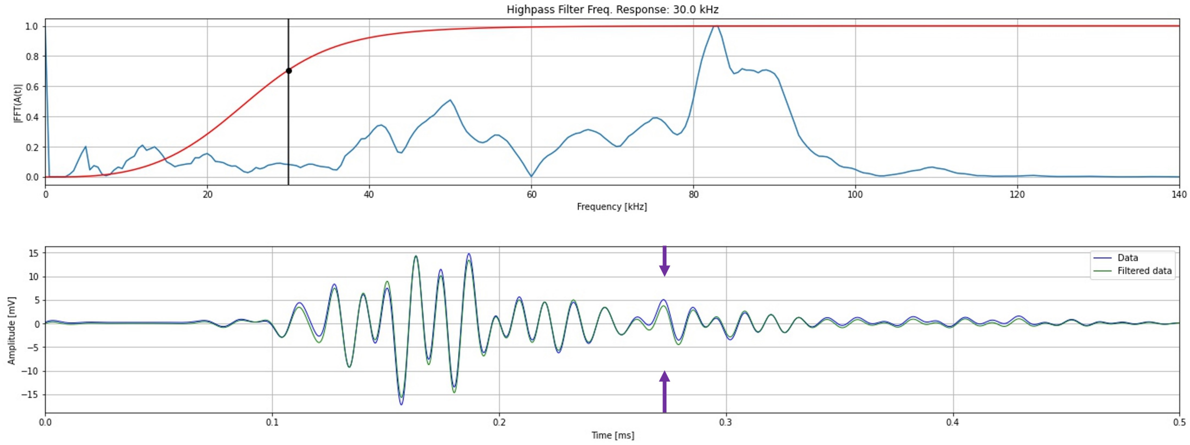

Figure 12.1: Frequency amplitude spectrum (top) and recorded and filtered signal for the third receiver from the right (bottom). A high-pass butterworth filter of 30 kHz was applied on the unprocessed signal from receiver 8 (third from the right). The purple arrows indicate the purple peak visible in the array measurements.

Therefore, the aforementioned peaks might be part of the reflected first direct arrival wave from the left side. This is reinforced by the fact that the peaks appear parallel to the expanded reflection from the left side in red in Figure 11.8a and 11.8b. Furthermore, the margin of error is greater than the time difference between the purple peaks and the red line.

The supposed reflection from the left side is much more clear in Figure 11.8b than the supposed reflection from the right side, which is hardly visible. This is in agreement with the expected attenuation being smaller due to shorter travel distances from the left side than the right side. The distance to the first receiver from the left side (14+14+5=33 cm) is shorter than from the right side (5+8*2+6+8*2=43 cm), see Figure 11.7 for the dimensions. The travel distance to the receiver closest to the right side after reflection (5+8*2+6+6=33 cm) is the same as the travel distance for a reflection from the left side. However, the stark difference in signal strength for the supposed reflection at the left and right side despite equal travel path lengths (Figure 11.8b is then contrary to what was assumed. Attenuation is expected to be large (reflection from the bottom is not clear), so it is still uncertain what causes the strong amplitudes at mainly the left side of the diagram in Figure 11.8b. One reason might be the linear factor that was applied along with the array, which interferes or even causes this trend.

In short: the purple peaks may indicate the targeted reflection for a velocity of 2842 m/s as the calculated margin of error is greater than the time difference between the peaks and the expected arrival time of the reflection.

One important remark is the spacing between the array receivers, which should be around half a wavelength of the used frequency. However, with the known maximum velocity of 2843 m/s, the spacing should be around $\frac{1}{2} \cdot \lambda = v_{seis}/(2 \cdot f) = 2843/(2 \cdot 100 \cdot 10^3) = 0.014 = 1.4$ cm. This means that the spacing ideally should have been chosen smaller to be able to interpret the results better. Also, the basalt rock shape was favorable, but the state (porosity) was less favorable, which makes interpreting the velocities and reflections more difficult. The difference between the 100 kHz input frequency and the received 20 kHz frequency after the transmission is large and most likely due to attenuation. This means that the wave already loses much of its energy before reflection, which could also be seen for the decreasing amplitude of the direct arrival travelling perpendicular to the receivers.

12.3. Applicability

First, the accuracy of the reflection measurements is determined based on the resolution and the obtained results. Then, the implications of the results for the broader project are given. Finally, a discussion regarding the applicability of the seismic reflection methods and the proposed approach to estimate the reflection depth is given.

12.3.1. Accuracy

The radial or vertical resolution of the transducers on sandstone was calculated to be around 0.7 cm and the line array measurement yielded a calculated resolution of 3.6 cm (keeping in mind that frequencies f<20 kHz are not considered). The decrease in resolution for the transducers in the line array measurement with respect to the sandstone is mostly explained by the high porosity of the basalt. This resulted in a low frequency of the propagating P-wave.

For the transducers in the reflection test, the resolution is in the same order as the found accuracy of the reflection as the expected arrival time of the reflection occurred within the margin of error based on the calculated resolution. The tests using the hammer are considered unreliable and therefore no meaningful discussion into the resolution or accuracy can be given.

Although the obtained accuracy for the reflections test was largely similar to the calculated resolution, some (general) remarks can be made that either influence the accuracy directly or prevent the reflection from being visible. The frequency of the emitted signal by the source is very important as:

- High frequencies attenuate too fast which decreases the visibility of reflections,
- Low frequencies give large wave periods of the direct wave which hide reflections,
- Low frequencies give larger radial resolutions.

Also, the results depend strongly on the rock used in the tests as:

- The shape influences interpretation of reflections,
- The size influences strength and visibility of reflections,
- The state (e.g. porosity) heavily influences the interpretation and visibility of the supposed reflections,
- The type influences the recommended frequency and accuracy through the propagation velocity.

12.3.2. Project

The results using seismic sources and receivers indicate that using transducers (transmitter and receiver) offers high accuracy measurements under the condition that the tests are performed on rocks with simple geometries. It ensures that a detected reflection can be linked to a rock face, which can be used to accurately assess the reflection depth. The geometry of the bearing stones of D14 is much more complex and the buried rock faces are not known, which makes interpreting the results much harder.

For the project, the seismic sources and receivers can therefore give a high accuracy, but they should first be used in the field to evaluate the effects of weathered rock requiring larger penetration depths than tested on the rocks in this thesis. The array measurements didn’t yield strong reflections yet, but a survey similar to the Common Offset Survey for the GPR could be considered. Then, the buried rock faces can be estimated following the proposed approach for the GPR.

12.3.3. Seismic application

As mentioned in the previous section more complex geometries should be evaluated using transducers before field measurements can be taken. The achieved accuracy of the transducers (order of 1 cm) is promising and future research should therefore first apply the transducers on rocks with increasingly more complex geometries depending on the results.

Furthermore, low-cut frequency filtering is recommended to increase the visibility of the reflections due to a) hiding of shallow reflections in the direct waves with relatively low frequencies or b) general interference of suspected surface or lamb waves due to their very low frequencies. Simple high-pass filters did not increase the visibility in this thesis, but more extensive research might yield better results.

Moreover, the offset between source and receiver is not trivial and should not be too small as interference of the source with receivers is can occur, although this was only considered a problem for a hammer which gave unreliable results.

13

Conclusion

This Chapter contains the conclusion in which the research questions are answered. First, the subquestions are answered using the proposed analysis approach for both non-destructive geophysical methods, namely the GPR and seismic techniques. The subquestions are mainly answered using Chapter 9 and 12, which contains the discussion of the results. The answers to the subquestions will help in answering the main research question. Finally, recommendations for further research are made.

Which geophysical methods are suitable for finding the buried rock contour of the bearing stones?
We chose two suitable geophysical methods to investigate the burial depth of the bearing stones of D14. First, we considered the Ground Penetrating Radar (GPR) as it is often used to investigate the near subsurface and to study, for example, bedrock, water tables, the preservation state of ancient monuments and to find utilities such as pipelines. We specifically chose one acquisition technique, the Common Offset Survey, which can map reflections from the subsurface, and therefore from rocks, in 2D. Secondly, we considered seismic methods as they are used to assess thickness and depths of weathering layers, state of cracking and fractures. We especially deemed the reflection acquisition geometry and processing useful.

How can geophysical methods be applied in order to find the buried rock contour of rocks with complex topography?
We proposed two analysis approaches to I) estimate the buried rock contour using the GPR (left) and to II) estimate the reflection depths using seismic sources and receivers (right).

Proposed approach GPR	Proposed approach seismics
1. Acquisition of GPR data	1. Acquisition of seismic data
2. Processing of GPR data	2. Calculation of seismic wave velocity
3. Identification of reflection surfaces	3. Calculation of reflection depth
4. Acquisition of exposed rock contour	
5. Calculation of rock surfaces	
6. Estimation of buried rock contour	
7. Modelling of GPR data	

In step 1, we applied the GPR in a Common Offset Survey on the keystone SI2. We also did transmission tests to estimate the propagation velocity through the rock. We processed the resulting radargrams in step 2 to increase the visibility of the reflections. We then identified reflection surfaces in step 3. We determined the exposed rock surface from 3D models of the keystone estimated by others in step 4. Then, we created the conceptual GPR point model to a) simplify the Common Offset Survey over a partially buried rock and to b) better interpret the results from this survey. We developed two mathematical models based on this conceptual model, which were used in steps 5, 6 and 7. We used the GPR point-to-GEO model in step 5 to calculate the (buried) rock surfaces from reflection surfaces identified in the

GPR radargrams. We used the GEO-to-GPR point model in step 7 to model GPR data based on an assumed buried rock contour determined in step 6. The last two steps are part of an iterative process in which the buried rock contour is continuously updated based on the fit of the modelled reflections with the acquired GPR data from the field until a satisfactory fit has been achieved. We also surveyed a non-buried boulder at the TU Delft campus similar to the keystone to a) evaluate the accuracy of the calculated rock surfaces and to b) optimise the survey on the keystone.

For the seismics in step 1, we performed simple seismic reflection measurements on various rock samples with different sources (hammers and seismic transducers) to detect reflections. Moreover, we performed a reflection test including an array of receivers on a cylindrical rock to improve the detection of reflections. We carried out transmission tests to estimate the seismic velocities in step 2. We calculated the expected arrival times of the reflection in step 3 based on the found velocities and compared them to the recorded signals. We mainly used the measurements to optimise the techniques, incl. the best type of seismic source, which could potentially be used in the field.

How can historic photographs assist in proving the buried rock contour derived from geophysical data?
The data from the Common Offset Survey appeared to lack information on the buried rock contour at so-called blind spots. This possibly resulted in wrongful interpretations of the buried rock contour. However, we used historic photographs from early excavations to gain insight into the blind spots. Therefore, more accurate predictions can be done concerning the burial depth and the buried rock contour using historic data. Moreover, the models used to derive rock contours from GPR data can be partially validated using historical photographs.

What is the accuracy of the found buried rock contour?
We estimated the accuracy of the buried rock contour coordinates resulting from the GPR point-to-GEO model to be 5-10 cm based on the fit between the exposed (and therefore known) rock contour and the calculated rock surfaces. The calculated rock surfaces appear as a ’point cloud’ of coordinates and are used in estimating the buried rock contour with help from the GEO-to-GPR point model. Consequently, a coherent buried rock contour needs to be formed from a partly incoherent set of buried rock surface coordinates. This requires shortcuts and decreases the accuracy of the estimated final (coherent) buried rock contour. At areas with many rock surface coordinates, the accuracy of the estimated buried rock contour can be assumed to be similar to the accuracy of the calculated rock surfaces (5-10 cm). However, this accuracy is most likely not achieved at the previously mentioned blind spots, which experience a lack of data. Therefore, the overall buried rock contour should be treated with caution at the blind spots.

We estimated the accuracy of the seismic reflection measurements with the 300 kHz transducers to be in the order of 1 cm. The other source we considered- a hammer- gave unreliable results, so it was not evaluated for its accuracy. The recommended transducers are accurate, but only for rocks with simple geometries of limited size, so the applicability of these transducers on more complex geometries such as the keystone for reflection depths larger than ±0.5 m remains a question.

What is the integrity of the bearing stones?
We investigated two rocks: the TU Delft boulder and the keystone SI2 of D14. From both analyses, we could distinguish reflections close to the top surface of the exposed rock. For the TU Delft boulder, the cause could not be determined as the boulder itself appears to be unharmed. However, the keystone was fractured in 1957 and subsequently repaired in 1959 and 1996. The location of this fracture coincides with the location of the aforementioned reflection close to the top surface of the keystone. It can thus be concluded that fractures can be detected with the GPR, which could explain the unidentified reflection at the top of the TU Delft boulder. Furthermore, some reflections occur near ground level in the center and at the side of the keystone. It is unlikely that they all indicate fractures as they appear in a small localised area. It could be explained by reflections from other bearing stones or boulders nearby.

In short: based on the GPR data, the keystone appears to have been fractured, which is confirmed by a previously repaired crack at the same location.

13.1. Main research question

What is the buried rock contour of the bearing stones of megalith D14 estimated using non-destructive geophysical methods?

The keystone Sl2 was one of the three bearing stones of capstone D9 before the position of Sl2 was altered around 1965. Then, Sl2 was tilted and partly re-buried so that one of its faces-its top face- laid horizontal. As a result, Sl2 no longer fulfilled its function as keystone. Moreover, it was no longer in direct contact with capstone D9. In 2019, capstone D9 fell off, which resulted in a free laying keystone. Therefore, the keystone can be surveyed using a GPR. We proposed an approach to estimate the buried rock contour using two developed mathematical models. We based these mathematical models on a conceptual model of a simplified GPR with antennas of zero dimension.

First, we calculated (buried) rock surface coordinates with an accuracy of 5-10 cm. Then, we estimated the buried rock contour on this partly incoherent set of coordinates. However, we encountered blind spots in the data, which caused difficulties in interpreting some buried rock surfaces. Therefore, the resulting coherent buried rock contour is expected to have a worse accuracy than the 5-10 cm given by the rock surface coordinates.

The bottom of the keystone is sloping downward starting at ground level at the northern side and ending at an estimated maximum burial depth of 80 cm at the southern side. The southern face itself is most likely steep and almost vertical. This is suggested by the lack of reflections in the data, which indicates a steep slope as no reflections could be received by the GPR. We estimated similar steep, vertical, rock faces for the eastern and western sides. While historic photos from an excavation between 1925-1927 seem to confirm a steep, almost vertical, rock face at the western side, the GPR data appears to indicate a slightly inward sloping rock face. This disagreement in different data leads back to the previously mentioned blind spots in the GPR data, which means that locally the exact shape of the contour should be treated with caution.

13.2. Recommendations

The GPR appears suitable for estimating the buried rock contour of the bearing stones of D14, but uncertainties regarding the executed surveys and therefore the results exist. Also, the seismic transducers were successful in detecting reflections, but only for a specific set of conditions. Consequently, various recommendations can be made regarding 1) acquiring accurate data, 2) improving data interpretation and 3) doing future research.

GPR

For the GPR, the following recommendations for acquiring accurate GPR data can be made:

- Acquire GPR data carefully. Attention should be paid to the GPR survey path in particular, which is measured with an odometer during a Common Offset Survey. Slip of the wheel or not starting exactly at a pre-defined point will cause steeper reflection surfaces or shifts of reflection surfaces, which influences the location of the calculated rock surface coordinates.
- Perform GPR surveys at the center of the rock to limit the interference of rock faces nearby with reflections from the buried rock bottom.
- Use a smaller and higher frequency GPR to survey the rocks. The rock surface can then be followed more accurately, which means better results compared to the 1000 MHz GPR data that have been acquired so far. Moreover, the higher frequency (up to 2.6 GHz) would provide a higher resolution. The penetration depth of the signals should still be large enough to capture the complete buried rock contour.

Then, recommendations to improve the interpretation of the GPR data can be made:

- Consult historic data, if existent, regarding presently buried rocks to gain information on possible blind spots in acquired GPR data, which exist mainly for steep rock faces for which no reflection can be received by the GPR.
- Identify reflections carefully as the interpretation of clear reflections is subjective. Strong reflections in the GPR radargram may not always be easily explained by a rock contour. This is also true regarding the polarity of the reflection which could indicate the type of boundary.

- Consider the three-dimensional nature of the origin of the reflections. While 3D effects are ignored in the current analysis, they should not be forgotten as they could explain unexplained reflections in the GPR radargram.
- Digitize reflection identification in GPR data. Instead of manually determining the reflection coordinates, (semi-)automating this process would make it faster and likely more accurate due to less human interference.
- Take the stiffness and size of the GPR into account when determining the GPR survey path. A 'smoothed' 3D model could offer more realistic results regarding the true travel path of the GPR than the true exposed rock contour that is used in the current approach.
- Preferably perform surveys on a (buried) hard rock in saturated conditions as the granite-saturated sand boundary is beneficial in identifying relevant reflection surfaces. The saturated boundary causes a reverse in polarity and a relatively strong reflection.

Finally, a more general recommendation for future research regarding the GPR can be made:

- Perform surveys on rocks with simple geometries to improve the assessment of the proposed approach. Many uncertainties exist due to the complex geometries of the surveyed rocks and the relatively large size of the 1000 MHz GPR.

Seismics

For the seismic methods, the following recommendations for acquiring accurate seismic data can be made:

- Use higher energy transducers to increase the strength of the recorded signals. Recorded signal frequencies of 80-100 kHz (not to be confused with the input signal frequency) should then improve the visibility of reflections.
- Ensure good contact between the transducers and rock surface. Stronger signals will then be emitted and recorded by the transducers.

Then, a recommendation to improve the interpretation of the seismic data can be made:

- Filter the recorded signals with low-cut frequency filters to prevent lower frequencies from interfering with the targeted reflections.

Finally, more general recommendations for future research regarding seismics can be made:

- Perform measurement on rocks with increasingly more complex geometries. Before applying the proposed approach and transducers in the field, the accuracy and applicability of the transducers should be evaluated on more complex geometries.
- Perform a Common Offset Survey with seismic transducers following the proposed approach of the GPR to estimate the buried rock contour. The results can be used to evaluate the accuracy of both methods.

References

Al-Harthi, A., Al-Amri, R., & Shehata, W. (1999). The porosity and engineering properties of vesicular basalt in saudi arabia. *Engineering Geology*, *54*(3), 313–320. https://doi.org/https://doi.org/10.1016/S0013-7952(99)00050-2

Bakker, J. A. (2010). *Megalithic research in the netherlands, 1547-1911 : 'from giant's beds' and 'pillars of hercules' to accurate investigations*. Sidestone Press.

Bekkema, M., Huisman, H., Van Balen, R., & Kluiving, S. (2014). Gidsgesteenten in hunebedden. *Grondboor en Hamer*, 93–99.

Benson, A. (1995). Applications of ground penetrating radar in assessing some geological hazards: Examples of groundwater contamination, faults, cavities. *Journal of Applied Geophysics*, *33*, 177–193. https://doi.org/10.1016/0926-9851(95)90040-3

Billings, S., & Kingdon, K. (2021). Uxo characterization: Comparing cued surveying to standard detection and discrimination approaches report 2 of 9 ground penetrating radar for unexploded ordnance characterization; fundamentals.

Capizzi, P., Cosentino, P., & Schiavone, S. (2013). Some tests of 3d ultrasonic traveltime tomography on the eleonora d'aragona statue (f. laurana, 1468). *Journal of Applied Geophysics*, *91*, 14–20. https://doi.org/10.1016/j.jappgeo.2013.01.012

Cardarelli, E., & Nardis, R. (2001). Seismic refraction, isotropic anisotropic seismic tomography on an ancient monument (antonino and faustina temple ad 141). *Geophysical Prospecting*, *49*, 228–240. https://doi.org/10.1046/j.1365-2478.2001.00251.x

Conyers, L., & Leckebusch, J. (2010). Geophysical archaeology research agendas for the future: Some ground□penetrating radar examples. *Archaeological Prospection*, *17*, 117–123. https://doi.org/10.1002/arp.379

Cosentino, P., Capizzi, P., Fiandaca, G., Martorana, R., & Messina, P. (2009). Advances in microgeophysics for engineering and cultural heritage. *Journal of Earth Science*, *20*, 626–639. https://doi.org/10.1007/s12583-009-0052-x

Dallimore, S., & Davis, J. (1987). Ground probing radar investigations of massive ground ice and near surface geology in continuous permafrost. *Current Research, Part A. Geological Survey of Canada, Paper*, 913–918.

Davis, J. L., & Annan, A. P. (1989). Ground-penetrating radar for high-resolution mapping of soil and rock stratigraphy1. *Geophysical Prospecting*, *37*(5), 531–551. https://doi.org/https://doi.org/10.1111/j.1365-2478.1989.tb02221.x

Dondurur, D. (2018). Chapter 9 - velocity analysis. In D. Dondurur (Ed.), *Acquisition and processing of marine seismic data* (pp. 421–457). Elsevier. https://doi.org/https://doi.org/10.1016/B978-0-12-811490-2.00009-8

Fort, R., Alvarez de Buergo, M., & Pérez-Monserrat, E. (2013). Non-destructive testing for the assessment of granite decay in heritage structures compared to quarry stone. *International Journal of Rock Mechanics and Mining Sciences*, *61*, 296–305. https://doi.org/10.1016/j.ijrmms.2012.12.048

Hardage, B. A. (1996). Combining p-wave and s-wave seismic data to improve prospect evaluation. (237), 47. https://doi.org/https://doi.org/10.23867/RI0237D

Kahraman, S. (2002). Estimating the direct p-wave velocity value of intact rock from indirect laboratory measurements. *International Journal of Rock Mechanics and Mining Sciences - INT J ROCK MECH MINING SCI*, *39*, 101–104. https://doi.org/10.1016/S1365-1609(02)00005-9

Longoni, L., Arosio, D., Scaioni, M., Papini, M., Zanzi, L., Roncella, R., & Brambilla, D. (2012). Surface and subsurface non-invasive investigations to improve the characterization of a fractured rock mass. *Journal of Geophysics and Engineering - J GEOPHYS ENG*, *9*, 461–472. https://doi.org/10.1088/1742-2132/9/5/461

Lualdi, M., & Zanzi, L. (2004). 2d and 3d experiments to explore the potential benefit of gpr investigations in planning the mining activity of a limestone quarry. *Proceedings of the Tenth International Conference Ground Penetrating Radar, GPR 2004*, *2*, 613–616. https://doi.org/10.1109/ICGPR.2004.179818

Ma, X., Kirichek, A., Shakeel, A., Heller, K., & Draganov, D. (2021). Laboratory seismic measurements for layer-specific description of fluid mud and for linking seismic velocities to rheological properties. *The Journal of the Acoustical Society of America*, *149*, 3862. https://doi.org/10.1121/10.0005039

Martinho, E., & Dionísio, A. (2014). Main geophysical techniques used for non-destructive evaluation in cultural built heritage: A review. *Journal of Geophysics and Engineering*, *11*, 053001. https://doi.org/10.1088/1742-2132/11/5/053001

Masini, N., Persico, R., & Rizzo, E. (2010). Some examples of gpr prospecting for monitoring of monumental heritage. *Journal of Geophysics and Engineering*, *7*, 190. https://doi.org/10.1088/1742-2132/7/2/S05

Mohamed Sutan, N., & Meganathan, M. (2003). A comparison between direct and indirect method of ultrasonic pulse velocity in detecting concrete defects. *Journal of Nondestructive Testing*, *8*, 1–9.

Nobes, D. C., & Deng, J. (2019). Ground penetrating radar resolution in archaeological geophysics. In G. El-Qady & M. Metwaly (Eds.), *Archaeogeophysics: State of the art and case studies* (pp. 183–204). Springer International Publishing. https://doi.org/10.1007/978-3-319-78861-6_9

Oldenburg, D., Jones, F., Heagy, L., Cockett, R., Astic, T., Devriese, S., & Kang, S. (2017a). *Basic principles*. Retrieved December 6, 2021, from https://gpg.geosci.xyz/content/GPR/GPR_fundamental_principles.html

Oldenburg, D., Jones, F., Heagy, L., Cockett, R., Astic, T., Devriese, S., & Kang, S. (2017b). *Ground penetrating radar: Survey and data*. Retrieved February 27, 2021, from https://gpg.geosci.xyz/content/GPR/GPR_survey_data.html

Oldenburg, D., Jones, F., Heagy, L., Cockett, R., Astic, T., Devriese, S., & Kang, S. (2017c). *Seismic velocities of rocks and various materials*. Retrieved March 22, 2021, from https://gpg.geosci.xyz/content/physical_properties/tables/seismic_velocity.html

Perez-Gracia, V., Gonzalez-Drigo, J., & Di Capua, D. (2008). Horizontal resolution in a non-destructive shallow gpr survey: An experimental evaluation. *NDT and E international*, *41*, 611–620. https://doi.org/10.1016/j.ndteint.2008.06.002

Petrowiki. (2015, June 3). *Seismic wave propagation*. Retrieved February 27, 2021, from https://petrowiki.spe.org/Seismic_wave_propagation

Rial, F. I., Pereira, M., Lorenzo, H., Arias, P., & Novo, A. (2009). Resolution of gpr bowtie antennas: An experimental approach [Advanced Applications, Systems and Modelling for GPR]. *Journal of Applied Geophysics*, *67*(4), 367–373. https://doi.org/https://doi.org/10.1016/j.jappgeo.2008.05.003

Rijksdienst voor Cultureel Erfgoed. (2020). *Monumentnummer: 45029 te eext*. Retrieved February 25, 2021, from https://monumentenregister.cultureelerfgoed.nl/monumenten/45029

Sawangsuriya, A. (2012). Wave propagation methods for determining stiffness of geomaterials. In P. Giovine (Ed.), *Wave processes in classical and new solids*. IntechOpen. https://doi.org/10.5772/48562

Semik Group P.C. (2021). *Gpr applications*. Retrieved December 6, 2021, from https://www.gpr-georadar.com/home/gpr-applications.html

Slob, E., Sato, M., & Olhoeft, G. (2010). Surface and borehole ground-penetrating-radar developments. *Geophysics*, *75*, 75A103–75A120. https://doi.org/10.1190/1.3480619

Stanchits, S., Vinciguerra, S., & Dresen, G. (2006). Ultrasonic Velocities, Acoustic Emission Characteristics and Crack Damage of Basalt and Granite. *Pure and Applied Geophysics*, *163*(5-6), 975–994. https://doi.org/10.1007/s00024-006-0059-5

Stevens, K., Lodha, G., Holloway, A., & Soonawala, N. (1995). The application of ground penetrating radar for mapping fractures in plutonic rocks within the whiteshell research area, pinawa, manitoba, canada. *Journal of Applied Geophysics*, *33*, 125–141. https://doi.org/10.1016/0926-9851(95)90036-5

Ten Anscher, T. (2019). *Hunebed d14-eexterhalte. een aanzet voor een hunebedbiografie met speciale aandacht voor deksteen d9* (tech. rep. RAAP-rapport 4112). RAAP Archeologisch Adviesbureau B.V. Weesp.

Theuws, E. (2021). *Analyzing reconstruction scenarios for dolmen d14 using non-destructive, digital methods* (Doctoral dissertation). http://resolver.tudelft.nl/uuid:78949524-5373-46e2-b46e-780c8e308aea

Timmer, R. (2019, April 25). *Deksteen valt van hunebed d14/eexterhalte; oorzaak onduidelijk*. Retrieved February 25, 2021, from https://www.dvhn.nl/drenthe/Deksteen-valt-van-hunebed-D14Eexterhalte-oorzaak-onduidelijk-24396313.html

Topczewski, L., Fernandes, F., Cruz, P., & Lourenco, P. (2007). Practical implications of gpr investigation using 3d data reconstruction and transmission tomography. *Journal of Building Appraisal*, *3*, 59–76. https://doi.org/10.1057/palgrave.jba.2950060

Tzanis, A. (2010). Matgpr release 2: A freeware matlab® package for the analysis & interpretation of common and single offset gpr data. *FastTimes*, *15*, 17–43.

Vasconcelos, G., Lourenco, P., Alves, C., & Pamplona, J. (2008). Ultrasonic evaluation of the physical and mechanical properties of granites. *Ultrasonics*, *48*, 453–66. https://doi.org/10.1016/j.ultras.2008.03.008

Wanniarachchi, A., P.G, R., Perera, S., Rathnaweera, T., Lyu, Q., & Mahanta, B. (2017). Assessment of dynamic material properties of intact rocks using seismic wave attenuation: An experimental study. *Royal Society Open Science*, *4*, 170896. https://doi.org/10.1098/rsos.170896

Wendrich, A., Trela, C., Krause, M., Maierhofer, C., Effner, U., & Wöstmann, J. (2006). Location of voids in masonry structures by using radar and ultrasonic traveltime tomography. *Proceedings of the 9th European Conference on NDT, september 25-29*.

Yelf, R. (2004). Where is true time zero ? *Electromagnetic Phenomena*, *7*, 279–282. https://doi.org/10.1109/ICGPR.2004.179979

A

Processed GPR diagrams rock TU Delft

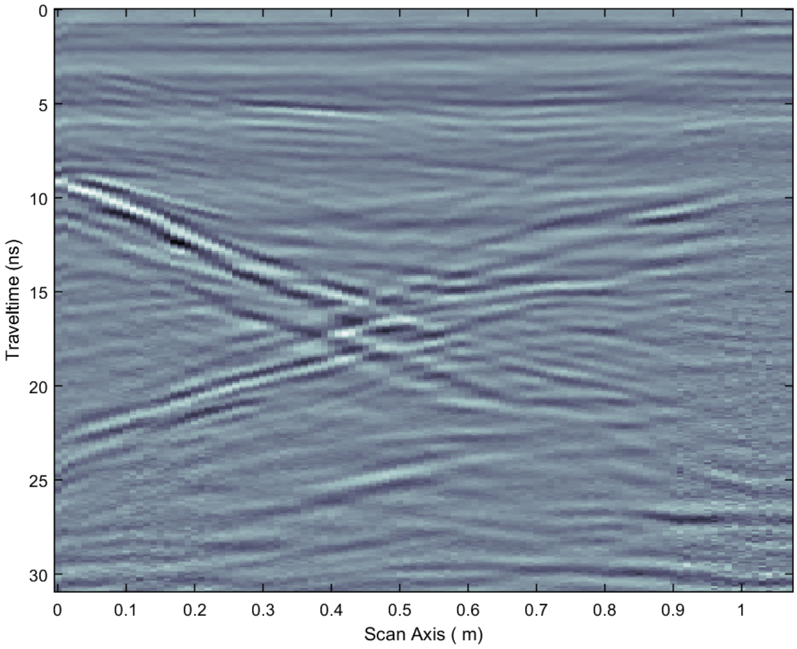

Figure A.1: Processed GPR diagram from line A

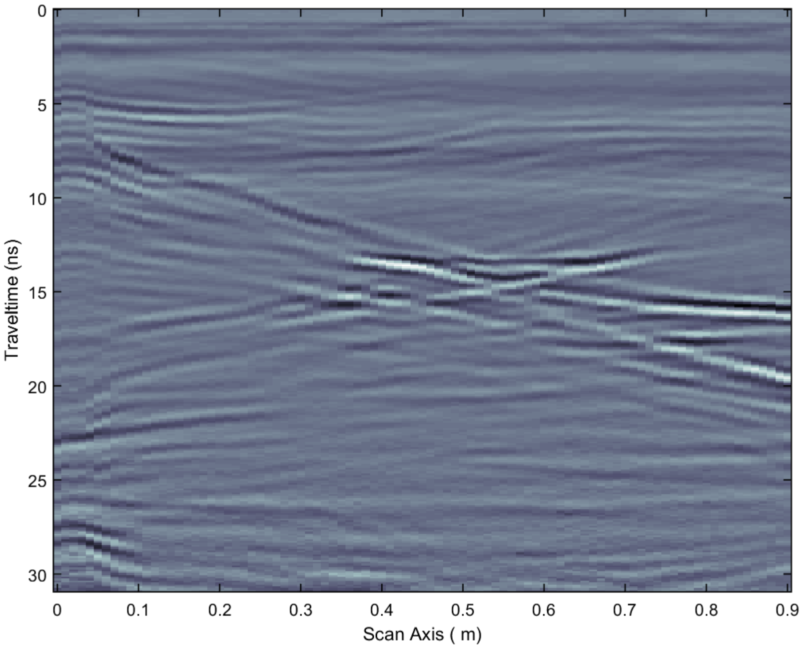

Figure A.2: Processed GPR diagram from line B

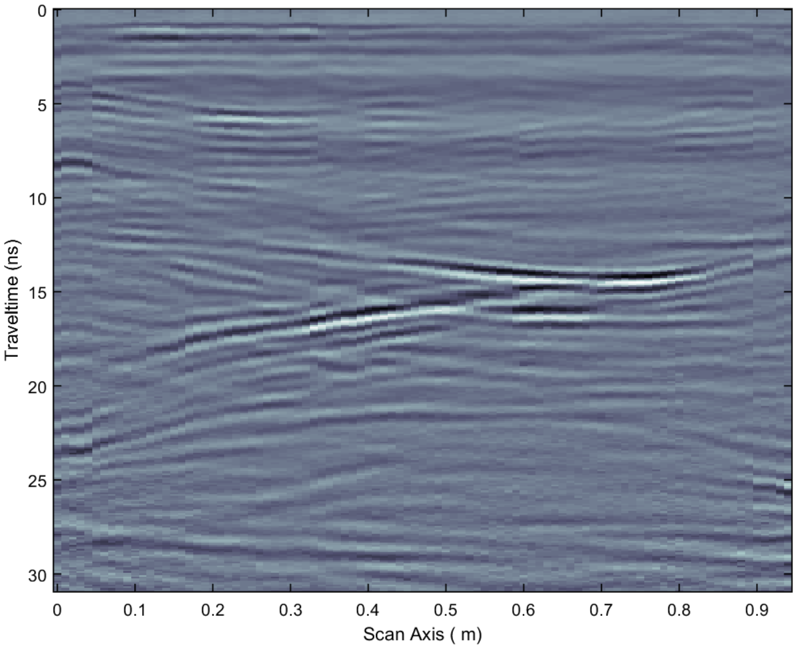

Figure A.3: Processed GPR diagram from line C

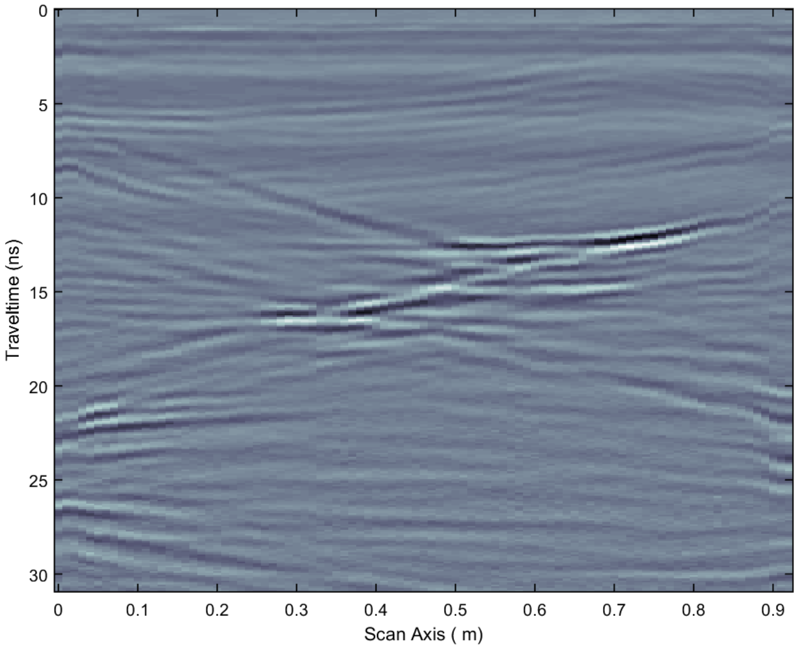

Figure A.4: Processed GPR diagram from line D

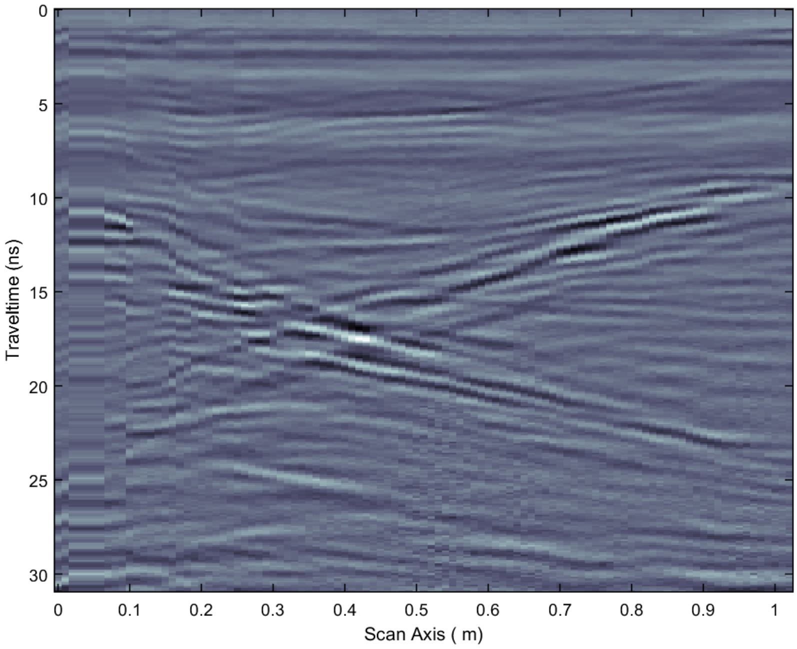

Figure A.5: Processed GPR diagram from line A reverse

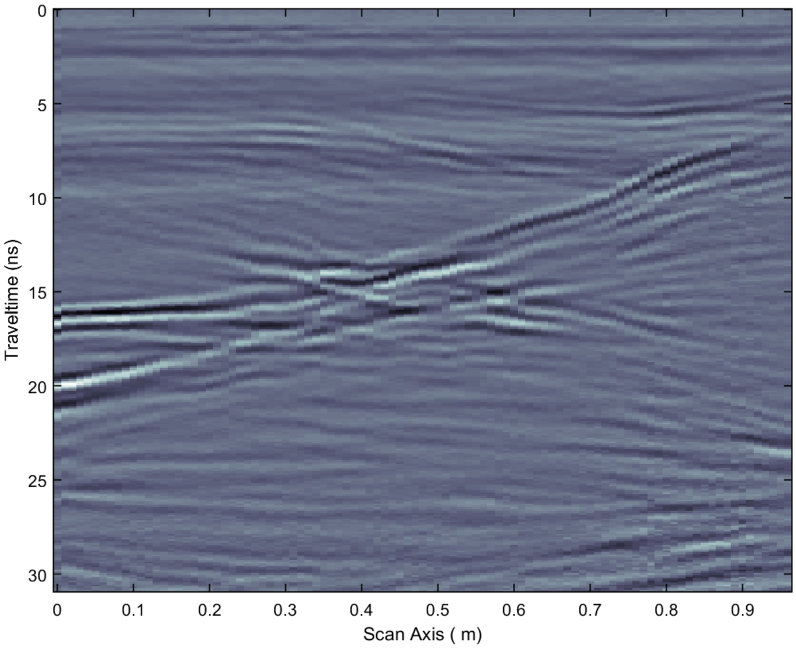

Figure A.6: Processed GPR diagram from line B reverse

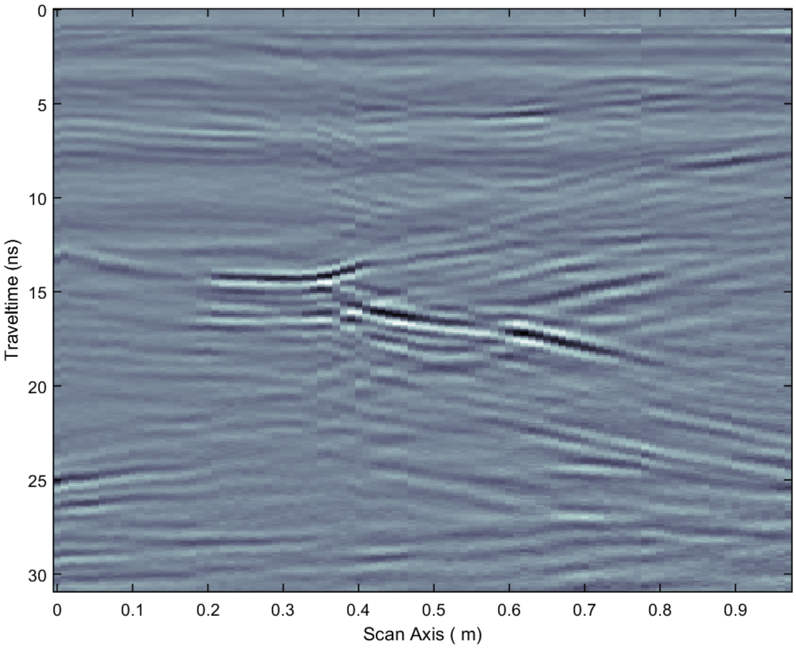

Figure A.7: Processed GPR diagram from line C reverse

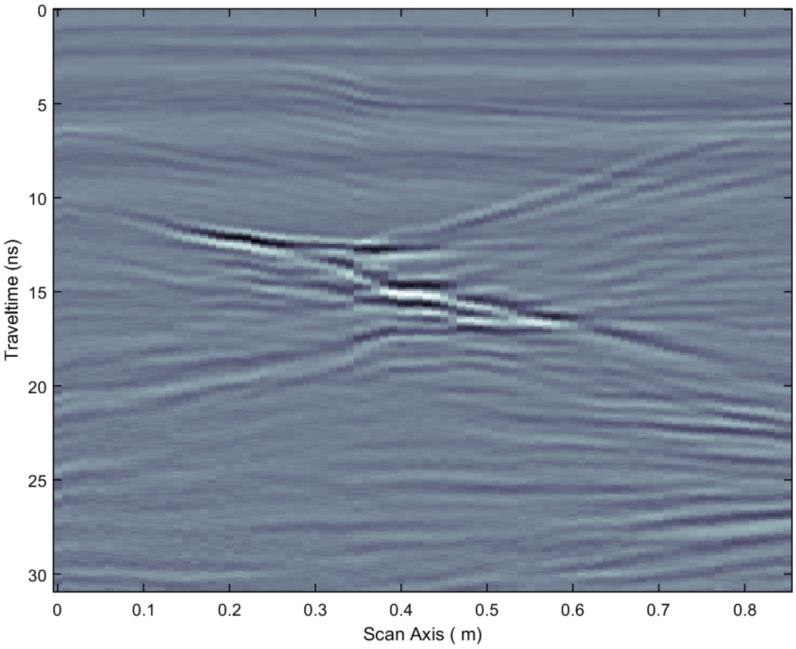

Figure A.8: Processed GPR diagram from line D reverse

B

Reflection surfaces rock TU Delft

Table B.1: Reflection surface coordinates of line A

Reflection surface coordinates				
$No.$	$s_0(m)$	$s_1(m)$	$t_0(ns)$	$t_1(ns)$
1	0.02	0.15	9.0	10.8
2	0.15	0.20	10.8	11.6
3	0.20	0.30	11.6	13.1
4	0.30	0.45	13.1	14.9
5	0.03	0.15	22.0	20.8
6	0.16	0.45	20.5	17.8
7	0.45	0.53	17.0	16.6
8	0.55	0.63	14.8	14.6
9	0.70	0.95	11.0	9.3
10	0.25	0.65	15.4	20.2
11	0.70	0.83	14.5	14.2
12	0.25	0.47	4.7	5.1
13	0.85	0.97	26.3	26.6
14	0.45	0.62	11.1	10.8
15	0.43	0.55	13.2	13.8
16	0.13	0.70	20.0	12.9

Table B.2: Reflection surface coordinates of line A reverse

Reflection surface coordinates				
$No.$	$s_0(m)$	$s_1(m)$	$t_0(ns)$	$t_1(ns)$
1	0.01	0.13	10.4	10.4
2	0.06	0.11	10.4	11.1
3	0.40	0.60	5.5	5.0
4	0.25	0.55	12.7	11.8
5	0.15	0.32	14.2	14.9
6	0.35	0.54	15.7	17.6
7	0.35	0.65	18.0	20.4
8	0.77	0.88	21.8	22.2
9	0.88	0.92	22.2	22.5
10	0.92	0.96	22.5	22.5
11	0.38	0.65	15.0	12.0
12	0.65	0.90	11.5	9.8
13	0.90	0.97	9.3	9.0
14	0.25	0.30	17.0	17.0
15	0.15	0.23	11.0	12.4
16	0.25	0.46	10.1	11.1

Table B.3: Reflection surface coordinates of line B

Reflection surface coordinates				
$No.$	$s_0(m)$	$s_1(m)$	$t_0(ns)$	$t_1(ns)$
1	0.05	0.10	4.5	4.9
2	0.10	0.20	4.9	5.2
3	0.20	0.30	5.2	5.0
4	0.05	0.10	6.8	7.7
5	0.10	0.30	7.7	10.8
6	0.30	0.40	7.3	7.1
7	0.40	0.55	7.1	5.9
8	0.30	0.50	10.8	12.7
9	0.60	0.90	16.0	19.0
10	0.37	0.90	12.7	15.2
11	0.54	0.74	14.9	12.8
12	0.45	0.54	15.0	14.9
13	0.50	0.70	13.0	12.7
14	0.69	0.90	17.4	16.8
15	0.09	0.23	16.4	15.6
16	0.30	0.44	14.7	14.7
17	0.05	0.25	22.0	21.0
18	0.10	0.30	19.0	17.6

Table B.4: Reflection surface coordinates of line B reverse

Reflection surface coordinates				
$No.$	$s_0(m)$	$s_1(m)$	$t_0(ns)$	$t_1(ns)$
1	0.00	0.20	15.6	15.1
2	0.00	0.14	19.8	18.6
3	0.20	0.25	15.1	14.8
4	0.25	0.45	12.8	13.4
5	0.25	0.45	13.2	15.8
6	0.30	0.60	15.7	13.0
7	0.23	0.32	16.5	16.7
8	0.30	0.65	17.2	14.3
9	0.45	0.72	12.8	10.0
10	0.72	0.80	10.0	8.5
11	0.80	0.90	8.5	7.0
12	0.55	0.80	14.0	16.4
13	0.54	0.66	16.0	16.9
14	0.45	0.55	6.9	7.7
15	0.55	0.68	7.7	8.2
16	0.78	0.95	5.1	4.3
17	0.65	0.78	4.9	5.1
18	0.89	0.96	22.2	22.9
19	0.74	0.81	13.1	12.7

Table B.5: Reflection surface coordinates of line C

Reflection surface coordinates				
$No.$	$s_0(m)$	$s_1(m)$	$t_0(ns)$	$t_1(ns)$
1	0.07	0.34	1.0	1.0
2	0.05	0.10	4.5	4.6
3	0.10	0.20	4.6	5.2
4	0.20	0.34	5.2	5.2
5	0.00	0.05	7.8	7.8
6	0.26	0.68	12.1	13.8
7	0.68	0.76	13.8	13.9
8	0.76	0.84	13.9	13.4
9	0.76	0.90	12.0	11.9
10	0.16	0.45	17.1	15.4
11	0.45	0.60	15.4	14.7
12	0.55	0.85	15.9	15.9
13	0.05	0.12	8.0	8.9
14	0.15	0.26	13.1	14.2
15	0.33	0.70	21.2	21.0

Table B.6: Reflection surface coordinates of line C reverse

Reflection surface coordinates				
$No.$	$s_0(m)$	$s_1(m)$	$t_0(ns)$	$t_1(ns)$
1	0.00	0.10	12.6	13.3
2	0.10	0.20	13.3	13.8
3	0.20	0.34	13.8	13.9
4	0.34	0.40	13.9	13.2
5	0.40	0.47	15.5	16.0
6	0.47	0.58	16.0	16.5
7	0.61	0.80	16.6	18.5
8	0.62	0.81	15.5	13.8
9	0.81	0.97	8.1	7.2
10	0.56	0.65	5.5	5.2
11	0.00	0.16	24.7	23.9
12	0.45	0.60	13.0	12.1
13	0.70	0.86	12.0	11.8
14	0.73	0.84	4.9	4.5
15	0.56	0.97	21.0	24.3
16	0.55	0.67	14.2	13.2

Table B.7: Reflection surface coordinates of line D

Reflection surface coordinates				
$No.$	$s_0(m)$	$s_1(m)$	$t_0(ns)$	$t_1(ns)$
1	0.00	0.02	8.0	8.0
2	0.02	0.10	8.0	9.3
3	0.10	0.15	9.3	9.7
4	0.20	0.45	8.6	11.8
5	0.30	0.60	12.0	12.0
6	0.60	0.70	12.0	11.9
7	0.70	0.82	11.9	10.9
8	0.35	0.65	15.8	13.0
9	0.25	0.33	15.7	15.7
10	0.60	0.70	14.0	14.0
11	0.03	0.07	21.2	20.9
12	0.07	0.33	21.6	21.0
13	0.28	0.41	16.3	16.3
14	0.70	0.80	19.1	20.1
15	0.82	0.87	10.9	10.8
16	0.87	0.92	10.8	10.1

Table B.8: Reflection surface coordinates of line D reverse

Reflection surface coordinates				
$No.$	$s_0(m)$	$s_1(m)$	$t_0(ns)$	$t_1(ns)$
1	0.07	0.15	10.3	11.3
2	0.15	0.28	11.3	12.2
3	0.28	0.45	12.2	12.3
4	0.37	0.75	12.2	6.8
5	0.38	0.46	16.6	16.8
6	0.34	0.38	17.0	16.6
7	0.30	0.38	12.8	14.1
8	0.38	0.46	14.1	14.1
9	0.46	0.75	14.9	17.9
10	0.75	0.85	20.0	21.0
11	0.46	0.58	16.3	16.5

C

Buried rock surfaces rock TU Delft

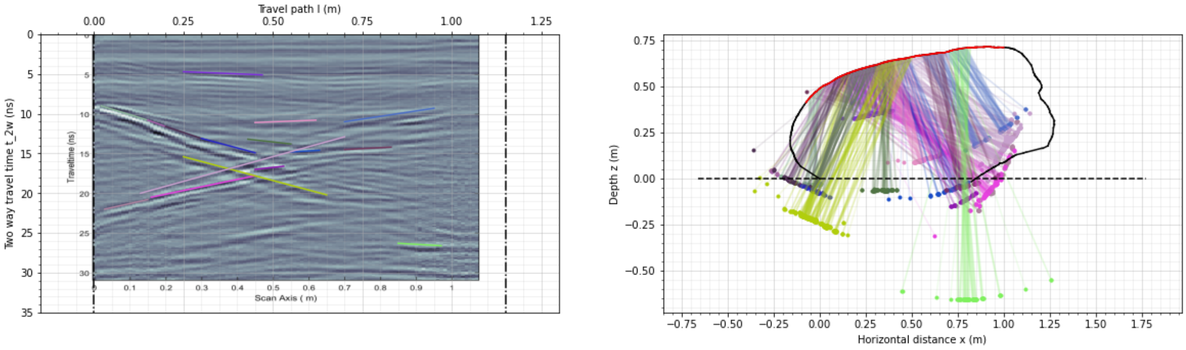

Figure C.1: Buried rock surface coordinates with respect to the exposed rock contour (incl. GPR survey path) for line A. Also including the processed GPR diagram and identified reflection surfaces

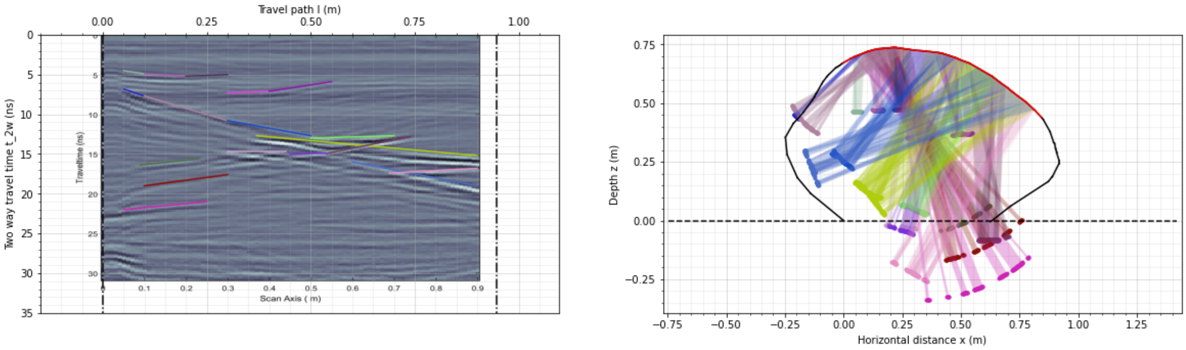

Figure C.2: Buried rock surface coordinates with respect to the exposed rock contour (incl. GPR survey path) for line B. Also including the processed GPR diagram and identified reflection surfaces

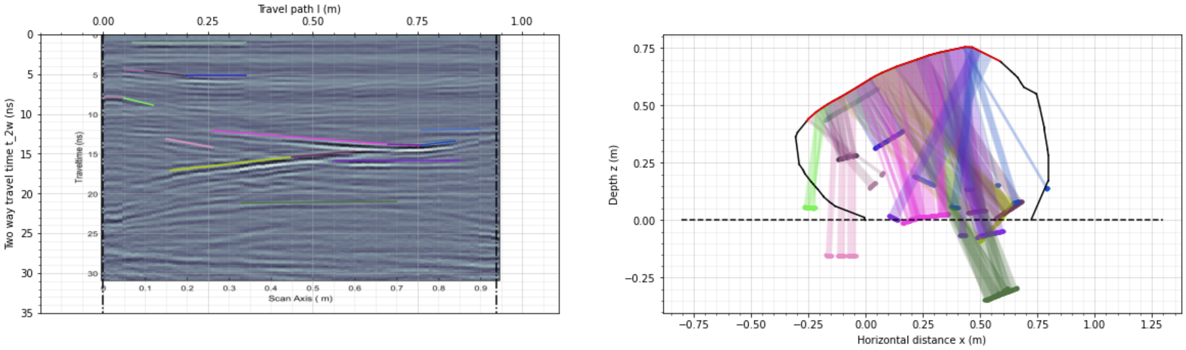

Figure C.3: Buried rock surface coordinates with respect to the exposed rock contour (incl. GPR survey path) for line C. Also including the processed GPR diagram and identified reflection surfaces

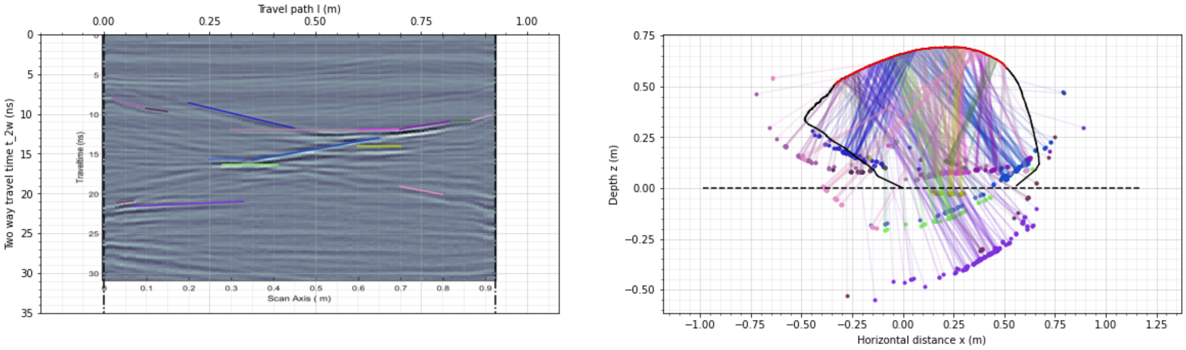

Figure C.4: Buried rock surface coordinates with respect to the exposed rock contour (incl. GPR survey path) for line D. Also including the processed GPR diagram and identified reflection surfaces

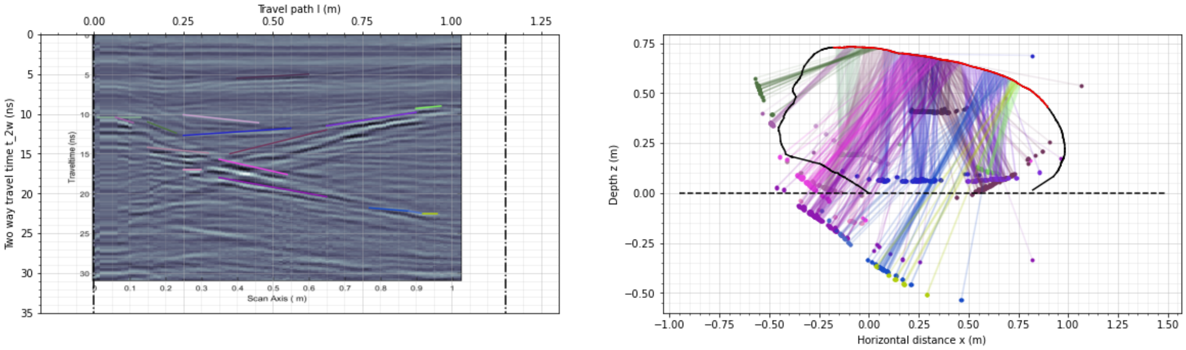

Figure C.5: Buried rock surface coordinates with respect to the exposed rock contour (incl. GPR survey path) for line A reverse. Also including the processed GPR diagram and identified reflection surfaces

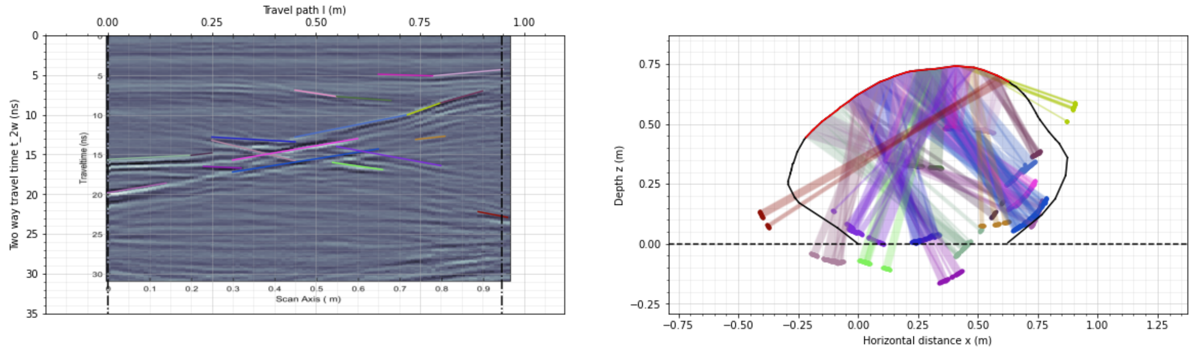

Figure C.6: Buried rock surface coordinates with respect to the exposed rock contour (incl. GPR survey path) for line B reverse. Also including the processed GPR diagram and identified reflection surfaces

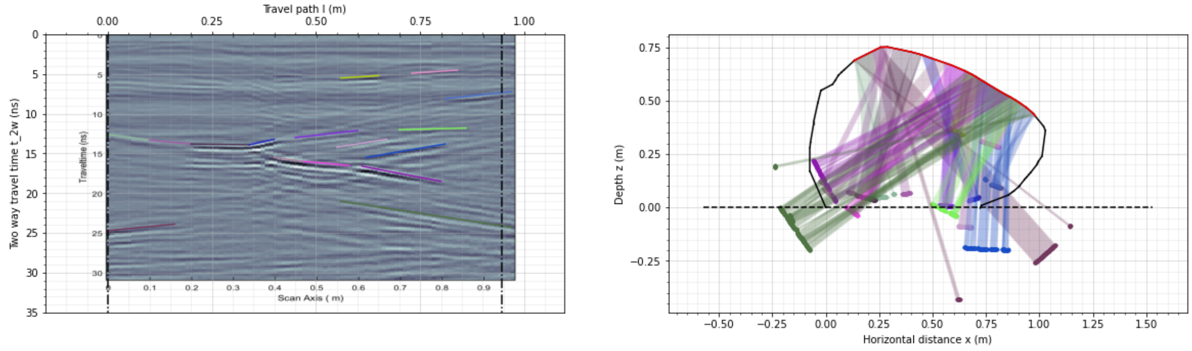

Figure C.7: Buried rock surface coordinates with respect to the exposed rock contour (incl. GPR survey path) for line C reverse. Also including the processed GPR diagram and identified reflection surfaces

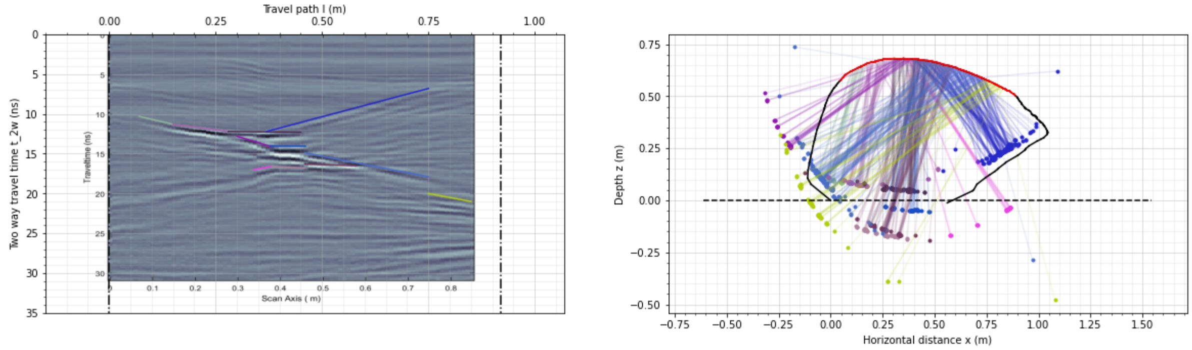

Figure C.8: Buried rock surface coordinates with respect to the exposed rock contour (incl. GPR survey path) for line D reverse. Also including the processed GPR diagram and identified reflection surfaces

D

Test survey keystone Hunebed D14

Figure D.1: GPR test survey

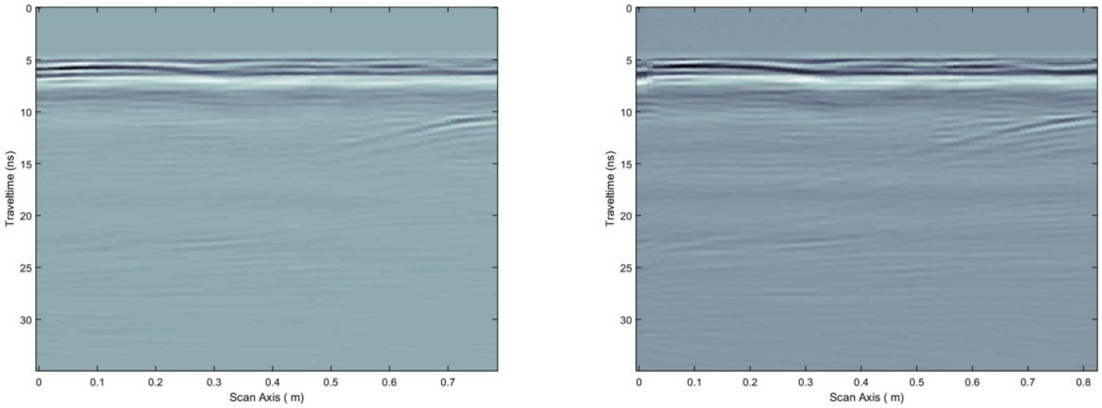

(a) Unprocessed GPR diagram for test survey during ’dry’ or original conditions

(b) Unprocessed GPR diagram for test survey during ’wet’ or saturated conditions

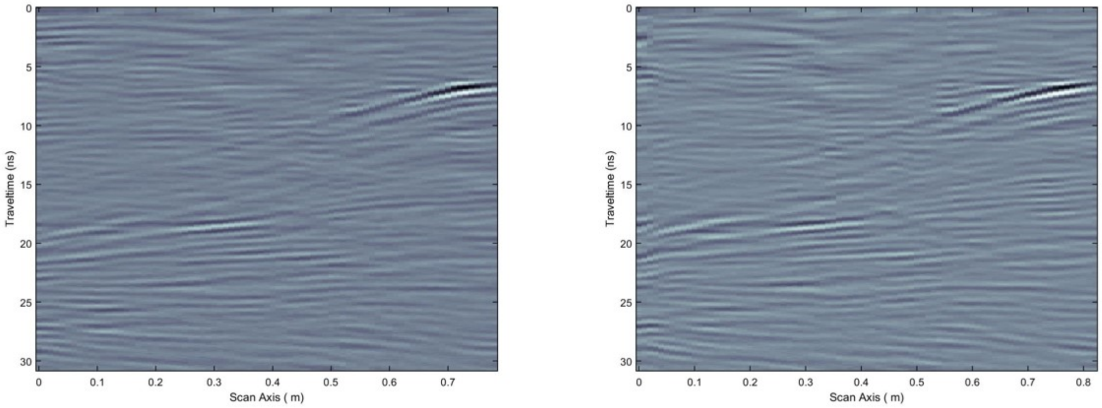

(c) Processed GPR diagram for test survey during ’dry’ or original conditions

(d) Processed GPR diagram for test survey during ’wet’ or saturated conditions

Figure D.2: GPR diagrams from test survey, in which saturated conditions were assumed 10 minutes after the perimeter of the rock was irrigated with approximately 6L of water.

E

Processed GPR diagrams keystone Hunebed D14

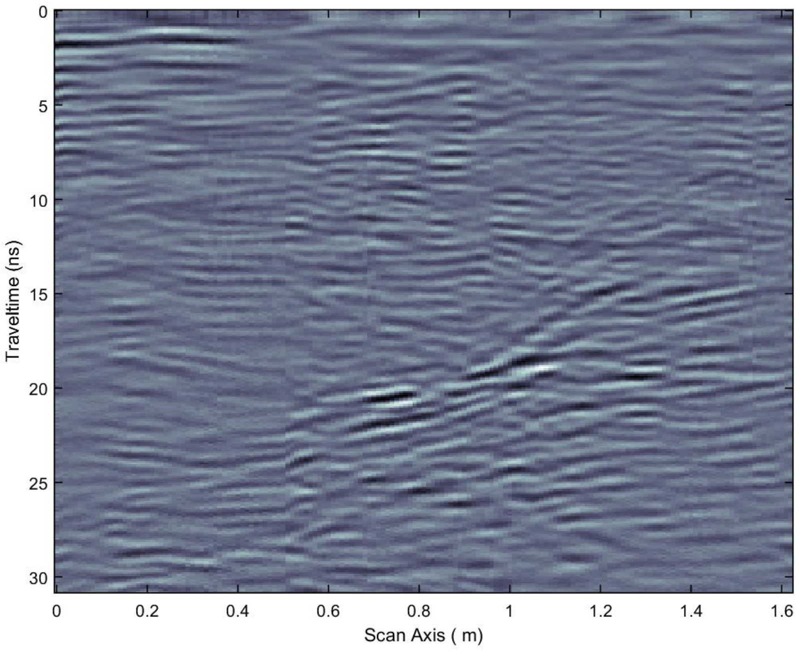

Figure E.1: Processed GPR diagram from line 1(N)

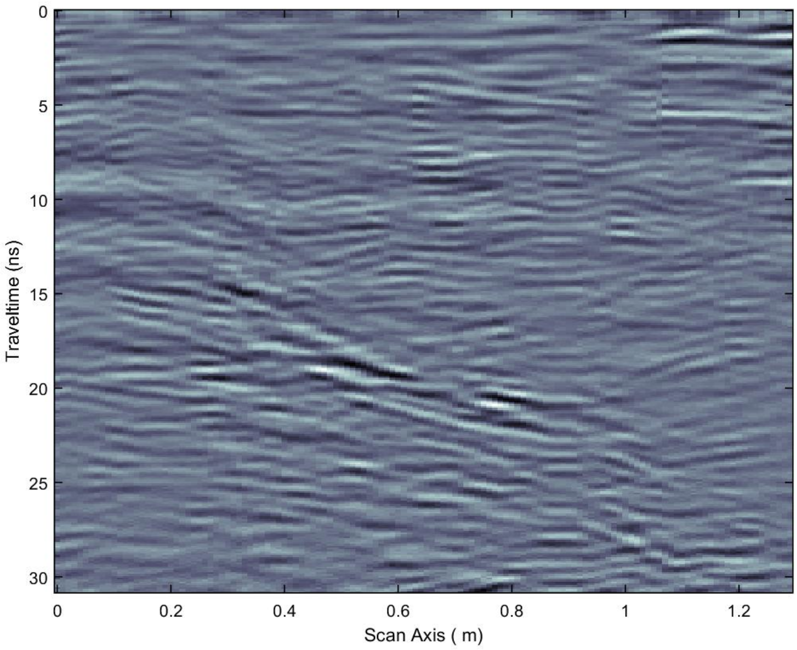

Figure E.2: Processed GPR diagram from line 1(R)

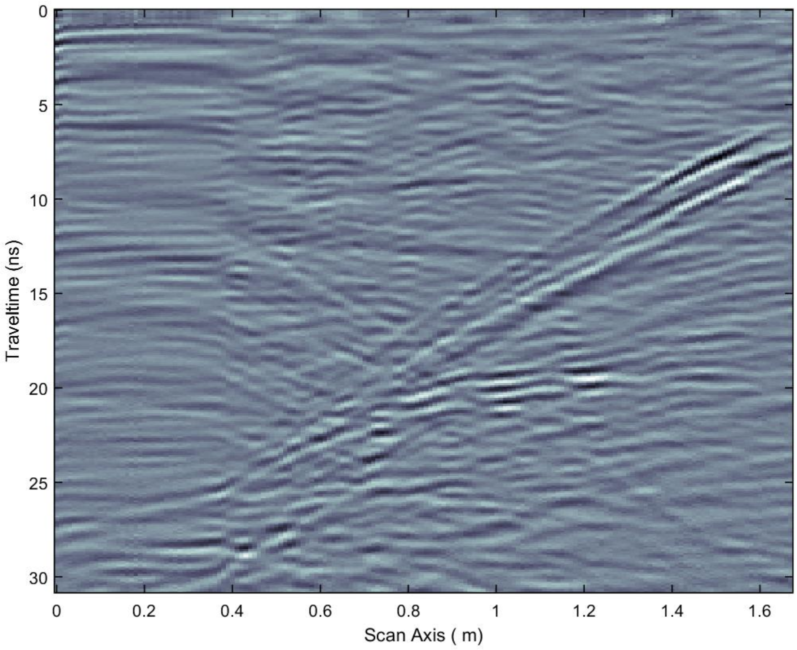

Figure E.3: Processed GPR diagram from line 2(N)

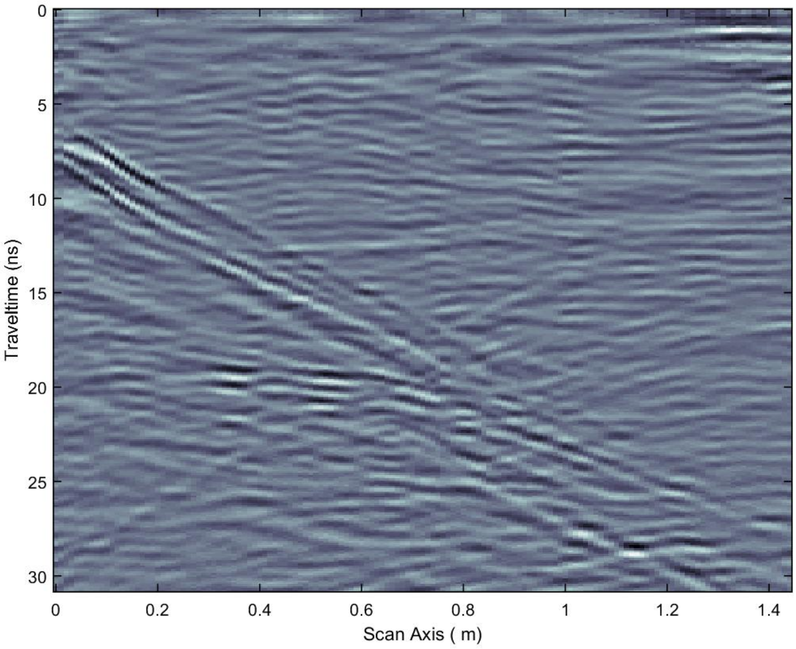

Figure E.4: Processed GPR diagram from line 2(R)

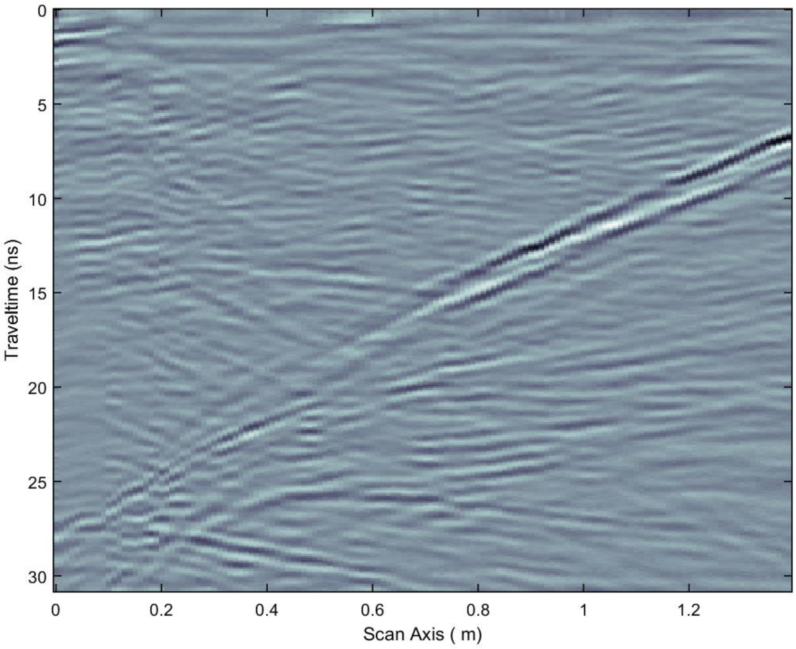

Figure E.5: Processed GPR diagram from line 3(N)

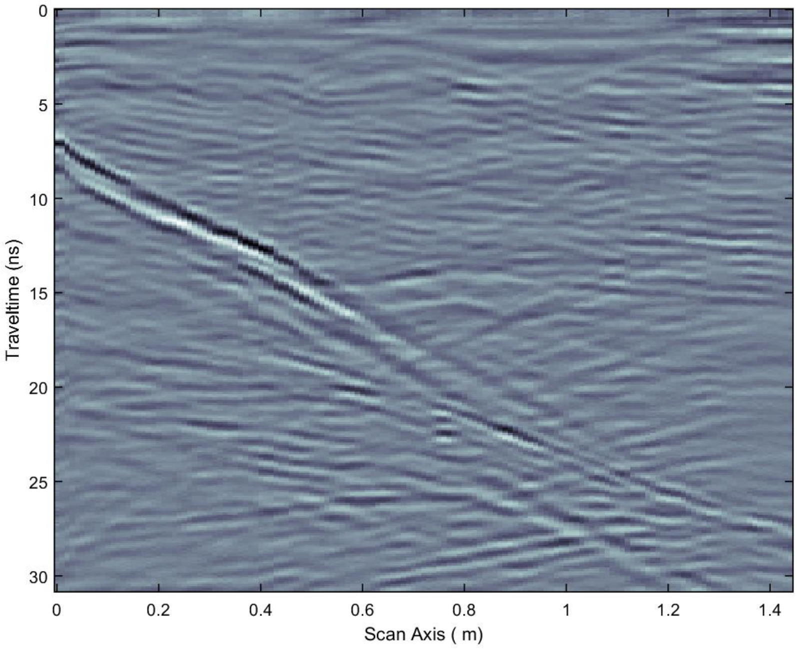

Figure E.6: Processed GPR diagram from line 3(R)

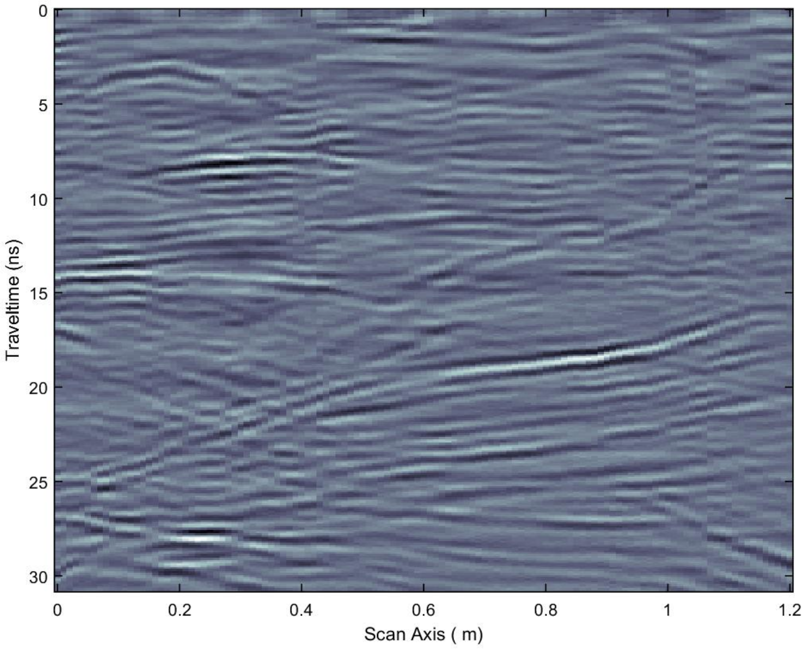

Figure E.7: Processed GPR diagram from line 4(N)

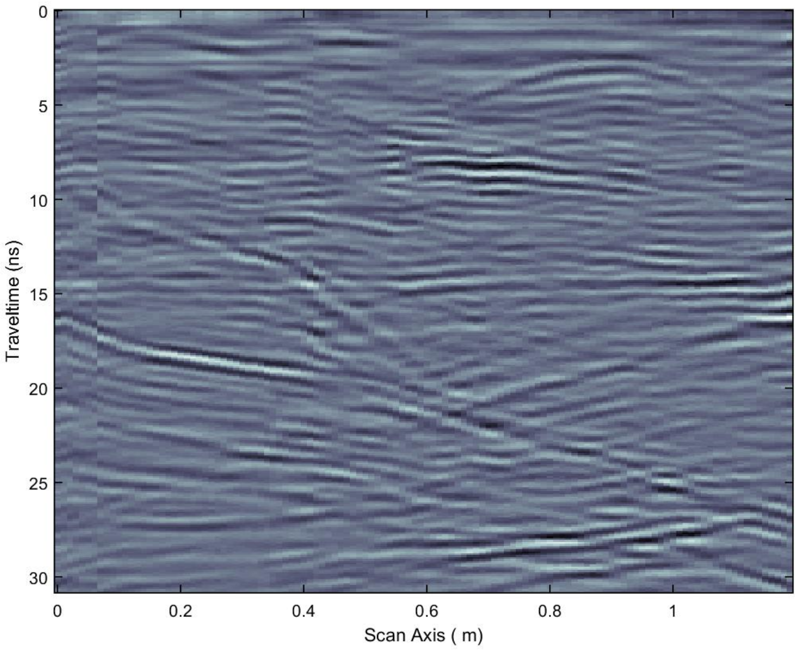

Figure E.8: Processed GPR diagram from line 4(R)

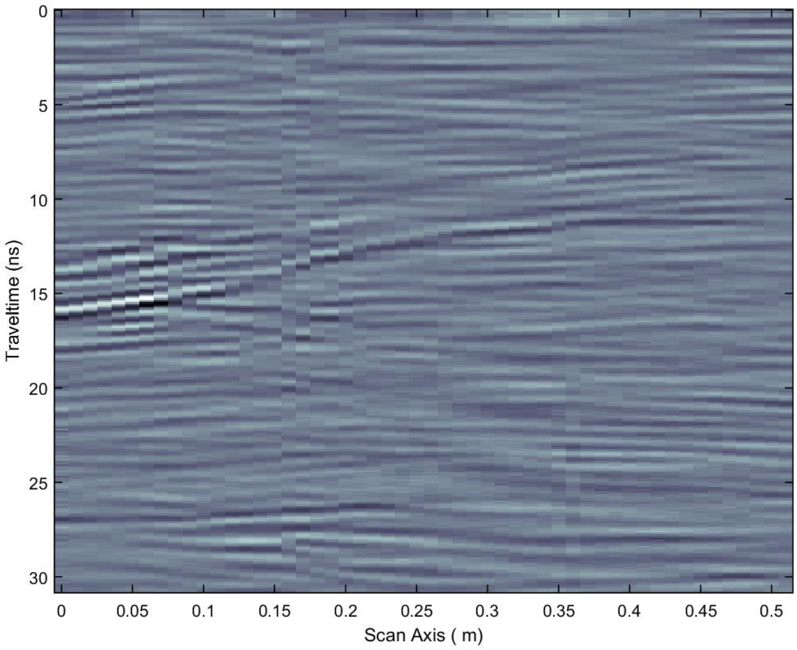

Figure E.9: Processed GPR diagram from line A(N)

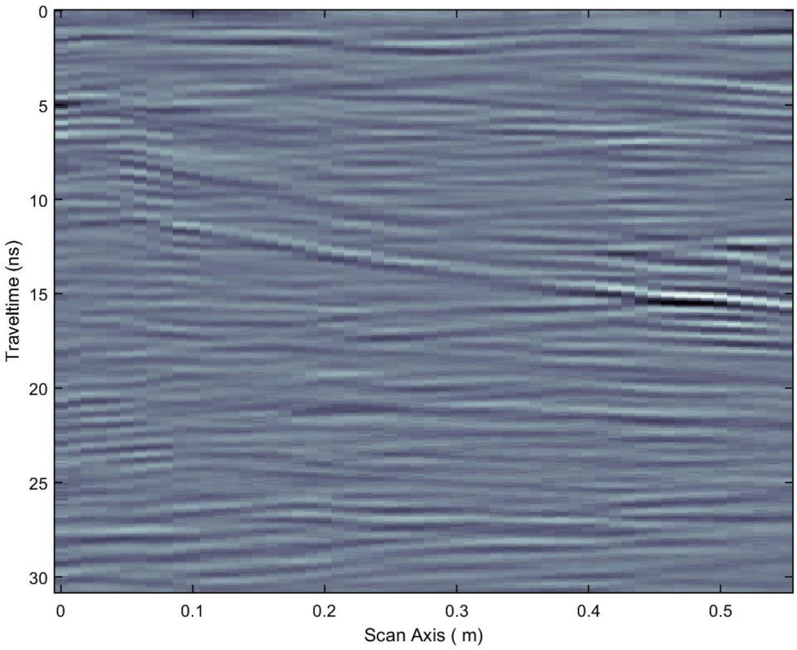

Figure E.10: Processed GPR diagram from line A(R)

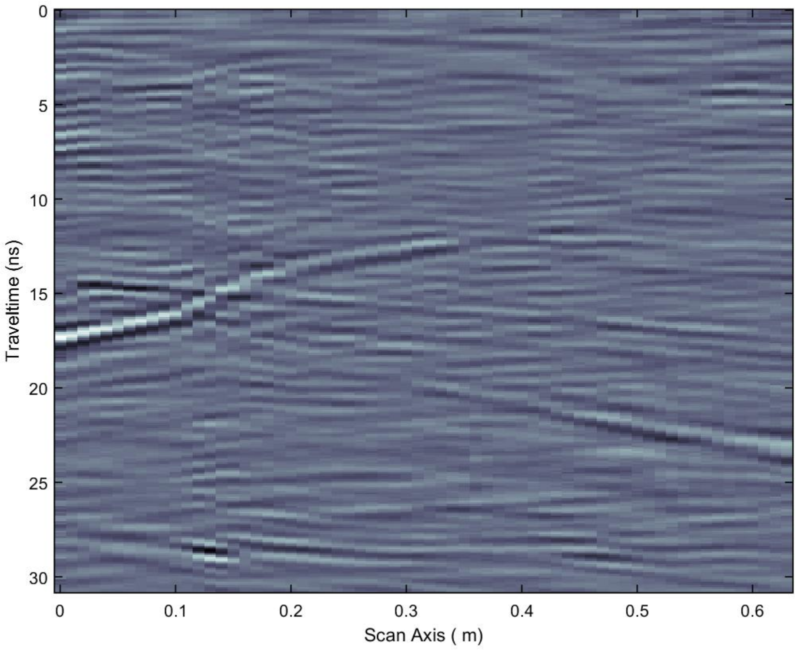

Figure E.11: Processed GPR diagram from line B(N)

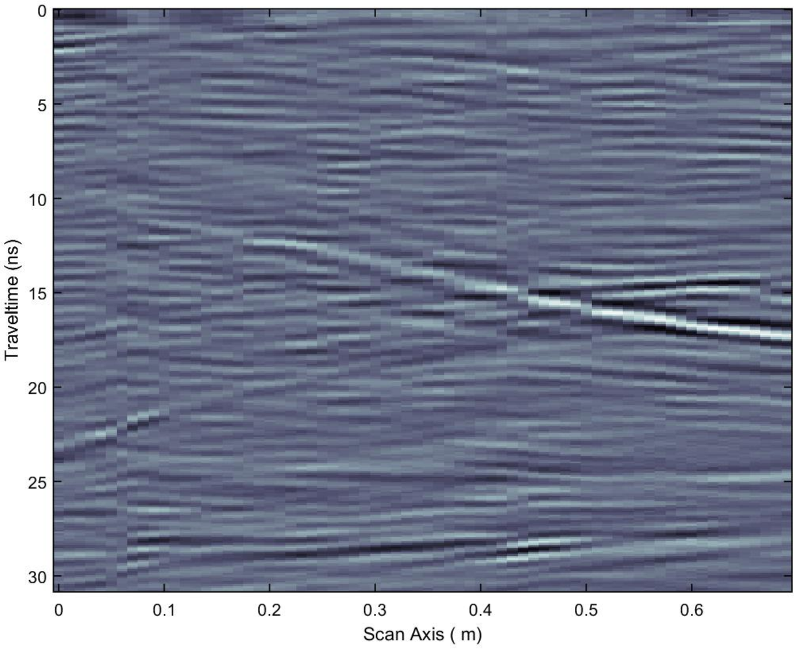

Figure E.12: Processed GPR diagram from line B(R)

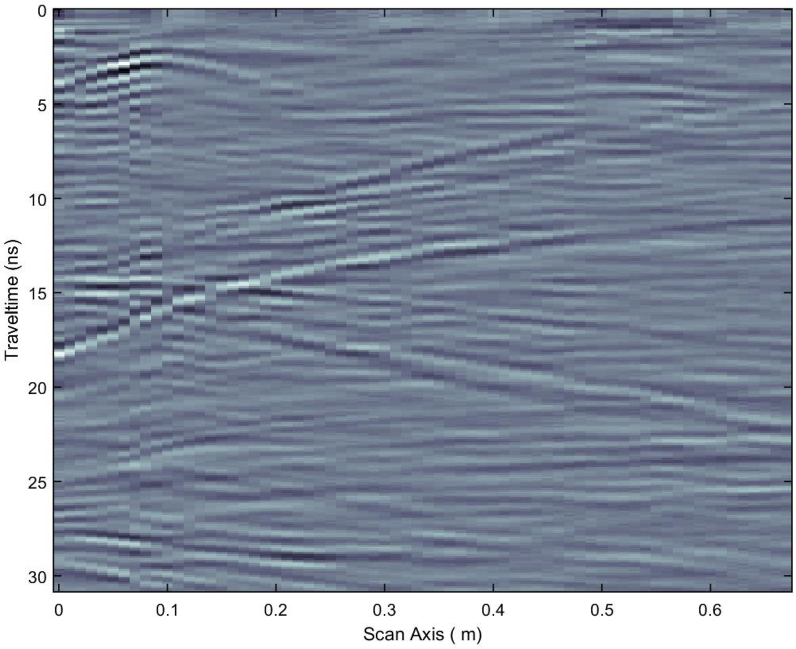

Figure E.13: Processed GPR diagram from line C(N)

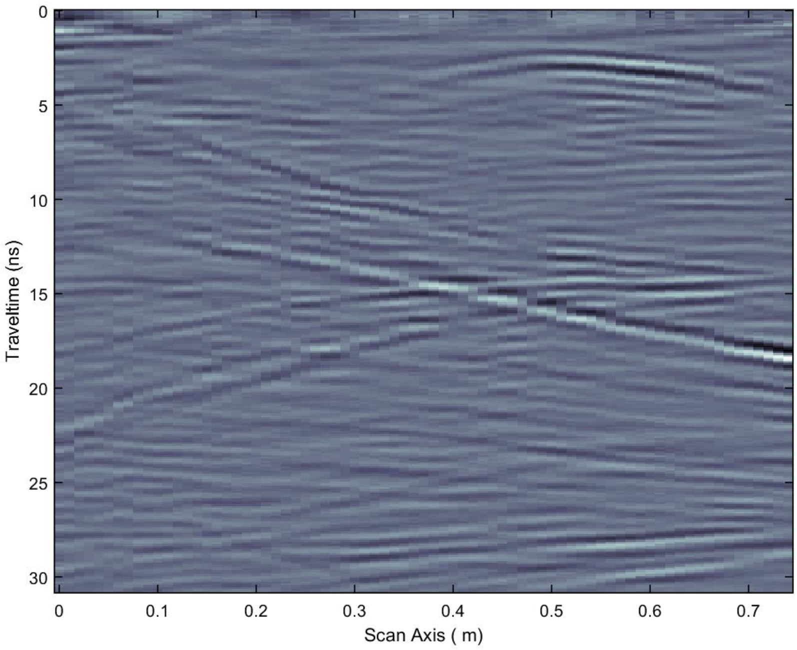

Figure E.14: Processed GPR diagram from line C(R)

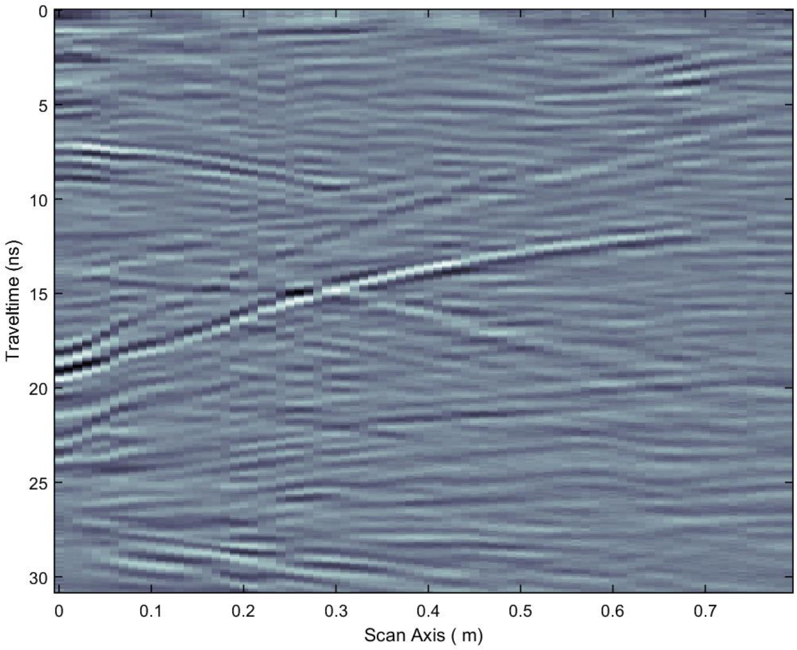

Figure E.15: Processed GPR diagram from line D(N)

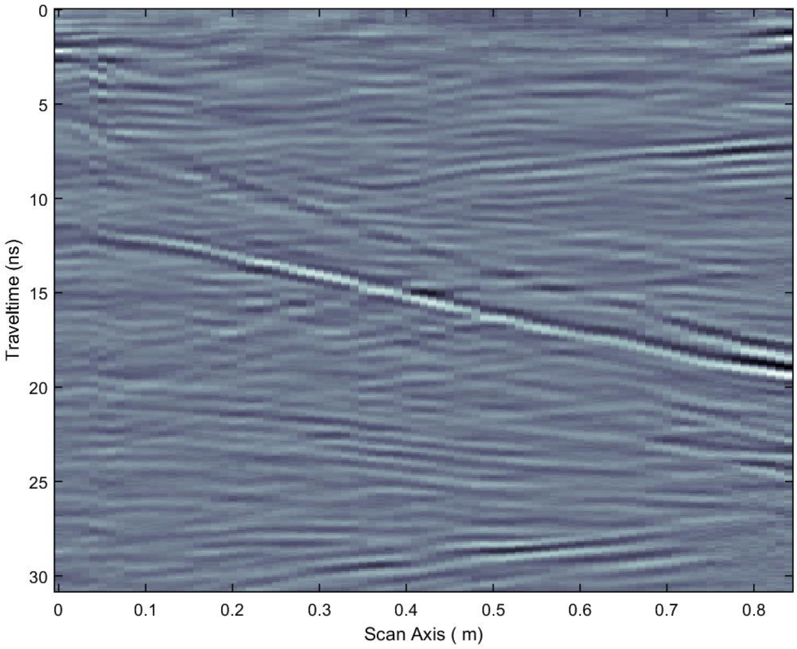

Figure E.16: Processed GPR diagram from line D(R)

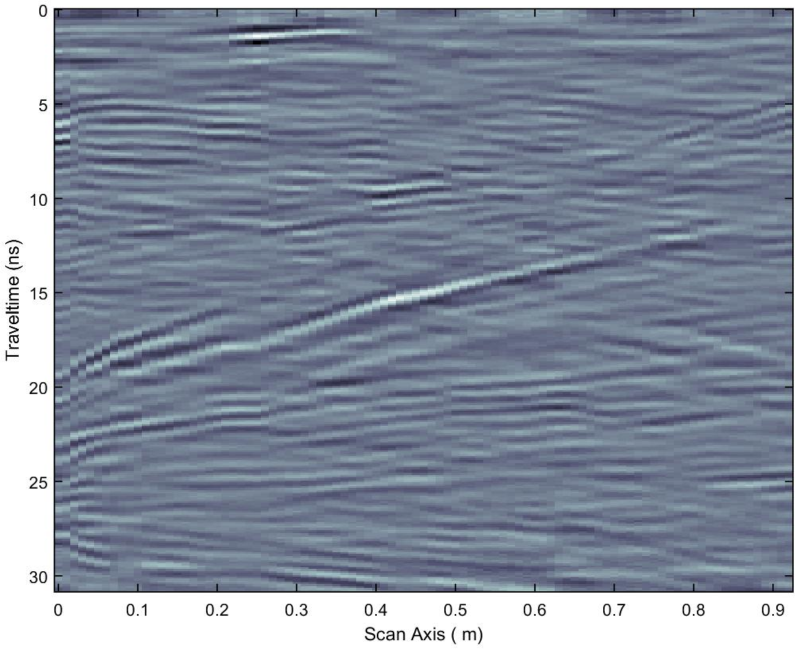

Figure E.17: Processed GPR diagram from line E(N)

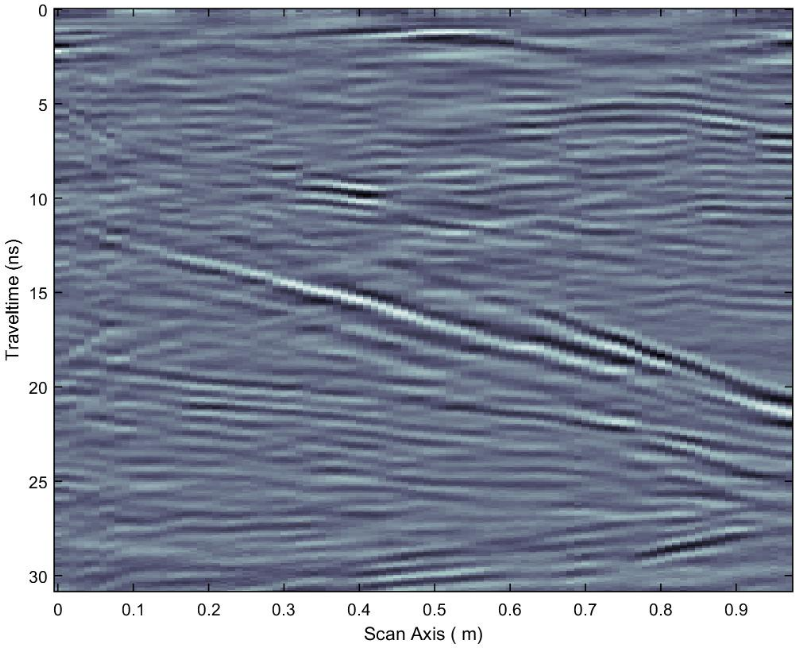

Figure E.18: Processed GPR diagram from line E(R)

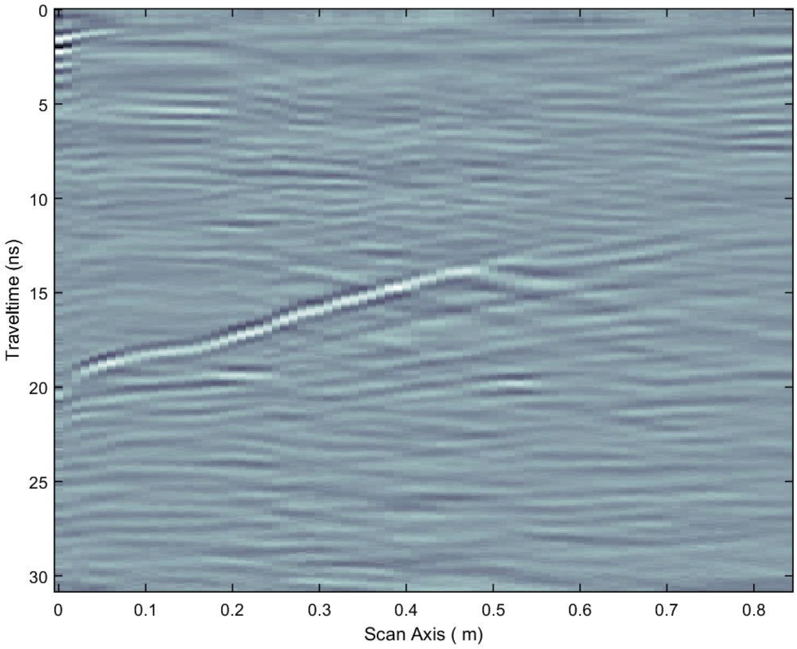

Figure E.19: Processed GPR diagram from line F(N)

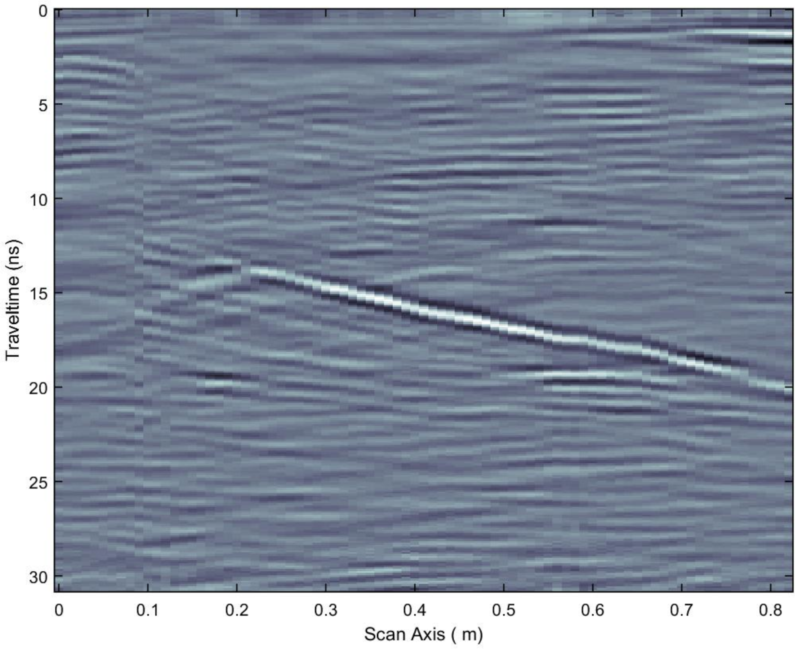

Figure E.20: Processed GPR diagram from line F(R)

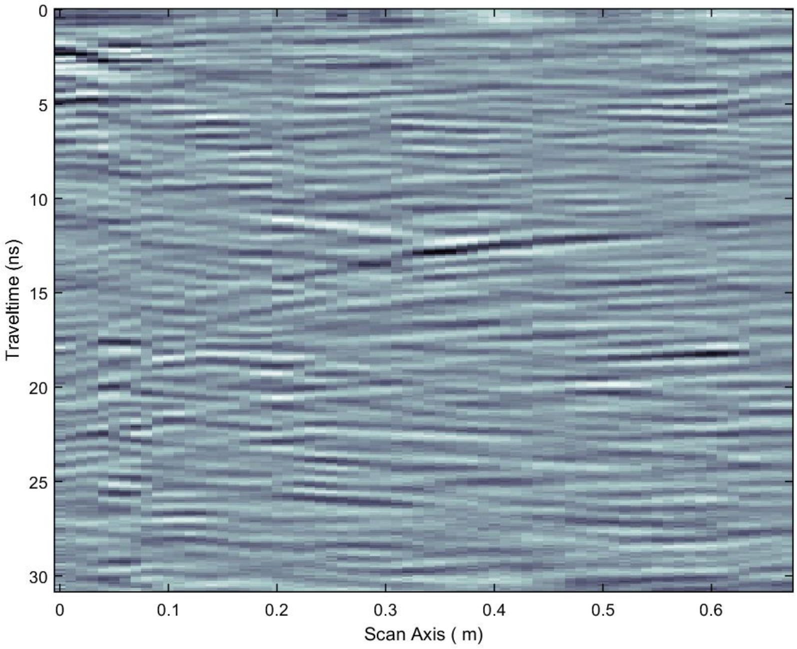

Figure E.21: Processed GPR diagram from line G(N)

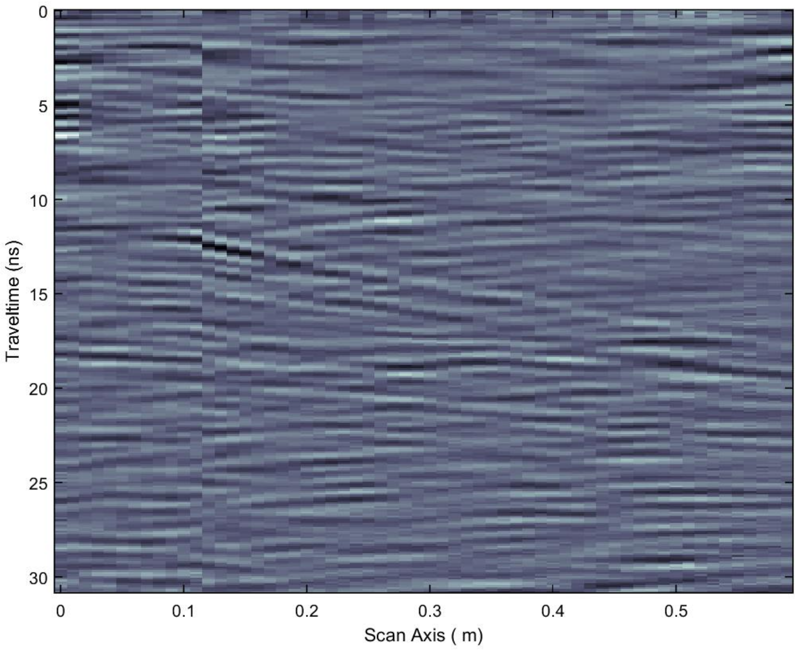

Figure E.22: Processed GPR diagram from line G(R)

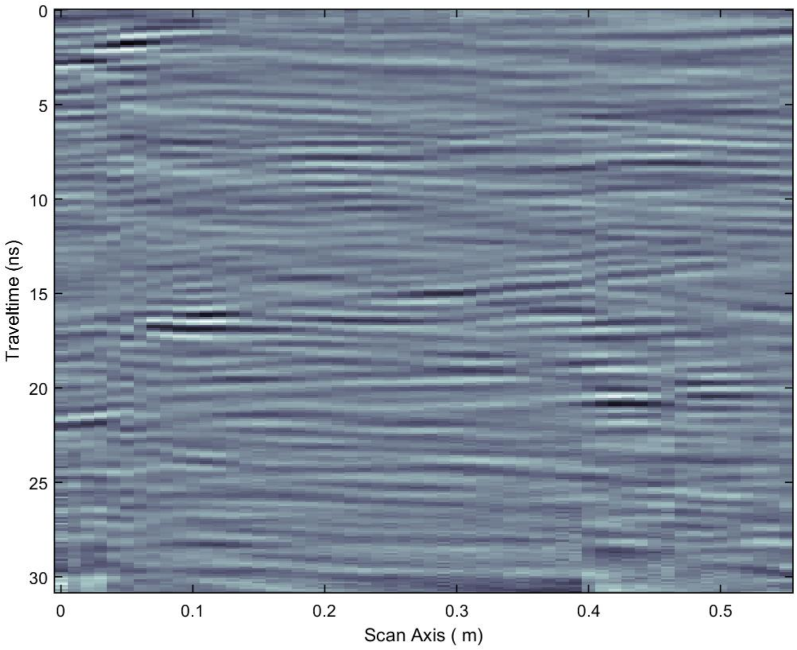

Figure E.23: Processed GPR diagram from line H(N)

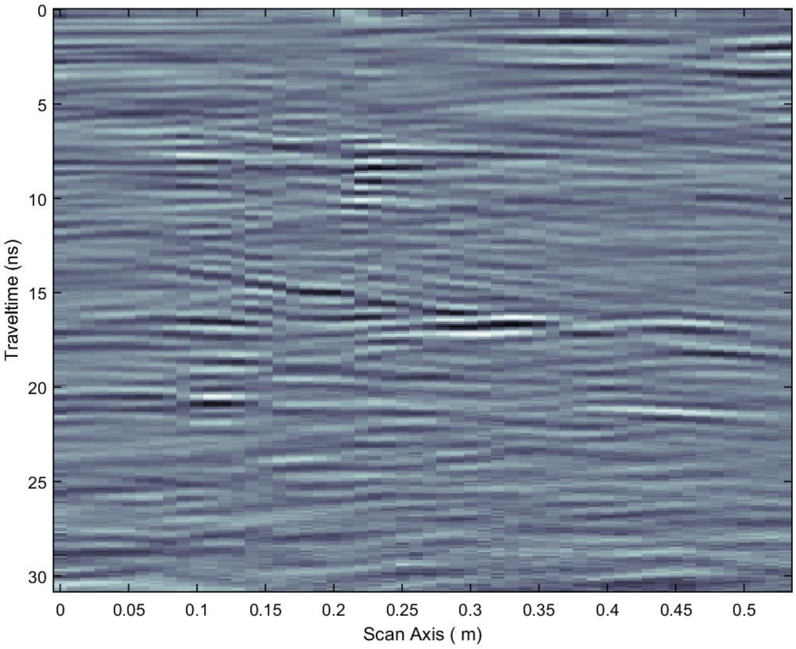

Figure E.24: Processed GPR diagram from line H(R)

F

Reflection surfaces keystone Hunebed D14

Table F.1: Reflection surface coordinates of line 1(N).

Reflection surface coordinates				
$No.$	$s_0(m)$	$s_1(m)$	$t_0(ns)$	$t_1(ns)$
1	0.57	0.80	20.5	19.7
2	0.80	0.95	20.0	18.8
3	0.95	1.00	18.7	18.1
4	1.00	1.10	18.0	17.9
5	1.22	1.32	17.8	17.3
6	1.15	1.28	14.7	14.0
7	1.33	1.55	15.7	14.6
8	1.00	1.15	17.1	15.1
9	1.10	1.16	17.9	17.6
10	0.65	0.75	22.0	21.6
11	0.75	0.85	21.6	21.1
12	0.85	0.96	21.1	20.3
13	0.85	1.05	20.1	19.6
14	1.25	1.35	18.9	18.9
15	1.36	1.55	19.4	19.6
16	1.55	1.60	19.6	19.6

Table F.2: Reflection surface coordinates of line 1(R).

Reflection surface coordinates				
$No.$	$s_0(m)$	$s_1(m)$	$t_0(ns)$	$t_1(ns)$
1	0.50	0.80	17.9	21.0
2	0.55	0.78	19.5	20.0
3	0.78	0.85	20.0	20.4
4	0.10	0.15	14.4	14.8
5	0.15	0.23	14.8	14.8
6	0.26	0.32	14.2	14.8
7	0.32	0.36	14.8	14.9
8	0.08	0.20	19.0	19.0
9	0.23	0.30	18.5	18.5
10	0.85	0.93	20.4	20.4
11	1.08	1.13	28.8	28.4
12	1.13	1.19	28.4	28.4
13	1.19	1.24	28.4	28.3
14	0.93	1.08	27.0	28.8

Table F.3: Reflection surface coordinates of line 2(N).

Reflection surface coordinates				
$No.$	$s_0(m)$	$s_1(m)$	$t_0(ns)$	$t_1(ns)$
1	0.40	0.90	11.8	18.8
2	0.50	1.00	21.8	14.0
3	1.00	1.45	14.0	8.0
4	1.45	1.60	8.0	6.4
5	0.80	0.92	20.0	19.1
6	0.92	1.00	19.1	19.1
7	1.00	1.10	19.1	18.8
8	1.15	1.26	19.0	18.9
9	1.44	1.55	17.3	17.0
10	0.40	0.55	24.8	22.9
11	0.55	0.65	22.9	22.0
12	0.20	0.40	25.9	24.8
13	1.25	1.55	11.9	8.7
14	0.00	0.10	26.9	26.7
15	1.44	1.51	19.2	19.2
16	0.72	0.76	21.0	20.9
17	1.55	1.65	8.2	7.2
18	0.80	1.20	18.5	13.0
19	0.50	0.80	23.0	18.5
20	0.20	0.39	28.1	28.0
21	1.15	1.21	18.3	18.2
22	1.21	1.30	18.2	17.9
23	0.72	0.80	25.1	25.1
24	0.80	0.88	25.1	24.8
25	0.88	0.95	24.8	24.9

Table F.4: Reflection surface coordinates of line 2(R).

Reflection surface coordinates				
$No.$	$s_0(m)$	$s_1(m)$	$t_0(ns)$	$t_1(ns)$
1	0.05	0.20	6.7	9.0
2	0.20	0.43	9.0	12.2
3	0.00	0.15	7.4	9.8
4	0.15	0.31	9.8	12.0
5	0.35	0.55	13.0	15.2
6	0.30	0.40	19.1	19.1
7	0.45	0.63	19.0	19.2
8	0.63	0.72	19.2	19.7
9	0.90	1.10	21.8	23.7
10	0.79	0.84	20.7	21.0
11	1.20	1.25	24.9	25.1
12	0.25	0.95	25.0	14.2
13	1.37	1.45	26.7	26.8
14	0.65	0.77	17.1	19.0
15	0.61	0.70	24.7	24.8
16	0.70	0.77	25.0	25.1
17	0.77	0.84	25.0	25.0
18	1.01	1.08	26.9	27.1
19	1.11	1.19	28.0	28.0
20	1.22	1.30	27.8	28.0
21	0.40	0.75	12.7	12.4

Table F.5: Reflection surface coordinates of line 3(N).

Reflection surface coordinates				
$No.$	$s_0(m)$	$s_1(m)$	$t_0(ns)$	$t_1(ns)$
1	0.67	1.40	15.0	6.1
2	0.10	0.30	26.0	23.0
3	0.30	0.50	23.0	20.6
4	0.20	0.60	27.3	29.3
5	0.72	0.85	18.6	18.0
6	0.43	0.55	25.4	25.3
7	0.58	0.73	25.5	25.7
8	0.10	0.30	30.0	26.4
9	0.61	0.72	19.5	18.6
10	0.75	1.12	25.9	27.0
11	0.66	1.05	22.7	21.8
12	0.37	0.76	14.0	14.8

Table F.6: Reflection surface coordinates of line 3(R).

Reflection surface coordinates				
$No.$	$s_0(m)$	$s_1(m)$	$t_0(ns)$	$t_1(ns)$
1	0.00	0.05	6.6	7.4
2	0.05	0.42	7.4	12.3
3	0.42	0.55	12.3	14.1
4	0.42	0.65	17.8	19.7
5	0.75	1.30	20.6	26.0
6	0.25	0.55	26.9	25.9
7	0.55	0.82	25.9	25.4
8	0.65	1.00	29.5	27.8
9	0.25	0.45	21.6	22.0
10	0.45	0.60	22.0	22.6
11	0.85	1.35	24.5	31.0
12	1.35	1.45	26.5	26.9
13	0.35	0.60	13.2	16.3
14	0.65	0.75	14.1	13.7

Table F.7: Reflection surface coordinates of line 4(N).

Reflection surface coordinates				
$No.$	$s_0(m)$	$s_1(m)$	$t_0(ns)$	$t_1(ns)$
1	0.00	0.20	13.3	12.9
2	0.13	0.25	8.5	7.8
3	0.25	0.40	7.8	7.8
4	0.05	0.52	24.6	19.5
5	0.60	0.88	18.9	17.9
6	0.88	0.97	17.9	17.3
7	0.97	1.13	17.3	15.7
8	0.17	0.30	27.2	27.2
9	0.30	0.37	27.7	27.8
10	0.37	0.47	27.8	27.7
11	0.42	0.75	21.3	19.8
12	0.40	0.60	11.2	10.8
13	0.60	0.70	10.8	10.8
14	0.05	0.10	3.9	3.2
15	0.10	0.15	3.2	2.8
16	0.15	0.20	2.8	2.8
17	0.20	0.26	2.8	3.4
18	0.20	0.35	14.0	14.1
19	0.35	0.45	14.1	14.3
20	0.45	0.51	14.5	15.1
21	0.51	0.55	15.1	15.1
22	0.55	0.67	14.5	13.2
23	0.67	0.80	13.2	12.3
24	0.82	0.90	11.8	11.7
25	0.90	1.00	11.8	11.0
26	0.98	1.06	10.1	9.0
27	0.00	0.05	16.8	17.2
28	1.05	1.20	27.3	28.8
29	0.00	0.10	26.8	27.3
30	0.00	0.08	29.3	28.2
31	0.70	0.78	10.8	11.1
32	0.78	0.88	11.1	10.9
33	0.45	0.90	26.0	27.0
34	0.90	1.00	27.0	26.9
35	0.83	1.12	13.8	13.8

Table F.8: Reflection surface coordinates of line 4(R).

Reflection surface coordinates				
$No.$	$s_0(m)$	$s_1(m)$	$t_0(ns)$	$t_1(ns)$
1	0.65	0.75	4.9	3.8
2	0.75	0.85	3.8	2.8
3	0.85	0.94	2.8	2.8
4	0.94	1.02	2.8	3.4
5	1.02	1.15	3.4	5.2
6	0.58	0.66	7.9	7.9
7	0.68	0.76	8.1	8.0
8	0.76	0.85	8.0	8.3
9	0.85	0.95	8.3	8.7
10	0.85	1.15	14.0	14.0
11	0.54	0.70	14.5	14.0
12	0.05	0.25	9.0	11.9
13	0.25	0.40	11.9	13.2
14	0.34	0.42	10.9	10.9
15	0.42	0.55	10.9	11.5
16	0.00	0.12	15.5	17.4
17	0.12	0.45	17.4	19.0
18	0.50	0.72	27.9	27.8
19	0.72	0.85	27.8	27.5
20	0.85	1.00	27.5	26.6
21	1.00	1.05	26.6	26.6
22	1.00	1.20	27.9	30.2
23	0.10	0.20	26.9	27.0
24	0.20	0.25	27.0	27.0
25	0.25	0.45	27.0	26.3
26	0.65	0.80	21.0	19.6
27	0.80	1.10	19.6	16.5
28	0.50	1.20	20.2	26.5

Table F.9: Reflection surface coordinates of line A(N).

Reflection surface coordinates				
$No.$	$s_0(m)$	$s_1(m)$	$t_0(ns)$	$t_1(ns)$
1	0.00	0.08	4.6	3.9
2	0.00	0.15	13.8	11.9
3	0.00	0.12	15.5	14.0
4	0.12	0.20	14.0	12.7
5	0.20	0.27	12.7	11.7
6	0.27	0.35	11.7	11.3
7	0.35	0.42	11.1	11.0
8	0.42	0.49	11.0	11.1
9	0.00	0.10	26.8	26.7
10	0.10	0.20	26.7	26.0
11	0.20	0.24	26.0	26.0

Table F.10: Reflection surface coordinates of line A(R).

Reflection surface coordinates				
$No.$	$s_0(m)$	$s_1(m)$	$t_0(ns)$	$t_1(ns)$
1	0.50	0.55	14.8	15.2
2	0.44	0.50	14.5	14.8
3	0.25	0.44	13.0	14.5
4	0.08	0.25	11.1	13.0
5	0.40	0.50	12.4	12.0
6	0.50	0.55	12.0	12.0

Table F.11: Reflection surface coordinates of line B(N).

Reflection surface coordinates				
$No.$	$s_0(m)$	$s_1(m)$	$t_0(ns)$	$t_1(ns)$
1	0.00	0.10	16.9	15.8
2	0.27	0.35	28.4	28.3
3	0.17	0.24	13.8	12.9
4	0.24	0.35	12.9	11.9
5	0.02	0.18	13.9	14.7
6	0.18	0.60	14.7	16.8
7	0.43	0.64	20.4	22.4
8	0.15	0.27	27.6	28.4

Table F.12: Reflection surface coordinates of line B(R).

Reflection surface coordinates				
$No.$	$s_0(m)$	$s_1(m)$	$t_0(ns)$	$t_1(ns)$
1	0.60	0.70	16.2	16.8
2	0.44	0.60	15.0	16.2
3	0.22	0.44	12.2	15.0
4	0.17	0.22	12.1	12.2
5	0.00	0.10	22.8	21.2
6	0.36	0.61	15.0	13.9
7	0.61	0.66	13.9	13.9
8	0.06	0.12	27.8	27.6
9	0.12	0.22	27.6	27.8
10	0.22	0.37	28.5	27.9
11	0.37	0.43	27.9	27.8
12	0.40	0.50	28.5	28.0

Table F.13: Reflection surface coordinates of line C(N).

Reflection surface coordinates				
$No.$	$s_0(m)$	$s_1(m)$	$t_0(ns)$	$t_1(ns)$
1	0.00	0.07	3.2	2.2
2	0.07	0.09	2.2	2.1
3	0.09	0.11	2.1	2.2
4	0.11	0.18	2.2	3.3
5	0.00	0.10	14.2	14.2
6	0.10	0.16	14.2	14.4
7	0.16	0.25	14.4	15.0
8	0.25	0.68	15.0	17.7
9	0.00	0.10	17.2	15.6
10	0.10	0.25	15.3	13.2
11	0.25	0.35	13.2	12.4
12	0.35	0.50	12.4	11.7
13	0.50	0.68	11.7	10.9
14	0.17	0.36	10.6	9.2
15	0.25	0.47	9.8	6.4
16	0.05	0.10	13.5	12.7
17	0.13	0.67	15.6	21.3
18	0.02	0.10	27.3	27.9
19	0.10	0.20	27.9	28.4
20	0.20	0.26	28.4	28.5

Table F.14: Reflection surface coordinates of line C(R).

Reflection surface coordinates				
$No.$	$s_0(m)$	$s_1(m)$	$t_0(ns)$	$t_1(ns)$
1	0.37	0.47	3.1	2.2
2	0.47	0.53	2.2	2.2
3	0.53	0.62	2.2	2.7
4	0.62	0.73	2.7	3.6
5	0.37	0.74	14.2	17.9
6	0.12	0.37	11.5	14.2
7	0.00	0.10	17.9	16.7
8	0.10	0.24	16.7	15.4
9	0.24	0.34	15.4	14.9
10	0.34	0.53	14.9	14.2
11	0.53	0.58	14.2	14.3
12	0.58	0.74	14.3	14.0
13	0.15	0.25	7.0	8.6
14	0.25	0.31	8.6	9.5
15	0.20	0.40	9.5	10.7
16	0.50	0.72	12.5	13.9
17	0.00	0.10	21.6	20.0
18	0.10	0.30	20.0	17.2
19	0.30	0.51	17.2	15.2
20	0.29	0.71	28.6	27.1

Table F.15: Reflection surface coordinates of line D(N).

Reflection surface coordinates				
$No.$	$s_0(m)$	$s_1(m)$	$t_0(ns)$	$t_1(ns)$
1	0.00	0.15	6.9	7.5
2	0.15	0.30	7.5	9.1
3	0.00	0.04	17.8	17.2
4	0.04	0.25	17.0	13.0
5	0.25	0.50	13.0	9.0
6	0.00	0.10	18.8	17.4
7	0.10	0.18	17.4	16.2
8	0.18	0.23	16.2	15.4
9	0.23	0.40	15.4	13.3
10	0.40	0.67	13.3	11.5
11	0.05	0.15	14.0	14.6
12	0.15	0.28	14.6	14.6
13	0.34	0.55	15.7	17.9
14	0.00	0.08	22.2	20.8
15	0.34	0.53	21.8	21.2

Table F.16: Reflection surface coordinates of line D(R).

Reflection surface coordinates				
$No.$	$s_0(m)$	$s_1(m)$	$t_0(ns)$	$t_1(ns)$
1	0.05	0.13	11.5	12.0
2	0.13	0.50	12.0	15.9
3	0.50	0.85	15.9	19.0
4	0.15	0.35	8.2	11.3
5	0.35	0.50	11.3	13.6
6	0.50	0.66	13.6	15.6
7	0.66	0.70	15.6	16.2
8	0.70	0.85	16.2	17.9
9	0.28	0.31	8.9	9.3
10	0.31	0.33	9.3	9.3
11	0.33	0.46	9.3	8.7
12	0.46	0.85	8.7	6.8
13	0.68	0.85	22.7	23.2
14	0.30	0.70	29.5	27.7
15	0.20	0.40	21.2	22.1

Table F.17: Reflection surface coordinates of line E(N).

Reflection surface coordinates				
$No.$	$s_0(m)$	$s_1(m)$	$t_0(ns)$	$t_1(ns)$
1	0.00	0.04	5.2	4.8
2	0.04	0.09	4.8	4.8
3	0.09	0.20	4.8	5.2
4	0.00	0.05	18.5	17.8
5	0.05	0.21	17.8	15.6
6	0.05	0.20	19.3	17.5
7	0.20	0.25	17.5	17.5
8	0.25	0.42	17.5	15.1
9	0.42	0.70	15.1	12.5
10	0.02	0.20	22.5	21.4
11	0.20	0.26	21.4	21.2
12	0.26	0.35	21.2	20.3
13	0.35	0.65	20.3	19.3
14	0.65	0.75	19.3	18.9
15	0.35	0.40	9.4	9.6
16	0.40	0.46	9.6	9.2
17	0.46	0.49	9.2	9.2

Table F.18: Reflection surface coordinates of line E(R).

Reflection surface coordinates				
$No.$	$s_0(m)$	$s_1(m)$	$t_0(ns)$	$t_1(ns)$
1	0.65	0.71	5.2	4.9
2	0.71	0.83	4.9	5.0
3	0.83	0.93	5.0	5.7
4	0.93	0.97	5.7	5.7
5	0.63	0.97	15.7	20.2
6	0.55	0.76	16.8	19.0
7	0.42	0.55	15.2	16.8
8	0.05	0.42	11.8	15.2
9	0.28	0.32	8.0	8.0
10	0.32	0.36	8.5	8.5
11	0.36	0.41	8.5	9.0
12	0.41	0.45	9.0	9.0
13	0.45	0.97	20.0	23.2
14	0.21	0.40	19.4	20.0
15	0.02	0.21	18.3	19.4
16	0.76	0.91	28.6	27.3
17	0.39	0.53	29.1	28.4
18	0.85	0.97	20.0	21.3
19	0.78	0.86	22.8	23.5
20	0.86	0.91	23.5	24.3
21	0.91	0.95	24.3	24.5
22	0.95	0.97	24.5	24.4

Table F.19: Reflection surface coordinates of line F(N).

Reflection surface coordinates				
$No.$	$s_0(m)$	$s_1(m)$	$t_0(ns)$	$t_1(ns)$
1	0.02	0.06	18.7	18.1
2	0.06	0.10	18.1	17.7
3	0.10	0.15	17.7	17.5
4	0.15	0.32	17.5	15.1
5	0.32	0.45	15.1	13.6
6	0.45	0.50	13.6	13.0
7	0.08	0.17	19.8	19.5
8	0.17	0.21	19.5	19.5
9	0.48	0.55	19.3	19.1

Table F.20: Reflection surface coordinates of line F(R).

Reflection surface coordinates				
$No.$	$s_0(m)$	$s_1(m)$	$t_0(ns)$	$t_1(ns)$
1	0.13	0.23	19.0	19.4
2	0.49	0.65	19.0	19.2
3	0.24	0.50	13.4	16.3
4	0.50	0.56	16.3	16.9
5	0.56	0.59	16.9	17.0
6	0.59	0.62	17.0	17.3
7	0.62	0.65	17.3	17.3
8	0.65	0.74	17.3	18.5
9	0.74	0.78	18.5	18.7
10	0.78	0.82	19.3	19.8
11	0.15	0.20	13.6	13.4

Table F.21: Reflection surface coordinates of line G(N).

Reflection surface coordinates				
$No.$	$s_0(m)$	$s_1(m)$	$t_0(ns)$	$t_1(ns)$
1	0.47	0.64	18.2	17.8
2	0.20	0.32	14.0	12.8
3	0.32	0.40	12.8	12.2
4	0.40	0.55	12.2	11.8
5	0.19	0.44	11.0	12.9
6	0.09	0.12	18.3	18.1
7	0.12	0.16	18.1	18.2
8	0.16	0.24	18.2	18.5
9	0.00	0.12	22.8	21.6
10	0.44	0.54	19.5	19.4

Table F.22: Reflection surface coordinates of line G(R).

Reflection surface coordinates				
$No.$	$s_0(m)$	$s_1(m)$	$t_0(ns)$	$t_1(ns)$
1	0.00	0.11	17.9	18.3
2	0.11	0.20	12.0	13.2
3	0.20	0.37	13.2	15.0
4	0.44	0.52	17.2	17.1
5	0.52	0.56	17.1	17.3
6	0.24	0.29	18.5	18.6
7	0.29	0.32	18.6	18.2
8	0.32	0.36	18.2	18.2
9	0.36	0.39	18.2	18.4
10	0.39	0.45	18.4	18.6
11	0.48	0.60	18.3	19.1
12	0.14	0.30	12.0	10.6

Table F.23: Reflection surface coordinates of line H(N).

Reflection surface coordinates				
$No.$	$s_0(m)$	$s_1(m)$	$t_0(ns)$	$t_1(ns)$
1	0.06	0.19	16.5	16.8
2	0.17	0.28	16.1	16.3
3	0.24	0.31	14.8	14.7
4	0.31	0.40	14.7	14.2
5	0.40	0.50	14.2	13.1
6	0.35	0.40	15.8	15.8
7	0.40	0.46	16.3	16.0
8	0.27	0.35	18.0	18.1
9	0.00	0.05	21.2	20.9
10	0.17	0.28	6.9	6.9
11	0.41	0.49	8.0	8.1
12	0.49	0.55	8.1	8.2
13	0.40	0.45	20.1	20.1
14	0.46	0.55	19.8	19.8

Table F.24: Reflection surface coordinates of line H(R).

Reflection surface coordinates				
$No.$	$s_0(m)$	$s_1(m)$	$t_0(ns)$	$t_1(ns)$
1	0.06	0.10	13.3	13.8
2	0.10	0.16	13.8	14.4
3	0.16	0.21	14.6	14.9
4	0.21	0.28	14.9	15.7
5	0.28	0.32	15.7	15.8
6	0.02	0.05	16.1	16.0
7	0.05	0.09	16.0	16.0
8	0.09	0.15	16.0	16.3
9	0.16	0.21	16.1	16.1
10	0.21	0.25	16.0	16.0
11	0.22	0.27	16.8	16.5
12	0.27	0.31	16.5	16.5
13	0.31	0.36	16.3	16.3
14	0.37	0.42	16.8	16.5
15	0.42	0.46	16.5	16.5
16	0.46	0.51	16.5	16.9
17	0.45	0.53	17.8	18.2
18	0.20	0.30	7.3	7.5
19	0.30	0.36	7.5	7.7
20	0.38	0.51	20.9	21.3
21	0.09	0.15	18.4	18.5
22	0.15	0.24	18.8	19.0
23	0.24	0.30	19.0	19.3

G

Buried rock surfaces keystone Hunebed D14

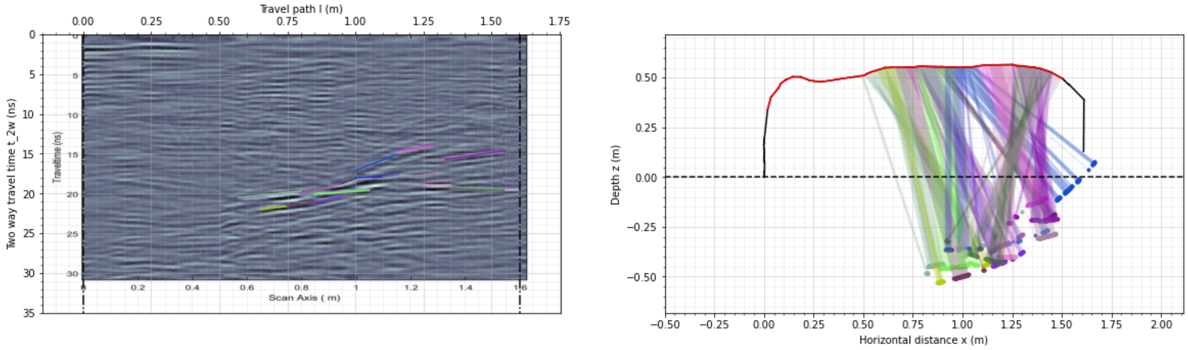

Figure G.1: Buried rock surface coordinates with respect to the exposed rock contour (incl. GPR survey path) for line 1(N). Also including the processed GPR diagram and identified reflection surfaces

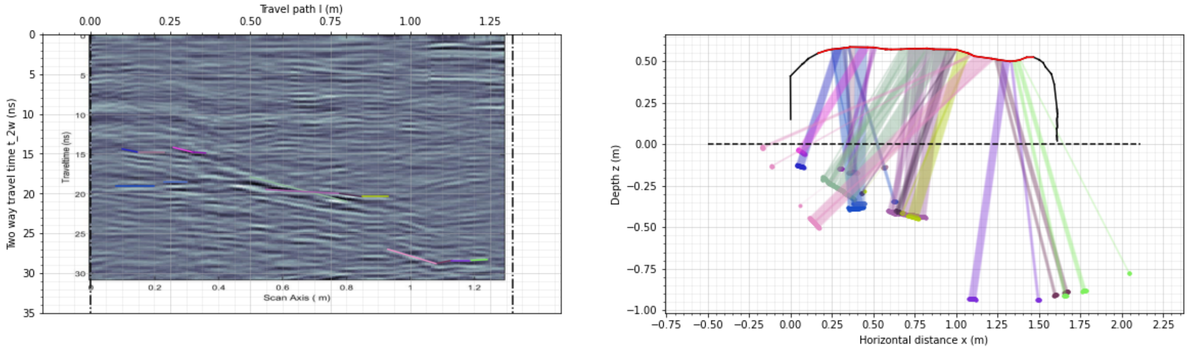

Figure G.2: Buried rock surface coordinates with respect to the exposed rock contour (incl. GPR survey path) for line 1(R). Also including the processed GPR diagram and identified reflection surfaces

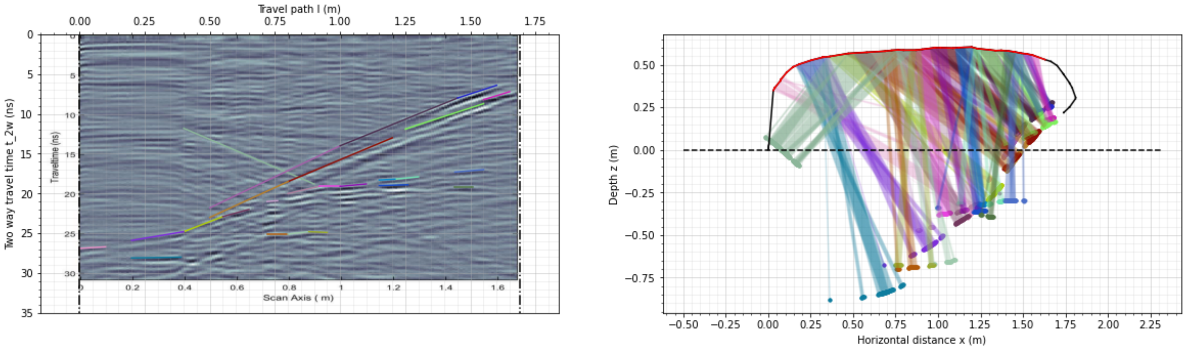

Figure G.3: Buried rock surface coordinates with respect to the exposed rock contour (incl. GPR survey path) for line 2(N). Also including the processed GPR diagram and identified reflection surfaces

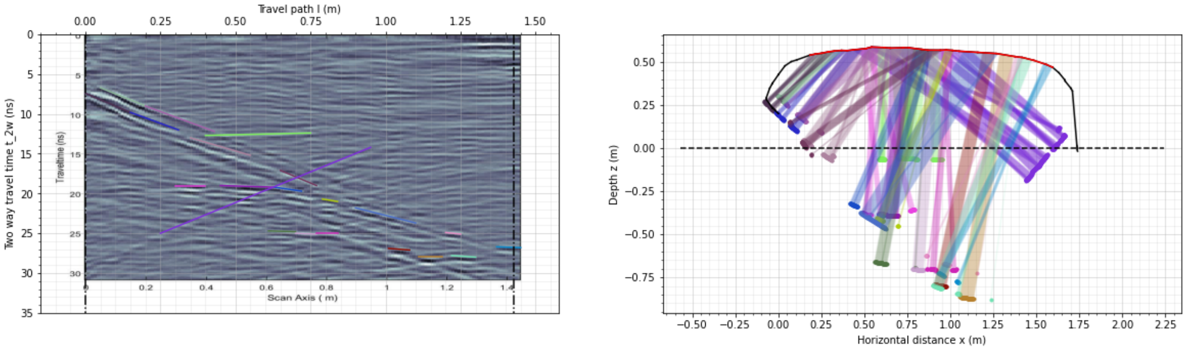

Figure G.4: Buried rock surface coordinates with respect to the exposed rock contour (incl. GPR survey path) for line 2(R). Also including the processed GPR diagram and identified reflection surfaces

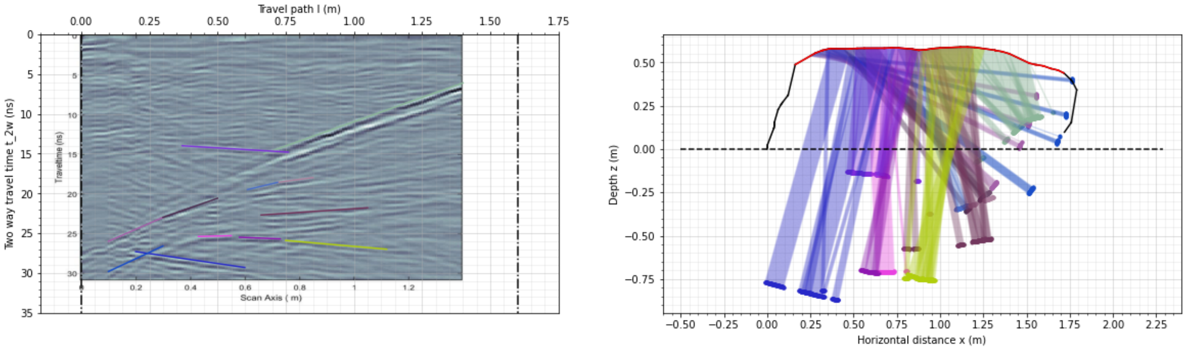

Figure G.5: Buried rock surface coordinates with respect to the exposed rock contour (incl. GPR survey path) for line 3(N). Also including the processed GPR diagram and identified reflection surfaces

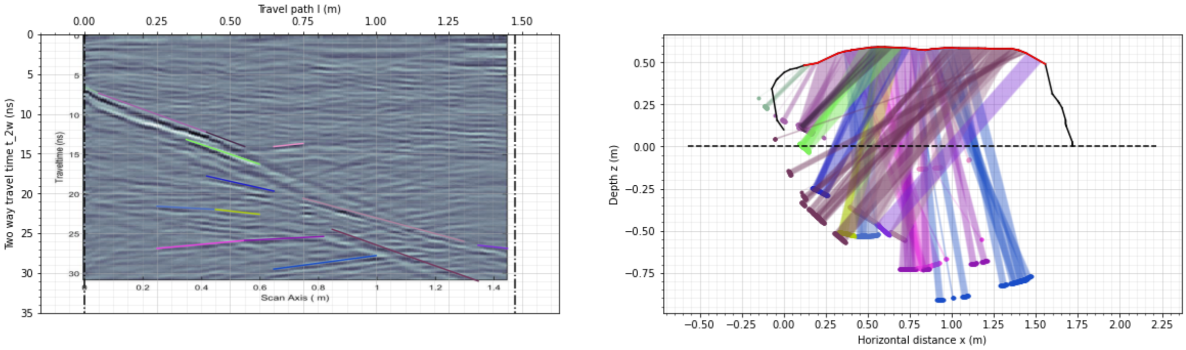

Figure G.6: Buried rock surface coordinates with respect to the exposed rock contour (incl. GPR survey path) for line 3(R). Also including the processed GPR diagram and identified reflection surfaces

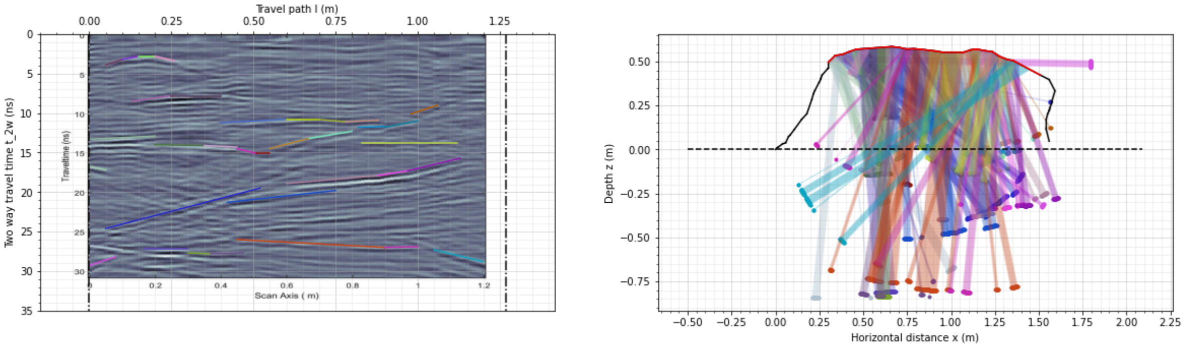

Figure G.7: Buried rock surface coordinates with respect to the exposed rock contour (incl. GPR survey path) for line 4(N). Also including the processed GPR diagram and identified reflection surfaces

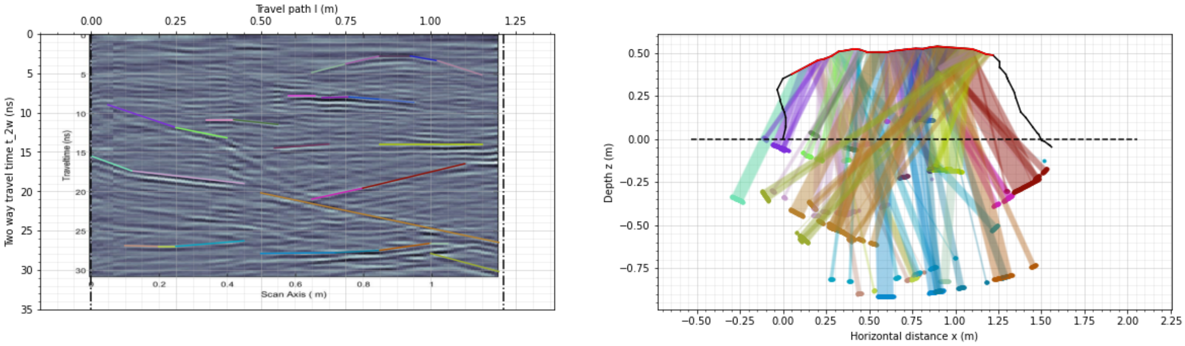

Figure G.8: Buried rock surface coordinates with respect to the exposed rock contour (incl. GPR survey path) for line 4(R). Also including the processed GPR diagram and identified reflection surfaces

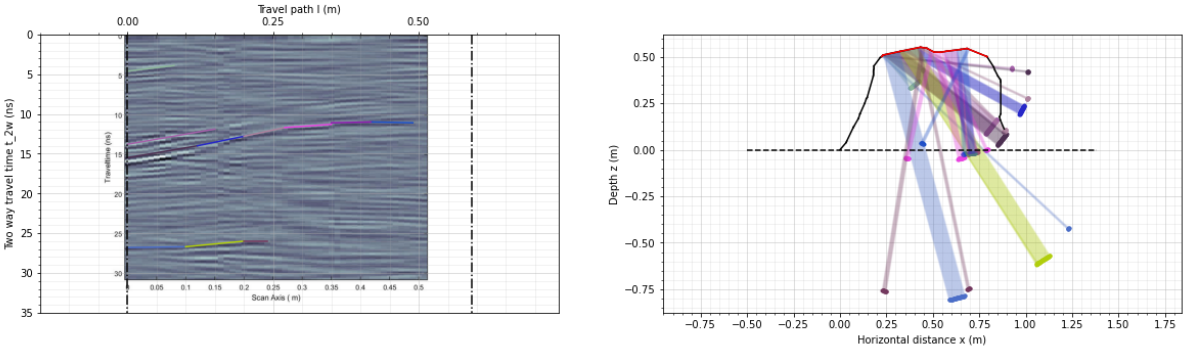

Figure G.9: Buried rock surface coordinates with respect to the exposed rock contour (incl. GPR survey path) for line A(N). Also including the processed GPR diagram and identified reflection surfaces

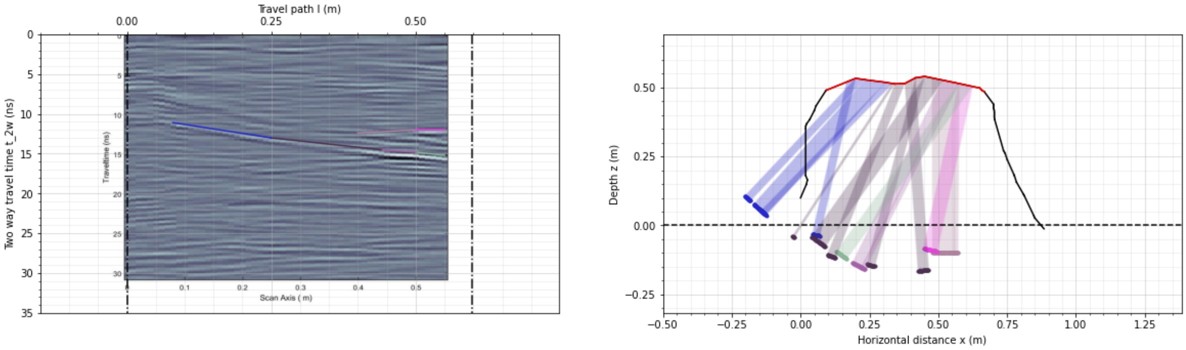

Figure G.10: Buried rock surface coordinates with respect to the exposed rock contour (incl. GPR survey path) for line A(R). Also including the processed GPR diagram and identified reflection surfaces

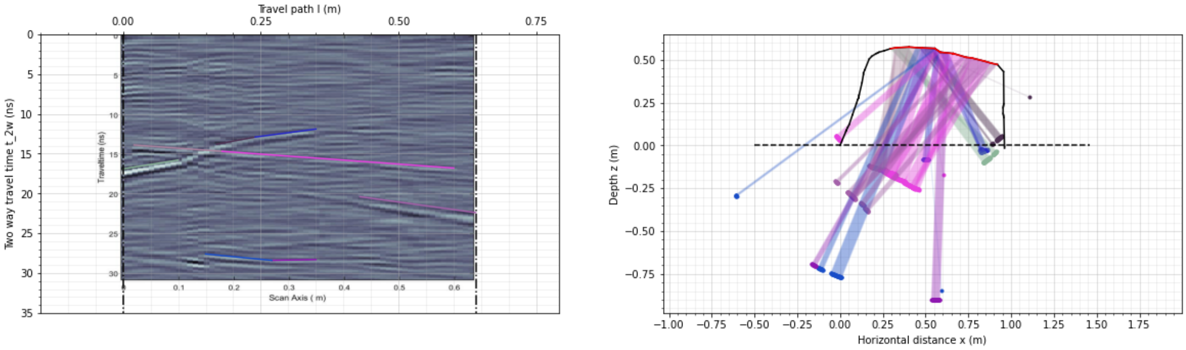

Figure G.11: Buried rock surface coordinates with respect to the exposed rock contour (incl. GPR survey path) for line B(N). Also including the processed GPR diagram and identified reflection surfaces

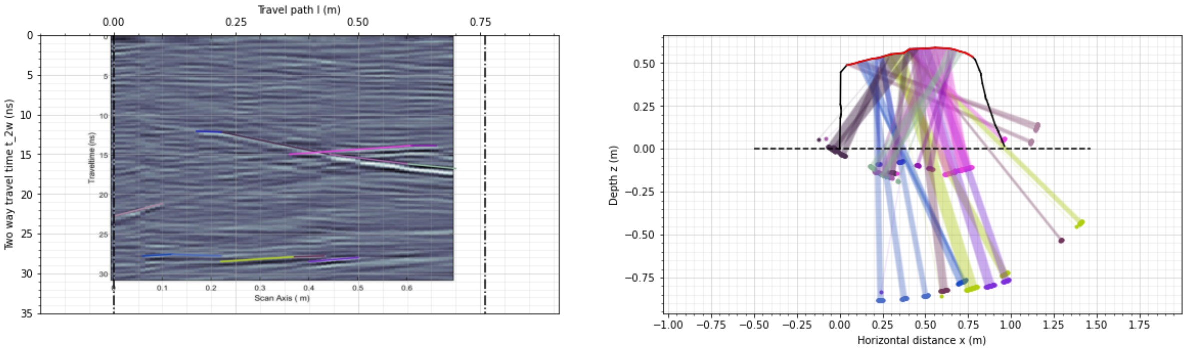

Figure G.12: Buried rock surface coordinates with respect to the exposed rock contour (incl. GPR survey path) for line B(R). Also including the processed GPR diagram and identified reflection surfaces

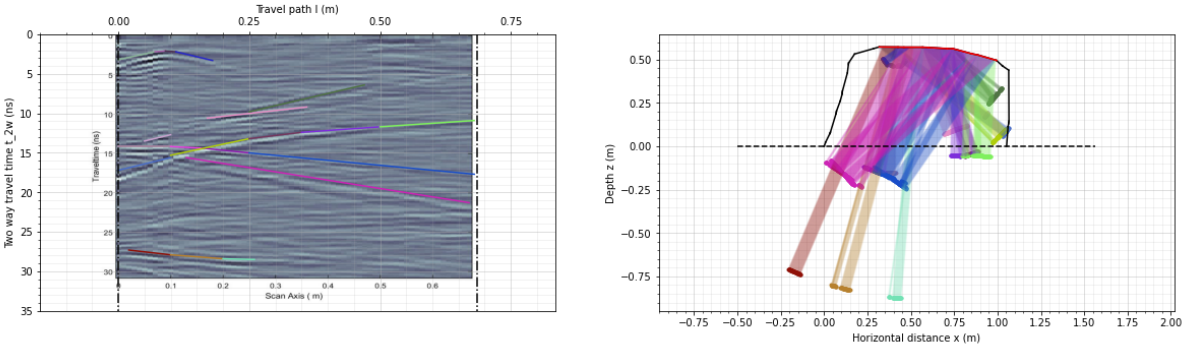

Figure G.13: Buried rock surface coordinates with respect to the exposed rock contour (incl. GPR survey path) for line C(N). Also including the processed GPR diagram and identified reflection surfaces

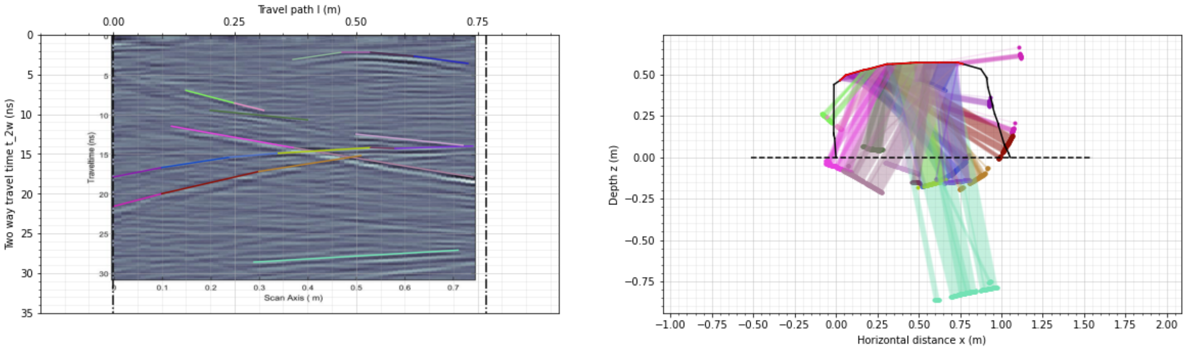

Figure G.14: Buried rock surface coordinates with respect to the exposed rock contour (incl. GPR survey path) for line C(R). Also including the processed GPR diagram and identified reflection surfaces

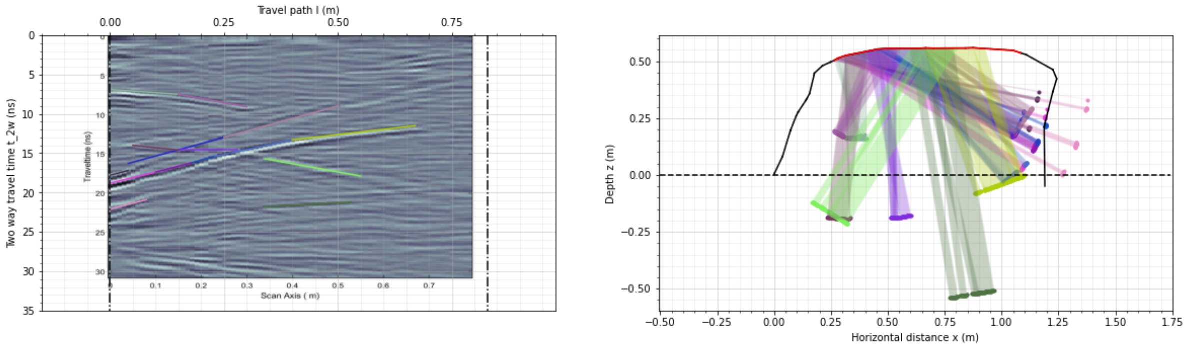

Figure G.15: Buried rock surface coordinates with respect to the exposed rock contour (incl. GPR survey path) for line D(N). Also including the processed GPR diagram and identified reflection surfaces

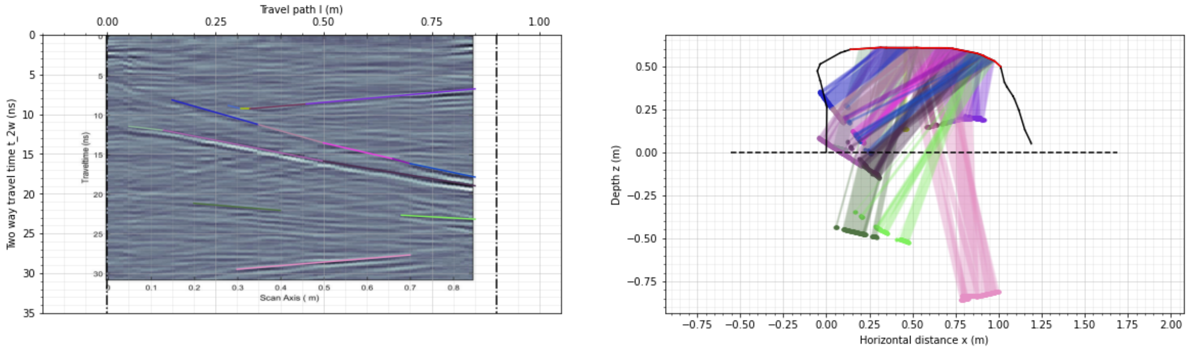

Figure G.16: Buried rock surface coordinates with respect to the exposed rock contour (incl. GPR survey path) for line D(R). Also including the processed GPR diagram and identified reflection surfaces

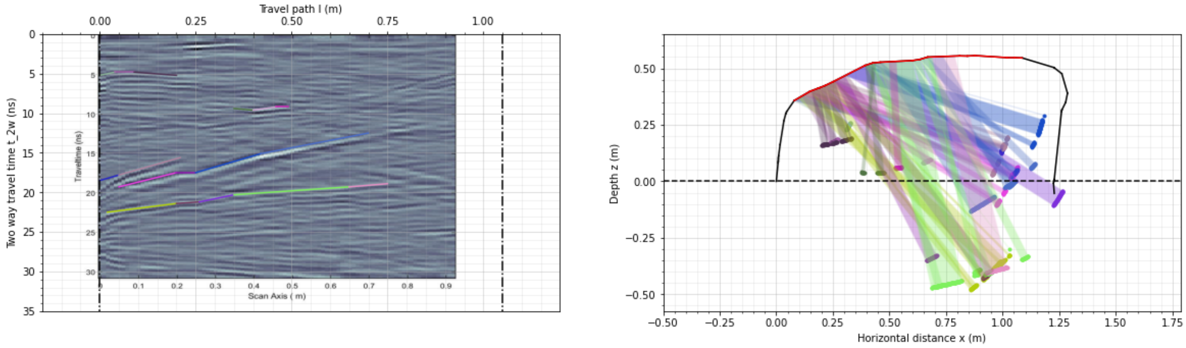

Figure G.17: Buried rock surface coordinates with respect to the exposed rock contour (incl. GPR survey path) for line E(N). Also including the processed GPR diagram and identified reflection surfaces

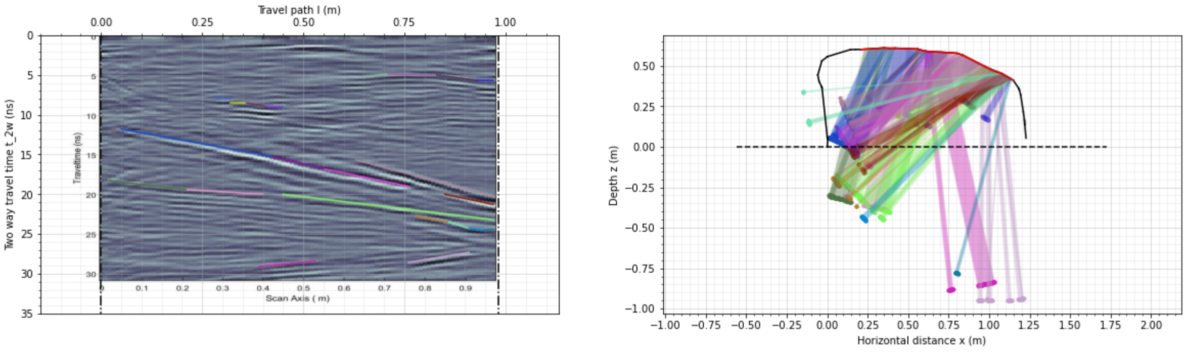

Figure G.18: Buried rock surface coordinates with respect to the exposed rock contour (incl. GPR survey path) for line E(R). Also including the processed GPR diagram and identified reflection surfaces

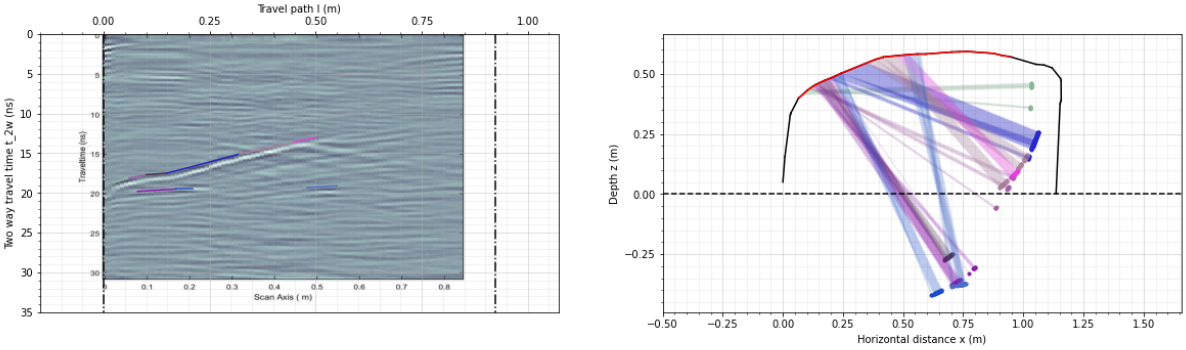

Figure G.19: Buried rock surface coordinates with respect to the exposed rock contour (incl. GPR survey path) for line F(N). Also including the processed GPR diagram and identified reflection surfaces

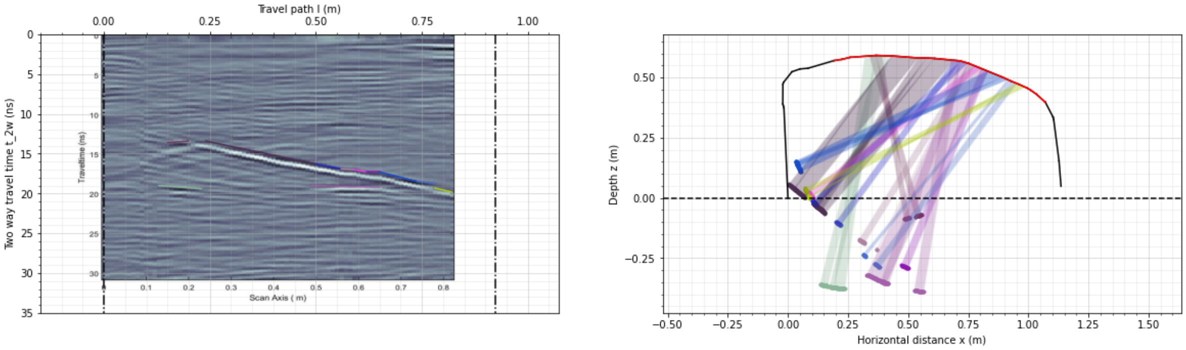

Figure G.20: Buried rock surface coordinates with respect to the exposed rock contour (incl. GPR survey path) for line F(R). Also including the processed GPR diagram and identified reflection surfaces

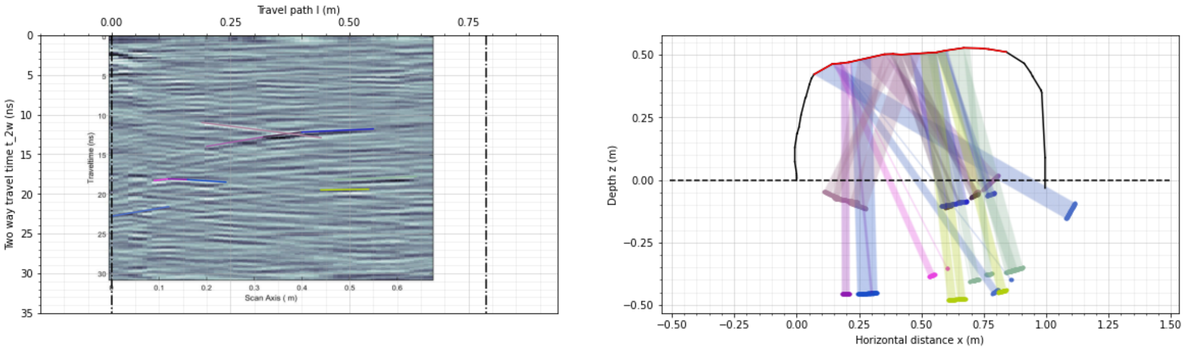

Figure G.21: Buried rock surface coordinates with respect to the exposed rock contour (incl. GPR survey path) for line G(N). Also including the processed GPR diagram and identified reflection surfaces

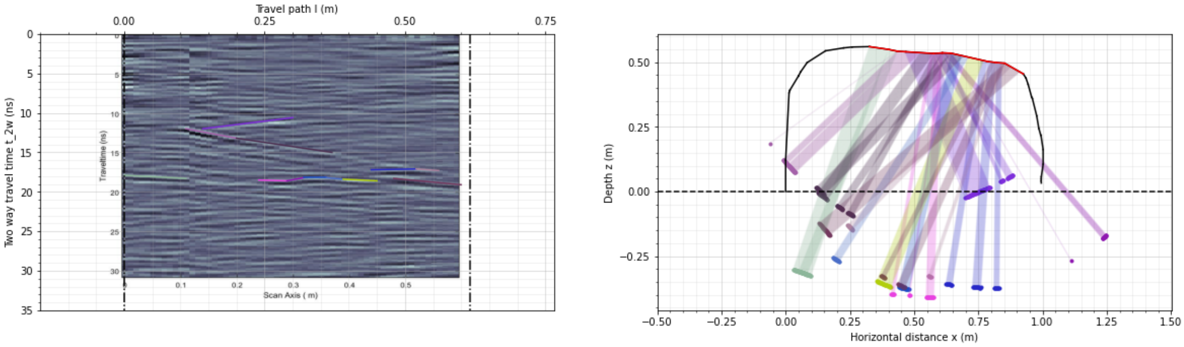

Figure G.22: Buried rock surface coordinates with respect to the exposed rock contour (incl. GPR survey path) for line G(R). Also including the processed GPR diagram and identified reflection surfaces

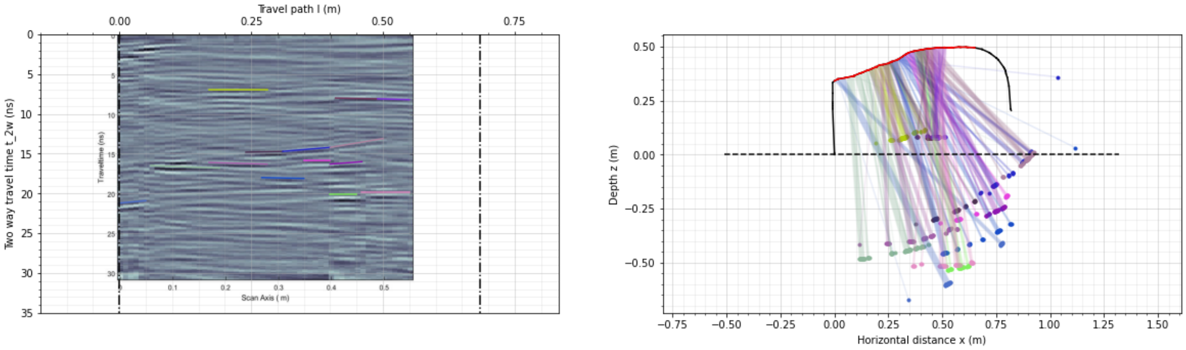

Figure G.23: Buried rock surface coordinates with respect to the exposed rock contour (incl. GPR survey path) for line H(N). Also including the processed GPR diagram and identified reflection surfaces

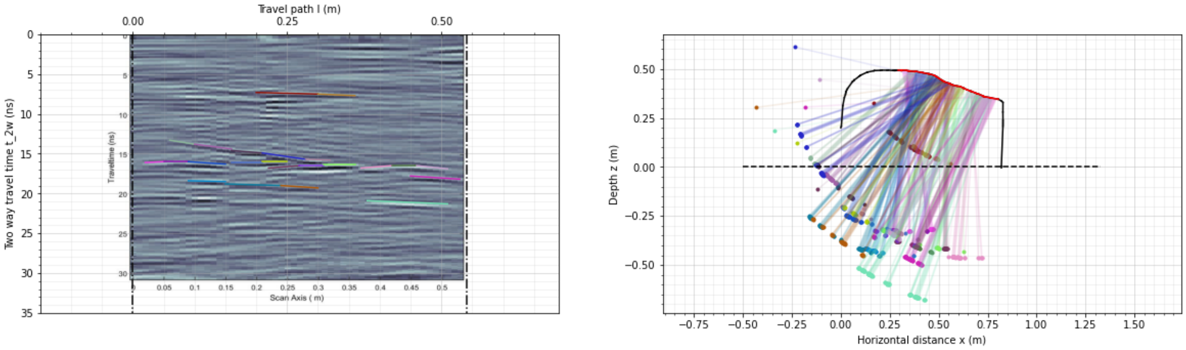

Figure G.24: Buried rock surface coordinates with respect to the exposed rock contour (incl. GPR survey path) for line H(R). Also including the processed GPR diagram and identified reflection surfaces

H

Modelled GPR diagrams keystone Hunebed D14

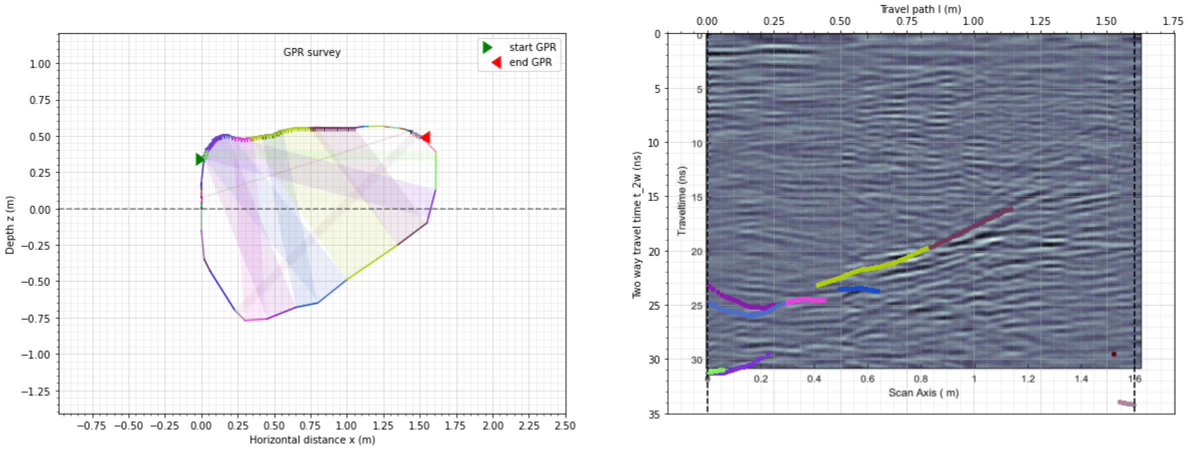

Figure H.1: Modelled GPR diagram of estimated rock contour 1 for line 1(N) showing the reflection surfaces in various colors corresponding to rock surfaces.

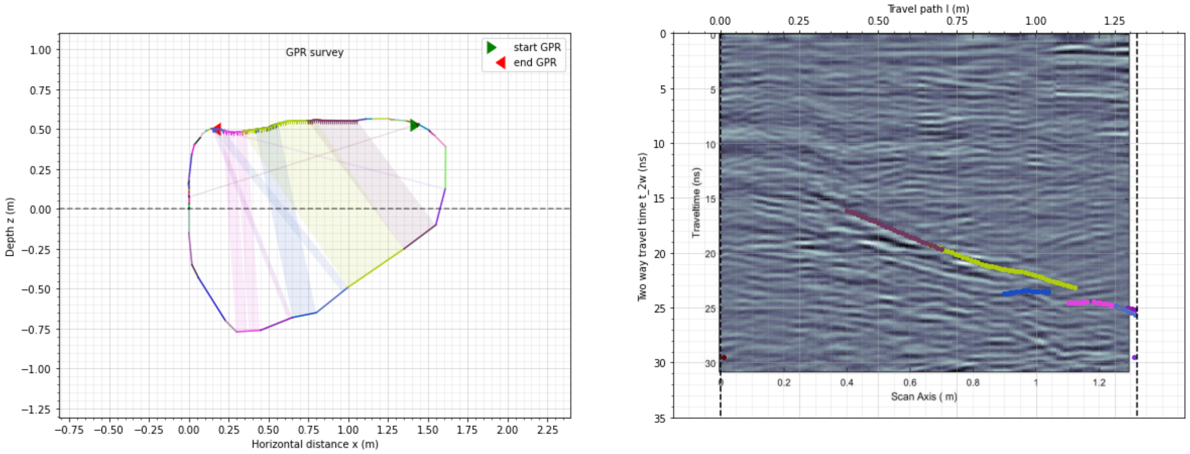

Figure H.2: Modelled GPR diagram of estimated rock contour 1 for line 1(R) showing the reflection surfaces in various colors corresponding to rock surfaces.

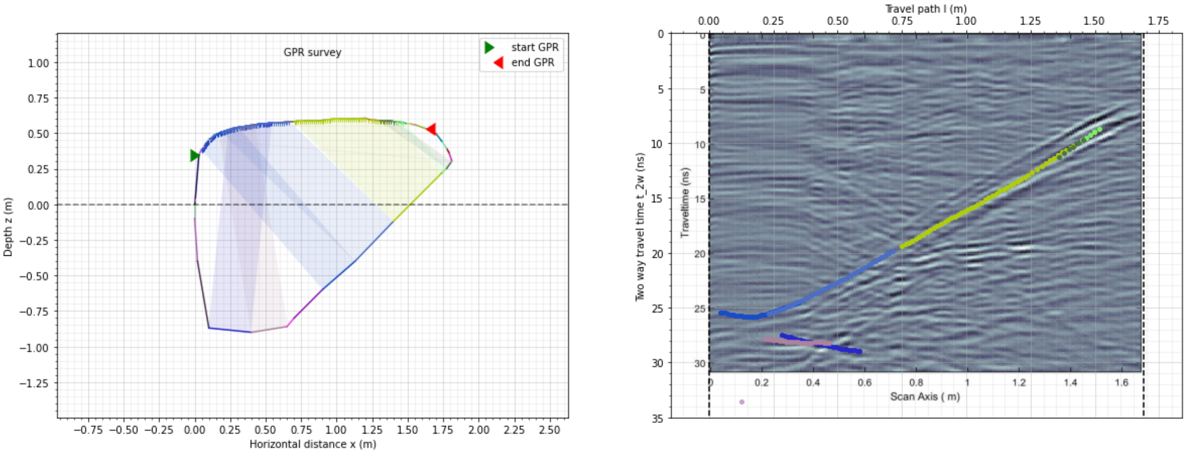

Figure H.3: Modelled GPR diagram of estimated rock contour 2 for line 2(N) showing the reflection surfaces in various colors corresponding to rock surfaces.

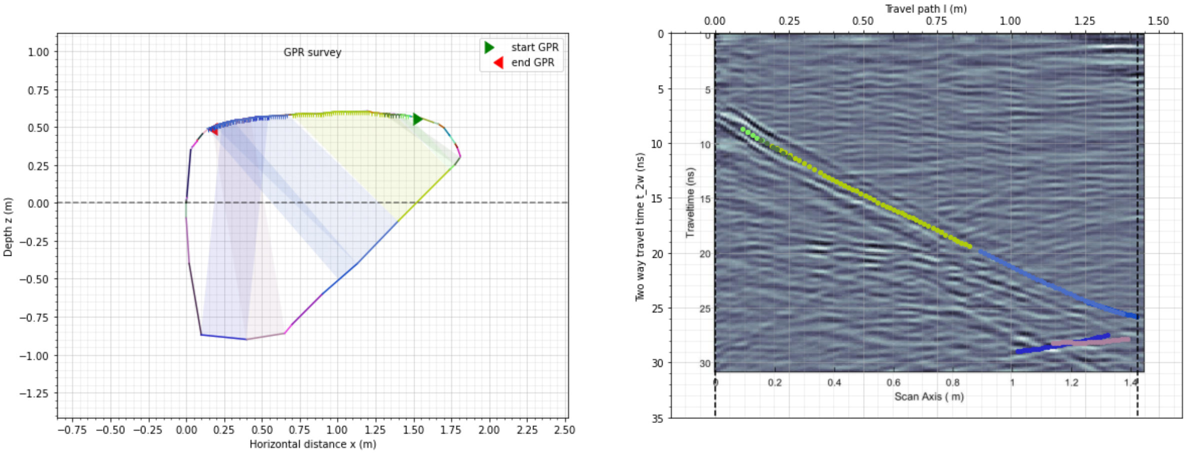

Figure H.4: Modelled GPR diagram of estimated rock contour 2 for line 2(R) showing the reflection surfaces in various colors corresponding to rock surfaces.

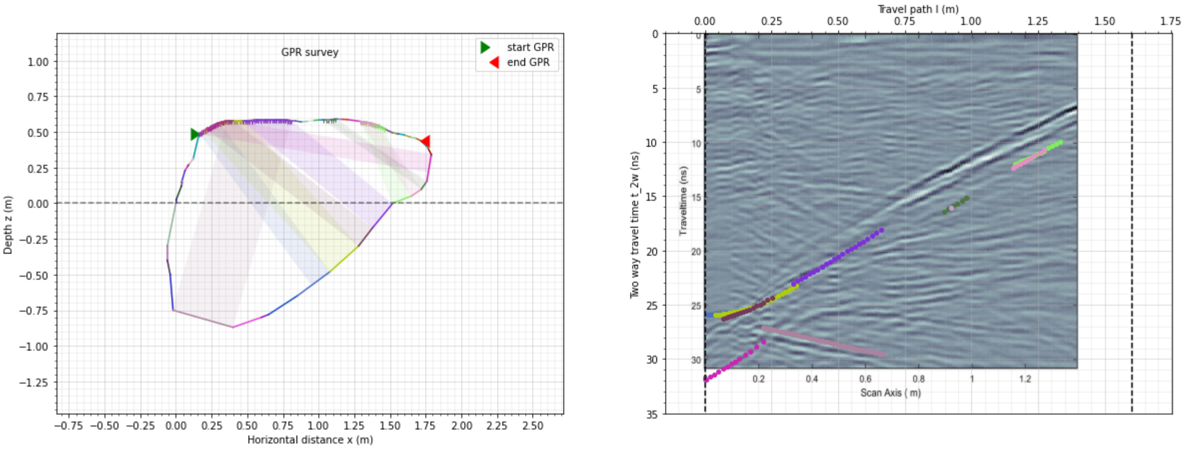

Figure H.5: Modelled GPR diagram of estimated rock contour 3 for line 3(N) showing the reflection surfaces in various colors corresponding to rock surfaces.

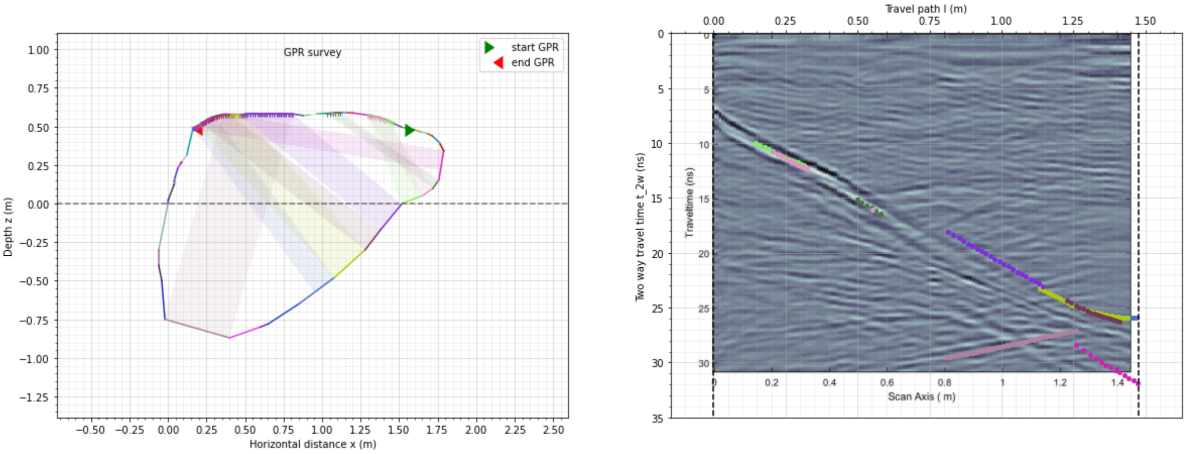

Figure H.6: Modelled GPR diagram of estimated rock contour 3 for line 3(R) showing the reflection surfaces in various colors corresponding to rock surfaces.

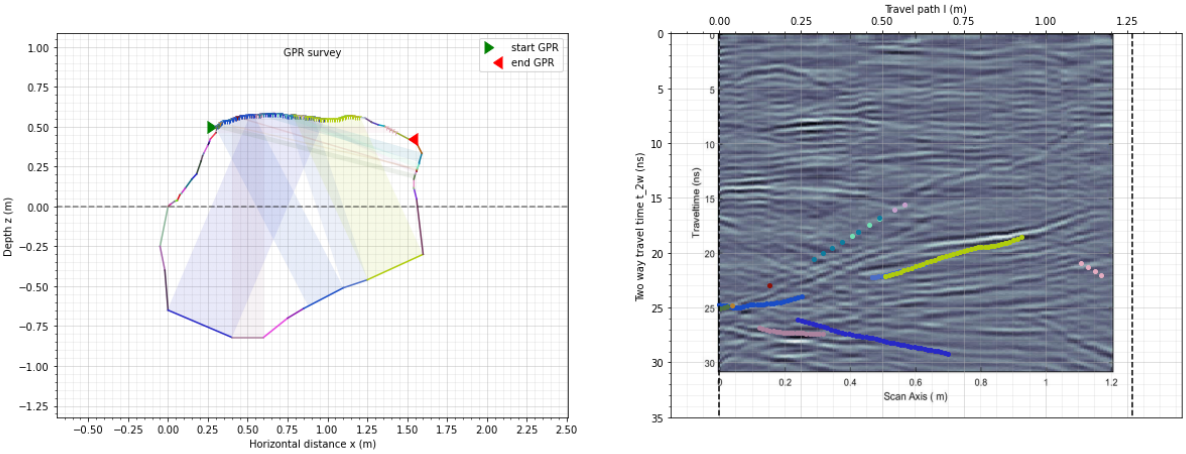

Figure H.7: Modelled GPR diagram of estimated rock contour 4 for line 4(N) showing the reflection surfaces in various colors corresponding to rock surfaces.

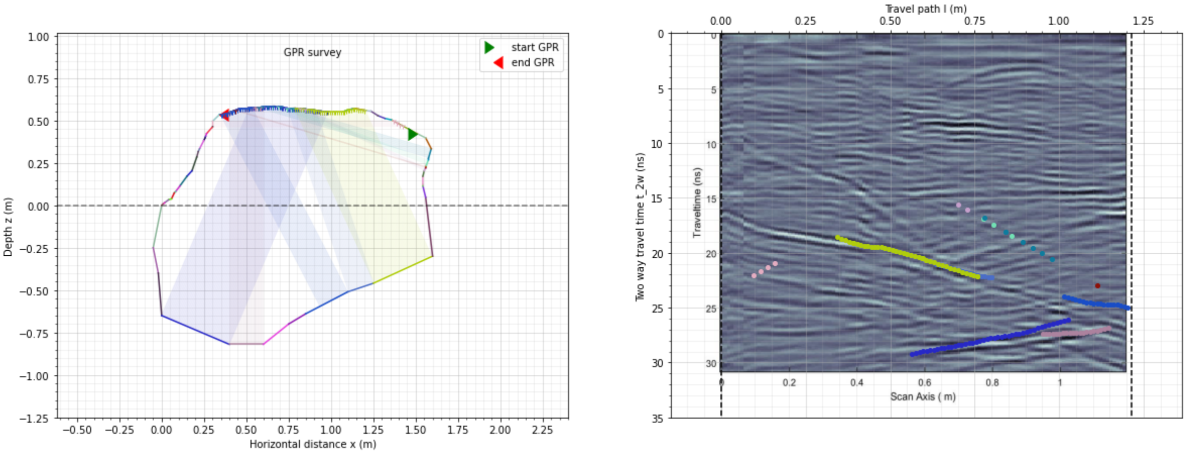

Figure H.8: Modelled GPR diagram of estimated rock contour 4 for line 4(R) showing the reflection surfaces in various colors corresponding to rock surfaces.

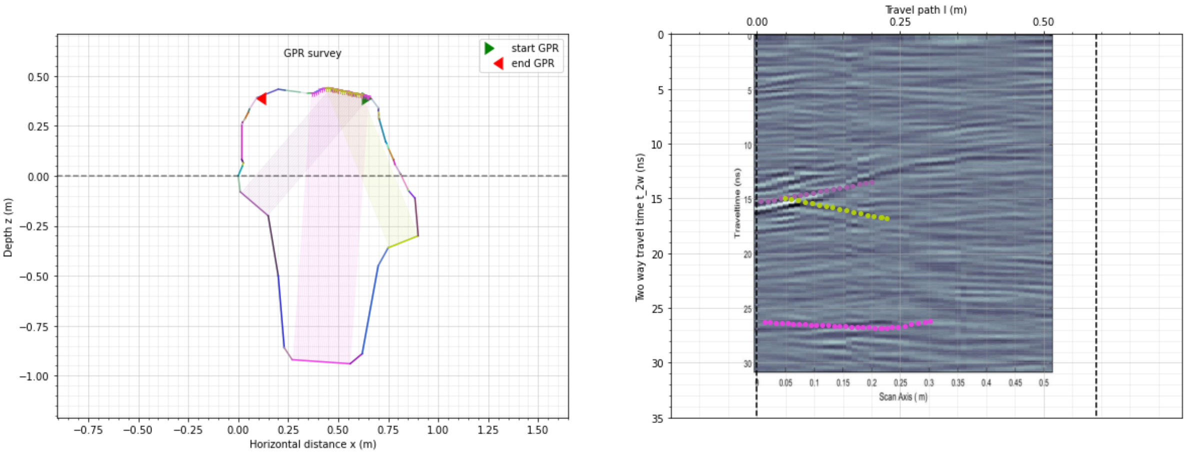

Figure H.9: Modelled GPR diagram of estimated rock contour A for line A(N) showing the reflection surfaces in various colors corresponding to rock surfaces.

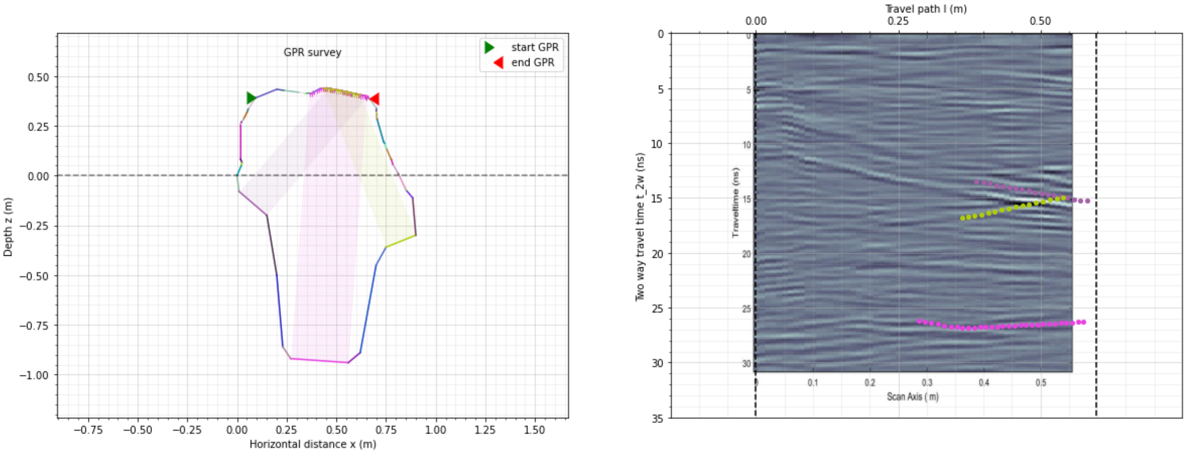

Figure H.10: Modelled GPR diagram of estimated rock contour A for line A(R) showing the reflection surfaces in various colors corresponding to rock surfaces.

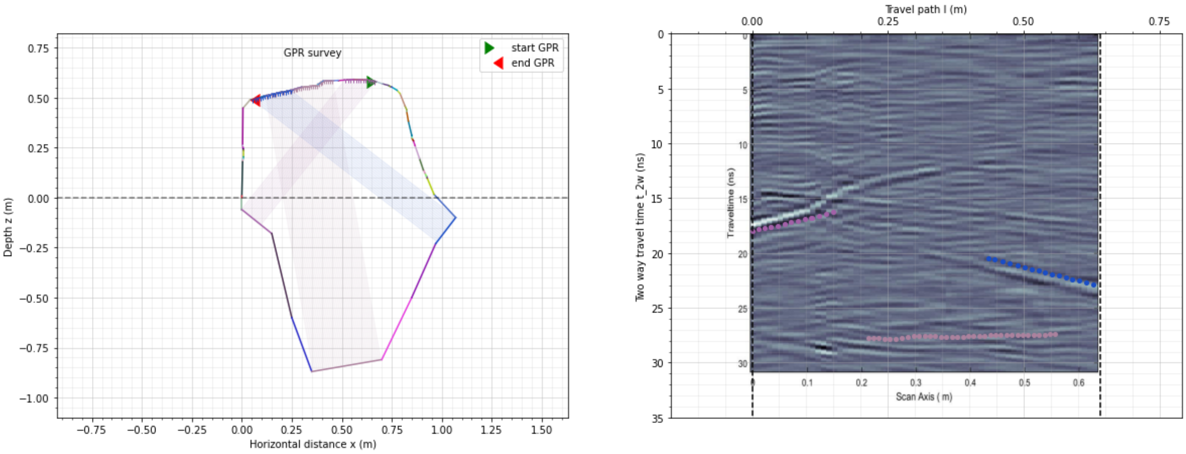

Figure H.11: Modelled GPR diagram of estimated rock contour B for line B(N) showing the reflection surfaces in various colors corresponding to rock surfaces.

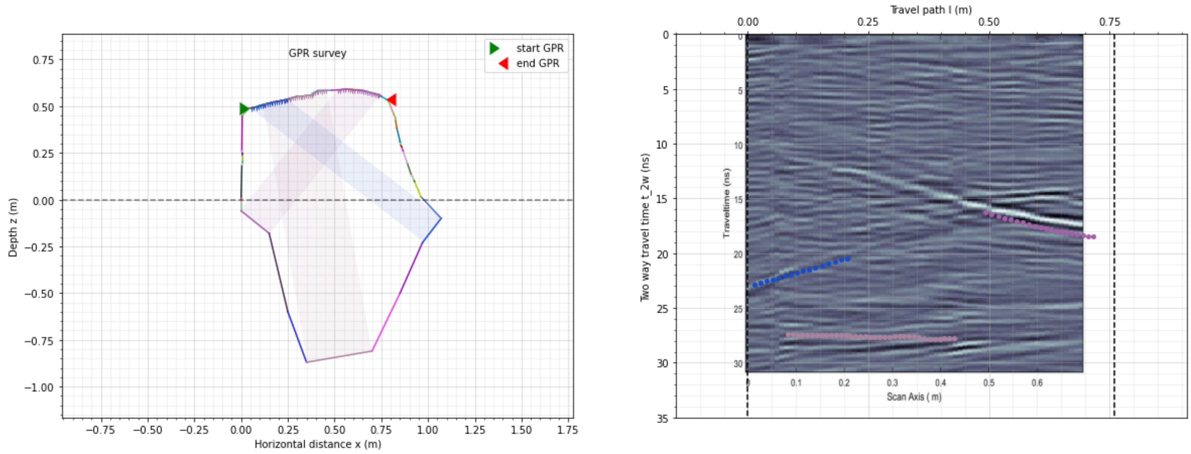

Figure H.12: Modelled GPR diagram of estimated rock contour B for line B(R) showing the reflection surfaces in various colors corresponding to rock surfaces.

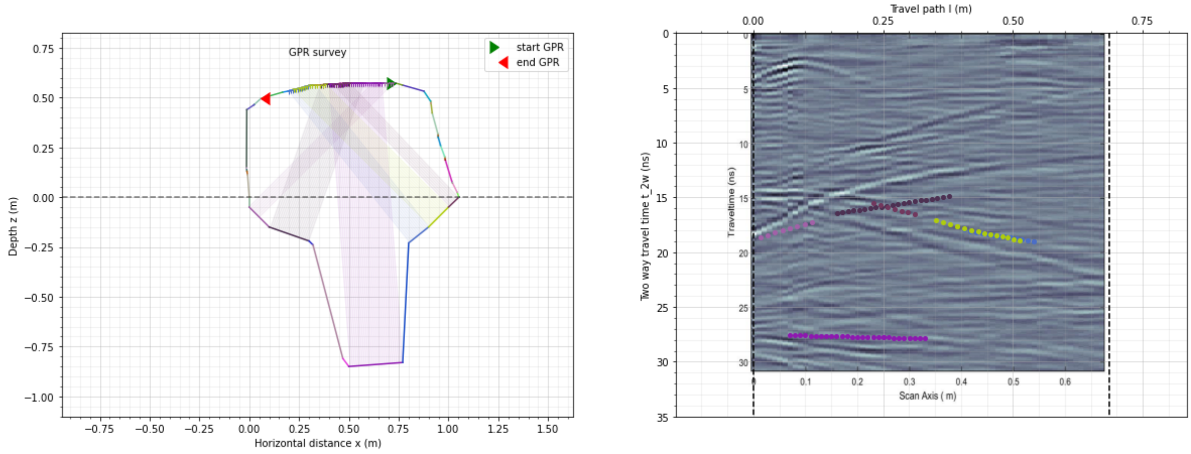

Figure H.13: Modelled GPR diagram of estimated rock contour C for line C(N) showing the reflection surfaces in various colors corresponding to rock surfaces.

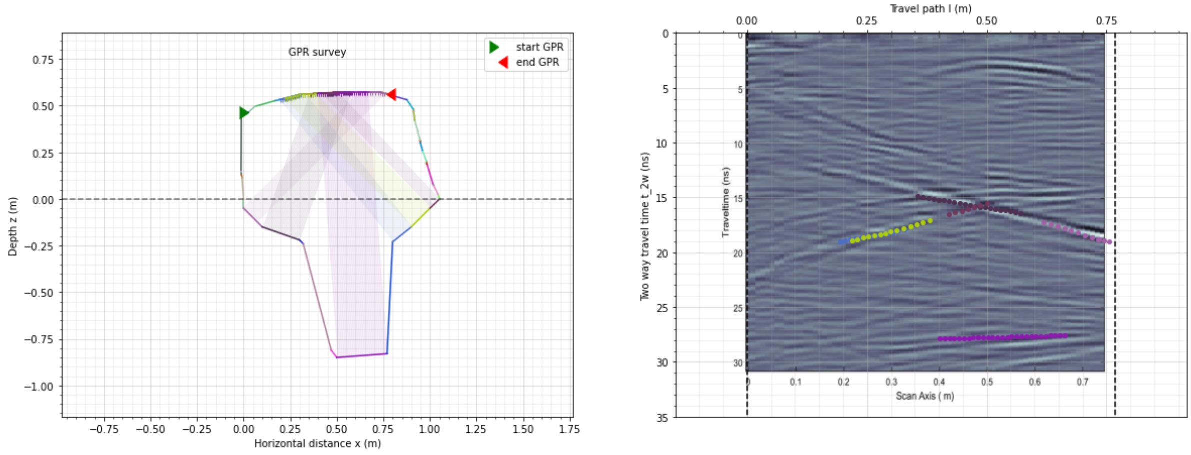

Figure H.14: Modelled GPR diagram of estimated rock contour C for line C(R) showing the reflection surfaces in various colors corresponding to rock surfaces.

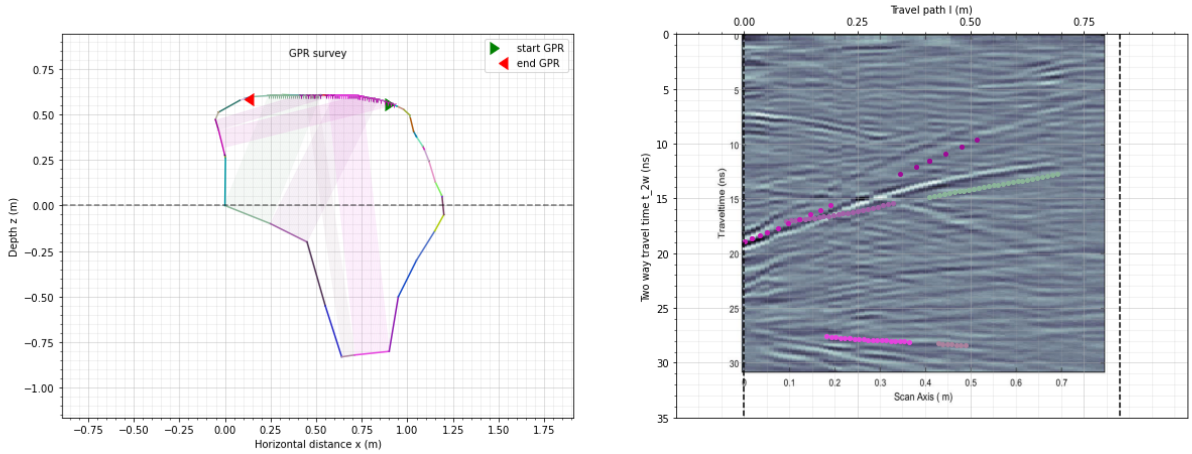

Figure H.15: Modelled GPR diagram of estimated rock contour D for line D(N) showing the reflection surfaces in various colors corresponding to rock surfaces.

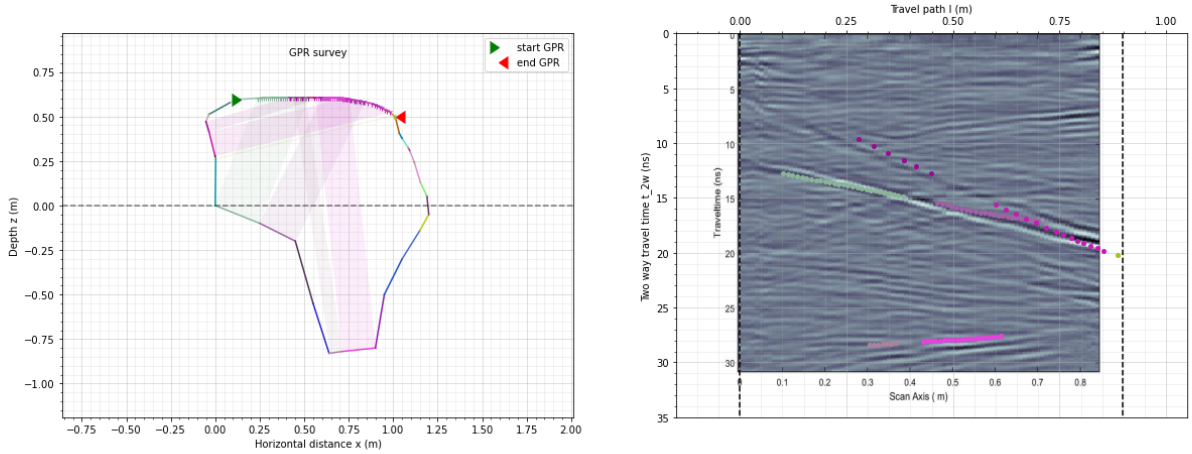

Figure H.16: Modelled GPR diagram of estimated rock contour D for line D(R) showing the reflection surfaces in various colors corresponding to rock surfaces.

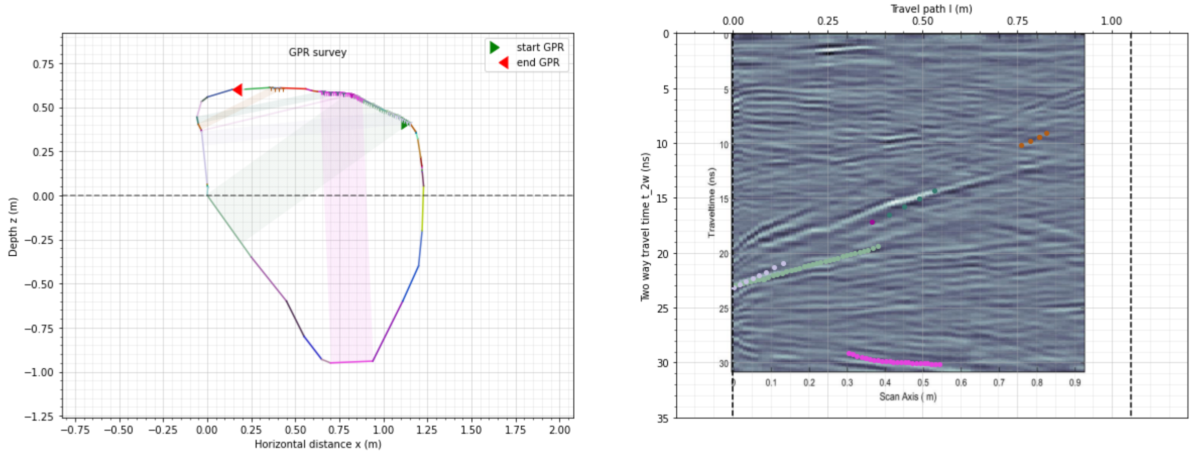

Figure H.17: Modelled GPR diagram of estimated rock contour E for line E(N) showing the reflection surfaces in various colors corresponding to rock surfaces.

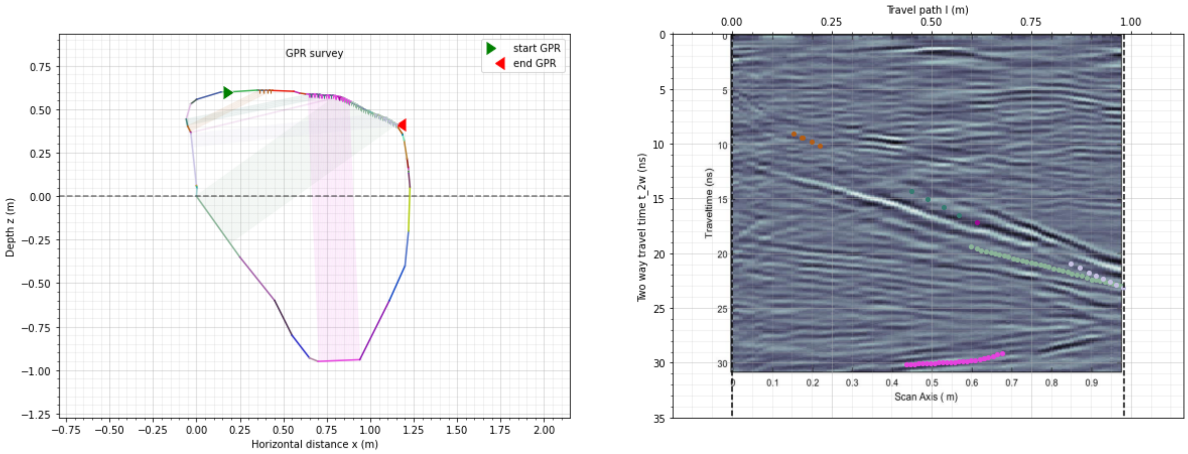

Figure H.18: Modelled GPR diagram of estimated rock contour E for line E(R) showing the reflection surfaces in various colors corresponding to rock surfaces.

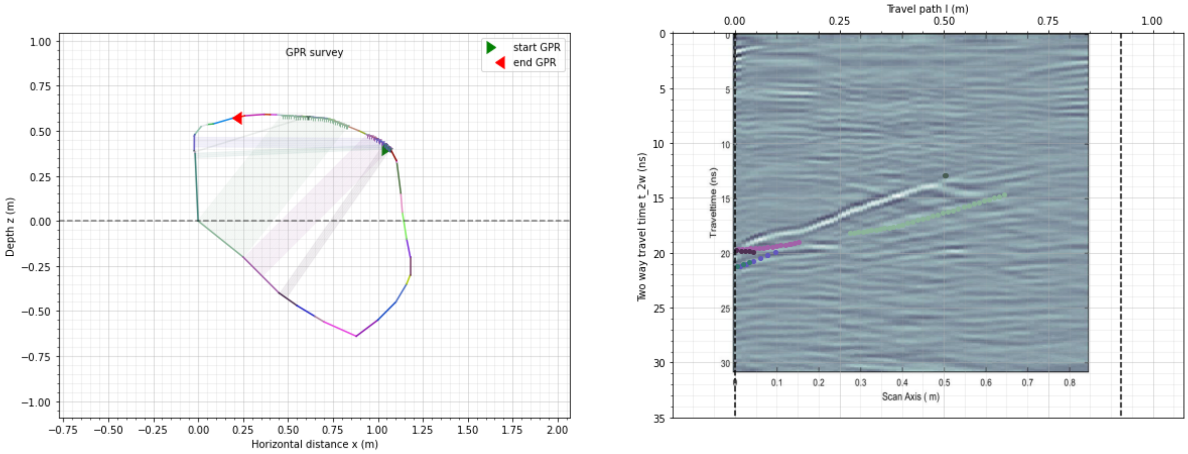

Figure H.19: Modelled GPR diagram of estimated rock contour F for line F(N) showing the reflection surfaces in various colors corresponding to rock surfaces.

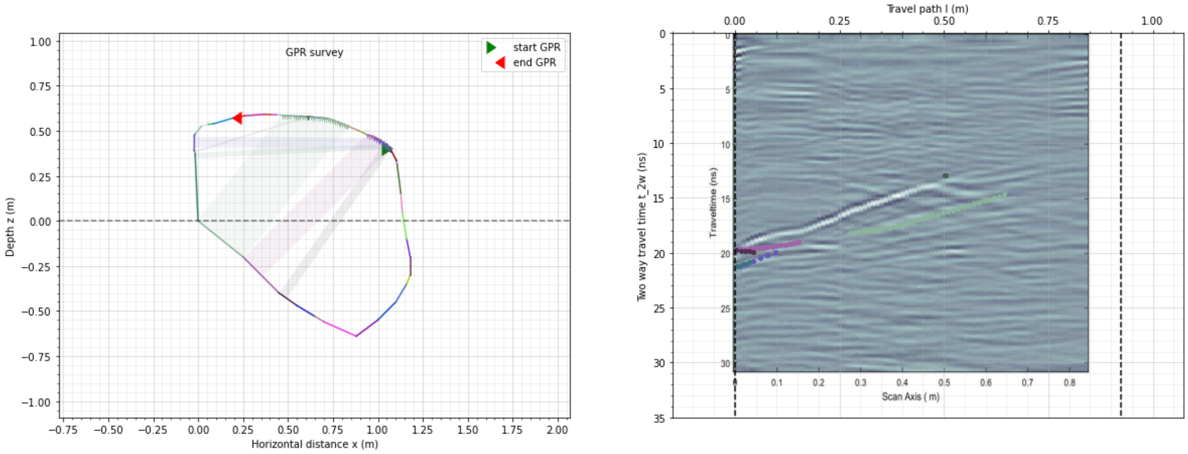

Figure H.20: Modelled GPR diagram of estimated rock contour F for line F(R) showing the reflection surfaces in various colors corresponding to rock surfaces.

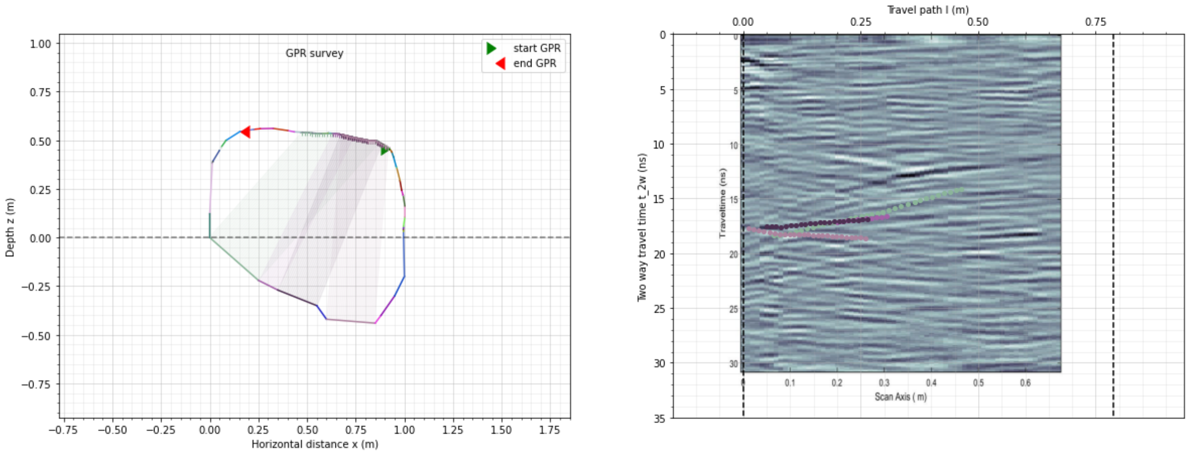

Figure H.21: Modelled GPR diagram of estimated rock contour G for line G(N) showing the reflection surfaces in various colors corresponding to rock surfaces.

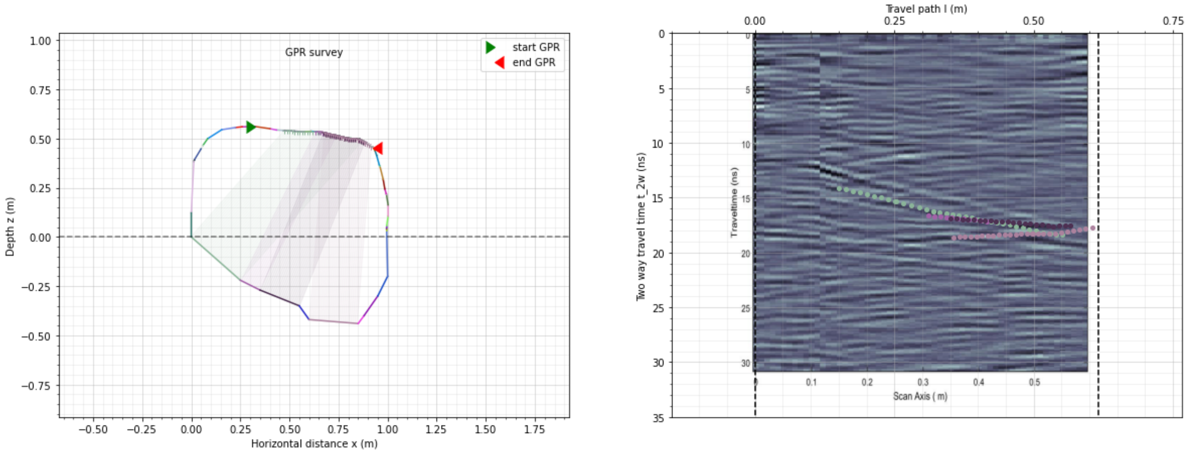

Figure H.22: Modelled GPR diagram of estimated rock contour G for line G(R) showing the reflection surfaces in various colors corresponding to rock surfaces.

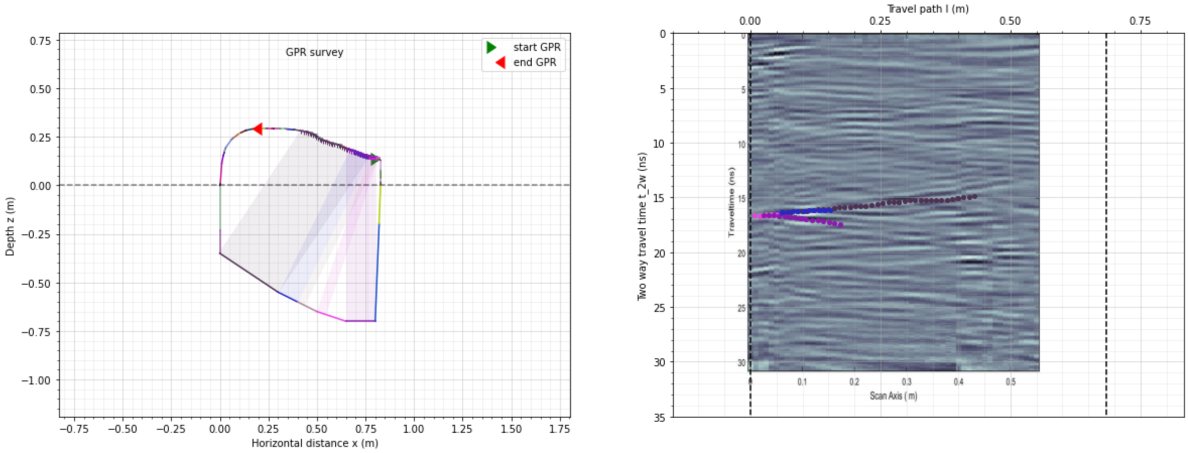

Figure H.23: Modelled GPR diagram of estimated rock contour H for line H(N) showing the reflection surfaces in various colors corresponding to rock surfaces.

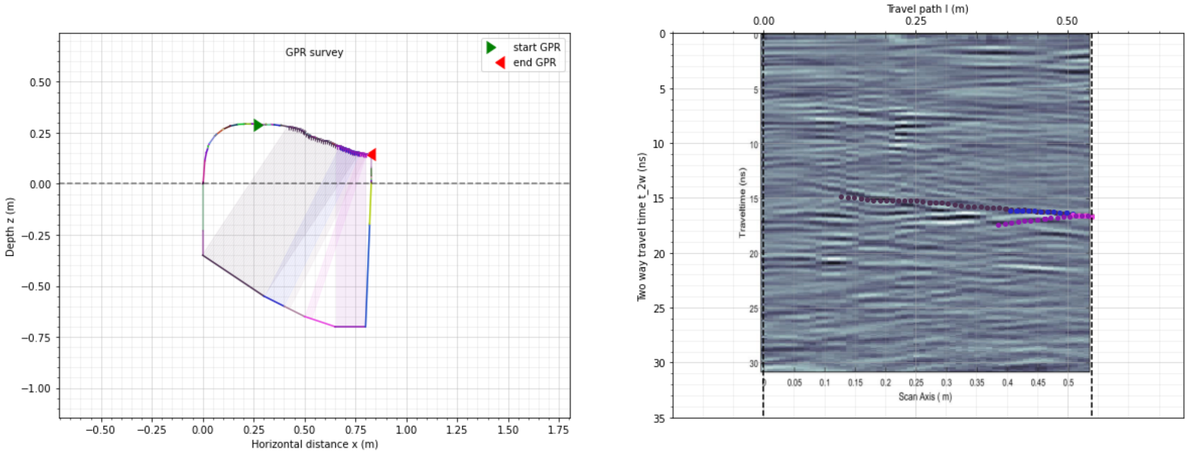

Figure H.24: Modelled GPR diagram of estimated rock contour H for line H(R) showing the reflection surfaces in various colors corresponding to rock surfaces.